

**AFRL-SN-HS-TR-2006-0047 Volume I**

---

**PROCEEDINGS OF THE 2006 ANTENNA APPLICATIONS SYMPOSIUM  
Volume I of II**

**Daniel Schaubert et al.**

**University of Massachusetts at Amherst  
Electrical and Computer Engineering  
100 Natural Resources Road  
Amherst MA 01003**

**Final Report**

**26 February 2007**

**APPROVED FOR PUBLIC RELEASE; DISTRIBUTION UNLIMITED**



**AIR FORCE RESEARCH LABORATORY  
Sensors Directorate  
Electromagnetics Technology Division  
80 Scott Drive  
Hanscom AFB MA 01731-2909**

## NOTICE AND SIGNATURE PAGE

Using Government drawings, specifications, or other data included in this document for any purpose other than Government procurement does not in any way obligate the U.S. Government. The fact that the Government formulated or supplied the drawings, specifications, or other data does not license the holder or any other person or corporation; or convey any rights or permission to manufacture, use, or sell any patented invention that may relate to them.

This report was cleared for public release by the Electronic Systems Center Public Affairs Office for the Air Force Research Laboratory Electromagnetic Technology Division and is available to the general public, including foreign nationals. Copies may be obtained from the Defense Technical Information Center (DTIC) (<http://www.dtic.mil>).

AFRL-SN-HS-TR-2006-0047 HAS BEEN REVIEWED AND IS APPROVED FOR PUBLICATION IN ACCORDANCE WITH ASSIGNED DISTRIBUTION STATEMENT.

//signature//

---

HARVEY TOBIN  
Monitor

//signature//

---

DAVID D. CURTIS  
Acting Chief, Antenna Technology Branch

//signature//

---

MICHAEL N. ALEXANDER  
Technical Advisor  
Electromagnetic Technology Division

This report is published in the interest of scientific and technical information exchange, and its publication does not constitute the Government's approval or disapproval of its ideas or findings.

# REPORT DOCUMENTATION PAGE

*Form Approved*  
*OMB No. 0704-0188*

Public reporting burden for this collection of information is estimated to average 1 hour per response, including the time for reviewing instructions, searching existing data sources, gathering and maintaining the data needed, and completing and reviewing this collection of information. Send comments regarding this burden estimate or any other aspect of this collection of information, including suggestions for reducing this burden to Department of Defense, Washington Headquarters Services, Directorate for Information Operations and Reports (0704-0188), 1215 Jefferson Davis Highway, Suite 1204, Arlington, VA 22202-4302. Respondents should be aware that notwithstanding any other provision of law, no person shall be subject to any penalty for failing to comply with a collection of information if it does not display a currently valid OMB control number. **PLEASE DO NOT RETURN YOUR FORM TO THE ABOVE ADDRESS.**

<b>1. REPORT DATE (DD-MM-YYYY)</b> 26-02-2007		<b>2. REPORT TYPE</b> FINAL REPORT		<b>3. DATES COVERED (From - To)</b> 20 Sep 2006 - 22 Sep 2006	
<b>4. TITLE AND SUBTITLE</b>  Proceedings of the 2006 Antenna Applications Symposium, Volume I				<b>5a. CONTRACT NUMBER</b> F33615-02-D-1283	
				<b>5b. GRANT NUMBER</b>	
				<b>5c. PROGRAM ELEMENT NUMBER</b>	
<b>6. AUTHOR(S)</b>  Daniel Schaubert et al.				<b>5d. PROJECT NUMBER</b>	
				<b>5e. TASK NUMBER</b>	
				<b>5f. WORK UNIT NUMBER</b>	
<b>7. PERFORMING ORGANIZATION NAME(S) AND ADDRESS(ES)</b> University of Massachusetts Amherst Electrical and Computer Engineering 100 Natural Resources Road Amherst, MA 01003				<b>8. PERFORMING ORGANIZATION REPORT</b>	
<b>9. SPONSORING / MONITORING AGENCY NAME(S) AND ADDRESS(ES)</b> Electromagnetics Technology Division Sensors Directorate Air Force Research Laboratory 80 Scott Drive Hanscom AFB MA 01731-2909				<b>10. SPONSOR/MONITOR'S ACRONYM(S)</b> AFRL-SN-HS	
				<b>11. SPONSOR/MONITOR'S REPORT NUMBER(S)</b> AFRL-SN-HS-TR-2006-0047	
<b>12. DISTRIBUTION / AVAILABILITY STATEMENT</b> APPROVED FOR PUBLIC RELEASE; DISTRIBUTION UNLIMITED; ESC 07-0269, 22 FEB 2007					
<b>13. SUPPLEMENTARY NOTES</b> Volume I contains pages 1 – 239 Volume II contains pages 240 - 494					
<b>14. ABSTRACT</b>  The Proceedings of the 2006 Antenna Applications Symposium is a collection of state-of-the art papers relating to antenna arrays, millimeter wave antennas, simulation and measurement of antennas, integrated antennas, and antenna bandwidth and radiation improvements.					
<b>15. SUBJECT TERMS</b> Antennas, phased arrays, digital beamforming, millimeter waves, antenna measurements					
<b>16. SECURITY CLASSIFICATION OF:</b>			<b>17. LIMITATION OF ABSTRACT</b>	<b>18. NUMBER OF PAGES</b>	<b>19a. NAME OF RESPONSIBLE PERSON</b>
<b>a. REPORT</b> Unclassified	<b>b. ABSTRACT</b> Unclassified	<b>c. THIS PAGE</b> Unclassified			Harvey Tobin
			UU	251	<b>19b. TELEPHONE NUMBER (include area code)</b> N/A

Standard Form 298 (Rev. 8-98)  
Prescribed by ANSI Std. Z39.18





## TABLE OF CONTENTS

**2006 ANTENNA APPLICATIONS SYMPOSIUM (Volume I & II),  
20 - 22 September 2006, Monticello, Illinois**

<b>Wideband Printed Antenna for Tactical Terrestrial Vehicles</b> R.B. Waterhouse and D. Novak	<b>1</b>
<b>Some Matched Resonators with Applications to Small Antennas</b> Paul E. Mayes and Paul W. Klock	<b>23</b>
<b>Planar and Conical Projections of Multifunctional Two-Arm Sinuous Antennas</b> Michael C. Buck and Dejan S. Filipovic	<b>37</b>
<b>Some Considerations for Compact Resonant UHF PIFAs</b> Sergey N. Makarov, Shashank D. Kulkarni and Reinhold Ludwig	<b>56</b>
<b>UHF Band RFID Tag Antenna with a Symmetric Structure Mountable on Metallic Platforms</b> Sung-Joo Kim, Hanphil Rhyu, Seung-Hoon Baek, Frances J. Harackiewicz and Byungje Lee	<b>68</b>
<b>Small Antennas and Arrays for Wireless Communications</b> Yuanxun Ethan Wang	<b>80</b>
<b>Development of a Slotted Substrate Integrated Waveguide (SIW) Array Antennas for Mobile DBS Applications</b> Songnan Yang, Aly E. Fathy and Shady H. Suleiman	<b>103</b>
<b>Direct Modulation of an L-Band Microstrip Patch Antenna Using Integrated Pin Diodes</b> Steven D. Keller, W. Devereux Palmer and William T. Joines	<b>132</b>
<b>Tri-band Reconfigurable Antenna for Active RFID</b> Wonbin Hong, Nader Behdad and Kamal Sarabandi	<b>141</b>
<b>A Wide Band, Low Profile Array of End Loaded Dipoles with Dielectric Slab Compensation</b> Ben A. Munk	<b>149</b>

<b>On the Performance Trade-Offs Associated with Modular Element of Single- and Dual-Polarized DmBAVA</b>	<b>166</b>
M.W. Elsallal and D.H. Schaubert	
<b>New Results Using Polyomino-Tiled Subarrays for Time-Delay Control of Wideband Arrays</b>	<b>188</b>
R.J. Mailloux, S.G. Santarelli and T.M. Roberts	
<b>High Efficiency SATCOM and MILSTAR Solid State Power Amplifiers</b>	<b>203</b>
Paul J. Oleski and Sarjit S. Bharj	
<b>A Constrained Pattern Synthesis Technique for a Circular IFF Array Antenna</b>	<b>210</b>
Matthew S. Lasater and Herbert M. Aumann	
<b>Generalized CoCo Antennas</b>	<b>240</b>
Branislav M. Notaros, Miroslav Djordjevic and Zoya Popovic	
<b>A Model for MEMS-Based Perturbations in Open (Leaky) Waveguide Structures: Application to the Trough Waveguide Antenna</b>	<b>258</b>
G.H. Huff and J.T. Bernhard	
<b>On Losses Due to an Air Gap and Lateral Displacements in a Junction of Two Collinear Rectangular Waveguides</b>	<b>272</b>
Jari Paunonen	
<b>Time/Space-Probing Interferometer for Plasma Diagnostics</b>	<b>281</b>
V.A. Manasson, A. Avakian, A. Brailovsky, W. Gekelman, A. Gigliotti, L. Giubolini, I. Gordion, M. Felman, V. Khodos, V. Litvinov, P. Pribyl and L. Sadovnik	
<b>Near Field Target DOA Simulation Using Antenna Arrays</b>	<b>294</b>
Louis Botha and Jacques Cilliers	
<b>Wideband Folded Horn Antenna Array for 20kV Impulse</b>	<b>314</b>
Jin-Seong Lee, Jin-Woo Park, Byungwoon Jung, Frances J. Harackiewicz and Byungje Lee	
<b>Development of Conformal Antenna Materials Technology to Enable “Paint-On” Antenna Arrays for Air Force Aerospace Applications</b>	<b>330</b>
Thomas G. Campbell, C.J. Reddy and Robert C. Boyd	

<b>Design, Analysis, and Experimental Test Results of a Conformal Phased Array Painted on a Composite Wing</b> M.C. Bailey, C.B. Ravipati, T.G. Campbell and C.J. Reddy	<b>358</b>
<b>Impedance Bandwidth of a Wire Dipole with the Split-Coaxial Balun</b> Sergey N. Makarov and Reinhold Ludwig	<b>388</b>
<b>Progress in the Design of a Small Wideband Antenna</b> Steven R. Best	<b>411</b>
<b>The Multi-Lens Array Architecture</b> Danh Luu	<b>429</b>
<b>Surface-Micromachined Ka-Band Phase-Array Antenna</b> Milan Lukic, Daniel Fontaine, Christopher Nichols and Dejan Filipovic	<b>455</b>
<b>Design and Development of Aircraft Antenna Interface Adapters – Conformal Couplers for USM-464 (EW) Test Applications</b> Thomas G. Campbell, M.C. Bailey and C.J. Reddy	<b>470</b>

## Identifiers for Proceedings of Symposia

### The USAF Antenna Research and Development Program

<b>Year</b>	<b>Symposium No.</b>	<b>Identifier</b>
1951	First	_____
1952	Second	ADB870006
1953	Third	ADB283180
1954	Fourth	AD63139
1955	Fifth	AD90397
1956	Sixth	AD114702
1957	Seventh	AD138500
1958	Eighth	AD301151
1959	Ninth	AD314721
1960	Tenth	AD244388 (Vol. 1) AD319613 (Vol. 2)
1961	Eleventh	AD669109 (Vol. 1) AD326549 (Vol. 2)
1962	Twelfth	AD287185 (Vol. 1) AD334484 (Vol. 2)
1963	Thirteenth	AD421483
1964	Fourteenth	AD609104
1965	Fifteenth	AD474238L
1966	Sixteenth	AD800524L
1967	Seventeenth	AD822894L
1968	Eighteenth	AD846427L
1969	Nineteenth	AD860812L
1970	Twentieth	AD875973L
1971	Twenty-First	AD888641L
1972	Twenty-Second	AD904360L
1973	Twenty-Third	AD914238L

## Antenna Application Symposium

<b>Year</b>	<b>Symposium No.</b>	<b>Technical Report No.</b>	<b>Identifier</b>
1977	First	_____	ADA955413
1978	Second	_____	ADA955416
1979	Third	_____	ADA077167
1980	Fourth	_____	ADA205907
1981	Fifth	_____	ADA205816
1982	Sixth	_____	ADA129356
1983	Seventh	_____	ADA142003; 142754
1984	Eighth	85-14	ADA153257; 153258
1985	Ninth	85-242	ADA166754; 165535
1986	Tenth	87-10	ADA181537; 181536
1987	Eleventh	88-160	ADA206705; 206704
1988	Twelfth	89-121	ADA213815; 211396
1989	Thirteenth	90-42	ADA226022; 226021
1990	Fourteenth	91-156	ADA237056; 237057
1991	Fifteenth	92-42	ADA253681; 253682
1992	Sixteenth	93-119	ADA268167; 266916
1993	Seventeenth	94-20	ADA277202; 277203
1994	Eighteenth	95-47	ADA293258; 293259
1995	Nineteenth	96-100	ADA309715; 309723
1996	Twentieth	97-189	ADA341737
1997	Twenty First	1998-143	ADA355120
1998	Twenty Second	1999-86	ADA364798
1999	Twenty Third	2000-008 Vol. I & II	ADA386476; 386477
2000	Twenty Fourth	2002-001 Vol. I & II	ADA405537; 405538
2001	Twenty Fifth	2002-002 Vol. I & II	ADA405328; 405327
2002	Twenty Sixth	2005-001 Vol. I & II	ADA427799; 427800
2003	Twenty Seventh	2005-005 Vol. I & II	ADA429122; _____
2004	Twenty Eighth	2005-016 Vol. I & II	ADA431338; 431339
2005	Twenty Ninth	2005-039 Vol. I & II	ADM001873
2006	Thirtieth	2006-0047 Vol. I & II	

## 2006 Author Index

Aumann, H.M.	210	Mayes, P.E.	23
Avakian, A.	281	Munk, B.A.	149
Baek, S-H.	68	Nichols, C.	455
Bailey, M.C.	358,470	Notaros, B.M.	240
Behdad, N.	141	Novak, D.	1
Bernhard, J.T.	258	Oleski, P.J.	203
Best, S.R.	411	Palmer, W.D.	132
Bharj, S.S.	203	Park, J-W.	314
Botha, L.	294	Paunonen, J.	272
Boyd, R.C.	330	Popovic, Z.	240
Brailovsky, A.	281	Pribyl, P.	281
Buck, M.C.	37	Ravipati, C.B.	358
Campbell, T.G.	330, 358, 470	Reddy, C.J.	330, 358, 470
Cilliers, J.	294	Rhyu, H.	68
Djordjevic, M.	240	Roberts, T.M.	188
Elsallal, M.W.	166	Sadovnik, L.	281
Fathy, A.E.	103	Santarelli, S.G.	188
Felman, M.	281	Sarabandi, K.	141
Filipovic, D.S.	37,455	Schaubert, D.H.	166
Fontaine, D.	455	Suleiman, S.H.	103
Gekelman, W.	281	Wang, Y.E.	80
Gigliotti, A.	281	Waterhouse, R.B.	1
Giubbolini, L.	281	Yang, S.	103
Gordion, I.	281		
Harackiewicz, F.J.	68, 314		
Hong, W.	141		
Huff, G.H.	258		
Joines, W.T.	132		
Jung, B.	314		
Keller, S.D.	132		
Khodos, V.	281		
Kim, S-J.	68		
Klock, P.W.	23		
Kulkarni, S.D.	56		
Lasater, M.S.	210		
Lee, B.	68, 314		
Lee, J-S.	314		
Litvinov, V.	281		
Ludwig, R.	56, 388		
Lukic, M.	455		
Luu, D.	429		
Mailloux, R.J.	188		
Makarov, S.N.	56, 388		
Manasson, V.A.	281		

## We Remember: John Dyson, the “Spiral-antenna Man”



John Dyson, a University of Illinois, Urbana-Champaign faculty member from 1957 to 1985, died on April 28 in Urbana at age 87.

Dyson was a key member of the famed Antenna Lab, where frequency-independent antennas were pioneered.

At the Fifth USAF Antenna Symposium in 1955 Dyson gave the paper, “The equiangular-spiral antenna” that was the first in a life-long series of publications that led to numerous applications of spiral antennas.





# WIDEBAND PRINTED ANTENNA FOR TACTICAL TERRESTRIAL VEHICLES

R. B. Waterhouse and D. Novak  
Pharad, LLC  
797 Cromwell Park Drive, Suite V  
Glen Burnie, MD 21061

***Abstract:*** There is a need for efficient, wideband radiators that can support multiple waveforms (JTRS, WNW, etc) over 225 – 2500 MHz and be readily mounted on tactical ground vehicles. Such antennas must be efficient and robust, occupy as little volume as possible, and direct most of the radiated power towards the horizon. This last requirement is very beneficial for improving terrestrial communication link performance. We have investigated a slot-based antenna that can meet these requirements. We created a wideband printed slot antenna and used exponential tapers to expand the slot. The resulting structure gives a very wideband efficient response and it also has inherently good impedance matching. To create a vehicle mount version of the antenna we placed the slot on its side perpendicular to the vehicle, avoiding the need to develop a cavity backed solution. A ruggedized version of the antenna has been developed and tested. The radiator has a gain greater than 0 dBi across the entire 225 – 2500 MHz frequency range and also directs most of the radiated power between the horizon and 45° elevation. In this paper we outline the design procedure for the antenna, present the test data, and compare the performance with other wideband technologies.

## 1 Introduction

One of the prime objectives of the Joint Tactical Radio System (JTRS) is to realize a single software radio capable of processing different waveforms from many different RF services over a wide band of frequencies [1]. The JTRS waveforms supported in the 2 MHz – 2 GHz frequency range include future Wideband Networking Waveform (WNW), Single Channel Ground Air Radio System (SINCGARS), UHF SATCOM, High Frequency (HF) Independent Side Band (ISB) with Automatic Link Establishment (ALE), Link-16, Identification Friend or Foe (IFF), Digital Wideband Transmission System (DWTS), Soldier Radio, Wireless Local Area Network (WLAN), Cellular Radio, Personal Communication Services (PCS), and future expansion of Mobile Satellite Services (MSS) [2]. The implementation of these services in JTRS will require the development of a wideband, vehicle mount antenna platform including a very sophisticated filtering procedure. The radiating structure is the key enabling technology for the proposed software defined radio since wideband amplifier technologies as well as the supporting control software for these communication links are reasonably well

advanced. The schematic in Fig. 1 highlights the multitude of communication levels and therefore the overall complexity of communications in a battlefield environment [3].

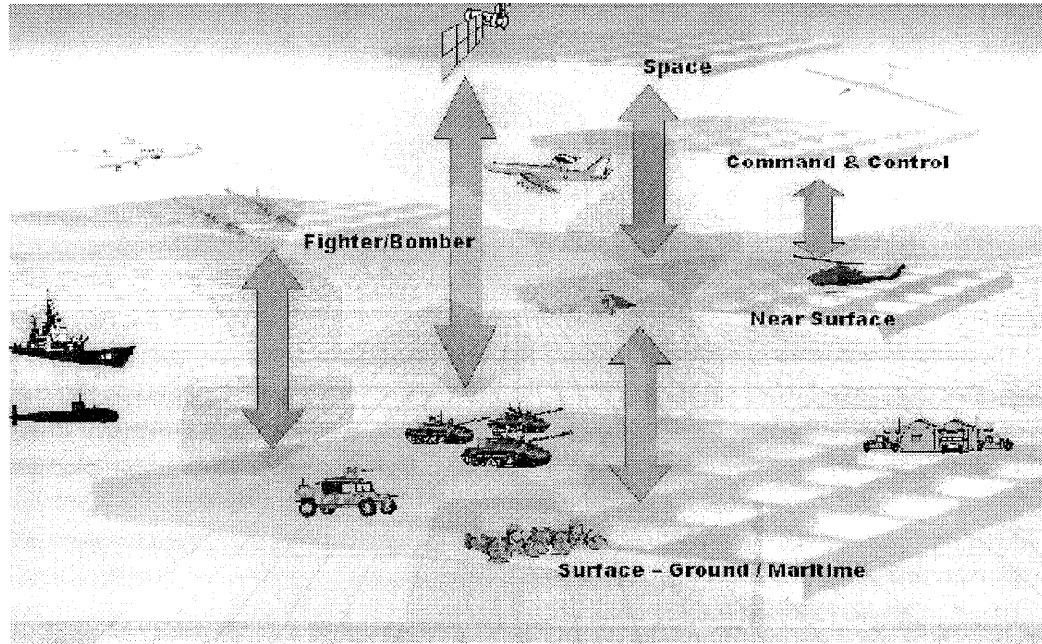


**Fig. 1** Schematic showing the levels of communications in a battlefield environment (from [3])

Of all the possible forms of radiators, probably the only class of antennas that operates over such wide bandwidths is traveling wave based. There are a variety of traveling wave based antennas that may appear suitable for this application and a summary of their general properties is given in Table I. Spiral antennas are the most common solution for wideband applications [4]. Although the cavity backed spiral antenna can give the required radiation performance, the size and weight associated with the cavity make this alternative not particularly attractive, especially for mounting on a vehicle. In contrast, the printed spiral with resistive or absorber loading [5] has all the features required for the WNW vehicle mounted antenna. However this antenna is still quite large due to the requirement of operating at frequencies near 225 MHz and also due to the loads it suffers from relatively poor efficiency, especially at the lower frequency edge.

Tapered slot antennas [6] can provide excellent bandwidth and are also very efficient as no power is wasted and dumped into a load element. However, tapered slots are usually quite large especially when required to operate at low frequencies. In addition, the radiation pattern of a tapered slot antenna is directional which prevents the use of this form of radiator for the vehicle mount since omni-directional coverage is required. The coupling to the tapered slot from a standard unbalanced transmission medium can also be inefficient, with losses greater than 3 dB.

**Table I** Comparison of wideband antenna solutions

Type of antenna	Overall complexity	Size	Bandwidth	Radiation pattern	Polarization	Efficiency	Feed complexity
Cavity backed spiral	High	Large (volume)	Large	Omnidirectional	All	moderate	Complicated
Printed spiral	Low	Moderate	Large	Omnidirectional	All	Moderate	Moderate
Tapered slot	High	Large	Large	Directional	Linear	High	Complicated
Bow tie	Low	Small	Large	Omnidirectional	Linear	Moderate	Complicated
Log periodic	Moderate	Large	Large	Directional	Depends on element	High	Moderate
Beverage	Simple	Long	Large	Directional	All	Moderate	Simple

As can be seen from Table I, bow tie slot antennas can provide a physically small radiating solution, however there is a drawback associated with this technology; in its conventional form this antenna needs a cavity backing, similar to the spiral radiator, and therefore is not really a practical solution. Also, the bandwidth of 225 – 2500 MHz is very large for conventional bow-tie slot or dipole radiators [7]. Other forms of low profile antennas such as log-periodic and Yagi-Uda arrays are simply too large for this application, even if applying fractal engineering techniques. Another point that should be made here is that fractal engineering could be applied to most of the antenna concepts summarized in Table I in order to reduce the size. However this is achieved at the expense of efficiency which can be dramatically reduced depending on the type and order of the unit cell.

The Beverage or long wire antenna in its original form is not suited to the WNW application. As summarized in Table I, this antenna is relatively long (of the order of 5 – 10 wavelengths) and its radiation pattern is typically oriented along the direction of propagation on the wire. We have recently developed printed versions of this form of radiator and have also folded the radiator back onto itself to create compact versions with omnidirectional radiation patterns [8]. However as with the previously mentioned spiral radiators, these antennas suffer from relatively low efficiency due to the required loading.

Typical specifications for the antenna assembly for a terrestrial vehicle-mount JTRS WNW antenna are summarized in Table II. As can be seen from these specifications/requirements it is imperative that most of the gain of the antenna be directed towards endfire (the horizon). This requirement is extremely difficult to meet with radiators that are integrated within the structure of the vehicle such as spirals, Beverage antennas, or conventional bow-tie slot antennas, where the maximum radiation is typically directed towards broadside (directly above the antenna).

**Table II** Pharad JTRS WNW vehicle mount antenna

<b>Frequency</b>	225 – 2500 MHz
<b>Gain</b>	0 to +3 dBi from 0 – 30° above horizon < 1000 MHz +3 to +5 dBi from 0 – 30° above horizon >1000 MHz
<b>Response</b>	Linear
<b>Polarization</b>	Vertical, Horizontal, or Circular
<b>VSWR</b>	< 2:1
<b>Impedance</b>	50 ohms
<b>Pattern</b>	Azimuth: omni-directional Elevation: Hemispherical, horizon to horizon
<b>Power</b>	100 Watts
<b>Connector</b>	Type N/TNC female, single feed
<b>Ground Plane</b>	None required
<b>Mounting</b>	4 × 3/8" bolts, 90° each on 4.5" bolt hole center
<b>Size</b>	
<b>Height</b>	10"
<b>Length</b>	19.75"
<b>Width</b>	7.5"

In this paper we present a wideband printed antenna designed for efficient operation over the JTRS WNW band of 225 – 2500 MHz and which also meets the size constraints highlighted in Table II. The antenna can be classified as a coplanar waveguide (CPW) fed profile optimized slot antenna, where we have shaped the expansion of the slot to optimize the return loss performance and efficiency of the radiator. For the vehicle mount application the slot resides perpendicular to the surface of the vehicle and therefore does not require any modifications to the vehicle surface. Importantly, such a mount directs the radiation of the antenna towards the horizon.

In this paper we summarize the design procedure for the vehicle mount antenna element as well as its radiation and return loss performance. We also present the physical design of the antenna. The paper is organized as follows. Section 2 gives an overview of the concept of the profile optimized slot antenna highlighting its generic shape and the design philosophy behind its creation. Also in this section, we summarize the design procedure for the antenna. In Section 3 we give an overview of the physical design of the antenna such as how the antenna is mounted onto a standard Army vehicle and also describe the interface to the RF cable. In Section 4 we present the measured responses of the antenna including its radiation performance and return loss response. In this section we also compare the performance of the antenna to another wideband printed antenna: the flared monopole. Finally we summarize our findings in Section 5.

## 2 Profile Optimized Slot Antenna

### 2.1 Overview

As mentioned earlier, the fundamental radiating structure we are proposing to use in this vehicle mount application is an optimized profile slot. A general schematic of the profile optimized slot is shown in Fig. 2. Here the radiator is fed by a CPW transmission line and in this particular example an exponential profile is used to taper the slot, while a parabolic tapered shape is incorporated to enclose the slot. These electromagnetically smooth transitions help give the radiator broadband characteristics. We use a CPW feed to reduce the manufacturing cost of the antenna as uni-planar structures are significantly cheaper to realize. In Fig.2 the impedance of the slot lines where the  $50 \Omega$  CPW transmission line is terminated is  $100 \Omega$ , ensuring an efficient transfer of power to the two arms of the radiator.

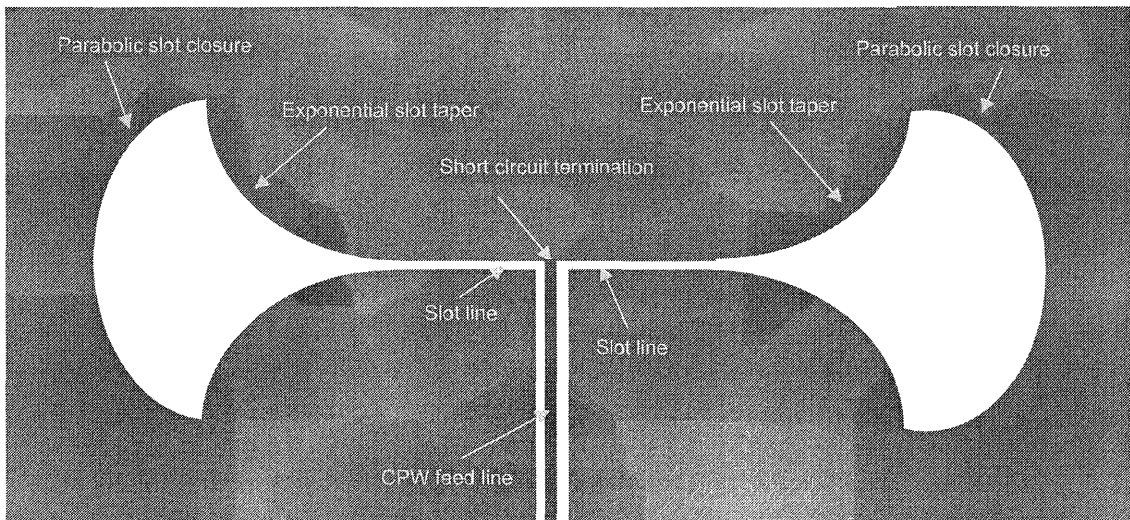


**Fig. 2** Schematic of the generalized profile optimized slot radiator

As described above, the input impedance of each half of the profile optimized slot radiator is matched to the required impedance in order to maximize the power transfer to the antennas. Fig. 2 shows the transition from the coplanar waveguide to the two slot lines of the antenna. Here a simple short circuit is used in conjunction with matching the parallel combination of the slot line impedances to the CPW impedance, in order to ensure optimum power transfer to the radiators. This design of using an impedance ratio to appropriately distribute the power inherently gives an efficient power divider. We have found through simulation that the simple transition shown in Fig. 2 gives very good wideband performance, without the need to implement more complicated transitions. We will discuss this further in the next sub-section.

## 2.2 Design Procedure

### 2.2.1 Starting Point

The design procedure always starts with the size constraints associated with the location and mounting of the antenna. As with all antennas, the larger the antenna the more efficient it will be, particularly at the lower end of the intended operating frequency range. The key is to maximize the size of the antenna for the given physical constraints. One advantage of the profile optimized printed slot is that there are many degrees of freedom in the design and we can take advantage of these to give an efficient solution for an area that may not be symmetric. Fig. 3 gives some examples of how we can apply the profile optimized printed slot to different conical geometries. As can be seen from the schematics, we can vary the individual slot profiles to accommodate different shapes.

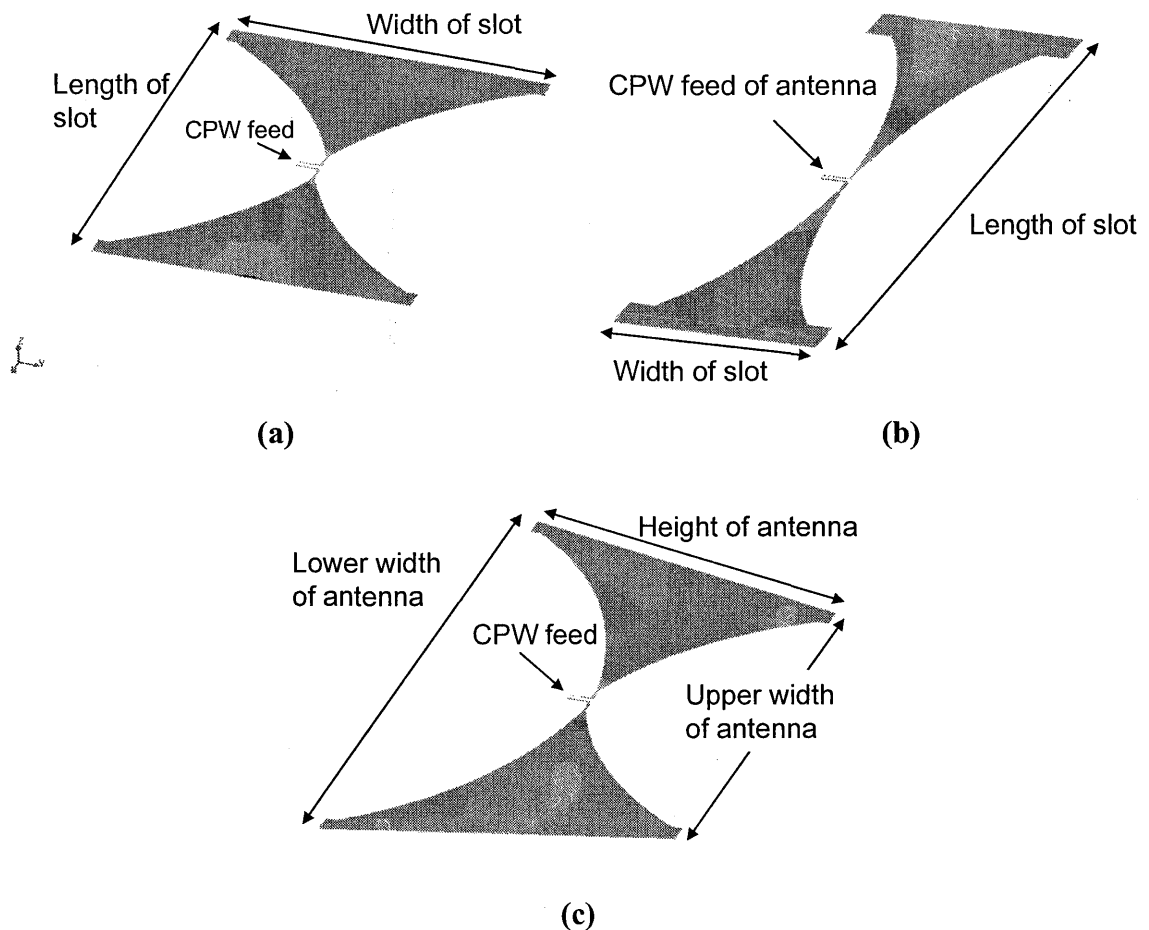


**Fig. 3** Examples of profile optimized slot shapes: (a) square; (b) rectangle; and (c) non-symmetric polygon

Once the size constraints have been established we then select the material to fabricate the radiator. As with most printed antennas, the higher the dielectric constant of the material, the physically smaller the radiator can be. Also, a higher dielectric constant material assists in the fabrication of the feed structure. As the profile optimized printed slot is typically fed by a CPW transmission line, the impedance of this line is directly related to the gaps between the ‘hot’ electrode and the two ground-planes. For CPW transmission lines, the higher the dielectric constant of the material, the larger the gaps for a  $50\ \Omega$  transmission line. Having larger gaps simplifies the fabrication process of the antenna. For the case presented here we selected a material with a thickness of 0.16 cm and a dielectric constant of 4.5 (Arlon AR 450).

### 2.2.2 Impedance transformer

Once the overall size constraint is known and the material to develop the radiator has been selected, the feed can be designed. As mentioned before, the feed for the profile optimized printed slot is relatively straightforward to design. Fig. 4 shows a photograph of the important junction of the feed, where power is delivered to each arm of the slot. Here we have a simple transition from CPW to two slot-line transmission lines. To ensure power is distributed to both arms and not reflected back to the source, we need to impedance match the ports. For a  $50\ \Omega$  CPW line, the impedance of the two slot lines must be  $100\ \Omega$  to ensure an efficient transition.

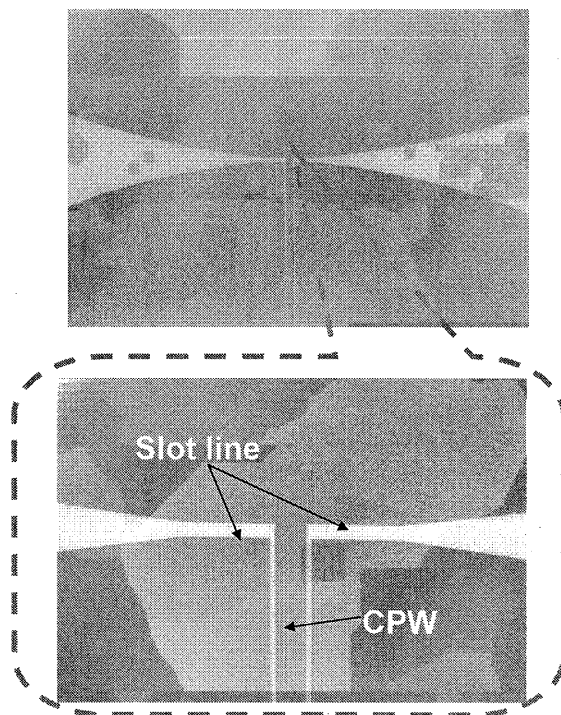


**Fig. 4** Photograph of transition for profile optimized slot

Fig. 5 shows the theoretical S-parameters of the transition shown in Fig. 4 designed on material with a dielectric constant of 4.5 and a thickness of 0.16 cm. As can be seen from the plot,  $S_{11}$  (where port 1 is the CPW port) is better than -10 dB for all frequencies across the 0.1 – 4 GHz frequency range and the power delivered to each slot line port is just below 3 dB, highlighting the efficiency of the transition. An interesting point to observe is that a complicated balun is not required for this transition, even over the large bandwidth shown in Fig. 5. This makes the solution very attractive as it simplifies the design and fabrication processes of the antenna.

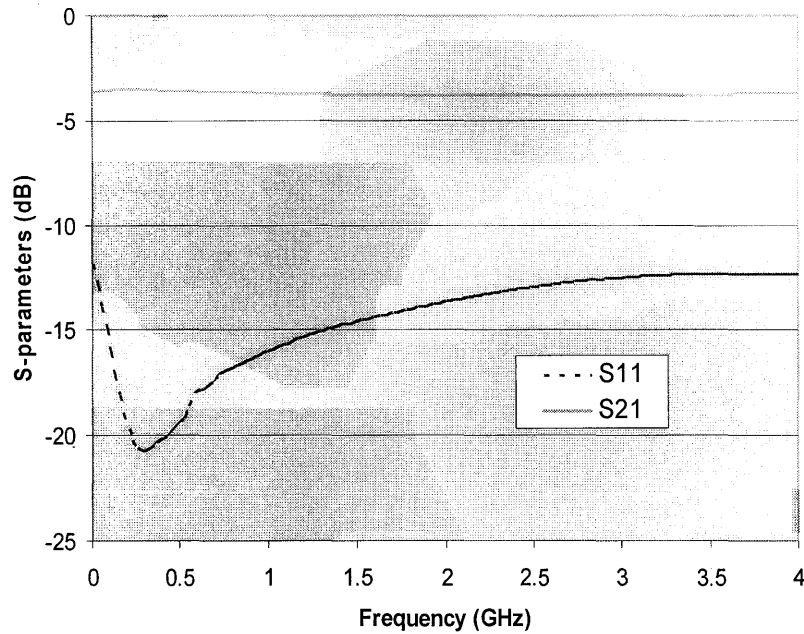


**Fig. 5** Predicted S-parameters of the transition

### 2.2.3 Profile Design

The next step in the design procedure is to develop the slot profile. There are several profiles that can be used, such as linear or piece-wise linear, however we have found that exponential profiles give the best bandwidth performance for a constrained size. This result is not surprising as it is similar to the findings for tapered slot antennas [9], with which the proposed solution shares several characteristics.

The opening factor of the profile ( $R$ ) is very important for the VSWR bandwidth of the antenna. Fig. 6 shows two cases for a profile optimized printed slot antenna, where the size of the antenna is kept constant, however the opening rate is different;  $R = 0.1$  and  $R = 0.3$  (the definition of  $R$  is highlighted in the insert of Fig. 6). As can be seen from the results presented, the lower the opening rate of the profile, the better the return loss (VSWR) performance, particularly at the lower frequency edge. For most profile optimized printed slot antennas we use profiles of less than 0.15.



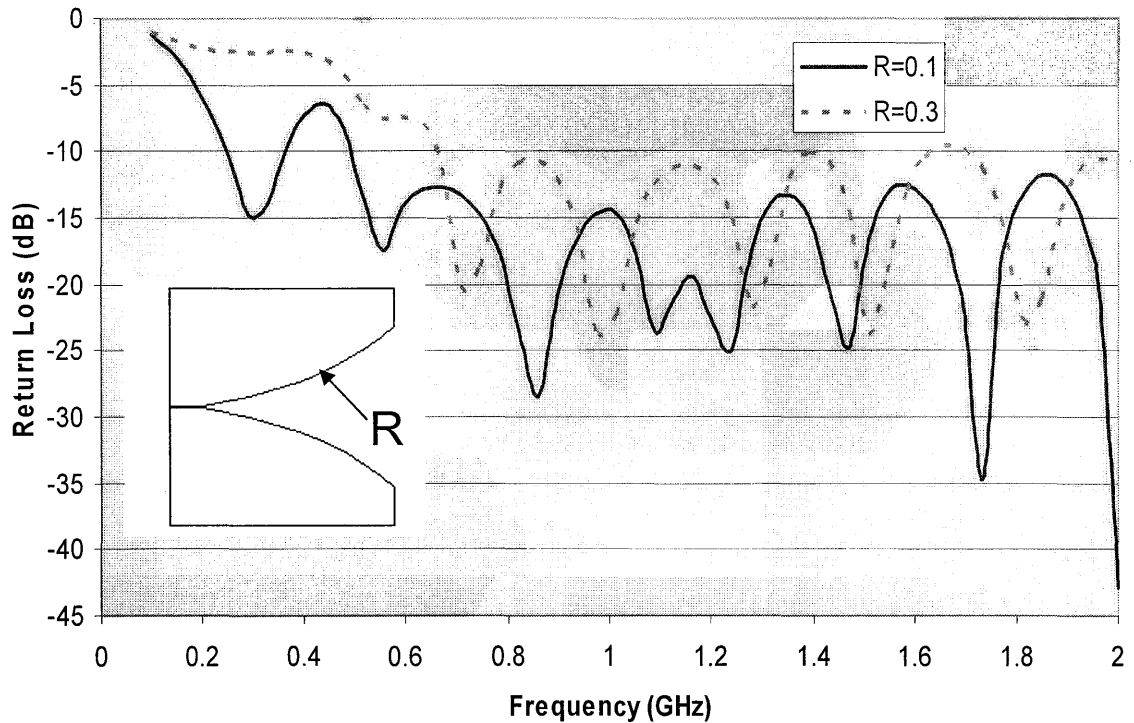


**Fig. 6** Impact of R on the return loss performance

#### 2.2.4 Design Trade-off Space

Naturally, as is the case with any antenna, size is very important and constraining the physical size compromises the performance of the radiator. It is important to establish the trade-off space in order to ensure that we achieve the best performing radiator for the given size constraints. For our base-line case a profile optimized slot of dimensions  $27.6'' \times 15.8'' \times 0.06''$  has a VSWR  $< 2:1$  between 100 MHz and 4 GHz and a gain greater than 0 dBi over this band.

We undertook a numerical investigation to determine the trade-offs associated with the size and the performance of the profile optimized slot. A profile optimized slot antenna constrained to  $13.8'' \times 7.9'' \times 0.06''$  had the following characteristics: VSWR  $< 2:1$  from 225 MHz to greater than 4 GHz; and a gain of greater than 0 dBi across this matched band. At 100 MHz, the smaller version of the profile optimized slot had a gain of -2.6 dBi and the return loss is only -4 dB. Intuitively this degradation in performance is logical as we have effectively halved the dimensions of the antenna, which we would expect should impact the return loss and gain performance. The return loss performance is directly related to the length of the tapered section of the slot; an electrically shorter tapered section will not provide effective matching between the impedance of the guided

medium and free space. Therefore we would expect more power to be reflected back to the input port of the antenna.

The gain trade-off associated with the size of the antenna is, once again, a relatively simple relationship; reducing the size of the antenna reduces the effective capture area and subsequently the gain. Through undertaking many numerical simulations we have established the following design guideline: the effective length and width of the profile optimized slot radiator must be greater than  $0.25 \lambda_0 \times 0.15 \lambda_0$  to achieve a gain of more than 0 dBi at the lowest 2:1 VSWR frequency. Here  $\lambda_0$  corresponds to the free-space wavelength at that frequency. It should be noted that this is a general guideline and does not take into consideration the properties of the material to fabricate the printed antenna.

Further size reduction of the profile optimized slot radiator can be achieved if high dielectric constant material is used, although the material needs to have low loss to ensure that the gain is not compromised. Using high dielectric constant material can improve the return loss response as it helps in the development of an efficient impedance transition from a CPW track to the coplanar stripline (CPS) (as shown in Fig. 4). As the dielectric constant of the substrate increases, it is easier to develop 50  $\Omega$  transmission lines in CPW and also 100  $\Omega$  transmission lines in CPS.

Another radiation characteristic that is directly related to the size of the antenna is the amount of ripple in the radiation patterns. Because the optimized profile slot is wideband in nature, at higher frequencies there is more ripple in the radiation patterns than at the lower frequencies. Simplistically this can be attributed to the excitation of more than one mode at higher frequencies. We have observed this phenomenon for many wideband radiators. Also, the depth of the ripple is dependent on the mounting platform.

### 2.2.5 JTRS WNW Vehicle Mount Design

Using the design strategies described in the previous paragraphs and the established radiator performance trade-off space, we designed a profile optimized slot that can perform efficiently over the 225  $\times$  2500 MHz band and is compliant with the size constraints highlighted in Table II.

Fig. 7 shows a photograph of a prototype radiator developed. In this photograph, the gold-colored metal square below the antenna is 12"  $\times$  12" in area. To maximize the dimension of the antenna, we placed it in the diagonal plane of the cube. For the radiator in Fig. 7, a profile of 0.15 was used for the slot opening. We used a rectangular section for the closure of the slot which extends 0.4" beyond the end of the exponential taper in the vertical direction and 0.7" in the lateral direction. Beyond this, we use a metallic border of 0.4" to enclose the slot. The antenna is CPW fed, which cannot be seen in Fig. 7.

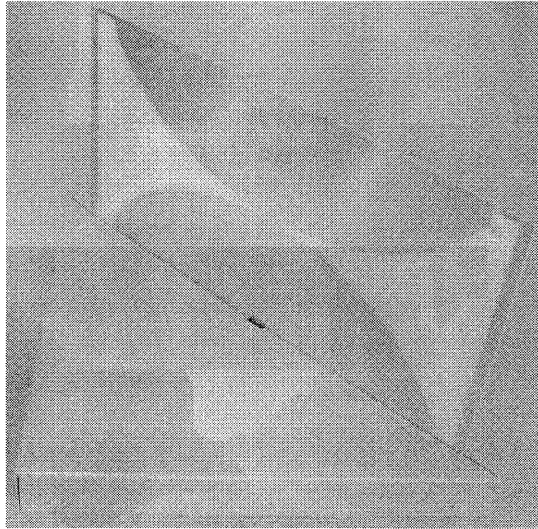


**Fig. 7** Photograph of a prototype of the vehicle mount profile optimized slot

### **3 Physical Design of Wideband Vehicle Mount Antenna**

Due to the environment in which the antenna is to be mounted, it is imperative that a ruggedized package for the radiator be developed. Here we developed a ruggedized, environmentally compliant prototype, illustrated in Fig. 8, suitable for testing in its intended environment. In this photograph, the radiator resides under the black-colored radome and its ground-plane is oval in shape. The antenna is shown sitting on a cylindrical mount in an anechoic chamber.

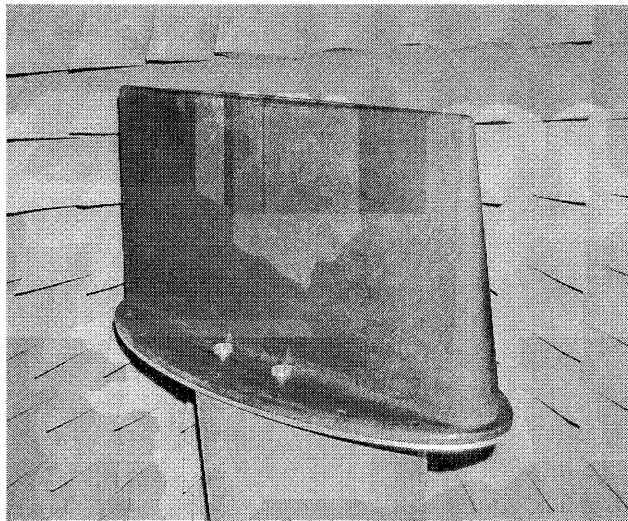


**Fig. 8** Photograph of the ruggedized vehicle mount antenna

The vehicle mount antenna assembly has three major components as shown in Fig. 9: (i) the radiator, (ii) the mounting plate, and (iii) the radome. In the exploded view shown below, the antenna is represented by a flared monopole for simplicity.

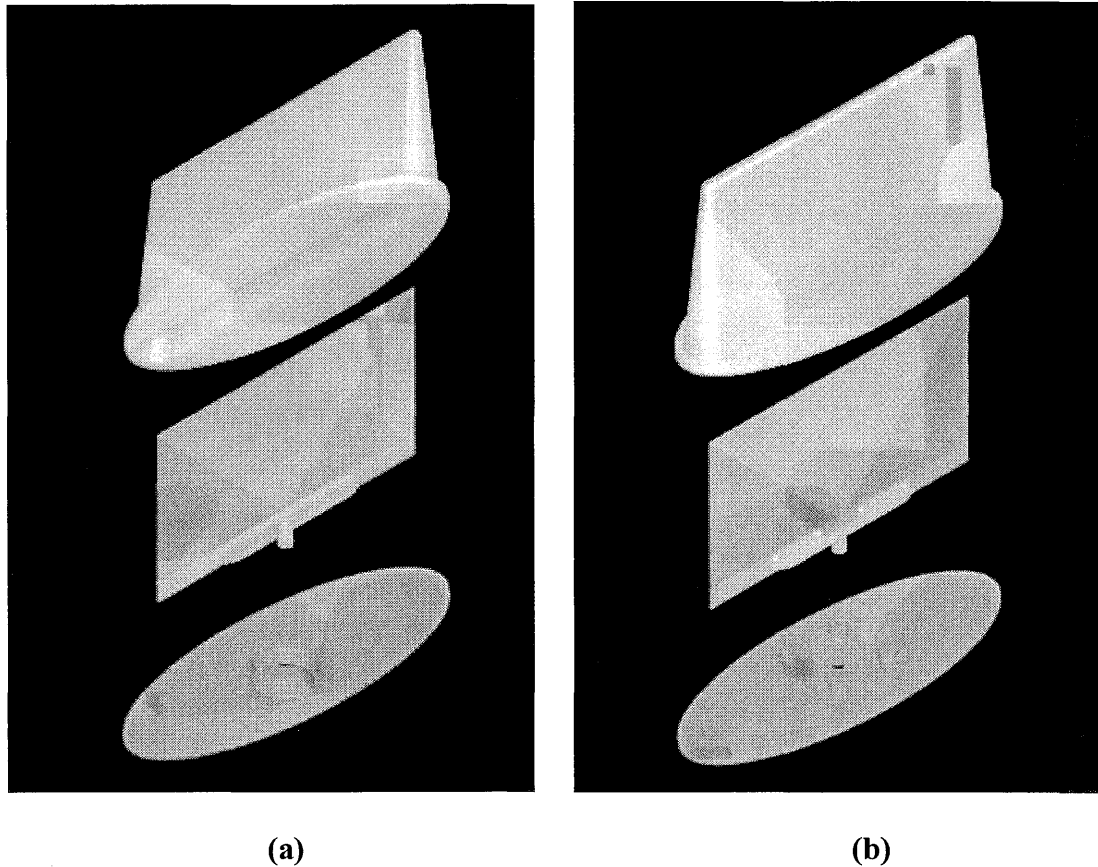


**Fig. 9** Exploded view of the vehicle mount antenna assembly: (a) from above, and (b) from below

As discussed earlier, the radiator is constructed from an Arlon 450 polytetrafluoroethylene (PTFE) microwave laminate. The radiator is attached via aluminum brackets to an aluminum mounting plate, which takes all of the stress related to the mounting. We decoupled the radiator from the TNC input connector by using coaxial cabling rigidly attached to the mounting plate between the TNC connector and the radiator. This decoupling shown in Fig. 10 ensures that the vibration of the radiator will not result in stresses on the feed connection to the radiator.

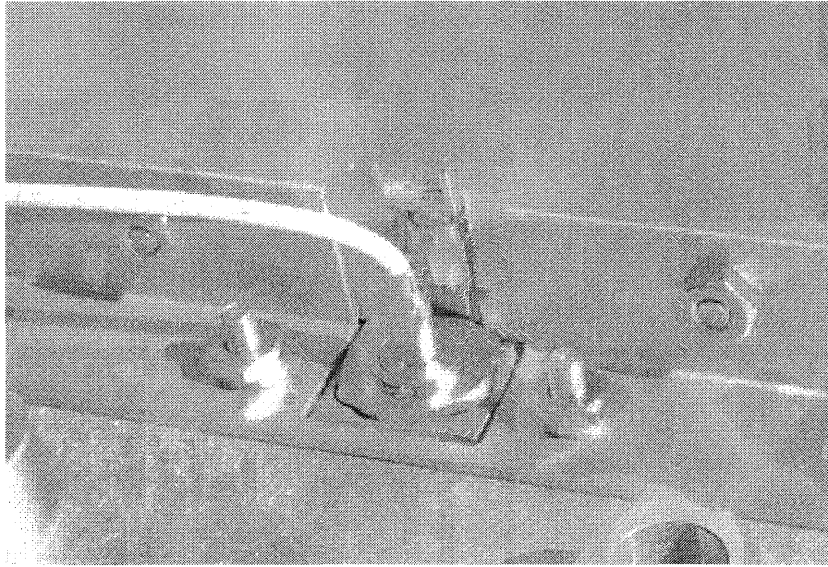
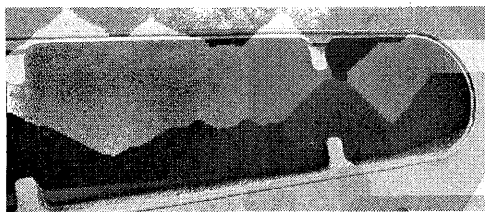
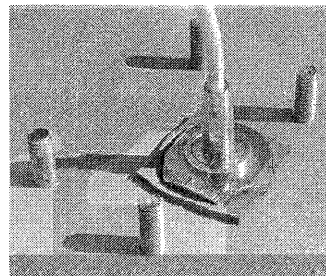


**Fig. 10** Photograph of the physical decoupling between the input TNC connector and the radiator

The entire antenna assembly is covered with a polyurethane radome. For this version we selected BJB Enterprises TC-854 rigid polyurethane for its physical properties and low cost. The silicone rubber gaskets are shown in Fig. 11 and are fitted to the inner opening of the radome and around the TNC connector, providing a weather tight seal around the radiator.



**(a)**



**(b)**

**Fig. 11** Photographs of sealing gaskets for the vehicle mount antenna assembly: **(a)** radome to mount seal, and **(b)** connector to mount seal

The antenna housing was also designed for ease of installation. An Army technician can simply attach the vehicle's TNC terminated cable to the antenna and then drop the antenna into the standard 4-hole US Army vehicle antenna mounting platform. The

antenna assembly is secured to the vehicle via the four standard  $\frac{3}{8}$ " bolts. A protective outer ring on the bottom of the antenna assembly shown in Fig. 12 protects the cable/antenna connection. The aluminum mounting plate detailed in Fig. 13 assumes all of the stress from the  $\frac{3}{8}$ " bolts, thereby preventing damage to the radome.

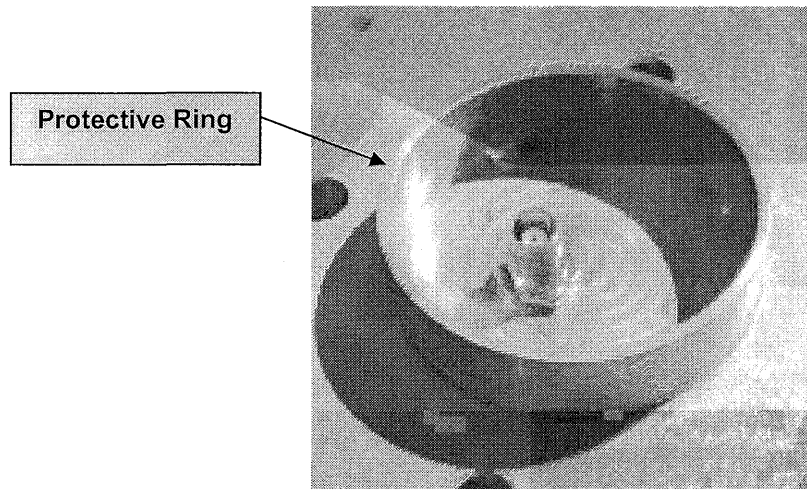


**Fig. 12** Photograph of the connector/cable protective ring

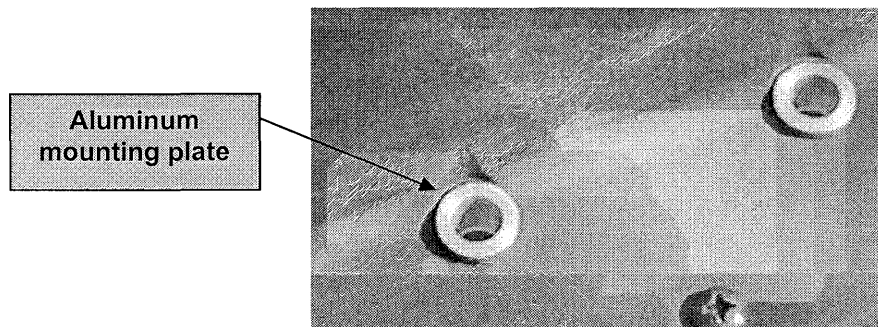


**Fig. 13** Photograph of the aluminum structure for the mounting bolts

#### **4 Results and Discussion**

In this section we summarize the experimental results for the wideband antennas developed. The return loss performance of the antennas was measured at our facilities at Pharad and the radiation patterns (including gain) were measured at NAVAIR, Patuxent River, Maryland. The coordinate system of the antenna measurement referenced in the radiation pattern plots is shown in Fig. 14.

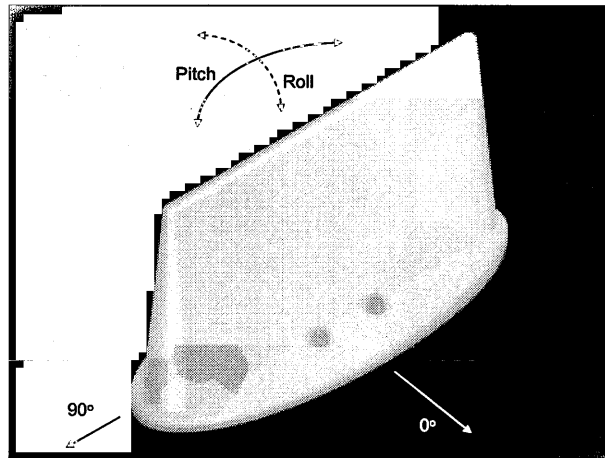


**Fig. 14** Coordinate system for the tested antennas

A summary of the radiation performance (including gain) of the profile optimized slot across the 225 – 2500 MHz frequency band is shown in Figures 15 – 21. For all these measurements a 3' × 3' ground plane was attached to the underside of the radiator. The gain of the profile optimized slot is approximately 2 dBi at 225 MHz, peaks at approximately 7 dBi at 2000 MHz, and is still greater than 3 dBi at 2500 MHz. Across the entire frequency range the gain is concentrated within 45° of the horizon, which is very beneficial for terrestrial communications to the vehicle. In fact, the profile optimized slot tends to direct significant energy towards the horizon.

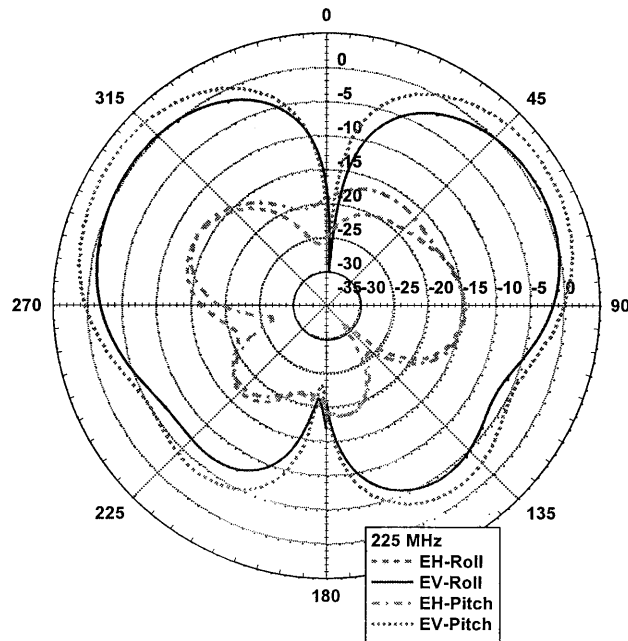


**Fig. 15** Measured radiation performance of the profile optimized slot at 225 MHz

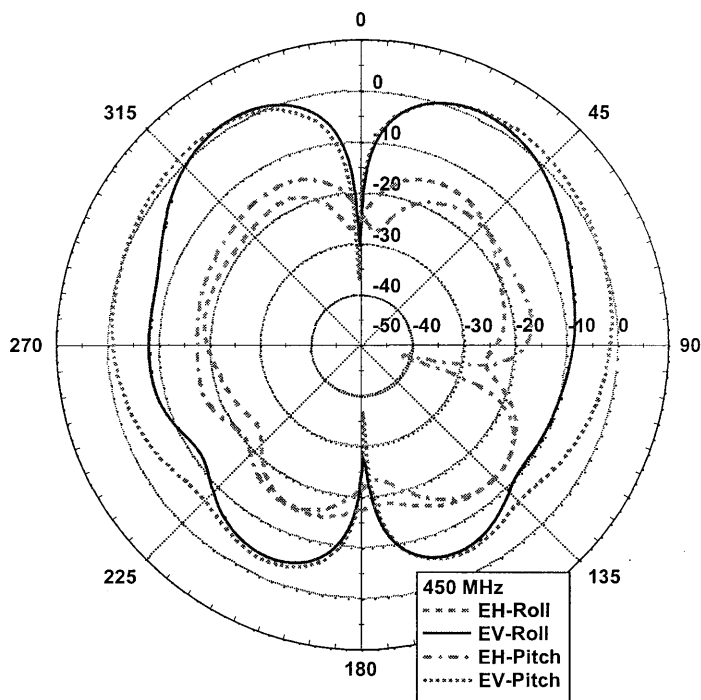


Fig. 16 Measured radiation performance of the profile optimized slot at 450 MHz

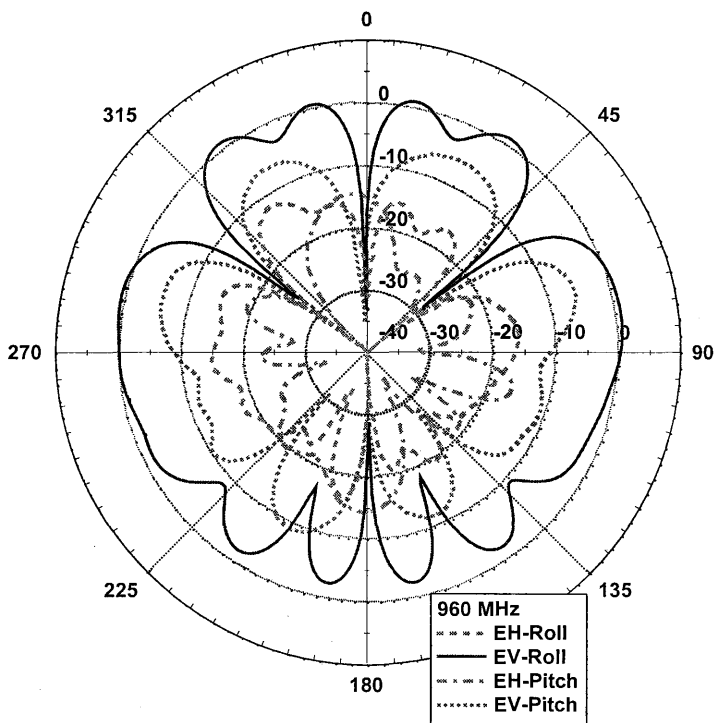
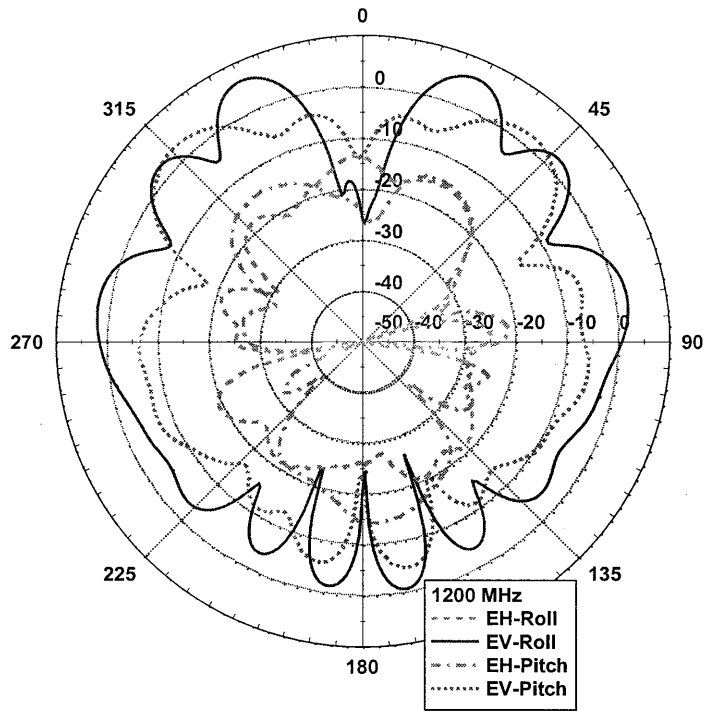
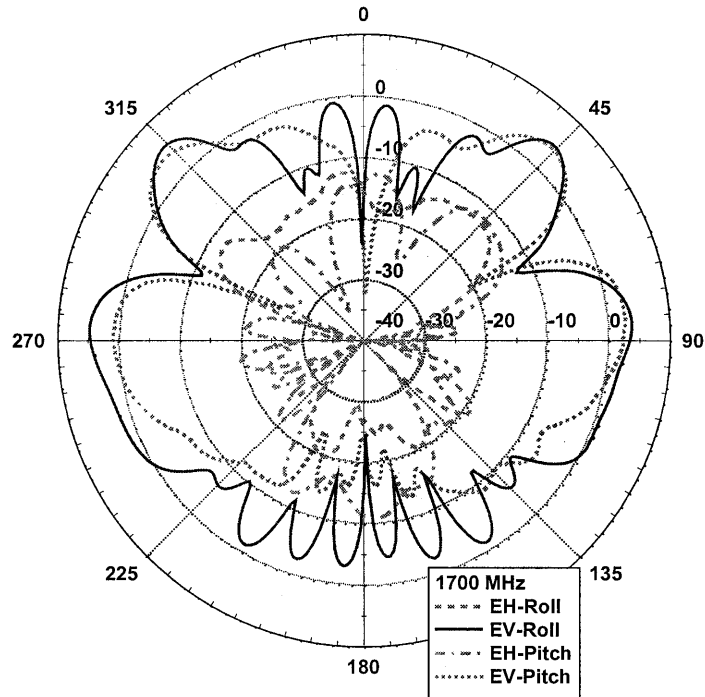


Fig. 17 Measured radiation performance of the profile optimized slot at 960 MHz





**Fig. 18** Measured radiation performance of the profile optimized slot at 1200 MHz



**Fig. 19** Measured radiation performance of the profile optimized slot at 1700 MHz

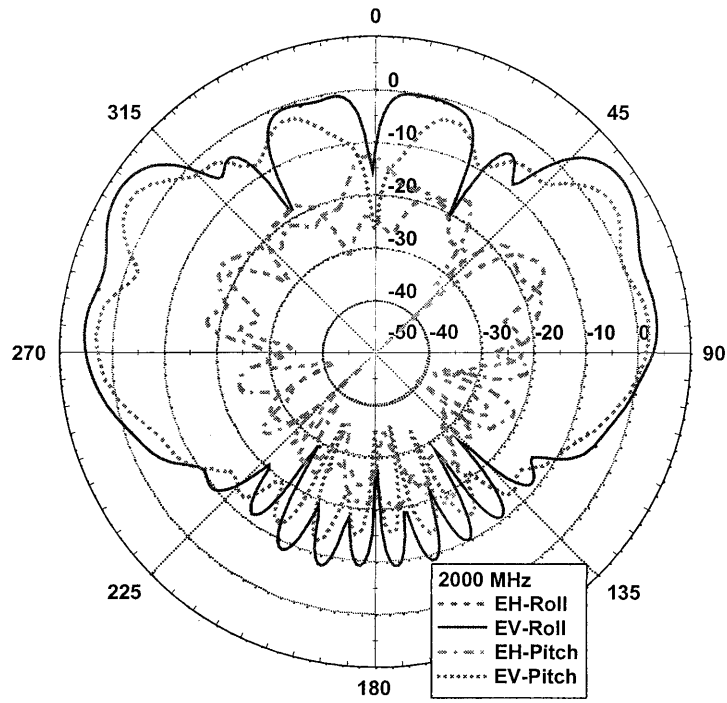


**Fig. 20** Measured radiation performance of the profile optimized slot at 2000 MHz

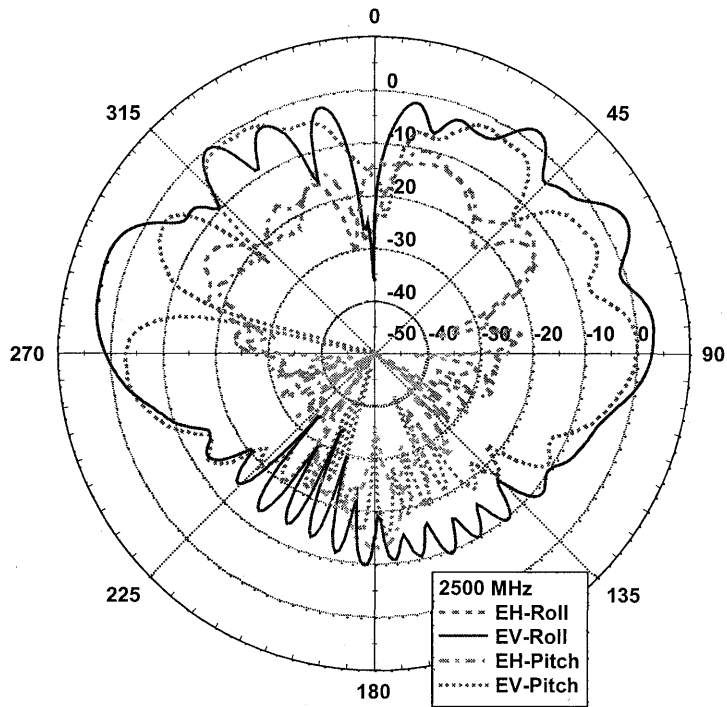


**Fig. 21** Measured radiation performance of the new profile optimized slot at 2500 MHz

We can see from the measured radiation patterns that as the frequency increases, particularly above 500 MHz, more gain undulation is present in the radiation patterns. This is a consequence of the wideband nature of the antenna and the possibility of modes being excited across it. We are presently exploring techniques to reduce the undulation.

The measured return loss of the profile optimized slot is shown in Fig. 22. The wideband nature of the radiator is evident in this return loss plot. Despite the electrically small size of the antenna, the return loss performance is very good. We believe this is due to the impedance matching approach used at the transition of the CPW to CPS transmission lines and also the exponential flaring of the slot arms. The slight mismatch in the return loss at approximately 1 GHz we believe is due to modes being excited across the slot.

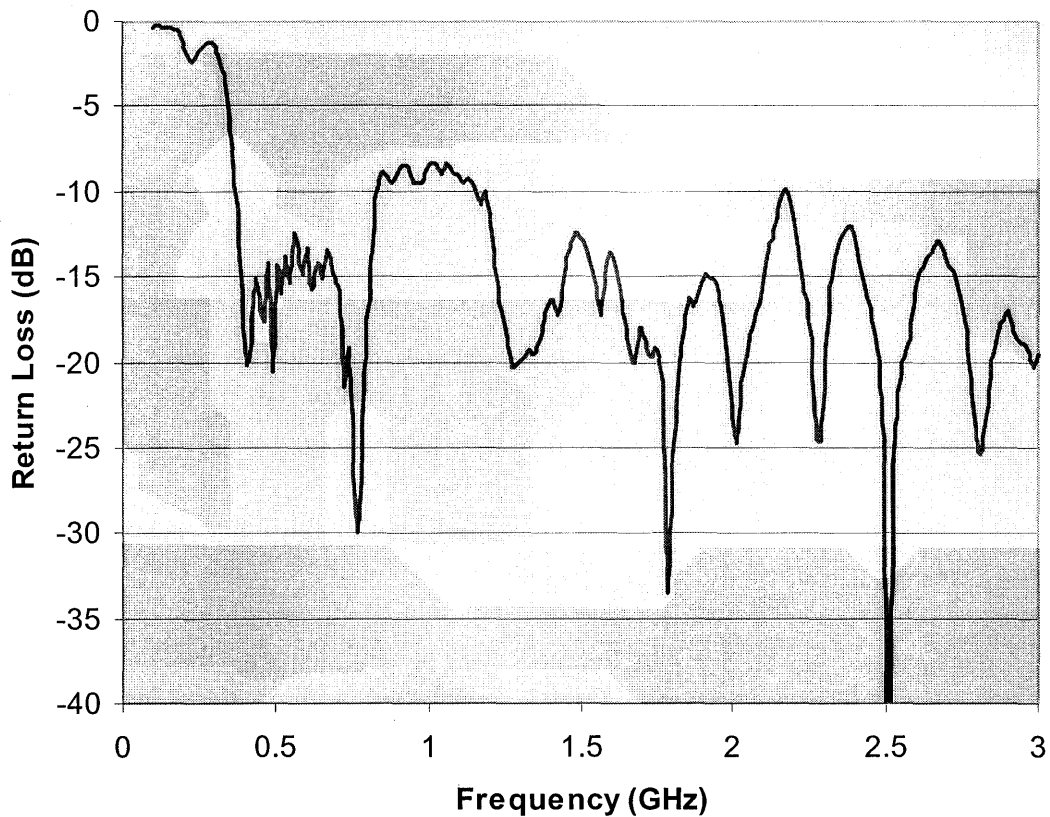


**Fig. 22** Return loss performance of new profile optimized slot

As mentioned before, we have developed other wideband radiators suitable for JTRS WNW vehicle mount systems. One in particular, which has the same overall dimensions as the radiator described in this paper, is a form of the printed flared monopole. A photograph of the radiator is shown in Fig. 23. This antenna can be readily placed in the enclosure discussed in Section 3. We have also thoroughly evaluated the performance of this antenna and we will now compare the performance of the flared monopole to the profile optimized slot.

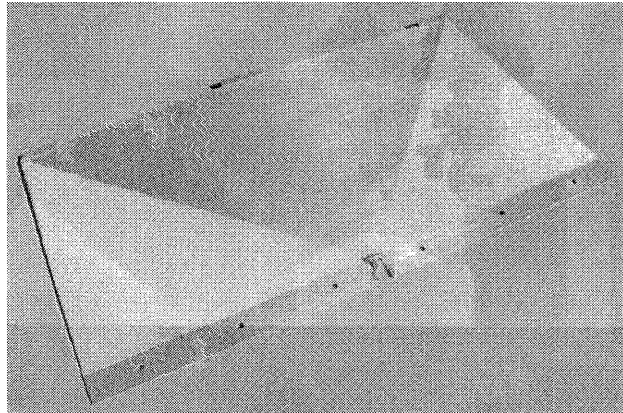


**Fig. 23** Photograph of the CPW fed printed flared monopole

Probably the most important parameter is the radiation performance of the antenna, and here the flared monopole and the profile optimized slot performed similarly. The profile optimized slot does outperform the flared monopole at the lower and upper limits of the frequency range, however in the mid frequency band the flared monopole operates better. One distinguishing characteristic between the two radiators is the amount of energy directed towards the horizon. Both radiators direct most of their energy between the horizon and  $45^\circ$  elevation, however the profile optimized slot does have higher gain towards the horizon. This may be more advantageous for terrestrial communications to the vehicle.

There is one characteristic in which there is a substantial difference between the radiators and this is the return loss performance. The profile optimized slot has a better return loss response than the flared monopole and this can be attributed to the smooth transition between the transmission line used to feed the radiator and the antenna itself. The return loss of the flared monopole can be improved by using a different taper (in Fig. 23 it is a linear taper), however this is only a second order effect. A summary of the comparison between these radiators is shown in Table III.

**Table III** Comparison of the electromagnetic performance of the flared monopole and profile optimized slot radiators

Antenna	Gain	Horizon Coverage	Return loss Bandwidth
Flared Monopole	✓✓✓	✓✓	✓✓
Profile Optimized Slot	✓✓✓	✓✓✓	✓✓✓

## 5 Conclusions

In this paper we have presented a wideband terrestrial vehicle antenna based on a printed profile optimized slot radiator mounted perpendicular to the surface of the vehicle. The antenna operates efficiently over the JTRS WNW band of 225 – 2500 MHz and inherently directs its radiation towards the horizon in the azimuth plane. We gave an overview of the basic radiating structure and summarized the design procedure to achieve a wideband solution. We also established the performance trade-offs associated with varying the size of the antenna.

In this paper we highlighted the physical design for a ruggedized terrestrial vehicle mounted version of the antenna. The radiation and return loss performance of the antenna were experimentally examined and a comparison with another wideband printed radiator was provided. The printed profile optimized slot antenna mounted perpendicular to the surface of the vehicle appears to be very suited to wideband wireless systems where most of the power needs to be directed towards the horizon.

## Acknowledgments

This project was funded under BAA #DAAB07-03-R-P650, Topic#: S0405-2. The authors are grateful to Steven Goodall, Tat Fung and George Palafox from US Army CERDEC, Ft. Monmouth, New Jersey for useful discussions and input with respect to the antennas provided during the course of the project.

## References

- [1] <http://jtrs.army.mil/>
- [2] Joint Tactical Radio System Operational Requirements Document (Extract of JROC approved final with waveform Table 4-2 and Annex E), Version 3.2, April 2003.
- [3] [www.army.mil](http://www.army.mil)
- [4] J. Dyson, “The equiangular spiral antenna”, IRE Trans. Ant. & Propn., vol AP-7, pp. 181 – 187, April 1959.
- [5] J. J. H. Wang, and V. K. Tripp, “Design of multioctave spiral-mode microstrip antennas”, IEEE Trans. Ant. & Propn., vol. 39, pp. 332 – 335, March 1991.
- [6] D. Schaubert, E. Kollberg, T. Korzeniowski, T. Thungren, J. Johansson, and K. Yngvesson, “Endfire tapered slot antennas on dielectric substrates”, IEEE Trans. Ant. & Propn., vol. 33, pp. 1392 – 1400, December 1985.
- [7] A. Serrano-Vaello and D. Sanchez-Hernandez, “Printed antennas for dual-band GSM/DCS 1800 mobile handsets”, IEE Electron. Lett., vol. 34, pp. 140 – 141, January 1998.

- [8] R. B. Waterhouse and D. Novak, "Printed Folded Beverage Antennas", to appear in *Printed Antennas for Wireless Systems and Related Applications*, R. B. Waterhouse, ed., Wiley, 2007.
- [9] C. H. Chio and D. H. Schaubert, "Parameter study and design of wide-band widescan dual-polarized tapered slot antenna arrays", *IEEE Trans. Ant. & Propn.*, vol. 48, pp. 879 – 886, June 2000.

# SOME MATCHED RESONATORS WITH APPLICATIONS TO SMALL ANTENNAS

Paul E. Mayes and Paul W. Klock  
Electromagnetics Laboratory  
University of Illinois at Urbana-Champaign  
Urbana, IL 61801  
[p.mayes@insightbb.com](mailto:p.mayes@insightbb.com), [p.klock@mail.ece.uiuc.edu](mailto:p.klock@mail.ece.uiuc.edu)

## Abstract

It has previously been demonstrated how the size of small, low-profile radiating resonators can be made even smaller by adding reactive loads across the radiating aperture. It has also been shown that the bandwidths of antennas composed of this type of small element can be increased by adding more resonators. These ideas have led to physical realizations in the form of both conical and (planar) triangular elements. However, a shortcoming of most of these antennas so far has been the need for adding an external transformer in order to change the mean impedance to levels that correspond more closely to values of commonly used devices. In this paper it is shown that many small resonators can be internally matched to a wide variety of impedances.

The internal matching technique is traced through circuit and transmission-line models to a full electromagnetic analysis that uses method of moments code. The procedures can be applied equally well to both series-connected parallel resonators and to parallel-connected series resonators. They are therefore capable of producing two physical realizations that have similar broadband impedance characteristics.

## 1. Introduction

A basic electrical resonator can be formed from only two ideal reactive elements: an inductor and a capacitor. There are two options for the connection of these elements to a source or load element. If the source/load is inserted in series (to form a loop) with the reactive elements, as shown in Figure 1, the resulting network is called a series resonant circuit and the impedance seen between terminals a-b is inductive at low frequencies, turning capacitive when the frequency exceeds the resonant value, the net reactance being zero at the resonant frequency. If the source/load is connected across each of the reactive elements, as shown in Figure 2, the resulting network may be called a shunt resonant circuit, although more popular names are “parallel resonator” or “tank.” The impedance between the source/load terminals c-d is now capacitive at low frequencies, turning

inductive above the frequency where resonance occurs (net susceptance equal to zero). Such two-element circuit resonators have a single frequency of resonance.

When the reactive elements in the above networks are taken to be lossless, the input reactance (or susceptance) moves around the rim of the Smith Chart as frequency changes. However, when resistance (conductance) is added to either of the reactive (susceptive) elements, the impedance (admittance) loci move to points in the interior of the Smith Chart. It is frequently assumed that the only power dissipated in the circuit resonator is that caused by the resistance of the inductor wire. Power lost from the network by radiation, although not possible if the network truly represents conditions at a point in space, can nevertheless be added to the circuit by the introduction of the appropriate resistive element. Such resistance therefore becomes an essential part of any point network that is an approximate equivalent of an antenna element.

Small antennas usually make use of radiating resonators that operate in the vicinity of the lowest resonant frequency where the net reactance (susceptance) is low. The impedance (admittance) of the source/load can be matched most easily if it is also predominantly real. The crux of the matching problem becomes that of making the resistance (conductance) of the antenna almost equal to that of the source or load. The problem is made difficult for small antennas because they are poor radiators. High levels of efficiency result only when power lost in the antenna is much smaller than that which is radiated. This means that the input resistance not only must be comparable to the load or source resistance, but also that the input resistance must be primarily caused by radiation loss.

We begin our consideration of the design of electrically small antennas that are capable of transferring power to or from conventional values of load/source impedance with the discussion of resonant networks of the above types that contain resistive elements that may represent radiation. Of course, when they do, these elements have values of resistance (conductance) that vary with frequency.

## 2. Circuit models

After adding resistance, the impedance (admittance) of the circuit in Figs. 1 and 2 can be written as [1]:

$$Z_n = R_n + jZ_{0n}F \left[ \frac{\omega}{\omega_n} \right] \quad (1.1)$$

$$Y_n = G_n + jY_{0n}F \left[ \frac{\omega}{\omega_n} \right] \quad (1.2)$$

where  $F \left[ \frac{\omega}{\omega_n} \right] = \frac{\left[ \frac{\omega}{\omega_n} \right]^2 - 1}{\frac{\omega}{\omega_n}}$ ,  $\omega = 2\pi f$  and  $f$  is the frequency in Hertz.  $Z_{0n} = \frac{1}{Y_{0n}} = \sqrt{\frac{L_n}{C_n}}$ ,

the “characteristic” impedance of the tank. The foregoing mathematical manipulations



have replaced the two parameters,  $L$  and  $C$  that describe a lossless tank, with two alternative parameters: the resonant frequency,  $\omega_0$ , and the characteristic impedance,  $Z_0$ . Equations (1.1) and (1.2) provide considerable information about what can be accomplished in shaping the Smith chart locus for the input impedance (admittance). It is clear that the loci will coincide with a resistance (conductance) circle on the chart, the radius of which is determined solely by the value of  $R_n(G_n)$ . By differentiating Equations

(1.1) and (1.2) with respect to  $u = \left[ \frac{\omega}{\omega_0} \right]$ , it is found that the slope of the reactance

(susceptance) plot versus frequency at resonance is proportional to  $Z_0(Y_0)$ . Hence, it is clear that, when restricted to resonant circuits, there is a limited amount of change that can be achieved in shaping the locus of input impedance (admittance). Even if the circuit representation is broadened to include loss elements that change with frequency, forcing the locus to pass near the center of the chart near resonance means that the size of the antenna in wavelengths must be adequate for that to happen.

### 3. Transmission-line models

Fortunately, the situation is changed considerably when the model is expanded to account for the finite dimensions of a radiating device. Admitting the possibility of dependence of the device fields upon a single coordinate is probably the simplest variant of the circuit model. A section of uniform transmission line proves to have an adequate approximation to the behavior of the fields in the vicinity of several antenna structures. An immediate consequence of consideration of one-dimensional radiators, in common with many antennas, is the presence of numerous resonances with limited match bands. However, the spacing of the bands around these multiple resonances may not coincide with the spacing in the bands of desired operation. Furthermore, it is often the case that each frequency of resonance is accompanied by a different radiation pattern, associated as it is with a resonant field distribution. For the applications under consideration here, namely, small antennas, only the lowest order of resonance is of interest and the accompanying radiation pattern is that typical of small antennas, yielding coverage of a broad region of space. A finite length of uniform transmission line that is terminated with mismatched loads on each end is an example of the type of one-dimensional resonator that we have in mind.

A section of line terminated in an open on one end and a short on the other, as shown in Figure 3, is resonant when the length is equal to one-quarter of the operating wavelength, half the length of the popular half-wave dipole. At any interior point on the line the impedance looking toward the open will be capacitive and that looking toward the short will be inductive. If a source/load is inserted (in a balanced way) at any point in the conductor(s) of the line, the impedance at the source/load will behave in a manner similar to that of the series resonator of Fig. 1. If a source/load is connected between the two conductors at any point of the line, the impedance at the source/load will behave in a manner similar to that of the parallel resonator of Fig. 2. However, the locus of the input impedance (admittance) versus frequency will depend upon the location of the point of observation (input). Once the input point has been established, the capacitive reactance on one side and the inductive reactance on the other side could be obtained by lumped elements and it would seem that the piece of transmission line would not be needed. If,

however, a major portion of the radiation from the structure or the desired impedance transformation is due to the length of the line section, then terminating resistance (conductance) would also change so that there would be a limit beyond which shorter lengths of line would not be practical.

Figure 5 is a Smith chart that illustrates how the input impedance changes as a function of the location of the sources of the system shown in Figure 4. It is apparent from these data that the locus would pass through the center of the chart when the feedpoints are located slightly more than 3 cm from the right-hand end of the resonator.

The length of the t-line resonator can be decreased by increasing the reactance of the terminations. Computed input impedance loci for a shorter resonator are shown in Figure 6. Once again, it is apparent that the proper choice of an offset feedpoint will result in a match.

#### 4. Electromagnetic Field Models

It is well known that the input impedance of a dipole antenna is capacitive for frequencies below resonance, displays a resonance when the length is slightly shorter than one-half wavelength, and is inductive for frequencies just above the first resonance. The dipole, like the t-line resonator, displays multiple higher-order resonances as frequency increases. Since we are here primarily interested in small antennas, we will consider only the lowest-order resonance. Comparing a dipole antenna with a t-line resonator, we expect the size to be reduced by increasing the capacitive reactance on one end and/or the inductive reactance on the other. Figure 7 shows the diagram of an offset-fed, loaded antenna of one type that has been investigated in this work. The open-circuited line has been replaced by a parallel-plate capacitor. This further reduces the size of the resonator. The other end takes the form of a line with expanding cross-section. For simplicity of description, the line is slightly non-uniform, having planar rather than conical top and bottom surfaces. The sides are open to allow radiation, but because of the close proximity of the top and bottom surfaces near the tip, the radiation mostly occurs at the larger open end. The radiating line is terminated with a pair of conducting straps. However, this termination does not provide a short circuit, but rather a low inductive reactance at the aperture. Since a surface patch code was used in the analysis, the rectangles and triangles that represent the patches are shown. The effect of applying voltage sources at several location within the antenna were achieved in the simulations by changing the value of the capacitance.

The geometry of the antenna was described to the computer by using some modified pieces of the FERM code [2]. The output of FERM was input to the Low-Frequency Moment Method Code [3]. Figure 8 is a Smith Chart of the input impedance for values of capacitance that result from the given dimensions. The impedance bandwidth corresponding to a mismatch VSWR of 2:1 can be read from the chart as approximately 150 MHz.

The electrical size of an antenna is often judged by the size of the smallest sphere that can contain all parts of the antenna [4]. Calling the radius of such a sphere “ $a$ ” and defining

$k = \frac{2\pi}{\lambda}$ , then  $ka = 1$  will be chosen to define the boundary within which an antenna must

reside to be considered electrically small. At resonance, the antenna of Figure 8 has  $ka \approx 1.9$  and is too large to be classified as electrically small. However, the mechanism is in place to reduce the size further by placing larger values of inductance across the aperture. The efficiency has been computed for a surface impedance of  $R_s = \sqrt{\frac{\omega\mu}{2\sigma}}$  ohms, where  $\sigma$  is the conductivity of copper ( $5.8 \times 10^7$  mhos/m),  $\mu$  is the permeability of free space ( $4\pi \times 10^{-7}$  H/m) and  $\omega = 2\pi f$  ( $f$  = frequency in Hertz and  $\omega$  is the radian frequency in radians/sec). The efficiency computed near resonance for the antenna of Fig. 8 was slightly greater than 0.9.

## 5. Increasing the bandwidth

Since the bandwidth of a single open resonator decreases as the size of the radiator decreases, the match bandwidth for the single resonators discussed above may be inadequate for many applications. The technique used in this paper for increasing the bandwidth of small antennas is to increase the number of resonators contained therein. It was previously shown [5] that increased match bandwidths could be obtained by connecting parallel resonators in series or by connecting series resonators in parallel as shown in Figure 11. When the operating frequency is between the resonant frequencies of two adjacent resonators, the resonators on one side will have a net reactance (susceptance) that is the opposite in sign to the net reactance (susceptance) of those on the other side. At some frequency in the band between any two adjacent resonances of the same type, the conditions will be right for the occurrence of a resonance of the opposite type. This point, a parallel (series) resonance occurring between two series (parallel) resonances will largely determine the diameter of a loop on the Smith chart.

## 6. Conclusions and future work

A technique has been given for designing small antennas having good match over bandwidths that are often acceptable. The procedure, internally feeding a radiating resonator, can provide a mean impedance level that corresponds closely to the input impedance of many attached devices. The laws of physics work against reducing the size of devices that must radiate. However, it is possible to reduce the size of radiating sectors by increasing the inductive terminations across the aperture. One consequence of reducing antenna size is decreased match bandwidth at high efficiency. Work has begun on applying the concepts of the circuits of Fig. 11 to increase the match bandwidth of the systems of radiating resonators with offset feeds.

Achieving a loop in the calculated impedance locus on a Smith Chart has been reported for the circuits of Figure 11. Calculations have recently confirmed that a loop can also be obtained from calculations of connections of transmission line resonators. However, in each of these cases it was simple to omit elements and thereby ignore the effects of coupling. Eliminating the coupling in systems of radiating resonators is not as easily done. Hence, it will be important in the future to use electromagnetic analysis to fully evaluate more complete models of antennas that make use of multiple radiating resonators.

The above procedures should work within the laws of physics to produce more useful devices because of the compromises made possible by increasing the complexity of the radiators in return for higher realizable gain over bandwidths of substantial width..

## 7. References

[1] P. E. Mayes and P. W. Klock, "Log-Periodic Networks of Resonant Circuits: Models for Wideband, Electrically Small Antennas," Proc. 28<sup>th</sup> Annual Antenna Applications Symp., Allerton Park, Illinois, Sept. 2004.

[2] S. Lee, D. A. Shnidman and E. A. Luchauco, "Numerical Modeling of RCS and Antenna Problems," Tech. Rep. No. 785, Lincoln Laboratory, Massachusetts Institute of Technology, December, 1987.

[3] J.-S. Zhao, W. C. Chew and P. E. Mayes, "Accurate Analysis of Electrically Small Conical Antennas by Using the Low-Frequency Method," Proc. 25<sup>th</sup> Annual Antenna Applications Symp., Allerton Park, Illinois, October 2001.

[4] H. A. Wheeler, "The Radiansphere Around a Small Antenna," Proc. IRE, vol. 47, pp. 1325-1331, August 1959.

[5] P. E. Mayes and P. W. Klock, "Models for Radiating Resonators with Applications to Electrically Small Antennas," Proc. 28<sup>th</sup> Annual Antenna Applications Symp., Allerton Park, Illinois, Sept. 2005.

**Figures**

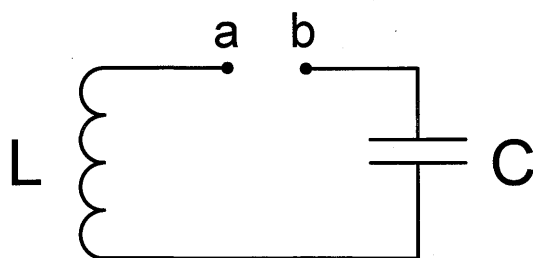


**Figure 1. A series resonant circuit.**

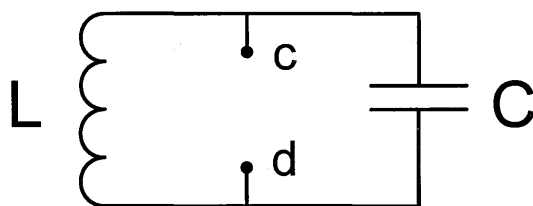


**Figure 2. A parallel resonant circuit.**

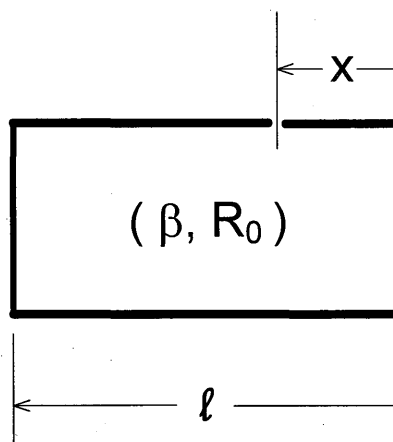


**Figure 3. A distributed resonator comprising a section of uniform transmission line terminated on one end in an open and on the other end in a short. The distance,  $x$ , from the open end is used to locate the position of a source.**

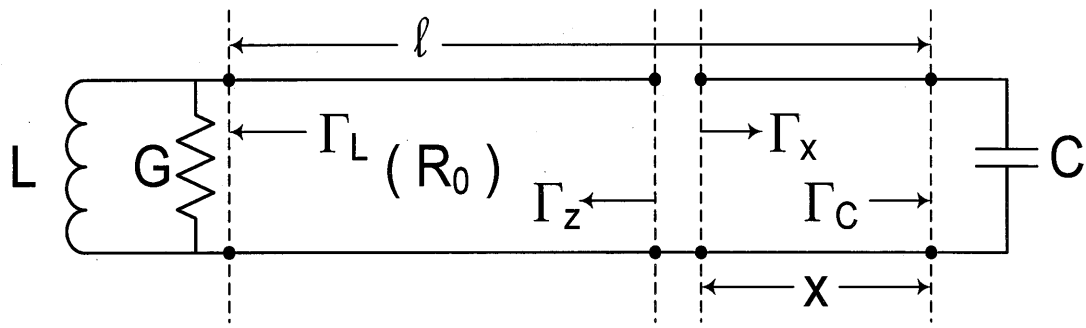


Figure 4. One-dimensional resonator comprising a section of uniform transmission line terminated on the left with an inductor and a resistor and on the right, with a capacitor. A balanced set of two voltage sources is inserted in the line at a distance  $x$  from the termination on the right.

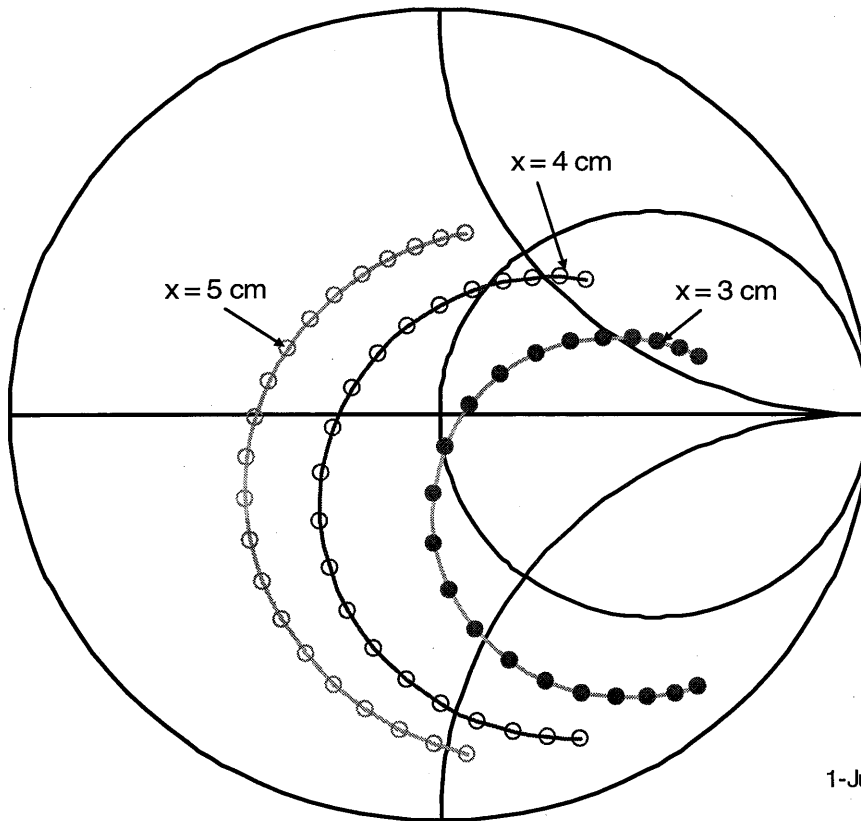
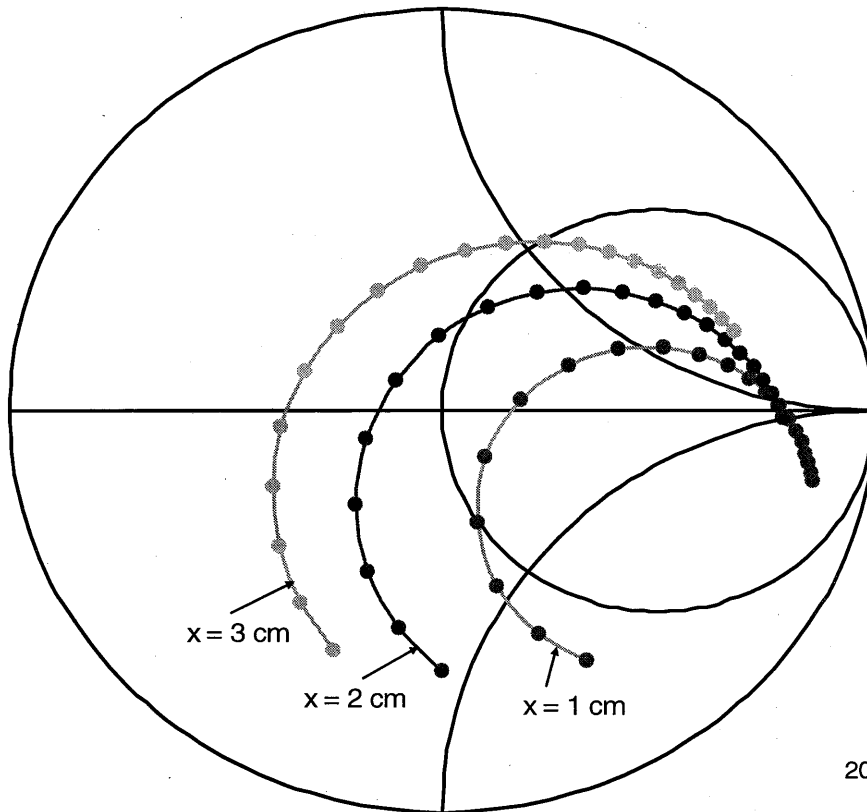
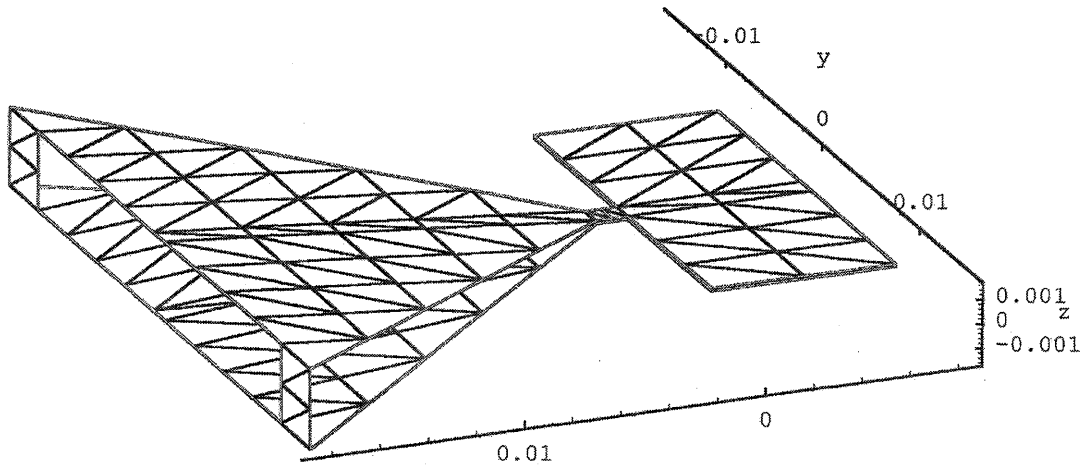


Figure 5. Loci of computed input impedance for circuit of Figure 4. “ $x$ ” is the displacement of the sources from the right-hand end of the resonator. In this example, the line section on the right is open, i.e.  $C = 0$ . The other parameters are given by  $R_0 G = 0.2$  and  $R_0 / \omega_0 L = 1$ .



**Figure 6. Loci of computed input impedances for circuit of Figure 4. “x” is the displacement of the sources from the right-hand end of the resonator. In this example, the capacitor on the right is given by  $R_o \omega_o C = 0.2$ . The other parameters are given by  $R_o G = 0.2$  and  $R_o / \omega_o L = 1$ .**



**Figure 7. Perspective drawing of a balanced, radiating sector antenna. The antenna is excited by voltage generators at the tips of the triangular walls. The two generators are joined on the right by a parallel-plate capacitor, simulated by two closely spaced plane conductors. The triangular sectors separate to form a rectangular aperture from which most of the radiation occurs. The slightly non-uniform line formed by the sectors is terminated in low-reactance strips.**



Computed Input Impedance for Two Triangular (80-deg) Sectors Canted at Ten Degrees  
Sector Length=5.59 cm, (Slant Length=7.3 cm), Equal Length Subdivisions  
with Two Terminating Strips, Widths=0.905, Lengths=0.975 cm  
Open stub across input, Height=0.035 cm, Push-pull voltages at input

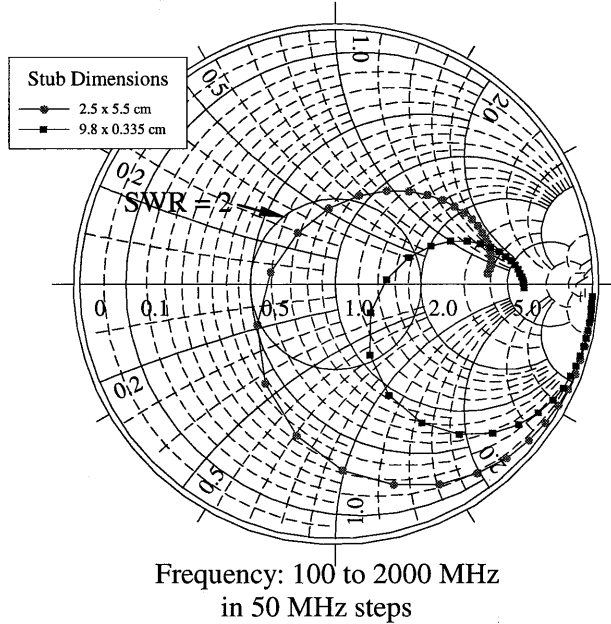


**Figure 8. Smith chart showing the computed values of the input impedance of the antenna of Figure 7.**

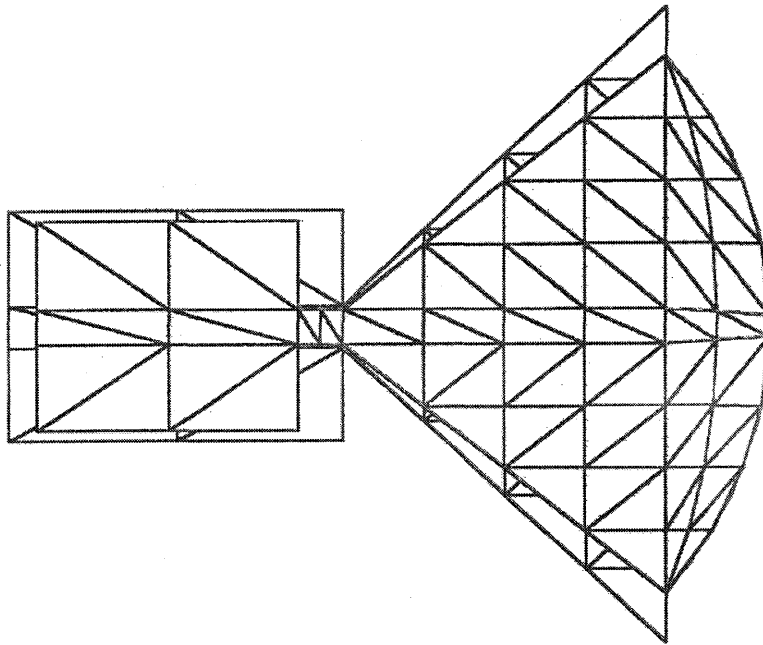
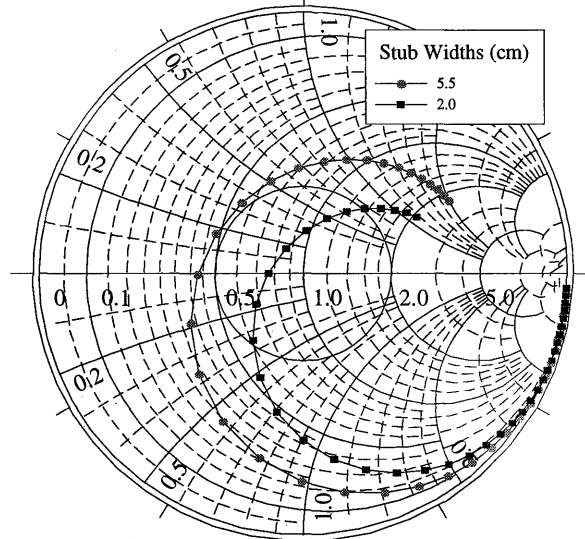


**Figure 9. Top view of an unbalanced, radiating sector antenna. The antenna is excited by one voltage generator at the tip of the upper triangular wall. The other terminal of the generator is connected to a flat conducting plate that serves as the upper part of a parallel-plate capacitor. The lower surface is a flat ground that is shaped similar to, but slightly larger than, the upper surface. The distance between the sector and the ground increases gradually to form a rectangular aperture from which most of the radiation occurs. The slightly non-uniform line formed by the sector and ground is terminated in a centered, low-reactance strip.**

Computed Input Impedance for Two Triangular (80-deg) Sectors Canted at Five Degrees  
 over a 90-degree Sector Ground, Circular Arc Truncations on Both,  
 Sector Length=4.0 cm, One Terminating Strip, Width=0.2, Length=0.35 cm  
 Open stub across input, Length=2.5, Height=0.0175 cm  
 Nlst=2, Nhwst=2, Voltage gen. at input, Ground surface 1.1 times other dims.



Frequency: 100 to 2000 MHz  
 in 50 MHz steps

**Figure 10. Smith chart showing the computed values of the input impedance of the antenna of Figure 9.**

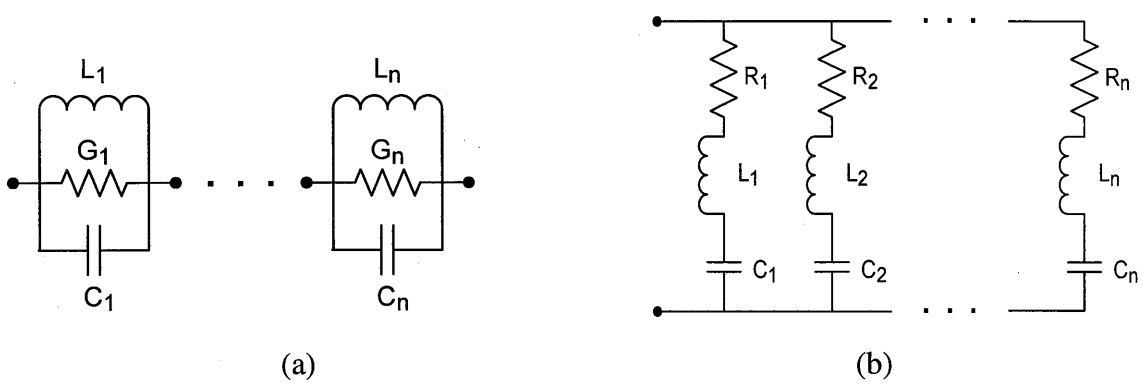


**Figure 11. One-port networks comprising (a) a series connection of parallel resonant circuits and (b) a parallel connection of series resonant circuits of simple combinations of R(G), L and C.**

# PLANAR AND CONICAL PROJECTIONS OF MULTIFUNCTIONAL TWO-ARM SINUOUS ANTENNAS

Michael C. Buck and Dejan S. Filipović  
Department of Electrical and Computer Engineering  
University of Colorado, Boulder, CO 80309-0425

**Abstract**—Two-arm, unconventionally phased sinuous antennas are proposed. Unlike traditional sinuous antennas that are operated in a broadband type mode, multiband and multipolarized performance can be achieved by taking advantage of the inability of the sinuous aperture to filter certain senses of circular polarization and by implementing a non-unique and ambiguous phase progression between the arms of the structure. By operating an antenna in this fashion, one can achieve bidirectional and multifunctional characteristics over a wide bandwidth, limited by the finite size of the sinuous aperture itself. In this manner, linear polarized bands occur between circularly polarized bands of opposite sense handedness. A conical projection of the planar sinuous geometry is also investigated to achieve unidirectional performance (front-to-back ratio > 10dB) without the use of lossy, absorptive materials typically used for planar, unidirectional sinuous and spiral-like antennas. The proposed antennas can be excited using simple and inexpensive feeds, eliminating the need for baluns, hybrids, etc. Validated numerical analyses will be presented. Parameters to be addressed include gain, axial ratio, azimuthal pattern symmetry (WoW), and input impedance.

## 1. Introduction

The sinuous antenna was originally conceived by DuHamel in 1982 [1]. This particular antenna is broadband and capable achieving dual orthogonal linear or circular polarizations from the same aperture. These antennas are based on the following equation:

$$\varphi(r) = (-1)^p \alpha_p \sin \left[ \frac{\pi \cdot \ln\left(\frac{r}{R_p}\right)}{\ln(\tau_p)} \right] \quad (1)$$

where  $\varphi$  is the angular position,  $r$  is the radial position,  $\tau$  is the growth rate,  $\alpha$  is the angular arm width,  $p$  is the cell number, and  $R_p$  is the radius of the  $p$ th cell. The growth rate can either be constant or vary logarithmically with radius. This results in the two forms shown in Fig. 1.

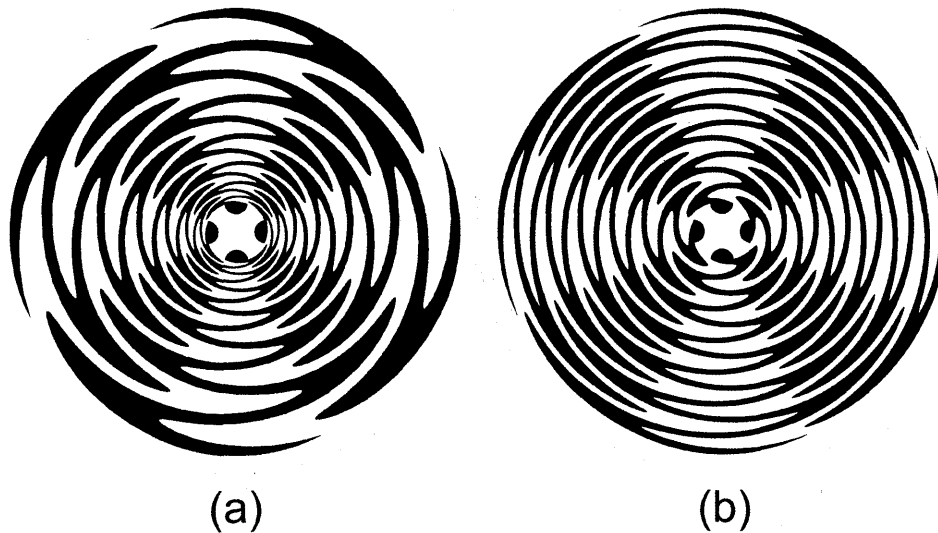


Fig. 1 - Typical four-arm sinuous antennas. (a) Constant growth rate and logarithmically varying arm width and (b) logarithmically varying growth rate and constant arm width.

However, recent research has shown that sinuous antennas can operate in a multiband and multipolarized manner [2-5] instead of the typical broadband mode. Sinuous antennas, in their typical broadband operation, can support  $(N-1)/2$  modes, where  $N$  is the number of arms the structure has. Therefore, for a single broadband mode, at least three arms are needed. In this work we will show that if an antenna is created with less than three arms for single mode operation, indeed we no longer have any broadband modes but have rather a multiband antenna at which the sense of polarization varies with each band. And like traditional broadband sinuous antennas, the operating frequency range if this multifunctional sinuous antenna is determined by the finite sizes of the feed region and the diameter of the antenna.

The planar sinuous antenna is a bi-directional structure, radiating in both half-spaces. If one desires unidirectional operation from this planar structure, an absorptive material must be placed on one side of the aperture and is typically enclosed in a cavity. An alternative to this cavity backed design is to project the planar geometry onto a cone. The resulting structure radiates from a backward traveling wave and a high front-to-back ratio is the result, without any use of lossy material as with the planar structure [6]. This work will also address the implementation of the conical projected structure on the performance of the multiband two-arm sinuous antenna.

This multiband and multipolarized operation is a result of an ambiguity in the phasing at the feed and the selective polarization filtering from alternating arm wrapping directions. So for the two-arm antenna, phase progressions of  $\{0^\circ, 180^\circ\}$  and  $\{0^\circ, -180^\circ\}$  are identical and both produce a mixture of alternating +1 and -1 modes at various bands.

This paper will present the work performed on this two-armed sinuous antenna in both planar form and conical form. For numerical analyses, EMSS's FEKO® (a method of moments software package) will be the primary tool with modeling validations from Ansoft's HFSS (a finite element software package). In the analyses ideal cases of perfect conductors (PEC) and lossless dielectrics were used. However, the addition of realistic ohmic and dielectric losses had very little effect on antenna performance.

## 1. Planar Two-Arm Sinuous Antenna

### 1.1 Geometry

For sinuous antennas, the most logical structure to begin with would be a self-complementary form. Self-complementarity refers to the ratio of metallic area to non-metallic area on the aperture plane of the antenna to be unity (or 50% metal). Self-complementary structures have shown to have the most consistent input impedance over large bandwidths than other metal to non-metal ratios [7]. For the self-complementary planar two-arm sinuous structure the multiband performance is poor in regards to the purity of the polarization at the bands. Shown in Fig. 2 is the far-field performance of several planar self-complementary geometries with a varying number of turns on each. Note that the axial ratio is greater than 4 dB at all the bands, for all geometries.

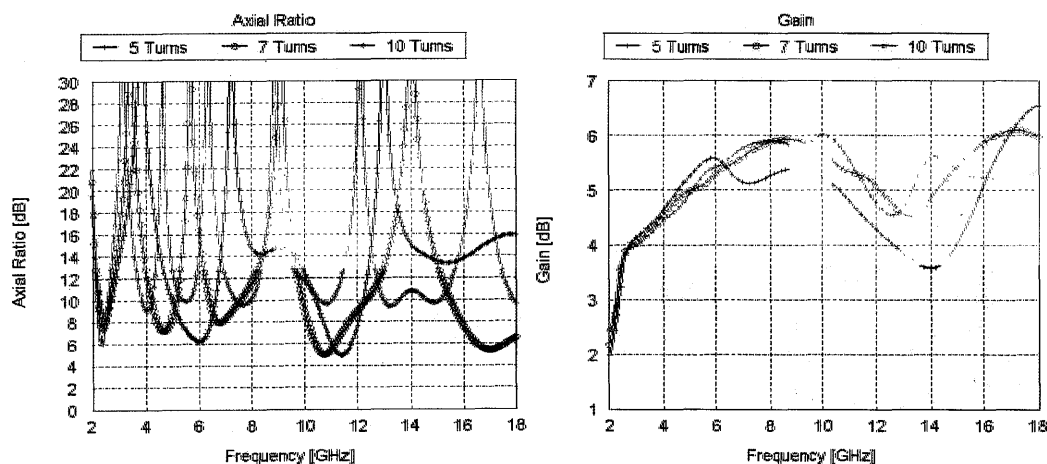


Fig. 2 - Axial ratio and gain at broadside for three planar, self-complementary two-arm sinuous antennas with varying number of turns within the same aperture size. Note the axial ratio is higher than desired for good polarization purity at the bands.

It is only when we deviate away from the 1:1 metal-to-slot ratio of self-complementarity that we achieve low axial ratios at the bands of the antenna. In addition to significantly improving performance of the antenna, narrow printed arms facilitate the fabrication by allowing one to realize the slot form of the antenna. The large area of metal in the slot antenna allows for the ease of using an infinite Dyson balun for feeding. The printed and slot geometries should vary little in their far-field performances. However, the slot geometry will have significantly reduced input impedance as given by Booker's extension of the Babinet principle [8]. But for these studies, the printed geometries will be focused on because of the much shorter computation time when compared with the slot structure.

To change the metal-to-slot ratio ( $R_{m-s}$ ) we modify both the angular cell width ( $\alpha$ ) and the rotation angle of the curve ( $\delta$ ). The effects of varying these parameters on the physical geometry are shown in Fig. 3. From Fig. 4 we can see that by varying the metal-to-nonmetal ratios that significant variations occur in axial ratio while total gain is relatively unchanged.

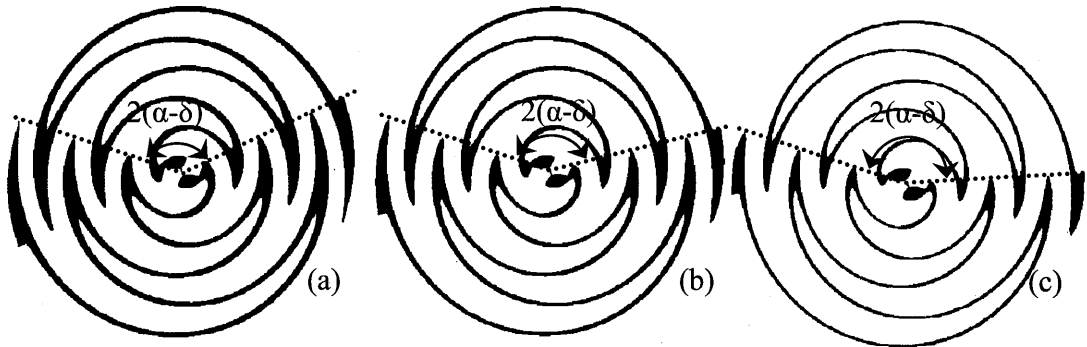


Fig. 3 – Two-arm sinuous geometry with different metal-to-slot ratios: (a)  $2(\alpha-\delta) = 140^\circ$ ,  $R_{m-s} = 0.28$  (b)  $2(\alpha-\delta) = 150^\circ$ ,  $R_{m-s} = 0.20$  (c)  $2(\alpha-\delta) = 160^\circ$ ,  $R_{m-s} = 0.12$ .

From these various geometries studied, 17% (0.20 metal-to-slot ratio) metal was the best and will be further characterized. This geometry demonstrated four bands with axial ratio better than 2 dB and gain greater than 4.5 dB at the center of the bands. In Fig. 5 both components of circular polarization can be seen showing the large cross polarization difference at the bands. Also shown are the far-field gain patterns at those bands computed with both FEKO® and HFSS®. In this plot, overlaid traces show different azimuthal cuts from  $\varphi=0^\circ$  to  $\varphi=360^\circ$ . The spread of these traces gives an indication of the WoW or azimuthal pattern symmetry. A summary of the performance characteristics of this design is shown in Table I.

A validation of the modeling for this type of structure is shown in Fig. 6, comparing FEKO® results (method of moments using the surface equivalence principle (MoM/SEP) and standard method of moments (MoM)) to HFSS® results (finite element method) for input impedance and far-field parameters. The MoM/SEP implementation allows the use of homogeneous dielectrics by meshing the surface of the dielectric using



triangular elements and applying appropriate basis functions to the elements. Boundary conditions result from the use of equivalent sources. For this SEP validation, a 0.5 mm substrate was used with a dielectric constant very close to one ( $\epsilon_r=1.001$ ). This analysis is compared to the standard MoM using the free space Green's function and to HFSS®.

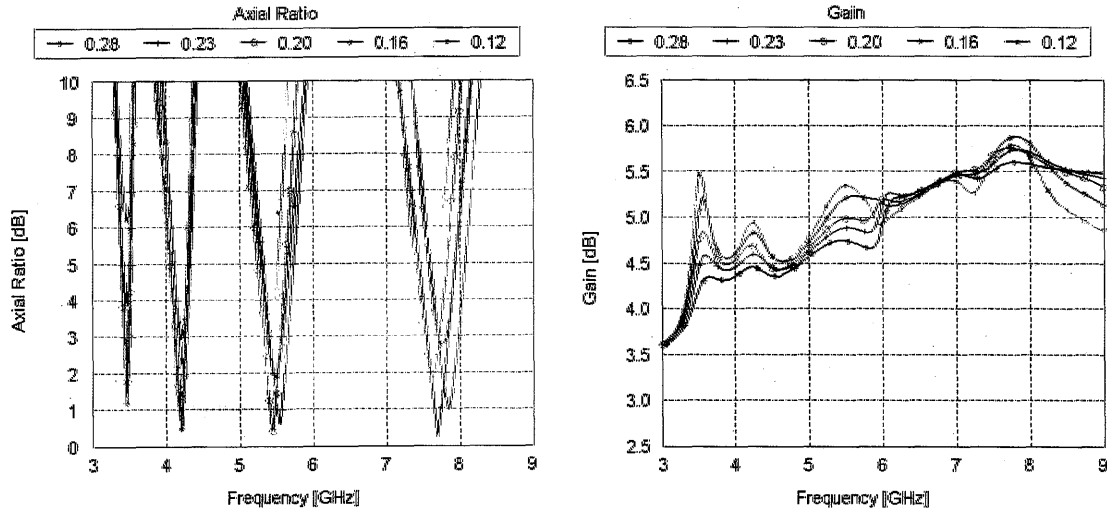


Fig. 4 - Effect of varying the metal-to-slot ratio upon axial ratio and total broadside gain.

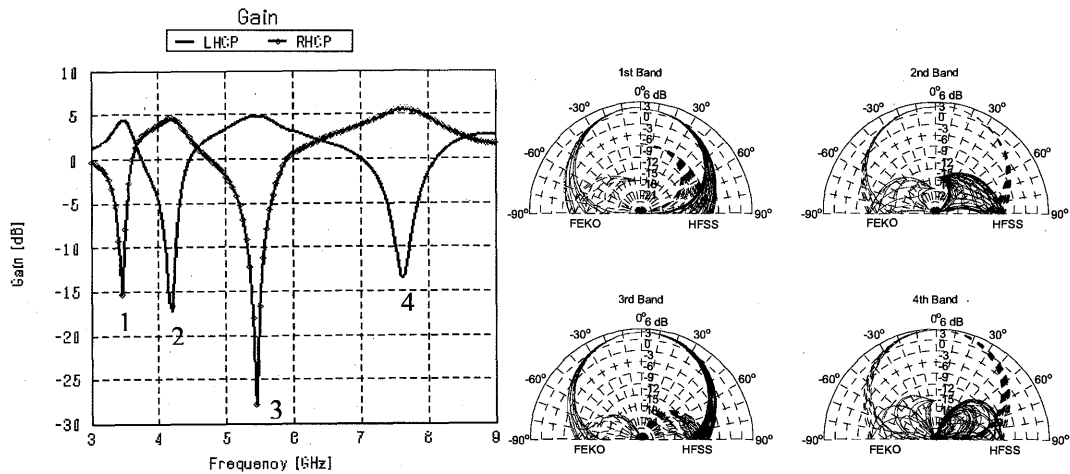


Fig. 5 – The multiband nature of this antenna can be seen from far-field broadside gain. The polarization handedness flips from band to band, with highly linear regions in between. Also shown are the co/cross polarized far-field patterns at the four bands with multiple azimuthal cuts (both FEKO® and HFSS® results are shown for comparison). The smaller the spread of azimuthal cuts, the better the WoW of the antenna.

TABLE I - TWO-ARM PLANAR SINUOUS PERFORMANCE ( $R_{M-S}=0.20$ )

Band	Polarization	Axial Ratio [dB]	Bandwidth [GHz]	Total Gain [dB]	$\theta_{3dB}$ [°]	WoW [dB]	$Z_{in}$ [ $\Omega$ ]
			(AR<4dB)			( $\theta_{3dB}$ )	
1	LH	1.63	0.11	4.8	36	0.9	275+j44
2	RH	1.43	0.18	4.8	38	0.4	383-j215
3	LH	0.80	0.30	5.1	36	0.7	149-j121
4	RH	2.10	0.30	5.8	38	1.3	544+j229
5	LH	2.67	1.30	5.2	22	2.8	81-j121

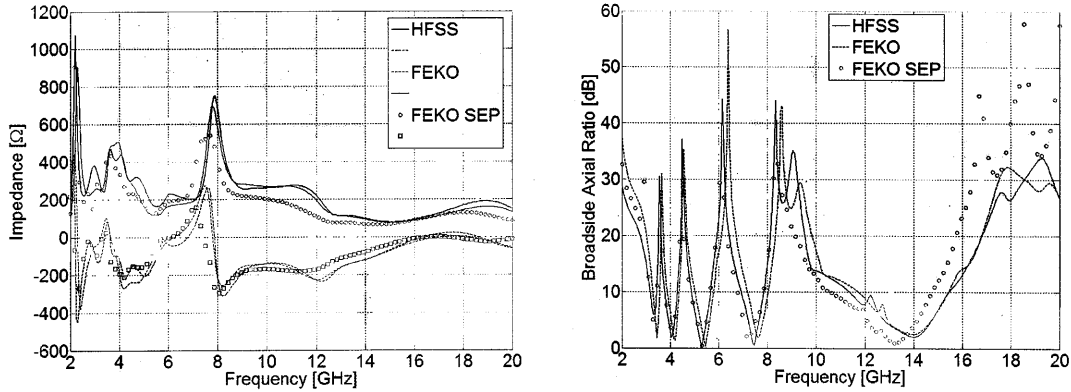


Fig. 6 – Comparison of FEKO® modeling with Ansoft’s HFSS®, a commercial finite element (FE) code. Shown is very good agreement between the two codes for input impedance and broadside axial ratio over a 10:1 bandwidth. Results given are for a 2-arm sinuous antenna with:  $\alpha=90^\circ$ ,  $\delta=15^\circ$ , Diameter = 5 cm, 5 cells, with the growth rate varying from approximately 0.8 at the outer radius to 0.4 at the center.

From this table, one can see the for higher frequency bands, the overall width of the bands is larger (i.e., 0.11 GHz at 3.45 GHz, 0.30 GHz at 5.45 GHz, and 1.30 at 13.9 GHz). The total gain remains relative constant over all the bands with a nominal value of 5.1 dB. The 3dB beamwidth also remains constant at approximately  $74^\circ$  except at the highest frequency band which is lower. Axial ratio is below 3dB at all bands and the best at central frequency bands.

In practicality, if this design were fabricated a dielectric substrate would be required. This substrate will affect the performance of this antenna in the following ways. First, the dielectric will add to the total losses in the antenna and as a result, the total gain will be reduced. Second, although the axial ratio magnitudes at the frequencies

of the bands do not change significantly with different substrate dielectric constants, their positions do. Larger dielectric constants slow the wave down and have a miniaturization effect on the performance. As a result, the bands shift toward lower frequencies with higher dielectric constants. What was the lowest band at 3.45 GHz for a dielectric of  $\epsilon_r = 1.0$  now is at 2.10 GHz with a 0.5 mm  $\epsilon_r = 9.8$  dielectric substrate.

A summary of the frequencies of the first five bands with varying substrate dielectric is shown in Table II. This substrate analysis is performed using the multi-layer Green's function implementation in FEKO®. Azimuthal pattern symmetry is improved for each band with increasing values of dielectric constant. However, this is merely a result of the shifting in frequency from the dielectric. With higher dielectrics, the frequency for a single band is lower and therefore there is reduced probability for higher order modes to be generated. This is one of the primary causes of poor WoW.

TABLE II - FREQUENCIES OF BANDS FOR VARYING SUBSTRATE DIELECTRICS (0.5MM)  
[GHZ]

Band	$\epsilon_r = 1.0$	$\epsilon_r = 2.2$	$\epsilon_r = 3.8$	$\epsilon_r = 9.8$
1	3.45	3.00	2.70	2.10
2	4.15	3.70	3.30	2.60
3	5.45	4.70	4.20	3.20
4	7.55	6.60	5.70	4.30
5	13.9	11.9	10.3	7.60

One other reason a low metal-to-slot ratio is advantageous is for the ease of feeding. With the printed structure presented here, with only a metal-to-slot ratio of 0.20, the complement of the structure can be utilized with an infinite Dyson balun feed. The complementary structure will have metal-to-slot ratio of 5 and will consist of a single, continuous slot. The infinite balun will be connected to the metal between the slots and connect across the slot at the center. The large percentage of metal will facilitate this type of connection. To maintain symmetry of the structure a dummy line will be used on the opposite side of the structure.

The complementary slot structure will have relatively unchanged far-field performance when compared to the printed structure, but will have significantly lower input impedance as stated from Booker's extension of the Babinet principle [8]. The far-field and input impedance comparison between the two complementary structures is shown in Fig. 7. The exact complement for the printed structure would be the slot in an infinite ground plane; however, in this analysis a finite ground plane was used. This is a possible cause of the small discrepancy seen in the far-field data.

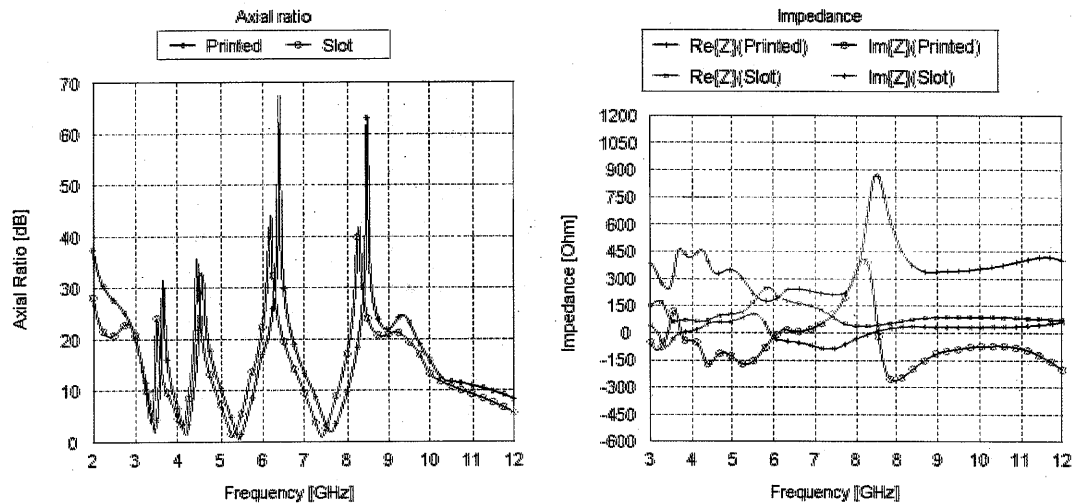


Fig. 7 - Comparison of axial ratio and input impedance for the printed and slot forms of the planar two-arm sinuous antenna. Note that for the slot structure, a finite ground plane was used (the exact complement would be an infinite ground plane).

## 2. Conical Two-Arm Sinuous Antenna

### 2.1 Geometry

To study the performance of a conically projected two-arm sinuous antenna the feed region size and aperture size are fixed to be 2 mm and 5 cm, respectively. Within this finite aperture size only a finite number of turns can fit which translates into a set of finite values for the growth rate,  $\tau$ . These values that can exist are shown in Table III and Fig. 8.

Three different cone angles were analyzed:  $50^\circ$ ,  $30^\circ$ , and  $20^\circ$ . An example of the two-arm structure at these three cone angles is shown in Fig. 9. From prior research [7], it was shown that for a traditional conical spiral-like antenna to operate effectively with a high front-to-back ratio, the cone angle must be  $< 30^\circ$ . For this research a design with total broadside gain  $\geq 5$  dB, axial ratio  $\leq 3$  dB, and front-to-back ratio  $\geq 10$  dB is required at the bands. Also investigated are the number of turns within the given aperture size, from 2 to 20 turns. The effect of dielectric substrates of various thicknesses and dielectric constants are also considered.

TABLE III - GEOMETRICAL PARAMETERS TO BE CONSIDERED

Growth Rate ( $\tau$ )	# of Cells
0.200	2
0.342	3
0.445	4
0.525	5
0.585	6
0.631	7
0.670	8
0.700	9
0.725	10
0.747	11
0.765	12
0.781	13
0.795	14
0.807	15
0.818	16
0.828	17
0.836	18
0.844	19
0.852	20

Antenna Aperture

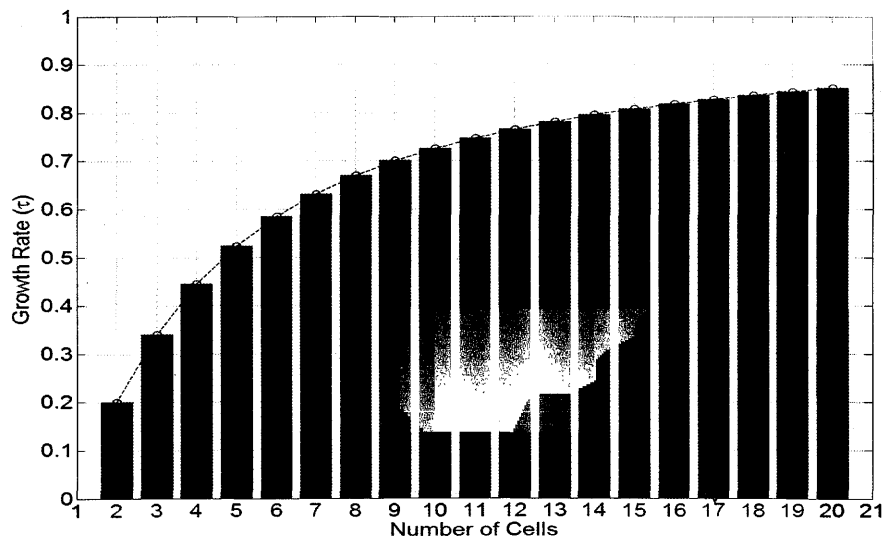


Fig. 8 - Shown is a plot of growth rate versus number of sinuous cells for the finite aperture given. As the growth rate approaches 1.0, the number of cells approaches infinity.

## 2.2 Results

Analysis of the conical two-arm sinuous structure involves using the fixed aperture size discussed in the prior section and characterizing the performance of several geometries with combinations of different number of turns and different cone angles. From this type of analysis we can observe trends in far-field performance as certain variables change.

Let us begin with the cone angle. With a fixed antenna diameter, the cone angle determines the height or depth that the antenna will have. In the limit as the cone angle approaches  $180^\circ$ , the structure becomes planar with bi-directional radiation. In the other limit as the cone angle approaches  $0^\circ$ , the antenna becomes infinitely long. Choosing a large angle will surely have very little effect since the geometry is quite similar to the planar, bi-directional structure. Choosing a relatively small cone angle and the antenna will not be realizable and large in depth. Knowing these constraints, three angles are investigated:  $20^\circ$ ,  $30^\circ$ , and  $50^\circ$ . These structures are shown in Fig. 9. With a constant aperture size, all structures, regardless of the number of turns and growth rate will have the same depth as shown also in Fig. 9.

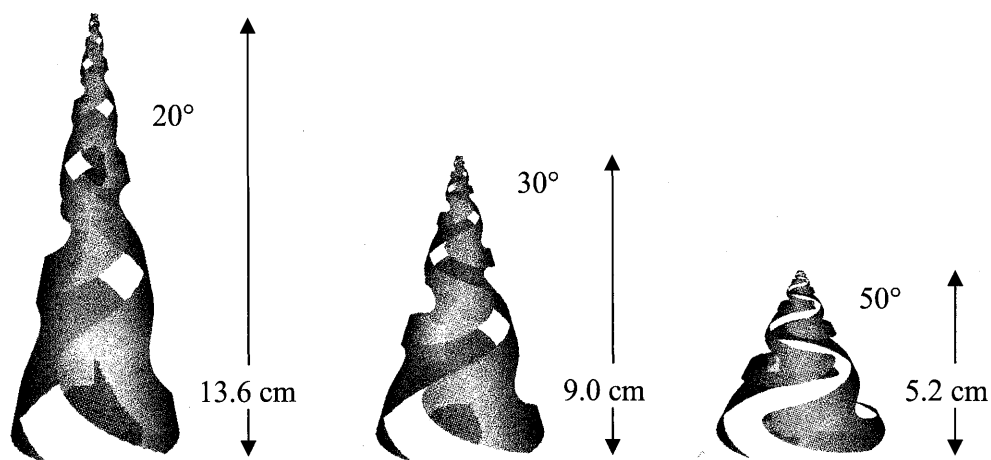


Fig. 9 - The two-arm sinuous geometry with a growth rate of  $\tau = 0.631$  (7 turns). Antenna diameter is 5 cm, feed region is 2 mm, and cone angle is either  $20^\circ$ ,  $30^\circ$ , or  $50^\circ$ .

For a given cone angle and aperture size, varying the number of turns for a structure significantly affects the far-field performance of the antenna. As the number of turns for a structure increases, the axial ratio also increases. This is believed to be a result of radiation from an active region that contains two or more turns. When radiation occurs from a region that contains two oppositely wrapped turns, there is a mixture of

both right and left handedness polarizations. This mixture degrades the purity of the polarization and increases the axial ratio at that frequency. Of course there is the case of a very small number of turns at which the axial ratio is also poor. But with this low of a growth rate, the turns of the structure cease to be circumferential about the antenna axis. Increasing the number of turns also increases the front-to-back ratio and total broadside gain at the bands.

For a constant aperture size and a given number of turns variations in cone angle have the most effect on front-to-back ratio and gain. For a small number of turns, smaller cone angles reduce the broadside gain. This is believed to result from the over-stretching of the sinuous turns in the  $z$  direction. With a little number of turns, a small cone angle results in a large pitch angle of the turns themselves. This reduces the circumferential nature of the currents along the arms about the axis of the antenna. It should be noted that at a large number of turns there is very little effect on gain. This can be explained similarly insofar as with a large number of turns, the pitch angle is very small initially and with most variations in cone angle, the resulting change in pitch angle is not significant enough to affect the gain. The increases front-to-back ratio with smaller cone angles is to be expected and is the primary advantage in utilizing a conical structure. Unidirectional radiation is possible without the use of absorptive backings of cavities.

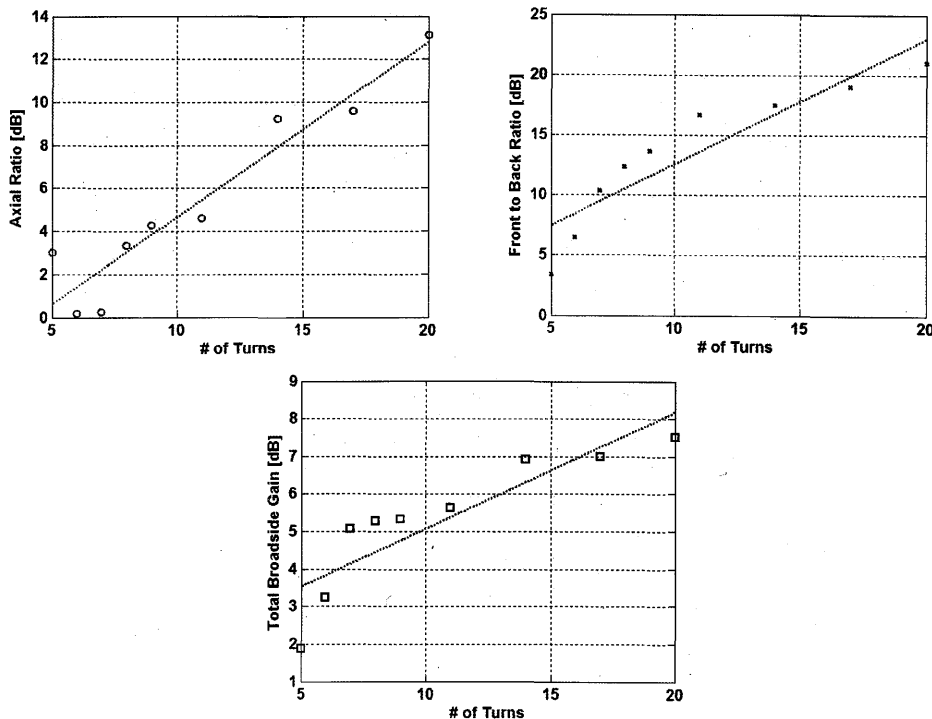


Fig. 10 - Effect of varying the number of turns for a constant cone angle ( $30^\circ$ ) and aperture size on axial ratio, front-to-back ratio, and total broadside gain.

Of the three cone angles analyzed, the 30° structure showed the best performance. The 20° structure had satisfactory axial ratio for the bands and very good front-to-back ratio, but for the growth rate which gave low axial ratio values, the total gain at broadside was <3dB. Higher number of turns did significantly increase the gain but also increased the axial ratio. The 50° structure had good axial ratio and gain, however, because of the large cone angle; the front-to-back ratio was low and was thus quite bi-directional. The intermediate cone angle, 30°, showed the best performance; a combination of the good front-to-back ratio of the smaller cone angle with the higher gain of the larger cone angle. This structure, which has 7 turns, resulted in the following data (averaged at three central, adjacent bands): axial ratio less than 1 dB, total gain greater than 5 dB, front-to-back ratio greater than 10 dB. Fig. 10 shows the effect of the number of turns on various far-field parameters with a constant aperture and a cone angle of 30°. For this free-space geometry without a substrate the bands -2 to 3 are located at 3.05 GHz, 4.60 GHz, 7.25 GHz, 11.4 GHz, and 17.6 GHz, respectively. Electric field magnitude plots in Fig. 11 show for higher frequencies that most of the attenuation through the active region occurs closer toward the tip of the cone and for lower frequencies, toward the base of the cone.

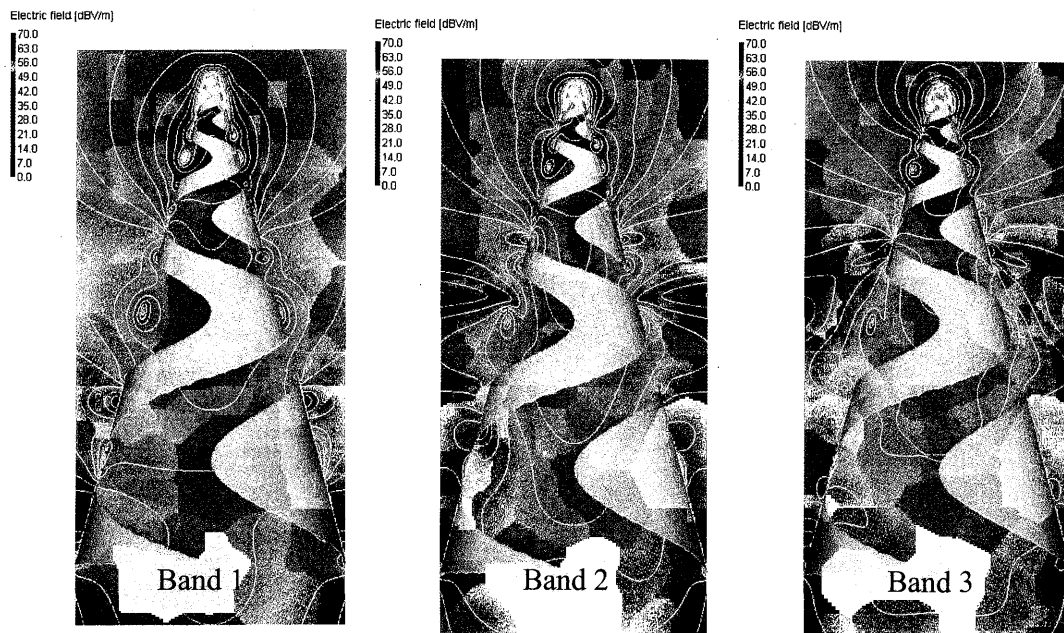


Fig. 11 - Electric field magnitudes through a cross-section of the conical structure at the three central bands. The color scale is the same at each frequency.



Shown in Table IV is a summary of all parameters for the five bands resulting from the two-arm conical sinuous structure with a cone angle of  $30^\circ$ , and a growth rate of  $\tau=0.631$  (7 turns). Front-to-back ratio is given as three values relating the co-polarized forward and co-polarized backward gains (Co/Co), co-polarized forward and cross-polarized backward gains (Co/X), and total forward and backward gains (T/T). The parameter of WoW shown in the table is a measure of the azimuthal pattern symmetry taken at  $\theta_{3dB}$  for the co-polarized gain at each band. For perfect symmetry the WoW is zero. However, WoW values less than 1 dB is considered very good. The input impedance maintains an average of approximately  $205+j16$  with a 12% maximum variation in input resistance for all the bands. Far-field gain patterns at bands 1-3 are shown in Fig. 12 for two azimuthal cuts ( $\phi=0^\circ$  and  $\phi=90^\circ$ ).

TABLE IV - TWO-ARM CONICAL SINUOUS PERFORMANCE CHARACTERISTICS

Band	Polarization	Axial Ratio [dB]	Bandwidth [GHz]	Total Gain [dB]	Front-to-Back Ratio [dB]			$\theta_{3dB}$ [°]	WoW [dB]	$Z_{in}$ [ $\Omega$ ]
			(AR<4dB)		Co/Co	Co/X	T/T		( $\theta_{3dB}$ )	
-2	LH	2.600	0.25	4.3	8.30	19.0	8.10	58	1.3	181+j37
-1	RH	3.500	0.45	4.9	12.9	14.1	10.6	48	0.3	185-j12
1	LH	0.170	0.60	5.1	13.0	17.6	11.9	45	0.9	209-j16
2	RH	0.550	1.00	5.1	11.4	17.5	10.4	45	0.9	228-j08
3	LH	0.064	1.40	4.9	9.60	13.9	8.20	43	1.0	223+j80

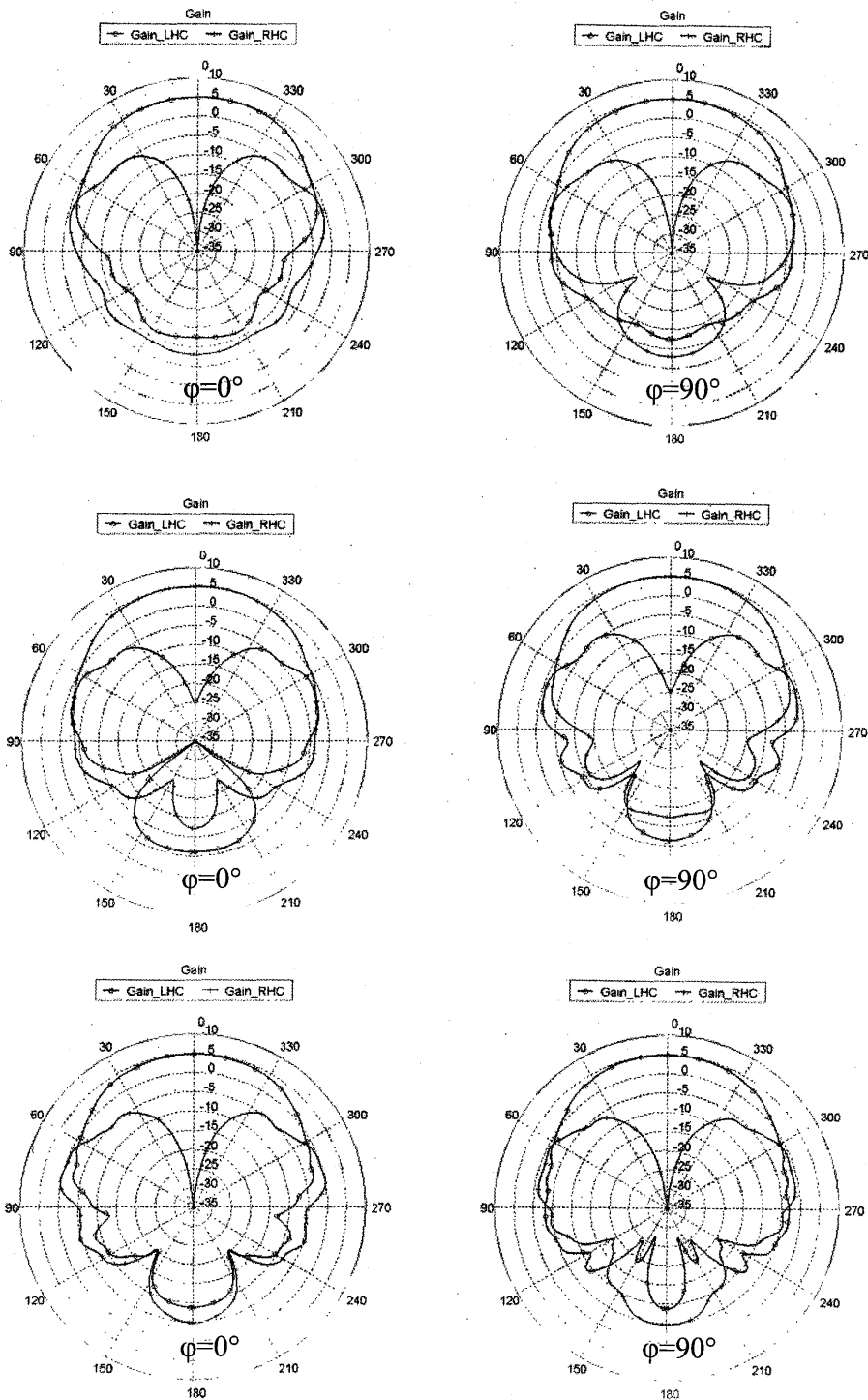


Fig. 12 - Far-field gain patterns at bands 1-3 (top to bottom, respectively). Note the polarization flip between adjacent bands.

The addition of a substrate to the conical geometry has several effects. Similar as with the planar structure, the dielectric has the effect of electrically miniaturizing the antenna. The frequencies of the bands are shifted lower in frequency, an amount directly related to the magnitude of the dielectric constant. Smaller values closer to 1.0 shift the bands very little while with larger values the shift is more pronounced. The resulting frequency locations of the bands are shown in Table V. A graphic of the modeled antenna with dielectric substrate is shown in Fig. 13.

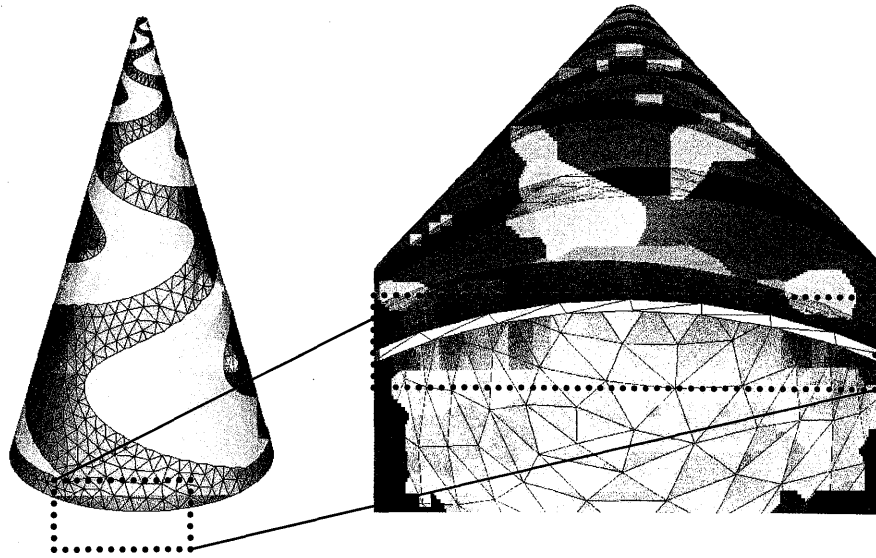


Fig. 13 - Conical two-arm sinuous antenna with added substrate of 0.5 mm thickness. The surface equivalence principle of FEKO® is used to model dielectrics on the presented conical structures.

TABLE V - EFFECT OF DIELECTRIC SUBSTRATE ON BAND FREQUENCY [GHz]				
Bands	$\epsilon_r=1.0$	$\epsilon_r=2.2$	$\epsilon_r=3.8$	$\epsilon_r=9.8$
-2	3.05	2.90	2.80	2.60
-1	4.60	4.40	4.10	3.70
1	7.25	6.80	6.50	5.10
2	11.4	10.5	9.80	8.40

TABLE VI - EFFECT OF DIELECTRIC SUBSTRATE ON AXIAL RATIO [dB]				
Bands	$\epsilon_r=1.0$	$\epsilon_r=2.2$	$\epsilon_r=3.8$	$\epsilon_r=9.8$
-2	2.60	2.20	2.10	1.20
-1	3.50	2.50	1.80	0.24
1	0.17	1.37	2.20	0.74
2	0.55	1.30	2.20	0.17

TABLE VII - EFFECT OF DIELECTRIC SUBSTRATE ON BAND WIDTH [GHZ]				
Bands	$\epsilon_r=1.0$	$\epsilon_r=2.2$	$\epsilon_r=3.8$	$\epsilon_r=9.8$
-2	0.25	0.26	0.25	0.25
-1	0.45	0.60	0.60	0.60
1	0.60	0.40	0.40	1.00
2	1.00	0.90	0.70	1.80

The second effect of the substrate is a reduction and improvement of axial ratio at lower frequencies. In addition, there is an increase in the width of the bands as well, particularly with the highest dielectric substrate,  $\epsilon_r=9.8$ . A summary of the axial ratio values at each band and the 4dB axial ratio band width are shown in Table VI and VII.

Upon realization a broadband feed will have to be implemented. One example of a useable feed is a coaxial bundle. One pair of coaxial cables, with outer conductors connected, will feed the two arms and is directed through the backward side of the cone, opposite the direction of radiation. An example of this type of feed is shown in Fig. 14.

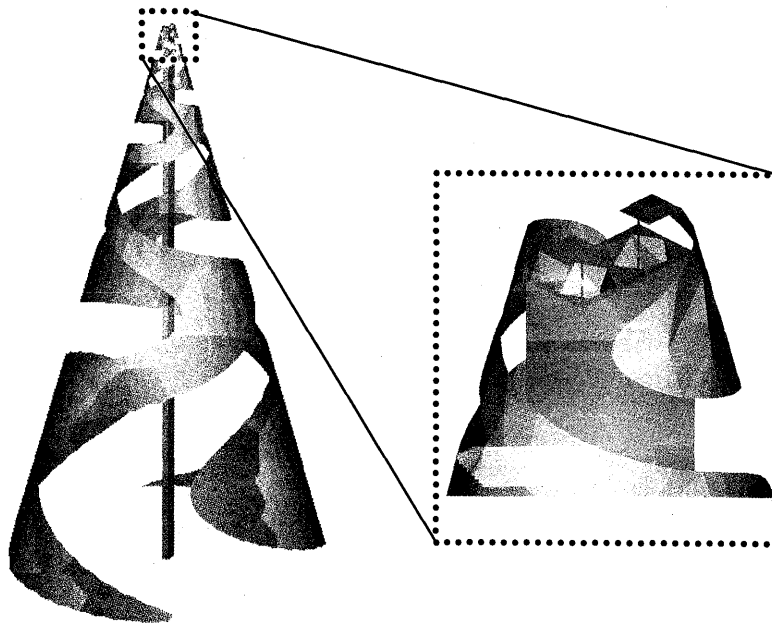


Fig. 14 - Two-arm conical sinuous antenna with coaxial bundle as feed source. The coaxial bundle extends from the feed point at the tip of the cone through the full height of the cone, to the base.

There is little degradation in far-field performance as a result of the addition of the coaxial bundle. The feed is balanced and any variation in far-field pattern would be expected to be at large elevation angles. Shown in Fig. 15 is the pattern at two different azimuthal cuts ( $\varphi = 0^\circ$  and  $\varphi = 90^\circ$ ) for the central band (band 1) with an ideal feed and with the coaxial bundle. Very little variation is seen even at high elevation angles with most of the variation in the cross-polarized component of the radiation. Other bands show similar behavior. Fig. 16 shows the azimuthal pattern for various elevation angles at the central band (other bands are again similar). The pattern symmetry is still very good, with a variation in gain (WoW) on the order of 1 dB or less. The total 3D gain patterns for the three central bands are shown in Fig. 17.

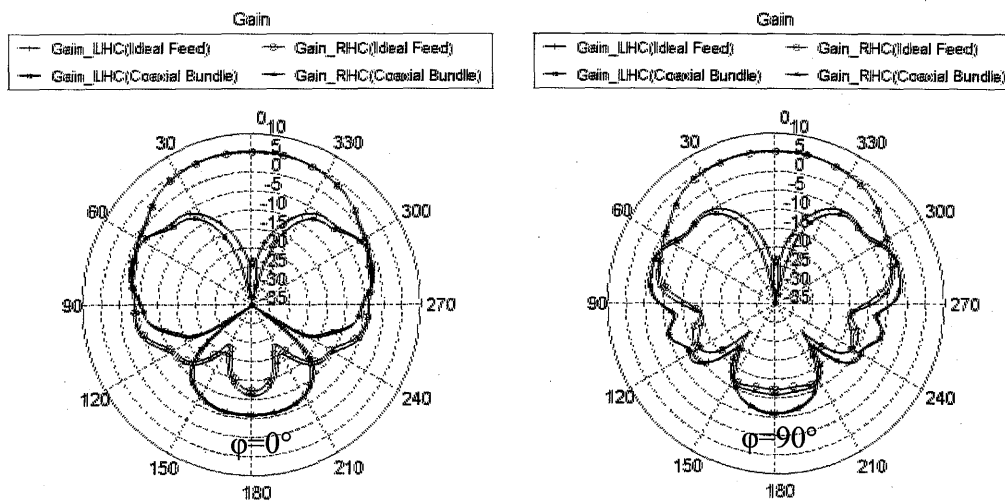


Fig. 15 - Gain Patterns showing very little variation in far-field due to the addition of a coaxial bundle feed through the cone as shown in Fig. 14.

### 3. Conclusion and Summary

A planar, bidirectional two-arm sinuous antenna has been demonstrated. This antenna has multiple bands of alternating handedness circular polarization, a result of the left and right varying wrapping direction of the arms of the structure and because of the ambiguity in the phasing of a two arm structure at the feed point. Both printed and slot type structures were considered; the latter because of the ease of feeding with an infinite Dyson balun. Similar far-field performance was shown between the two structures.

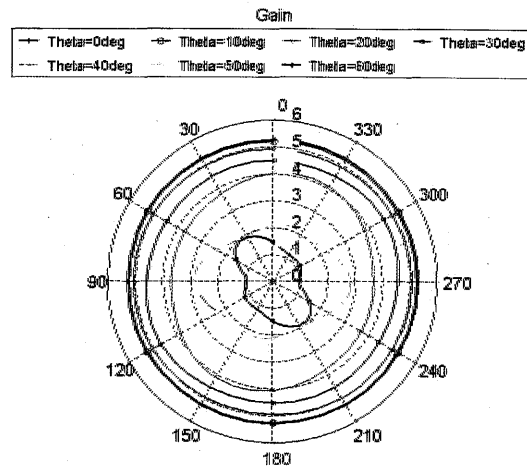


Fig. 16 - Total gain at various elevation angles taken in the azimuthal plane. Very little variation in gain ( $< 1$  dB) is shown with the coaxial bundle implemented in feeding the two-arm conical sinuous antenna.

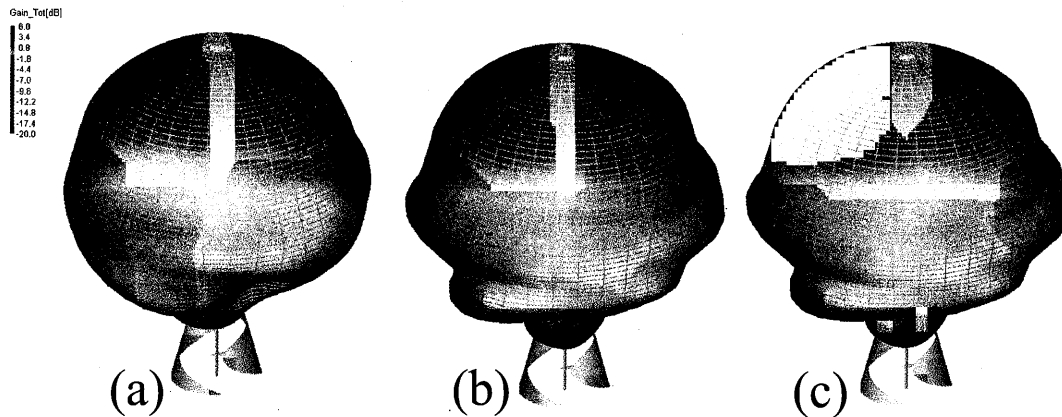


Fig. 17 - Far-field patterns for two-arm conical sinuous antenna with coaxial bundle feed. (a) Band 1, 7.25 GHz (b) Band 2, 11.4 GHz and (c) Band 3, 17.6 GHz.

A conical projection of the two-arm sinuous structure was analyzed in depth. This structure when compared to the planar structure has unidirectional as opposed to bidirectional radiation. It must be noted that unidirectional operation for the conical sinuous antenna is possible without the use of any absorptive cavity or backing. A parametric study of the effect of the number of turns (growth rate) and cone angle was performed and summarized with the most favorable design noted and characterized further. For this design substrate effects and dielectric and conductor losses were considered as well as effects of a coaxial bundle feed.

## REFERENCES

- [1] R. H. DuHamel, "Dual Polarized Sinuous Antennas," U.S. Patent 4658262, April 14, 1987.
- [2] M. C. Buck, A. Bhoje, and D.S. Filipović, "A Flush-Mounted Multi-Band/Broadband Sinuous-Like Slot Antenna for Terrestrial Communications," URSI National Radio Science Meeting, June 2003.
- [3] M. C. Buck and D.S. Filipović, "Split-Beam Mode Four-Arm Slot Sinuous Antenna," *Antennas and Wireless Propagation Letters*, Volume 3, Issue 1, 2004 Page(s): 83 - 86.
- [4] M. C. Buck, J. Burford, and D.S. Filipović, "Multiband Two Arm Slot Sinuous Antenna," *IEEE Antennas and Propagation Society Symposium Proceedings*, Volume 1, 20-25 June 2004 Page(s): 165 – 168.
- [5] M. C. Buck, T. Cencich, J. Burford, and D.S. Filipović, "Multi-band, Multi-polarized Sinuous Antennas for Satellite and Terrestrial Applications," *Antenna Applications Symposium Proceedings*, 20-22 September 2004.
- [6] J. Dyson, "The Characteristics and Design of Conical Log-Spiral Antennas," *IEEE Transactions on Antennas and Propagation*, Vol. 13, No. 4, pp. 488-499, July 1965.
- [7] R. C. Johnson, *Antenna Engineering Handbook*, Chapter 14, pp. 14-1 - 14-68, Third Edition, McGraw-Hill, 1993.
- [8] H.G. Booker, "Slot Aerials and Their Relation to Complementary Wire Aerials (Babinet's Principle)," *J. IEE*, Vol. 93, Part 3A, pp. 620-626, 1946.

# Some Considerations for Compact Resonant UHF PIFAs

Sergey N. Makarov, Shashank D. Kulkarni, and Reinhold Ludwig

ECE Dept., Worcester Polytechnic Institute, Worcester, MA 01609-2280  
[makarov@wpi.edu](mailto:makarov@wpi.edu), [kulkarni@wpi.edu](mailto:kulkarni@wpi.edu), [ludwig@wpi.edu](mailto:ludwig@wpi.edu)

**Abstract:** In this paper, the resonant impedance bandwidth of four basic types of rectangular PIFA is estimated as a function of their antenna height. Extensive numerical simulations are performed over a representative domain of the antenna height and antenna length/width ratio. It is found that the relative half-power bandwidth for all antenna types is described by the inequality  $0.5h/\lambda < B < 3h/\lambda$  where  $h$  is the antenna height. The upper estimate for the bandwidth ( $B=3h/\lambda$ ) corresponds to a shunt-shunt PIFA with a top-located feed, optimized for maximum impedance bandwidth. The lower estimate ( $B=0.5h/\lambda$ ) belongs to a shunt-open planar inverted L-antenna (PILA), also optimized for maximum impedance bandwidth. It is found that the majority of collected literature data for the PIFAs with real or complex input impedances are within this range. This suggests a simple estimate for the achievable bandwidth of a low-height PIFA.

## I. Introduction

A motivation for this work was a request from a local company to estimate the bandwidth of a PIFA antenna for an RFID tag chip operating at 915 MHz as a function of antenna height. The PIFA is less dependent on the platform than conventional printed dipoles. Hence, may be used in close proximity to metal objects or high dielectric-constant objects. Furthermore, the PIFA is smaller than a patch antenna, which makes it more attractive for tag miniaturization. The antenna height should be reasonably small; a small height may be a critical requirement from the production point of view.

To date, a significant body of work on RFID tag PIFA antennas exists - see for instance [1]-[6]. Information can also be obtained for standard PIFAs that are used for communication purposes and whose typical input impedance is  $50 \Omega$  [7]-[9]. A problem is that different PIFA antennas use different geometries and are designed for different (and generally reactive) matching impedances that are chip-dependent.

In order to obtain the chip-independent results we suggest estimating the *resonant* half-power impedance bandwidth of a PIFA antenna. The resonant impedance bandwidth is



obtained vs. resonant antenna resistance that may itself have different values. Such an estimate gives us the exact bandwidth for a real matching impedance that is equal to that of the antenna and a good approximation for a complex matching impedance if the reactance of an antenna is a linear function of frequency near the resonance. The latter behavior (series LCR circuit) is typical for (printed) RFID tag dipoles and some PIFA antennas, see below. To simplify the analysis we only considered an air-filled PIFA without a dielectric medium.

## 2. PIFA setup

### 2.1 Transmission line model

Fig. 1 shows three possible PIFA modifications that have been considered for the present task. The first antenna is a conventional PIFA. Instead of the probe feed, a slot feed or another kind of capacitive/inductive coupling can be used. This antenna configuration is mostly used in mobile communications. The second antenna (PIFAI) implies a top-located voltage feed without a circuit board via; such an antenna is also called planar-inverted L-antenna (PILA) [10] and is more convenient for the RFID tag chips, which can be located on the top layer. The third antenna (PIFAII) is the PILA with a shorted patch.

The input impedance of either antenna is given by

$$Z_{in} = \frac{V^*}{I^*} \quad (1)$$

where  $V^*$  and  $I^*$  are the voltage and current recorded at the antenna terminals. To qualitatively describe the input impedance it is suggested to use a transmission line model, where loss per unit length,  $\alpha$ , will approximately describe the radiation losses of the corresponding (wide) microstrip. Every antenna in Fig. 1 includes two transmission lines labeled TLA and TLB. The input impedance is given by a parallel or series combination of the stub impedances  $Z_A$  and  $Z_B$ . In terms of the propagation constant  $\gamma$ , the characteristic impedance  $Z_0$ , and the load impedance  $Z_L$  (short or open), one finds

$$l = \lambda/4, \quad \gamma = \alpha + jk, \quad Z_A = Z_0 \frac{Z_L + Z_0 \tanh \gamma(l - \Delta)}{Z_0 + Z_L \tanh \gamma(l - \Delta)}, \quad Z_B = jZ_0 \tan k\Delta \quad (2)$$

We will consider this model using two inequalities

$$\alpha l \ll 1, \quad k\Delta \ll 1 \quad (3)$$

which imply relatively low radiation losses and a relatively short offset length  $\Delta$ .

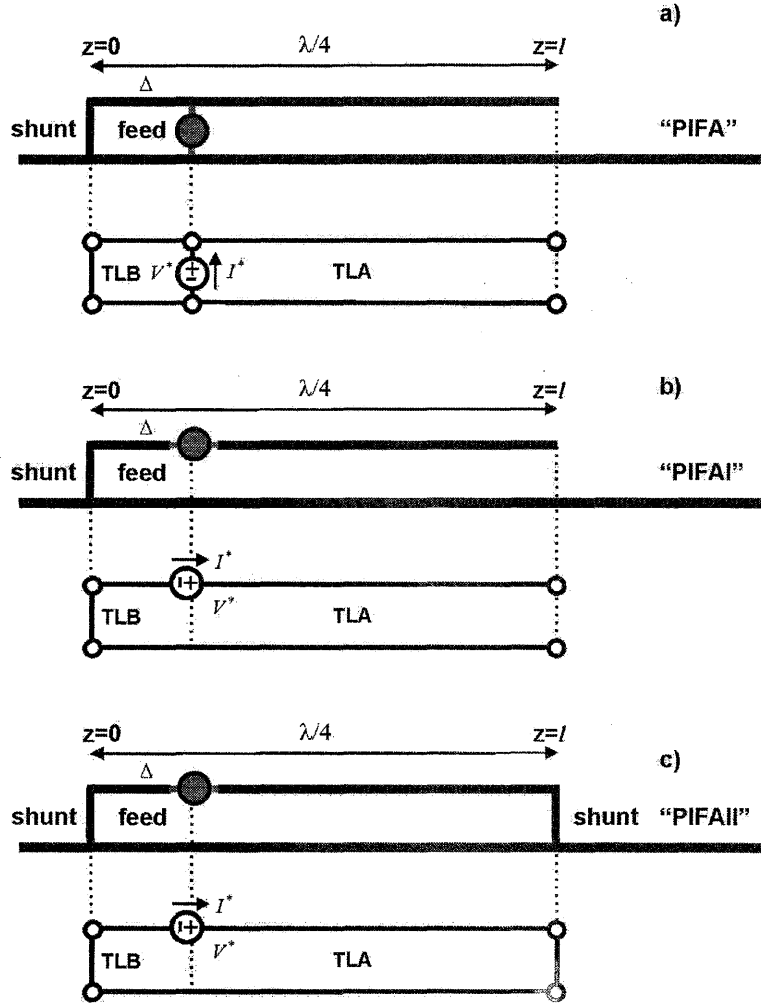


Fig. 1. Three modification of PIFA: a) conventional PIFA, b) - PIFA with a top-located feed (PILF according to Ref. [10]); c) - the same as b) but with a shunted  $\lambda/4$  resonator.

## 2.2 PIFA

The case of a conventional PIFA is shown in Fig. 1a. To find the input impedance, one combines two transmission lines TLA and TLB in parallel. To within an order of approximation, one has

$$\begin{aligned}
 Z_A &= Z_0(\alpha l - jk\Delta), & Z_B &= jZ_0 k\Delta \\
 Z_{in} &= Z_A \parallel Z_B = Z_0 \frac{(k\Delta)^2}{\alpha l} + jZ_0 k\Delta, & Z_{in} &\approx Z_0 \frac{(k\Delta)^2}{\alpha l} \quad \text{if } k\Delta \gg \alpha l
 \end{aligned} \tag{4}$$

The presence of an imaginary part of the input impedance at  $l = \lambda/4$  in Eq. (4) is not of significant importance. It appears because the PIFA does not resonate at exactly  $l = \lambda/4$ . The reactance may be eliminated by a slight deviation of the PIFA resonant length from  $\lambda/4$ .

The PIFA indicates a parallel LCR resonator behavior - the magnitude of the input impedance has a maximum at the resonance. The resistance of the resonant PIFA can have arbitrary values - the control of the resistance is achieved by the feed shift  $\Delta$ . Note also that the PIFA bandwidth depends on the size of the shunt stub, as discussed below.

### 2.3 PIFAI or PILA

The case of PILA is shown in Fig. 1b. For the input impedance, one again combines two transmission lines TLA and TLB in series. One has

$$\begin{aligned} Z_A &= Z_0(\alpha l - jk\Delta), & Z_B &= jZ_0k\Delta \\ Z_{in} &= Z_A + Z_B = Z_0\alpha l \end{aligned} \quad (5)$$

In contrast to the PIFA, the PILA indicates a series LCR resonator behavior - the magnitude of the input impedance has a minimum at the resonance. The resonance is achieved at exactly  $l = \lambda/4$ . The resistance of the resonant PILA is generally small (on the order of 0.1-10 $\Omega$ ); its control may be partially achieved by changing  $Z_0$ ; increase in  $Z_0$  (decrease in line capacitance) leads to larger values of the resistance.

### 2.4 PIFAI

This case is shown in Fig. 1c. For the input impedance, one combines two transmission lines TLA and TLB in series. One has

$$\begin{aligned} Z_A &= \frac{Z_0}{\alpha l - jk\Delta}, & Z_B &= jZ_0k\Delta \\ Z_{in} &= Z_A + Z_B = Z_0 \frac{1 + jk\Delta\alpha l + (k\Delta)^2}{\alpha l - jk\Delta}, & Z_{in} &\approx Z_0 \frac{1}{\alpha l} \quad \text{if } k\Delta \ll \alpha l \end{aligned} \quad (6)$$

This antenna indicates a parallel LCR resonator behavior similar to the PIFA. The resistance of the resonant antenna is generally large (on the order of 100-100000 $\Omega$ ); its control may be partially achieved by changing  $Z_0$ ; decrease in  $Z_0$  (increase in line capacitance) leads to smaller values of the resistance. Table 1 below summarizes the resonant impedance data on three antenna types considered above. The conventional PIFA in Fig. 1a is subdivided into two antennas - see below.

### 3. PIFA modeling

The conventional PIFA shown in Fig 1a has a different bandwidth depending on the width of the shunt. Therefore, we further subdivide this case and consider not three, but four basic PIFA cases as shown in Fig. 2. The antenna parameters are as follows:

$$\begin{aligned} a=300\text{mm}, b=200\text{mm}, l=100\text{mm}, d=5\text{mm}:15\text{mm}:275\text{mm}, h=1,2,5,10\text{mm}, \\ f=250:0.1:1200 \text{ MHz, centered antenna} \end{aligned} \quad (7)$$

For antenna simulations, ANSOFT HFSS v10.1 parametric sweeper was primarily used and then controlled by a slightly faster in-house MoM solver. Both methods gave close results. An antenna resonance was found for every geometry configuration, and every antenna geometry set was then rescaled to 915 MHz. Note that antenna PIFA b) has an inductive reactance component at the resonance that increases with increasing  $d$ . Therefore, this antenna was matched with a series capacitance to achieve truly resonant behavior and be consistent with the others. Table 1 below lists some antenna impedance characteristics.

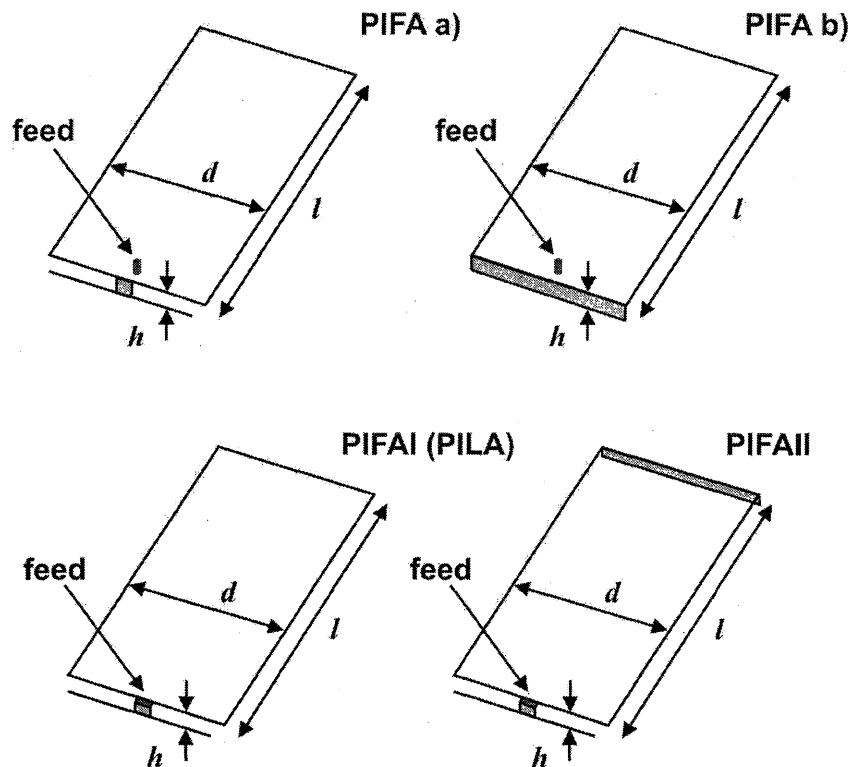


Fig. 2a. Four different base PIFA configurations: a) - PIFA with a short shunt; b) - PIFA with a wide shunt; c) - PIFAI (PILA); d) - PIFAIL.

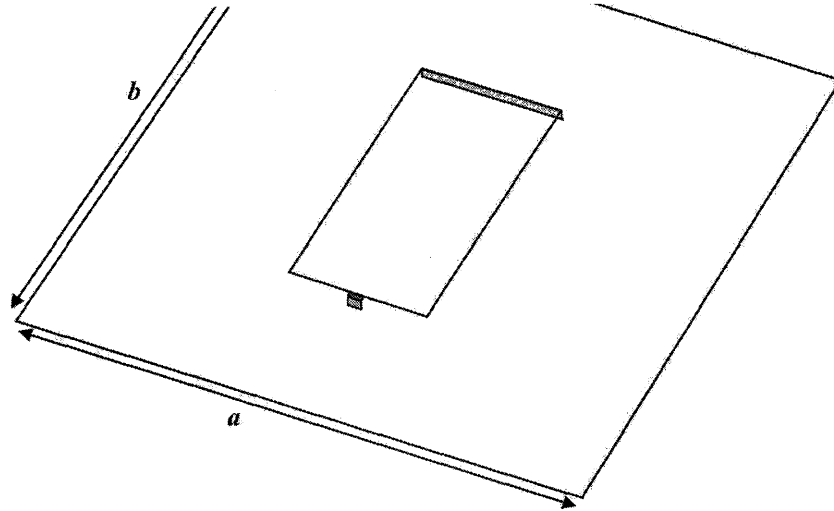


Fig. 2b. Ground plane and centered PIFA used for the simulations<sup>1</sup>.

Table. 1. Resonant behavior of four PIFA antennas.

Antenna	Resonance type	Resonant $d$ for maximum bandwidth	Typical resonant $Z_{in}$ at 915 MHz without an impedance matching network	Typical real part of $Z_{in}$ with 100 $\Omega$ inductance
PIFA a)	Parallel LCR	$\sim 0.4-0.5\lambda$ then saturated	Arbitrary	--
PIFA b)	Parallel LCR with a series inductor	$0.07\lambda$	Arbitrary (with a series matching capacitor)	--
PIFAI or PILA	Series LCR	$0.07\lambda$	$0.001\Omega$ ( $h=1.0\text{mm}$ ) $1.0\Omega$ ( $h=10\text{mm}$ )	5-10 $\Omega$ ( $h=10\text{mm}$ )
PIFAII	Parallel LCR	$\sim 0.4-0.5\lambda$ then saturated	250 $\Omega$ ( $h=10\text{mm}$ ) 150k $\Omega$ ( $h=1.0\text{mm}$ )	--

<sup>1</sup> Simulations were also carried out for non-centered antennas. The results generally appear similar and are not discussed here.

#### 4. Bandwidth results

Fig. 3 below shows the data on the half-power resonant impedance bandwidth for four antennas extracted from simulations as functions of the normalized antenna height. A linear behavior of the bandwidth is observed for all antennas except PIFA b) (with a matching capacitor) where certain nonlinearity becomes apparent.

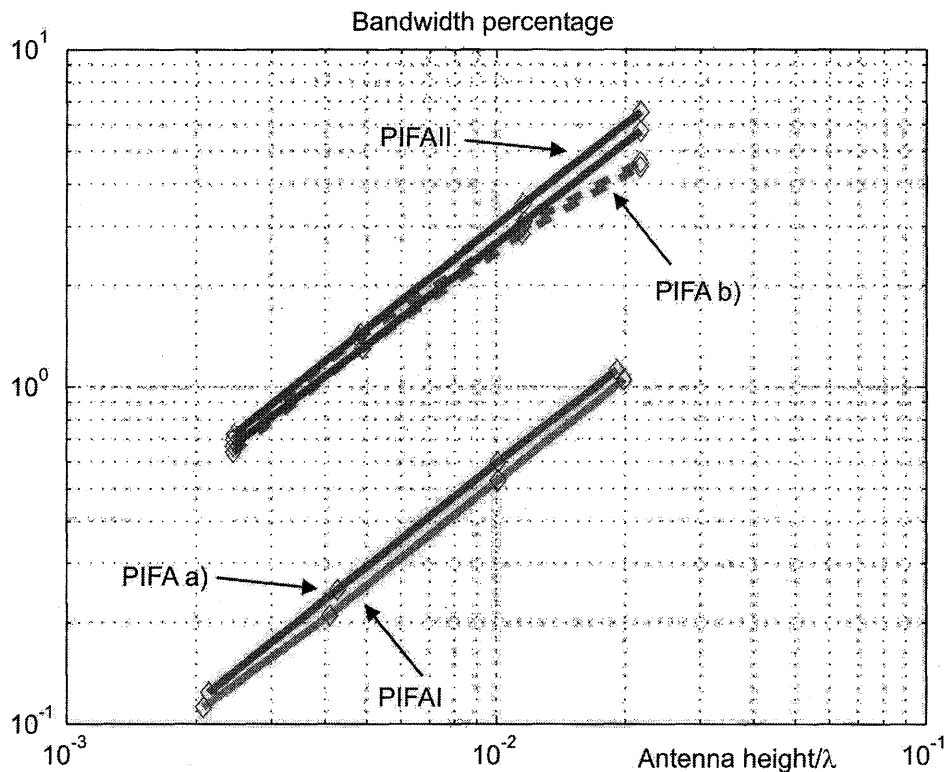


Fig. 3. Half-power antenna bandwidth vs. normalized antenna height for base PIFA configurations shown in Fig. 2. Two PIFAII curves correspond to  $h = 0.5\lambda$  (above) and  $h = 0.4\lambda$  (below), respectively. The same is valid for two PIFA b) antennas shown by dashed curves.

The results for PIFAII at  $h = 0.5\lambda$  almost perfectly follow the linear dependence

$$B = 300 \frac{h}{\lambda} \quad [\%] \quad (8)$$

with the standard deviation of 1.1%. The results for PIFAII at  $h = 0.4\lambda$  follow the dependence

$$B = 270 \frac{h}{\lambda} \quad [\%] \quad (9)$$

with the standard deviation of 1.6%. The results for PIFA a) ( $h \sim 0.07\lambda$  - optimized for a maximum bandwidth) follow

$$B = 59 \frac{h}{\lambda} \quad [\%] \quad (10)$$

with the standard deviation of 1.1%. Finally, the results for PIFAI ( $h \sim 0.07\lambda$  - optimized for a maximum bandwidth) follow the dependence

$$B = 53 \frac{h}{\lambda} \quad [\%] \quad (11)$$

with the standard deviation of 2.0%.

All intermediate results are confined between the curves for PIFAI and PIFAI. Thus, one approximately has for the relative bandwidth (not percentage)

$$0.5 \frac{h}{\lambda} < B < 3 \frac{h}{\lambda} \quad (12)$$

## 5. Comparison with literature data

Table 2 lists some collected literature data. References [1]-[9] include both RFID tag PIFAs [1]- [6] and the conventional PIFAs [7]- [9] matched to  $50 \Omega$ . However, only the RFID tag-related references are included into the table. The original PIFA design suggested by Taga *et al* is also included. We did not pay special attention to the size of the ground plane and used the reported bandwidth for generally varying ground plane sizes. When several ground planes have been used, the largest value of the bandwidth was usually retained. It is known that the impedance bandwidth increases with increasing the ground plane size [9].

The bandwidth for different PIFA antennas is then plotted as a function of the dimensionless antenna height in Fig. 4, similar to Fig. 3. In Fig. 4, we simultaneously plot two extreme curves from Fig. 3: the results for PIFAI optimized for maximum bandwidth and given by Eq. (8) and the result for PIFAI again optimized for maximum impedance bandwidth and given by Eq. (11). It can be seen that the majority of collected literature data for the PIFAs with real or complex input impedances are within the range bounded by two curves that follow Eqs. (8) and (11), respectively. The combined inequality is Eq. (12). This is a remarkable observation that suggests a simple impedance-

Table 2. Some platform-independent UHF PIFA/patch RFID antennas in 915 MHz and 869 MHz bands. The effect of the finite ground plane is not separately investigated; the highest bandwidth value for multiple ground planes is used wherever possible.

Ref.	Type	Center frequency	Required antenna impedance <sup>2</sup>	Size	Height	Half-power bandwidth (VSWR<6; $ \Gamma <\sqrt{0.5}$ )
[1]	Three-layer <sup>3</sup> PIFA; three shunts	915 MHz	$Z_{in}=(6+j127)\Omega$	Patch: 74.5×24.5mm GP: 400×400 mm <sup>4</sup>	3mm	51-57 MHz
[2]	Two-layer <sup>5</sup> PIFA (PIFAII)	869 MHz	$Z_{in}=(7+j170)\Omega$	Patch: 45×45mm GP: 59×59mm	3mm	~16 MHz
[3]	Three-layer patch with EBG	916 MHz	$Z_{in}=1200\Omega$	Patch: 49×47mm GP: 100×100mm	6.4 mm	~20 MHz
[4]	Two-layer slotted PIFA	915 MHz	$Z_{in}=(7+j197)\Omega$	Patch: 82×46mm GP: 90×54mm	5mm	~26 MHz
[5]	Two coupled two-layer PIFAs (PIFAII)	915 MHz	$Z_{in}=(10+j150)\Omega$	Patch: 46×54mm GP: NA	3mm	~17 MHz
[6]	Three-layer slotted PIFA	914 MHz	$Z_{in}=(77+j100)\Omega$	Patch: 46×46mm GP: NA	3.25 mm	~8 MHz

<sup>2</sup> Chip impedance to be matched is a complex conjugate of this value.

<sup>3</sup> Antenna with three layers, each of which includes metal stubs.

<sup>4</sup> Dual-resonance antenna with this ground plane.

<sup>5</sup> Antenna with only two layers containing metal stubs.



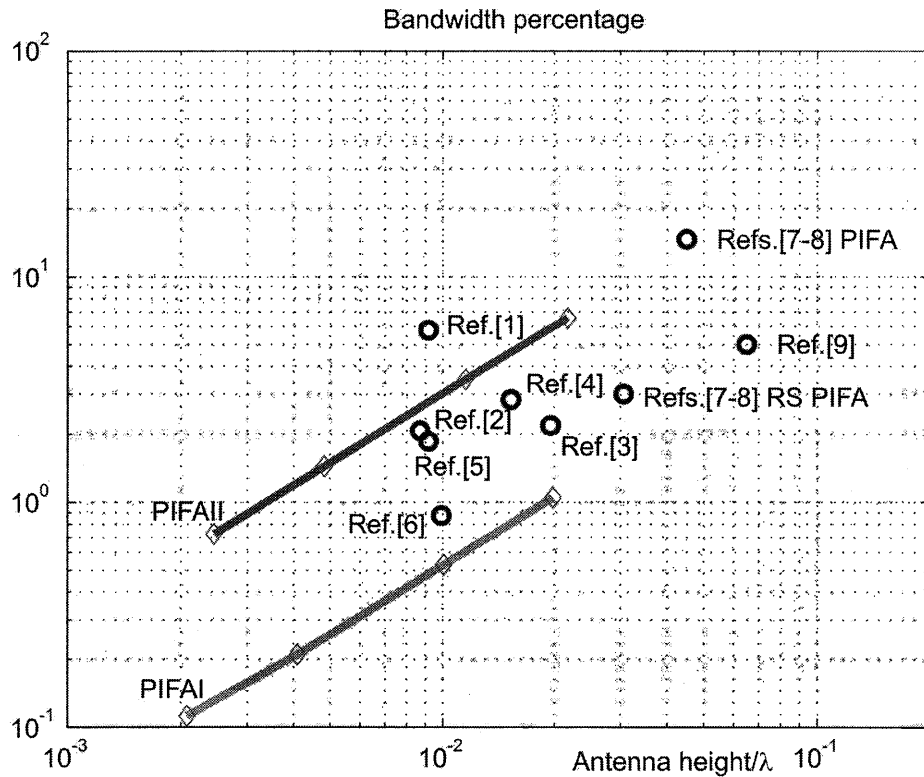


Fig. 4. Literature data on PIFA bandwidth. Refs. [1]-[6] - RFID tag PIFA/patch antennas; Refs. [7]-[9] - conventional PIFAs. In Ref. [9], the ground plane is  $0.5\lambda \times 0.5\lambda$ .

independent estimate for the achievable bandwidth of a low-height PIFA. However, the antenna "position" within the allowed domain is impedance-dependent.

One exception seems to be reference [1], which predicts a considerably larger impedance bandwidth than the others. Note that this reference suggests a PIFA with two closely spaced resonances, in contrast to some other antennas. A recent design by the authors of a wearable foam-based communication PIFA at 440 MHz [11] also indicates a large half-power impedance bandwidth. However, this antenna has a significant dimensionless height. The present study is limited to low-height antennas with  $h/\lambda < 0.02$ .

## 6. Conclusion

In this paper, the resonant impedance bandwidth of four basic types of rectangular PIFA has been estimated as a function of antenna height. Extensive numerical simulations are performed over a representative domain of the antenna height and antenna length/width ratio. It is found that the relative bandwidth for all antenna types is described by the inequality  $0.5h/\lambda < B < 3h/\lambda$  where  $h$  is the antenna height. The upper estimate for the bandwidth ( $B=3h/\lambda$ ) corresponds to a shunt-shunt PIFA with a top-located feed, optimized for maximum impedance bandwidth. The lower estimate ( $B=0.5h/\lambda$ ) belongs to a shunt-open planar inverted L-antenna (PILA), also optimized for maximum impedance bandwidth. It is found that the majority of collected literature data are within this range. This is a remarkable observation that suggests a simple impedance-independent estimate for the achievable bandwidth of a low-height PIFA. Indeed, the antenna "position" within the allowed domain is impedance-dependent and geometry-dependent. PIFA antennas matched to a large real impedance seem to have a larger bandwidth (and simultaneously larger length and width) compared to the non-resonant antennas with inductive reactance on the order of approximately  $100\Omega$ .

## 6. Acknowledgement

Support of Tego, Inc, MA is greatly appreciated. The authors thank the computer facilities staff of the ECE Department of WPI and in particular Mr. Robert Brown for supporting the computationally extensive Ansoft optimization tasks with a distributed server network.

## References

- [1]. H.W. Son, J. Yeo, G.Y. Choi, and C.S. Pyo, "A Low-Cost, Wideband Antenna for Passive RFID Tags Mountable on Metallic Surfaces," in *Proc. IEEE Antennas and Propagation Society Int. Symp.*, Albuquerque, NM, 2006, pp. 1019–1022, July 2006.
- [2]. M. Hirvonen, P. Pursula, K. Jaakkola, and K. Laukkanen, "Planar inverted-F antenna for radio frequency identification", *Electron. Lett.*, vol. 40, no. 14, pp. 848–850, July 2004.
- [3]. L. Ukkonen, L. Sydänheimo, and M. Kivikoski, "Patch antenna with EBG ground plane and two-layer substrate for passive RFID of metallic objects", *IEEE Antennas and Propagation Society Int. Symp.*, Monterey, CA, 2004, vol. 1, pp.93-96, July 2004.
- [4]. Sung-Joo Kim, Byongkil Yu, Ho-Jun Lee, Myun-Joo Park, Frances J. Harackiewicz, and Byungje Lee, "RFID Tag Antenna Mountable on Metallic Plates," *Microwave Conference Proceedings*, 2005. APMC 2005. Asia-Pacific Conference Proceedings, vol. 4, 4-7 Dec. 2005.
- [5]. Byunggil Yu, Sung-Joo Kim, Byungwoon Jung, Frances J. Harackiewicz, Myun-Joo Park, and Byungje Lee, "Balanced RFID Tag Antenna Mountable on Metallic Plates," in *Proc. IEEE Antennas and Propagation Society Int. Symp.*, Albuquerque, NM, 2006, pp. 3237–3240, July 2006.
- [6]. W. Choi, H. W. Son, Ji-H. Bae, G. Y. Choi, C. S. Pyo, and J.-S. Chae, "An RFID tag using a planar inverted-F antenna capable of being stuck to metallic objects," *ETRI Journal*, vol. 28, no. 2, April 2006, pp.216-218.
- [7]. T. Taga, K. Tsunekawa, and A. Sasaki, "Antennas for detachable mobile radio units," *Review of the ECL, NTT*, Japan, vol. 35, no. 1, pp. 59-65, Jan. 1987.
- [8]. R. Bancroft, *Microstrip and Printed Antenna Design*, Noble Publishing, 2004, Atlanta, GA.
- [9]. M.-C. Huynh and W. Stutzman, "Ground plane effects on planar inverted-F antenna (PIFA) performance," *IEE Proceedings on Microwaves, Antennas and Propagation*, vol. 150, no.4, 8 Aug. 2003, pp. 209 - 213.
- [10]. K. Boyle, "Radiating and balanced mode analysis of PIFA shorting pins," *IEEE Antennas and Propagation Society Int. Symp.*, San Antonio, TX, 2002, pp. 508–511, June 2002.
- [11]. S. Kulkarni and S. Makarov, "A Compact Dual-Band Foam-Based UHF PIFA," in *Proc. IEEE Antennas and Propagation Society Int. Symp.*, Albuquerque, NM, 2006.

# UHF BAND RFID TAG ANTENNA WITH A SYMMETRIC STRUCTURE MOUNTABLE ON METALLIC PLATFORMS

Sung-Joo Kim<sup>1\*</sup>, Hanphil Rhyu<sup>1</sup>, Seung-Hoon Baek<sup>2</sup>, Frances J. Harackiewicz<sup>2</sup>, and  
Byungje Lee<sup>1</sup>

<sup>1</sup>RFIC Research and Education Center, Kwangwoon University  
447-1, Wolgye-Dong, Nowon-Gu, Seoul, 139-701, Korea

\*Currently a Ph. D. Candidate at Kwangwoon University, Seoul, Korea

<sup>2</sup>Department of Electrical and Computer Engineering  
Southern Illinois University  
Carbondale, Illinois 62901-6603

**Abstract:** A compact tag antenna which can mitigate the effect of the supporting metallic platform is proposed for UHF band (902-928 MHz) RFID systems in North America. The overall dimension of the proposed antenna is 88.4 mm x 18 mm x 6 mm, and it consists of the two parts, a meandered half wavelength radiator and proximity coupled-meandered feed network. The meandered feed network, which is layered between the radiator and ground plane, is designed to have a self inductance to cancel out the capacitive reactance ( $9-j127 \Omega$ ) of a tag chip. The antenna is analyzed by Ansoft's HFSS simulator. For various sizes of the metallic platforms, antenna performances, such as the impedance characteristics, radiation pattern, and maximum reading distance, will be measured and discussed.

## 1. Introduction

Radio frequency identification (RFID) technology is an area of automatic identification which has attracted remarkable attention in recent years. RFID not only replaces traditional barcode technology, it also provides additional features and removes boundaries that limited the use of previous alternatives. The basic RFID system consists of three components such as an antenna, a reader and a transponder, commonly called a tag. In essence, an RFID system is just a reader and a tag communication over the air at a certain frequency, like any other radio communication. Recently, the UHF band passive

RFID system has become more attractive and adaptable for many applications than the LF band system due to fast reading speed, long range operation, anti-collision, and various optional functions. As the frequency for RFID moves into the microwave region, proper antenna design becomes more essential to improve the RFID system performance. In general, a tag antenna has to be designed and optimized for particular objects and locations on that object. Many objects for passive RFID tags contain conductive materials or are totally made of metals. However, generally used label-fabricated RFID tags do not work attached to metallic platforms. Therefore, a passive RFID tag mountable to various metal sizes without major degradation of its performance is very useful for specific applications [1], [2].

In this work, the UHF band RFID tag antenna with a small performance variation for various sizes of metallic platform mounts is proposed. The rotationally symmetric feed network with a proximity coupling technique is used to obtain the impedance matching between the radiating element and the RFID tag chip. The half wavelength radiating element has a meandered symmetric structure for size reduction. The proposed antenna is designed and analyzed by using the full-wave 3D EM simulator, HFSS [3]. The simulated and measured results agree well each other. Using the commercial RFID system, the performances such as radiation pattern and maximum reading distance are measured for the proposed antenna with a tag chip.

## **2. Design of Proposed Tag Antenna**

Several UHF band RFID tag antennas mountable on metallic objects have been studied by using the structure of PIFA or IFA [4], [5]. Since they are resonated at a quarter wavelength, their size is essentially compact. However, because the ground plane acts as a part of an antenna and they have unbalanced structures, they can work with the specific ground condition. Hence, they have considerable degradation of performance by changing the ground plane [6]. Metallic objects, such as aluminum cans and foil wrapped packages, are common in most applications that utilize passive RFID systems. Therefore, tag antennas must be designed to enable passive tags to be read near and on metallic objects without performance degradation.

In this work, we will design the feed network to match the impedance between the antenna and the tag chip. Then, the balanced radiating element will be designed to mitigate the effect of the supporting metal size.

## 2.1 Feed Network Design

Over the years, antennas have been developed to match 50ohms. In RFID applications, the input impedance of the tag chip is no longer 50ohms; it may be an arbitrary value. In general, a tag chip has a small resistance and hundreds capacitive reactance due to the capacitance of a rectifier in a tag chip to harvest the operating power from the RFID reader's communication signal. The input impedance of the tag chip used in this work is  $(9 - j127)\Omega$ . Thus, a perfect impedance match between the tag antenna and the RFID microchip is essential in order to sustain the power supply of the chip. Moreover, the impedance tolerance to various platforms is a very important factor. Figure 1 shows the overall geometry and dimension of the proposed antenna. Figure 1(b) shows the proposed feed network. Basically, it has the ground plane to reduce the effect of the metallic object where the tag is mounted. The feed network consists of two rotationally symmetric microstrip lines printed on FR4 substrate ( $\epsilon_r = 4.4$ , height = 1 mm). It is designed to have a self-inductance to conjugately match to the capacitive reactance of the tag chip and meandered to reduce the occupied area. An approximated equivalent circuit of the proposed antenna is shown in Figure 2. The feed network in the equivalent circuit consists of a resistor which represents ohmic loss, a self-inductor, and two capacitors, a radiator, and the ground plane. A proximity coupling to the radiator mainly occurs at the open end parts of two microstrip lines. Figure 3 and 4 show the simulated and measured resistance and reactance with varying the length (A) shown as in Figure 1(b). Figure 3 shows the simulated (A = 8, 11, 14 mm) and the measured (A = 11 mm) resistance at the center frequency (915MHz). Notice that there is a small variation in the resistance and that the simulated and measured results agree. As shown in Figure 4, when the length (A) is 8 mm, 11 mm, and 14 mm, the simulated reactance at center frequency (915 MHz) is  $j98 \Omega$ ,  $j126 \Omega$ , and  $j163 \Omega$ , respectively. When the length (A) is 11 mm, the measured reactance is  $j122 \Omega$  which agrees with the simulated result as well.

## 2.2 Radiating Element Design

Figure 1(a) shows the radiating element of the proposed antenna. Its overall size is 88.4 mm x 18 mm. It is supported by foam (height = 5 mm). The electrical length of the radiator is a half wavelength long to obtain the performance of the balanced structure which is different with quarter wave length PIFAs or IFAs. It is symmetrically meandered

for compact size as is the feed network. The amount of coupling between the radiator and the feed network can be determined by series coupling capacitors as shown in Figure 2. Therefore, the resistance of the impedance can be matched by adjusting the coupling capacitance [7]. Figure 5 and 6 show the simulated and measured impedance of the proposed antenna. They are agreed well each other. The simulated and measured return loss which are renormalized by the impedance of the tag chip ( $(9 - j127) \Omega$ ) are shown in Figure 7. The bandwidth is measured to be about 53 MHz (891 MHz - 944 MHz) which satisfies UHF band (902 MHz - 928 MHz) of RFID systems in North America.

### **3. Measurement Using the Commercial RFID System**

The proposed antenna is combined with the commercial tag chip. Then, using the commercial RFID reader (ALR-9780) [8], its performances are measured based on the back-scattering method in an anechoic chamber as shown in Figure 8. The measurement setup consists of the transmission and receiving parts. The transmission part includes a computer, RFID reader, variable attenuator, directional coupler, and spectrum analyzer. The minimum power signal from the reader is sent to wake up the tag. The spectrum analyzer of the receiving part distinguishes whether the tag is woken up or not regardless of the reader's performance at the same time. For the measurement of the radiation pattern, the minimum level of reader's power to wake up the tag is measured with a horizontally rotating the tag. Figures 9 and 10 show the measured radiation pattern of the proposed tag mounted on two different sizes of metal plates, 108 mm x 52 mm and 300 mm x 300 mm. As the mounted metal plate size becomes larger, the directivity is increased and the back radiation is reduced. Using the commercial RFID reader system (EIRP = 36 dBm), the maximum reading distance of the proposed tag mounted on 108 mm x 52 mm and 300 mm x 300 mm metal plates is measured 3.5 m and 5 m, respectively.

### **4. Conclusions and Future Works**

In this work, the UHF band passive RFID tag antenna, which is effectively mountable on metallic objects, is proposed and designed with a symmetric feed network and radiating element. Using the commercial RFID reader system, the radiation pattern and the maximum reading distance are measured. The proposed antenna is very tolerant of

large metallic platforms and can be applied to RFID systems whose tags are mounted on metallic objects. In the future, the size of the proposed antenna will be further reduced. The matching network for arbitrary impedance of the tag chip will be studied also.

## 5. Acknowledgement

This work is financially supported by the Ministry of Education and Human Resources Development (MOE), the Ministry of Commerce, Industry and Energy (MOCIE) and the Ministry of Labor (MOLAB) through the fostering project of the Lab of Excellency, and supported in part by the post BK21.

## 6. References

- [1] F. Mohd-Yasin, M. K. Khaw, and M. B. I. Reaz, "Radio Frequency Identification: Evolution of Transponder Circuit Design", *Microw. J.*, vol. 49, no. 6, pp. 56-68, June 2006.
- [2] R. Glidden, C. Bockorick, S. Cooper, C. Diorio, D. Dressler, V. Gutnik, C. Hagen, D. Hara, T. Hass, T. Humes, J. Hyde, R. Oliver, O. Onen, A. Pesavento, K. Sundstrom, and M. Thomas, "Design of Ultra-Low-Cost UHF RFID Tags for Supply Chain Applications", *IEEE Comm. Mag.*, vol. 42, no.8, pp. 140- 151, August 2004.
- [3] HFSS, Version 9.2, Ansoft Corporation, Pittsburgh, Pennsylvania.
- [4] L. Ukkonen, L. Sydanheirno, and M. Kivikoski, "A Novel Tag Design Using Inverted-F Antenna for Radio Frequency Identification of Metallic Objects", *IEEE Advances in Wired and Wireless Communication*, pp. 91- 94, April 2004.
- [5] M. Hirvonen, P. Pursula, K. Jaakkola, and K. Laukkanen, "Planar Inverted-F Antenna for Radio Frequency Identification", *Electron. Lett.*, vol.40, no.14, pp. 848-850, July 2004.
- [6] H. Morishita, H. Furuuchi, and K. Fujimoto, "Performance of Balance-Fed Antenna System for Handsets in the Vicinity of a Human Head or Hand", *IEE Proc.- Microw. Ant.*



Propagat., vol.149, no.2, pp.85-91, April 2002.

[7] D. M. Pozar, Microwave Engineering, pp. 334-337, 2nd ed., New York: John Wiley and Sons, 1998.

[8] <http://www.alientechnology.com/>

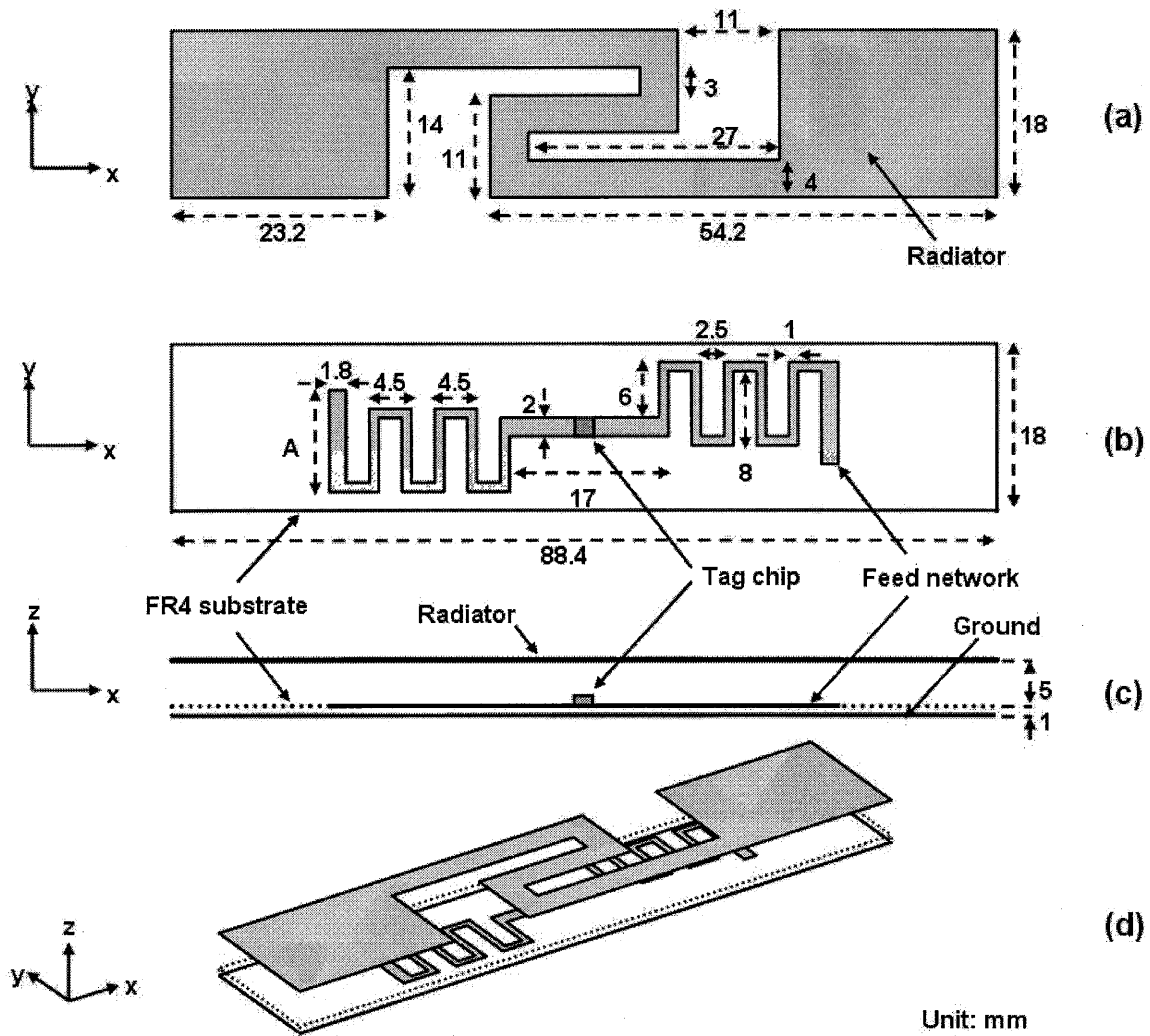


Figure 1. Geometry of the proposed antenna  
 (a) Top view of a radiator, (b) Top view of a feed network,  
 (c) Side view of the proposed antenna, (d) Overall view of the proposed antenna

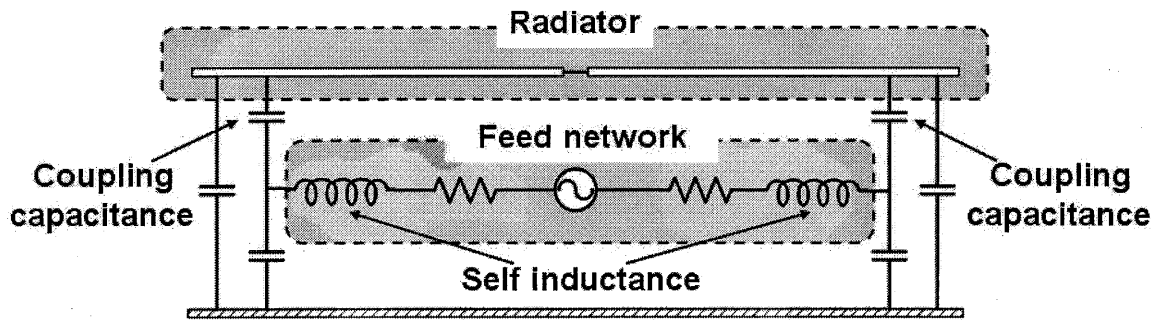


Figure 2. Approximated equivalent circuit of the proposed antenna

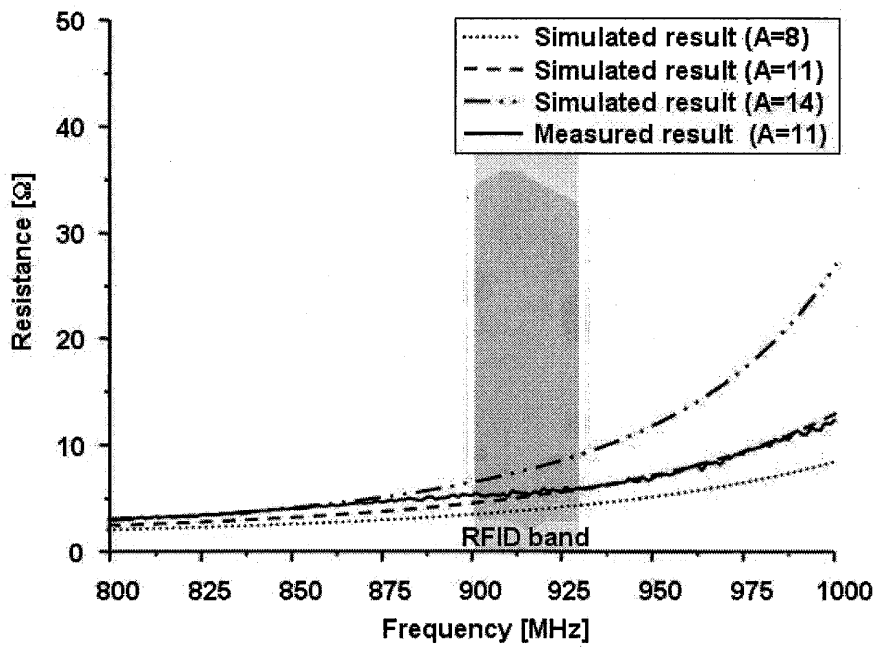


Figure 3. Simulated and measured real part of impedance of the feed network without radiating element

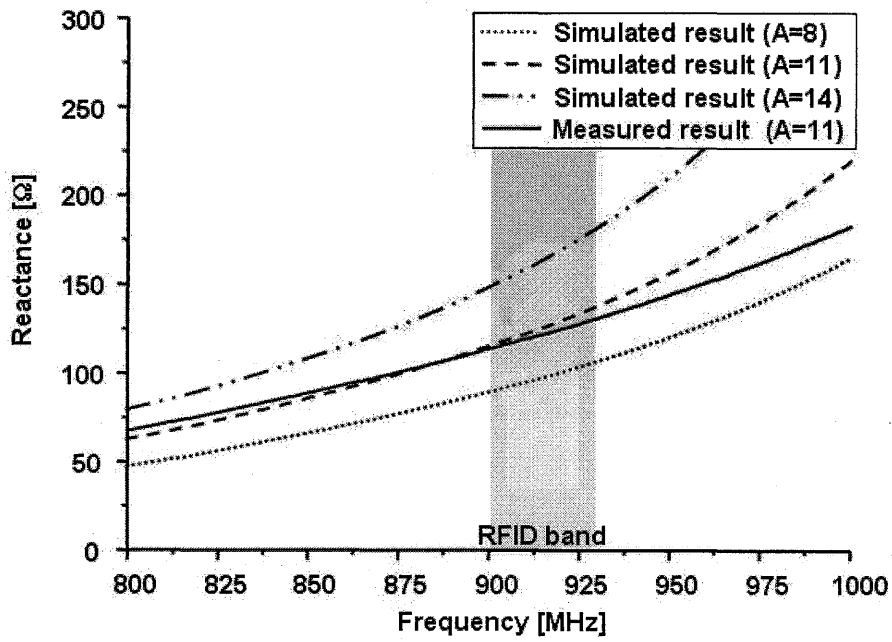


Figure 4. Simulated and measured imaginary part of impedance of the feed network without radiating element

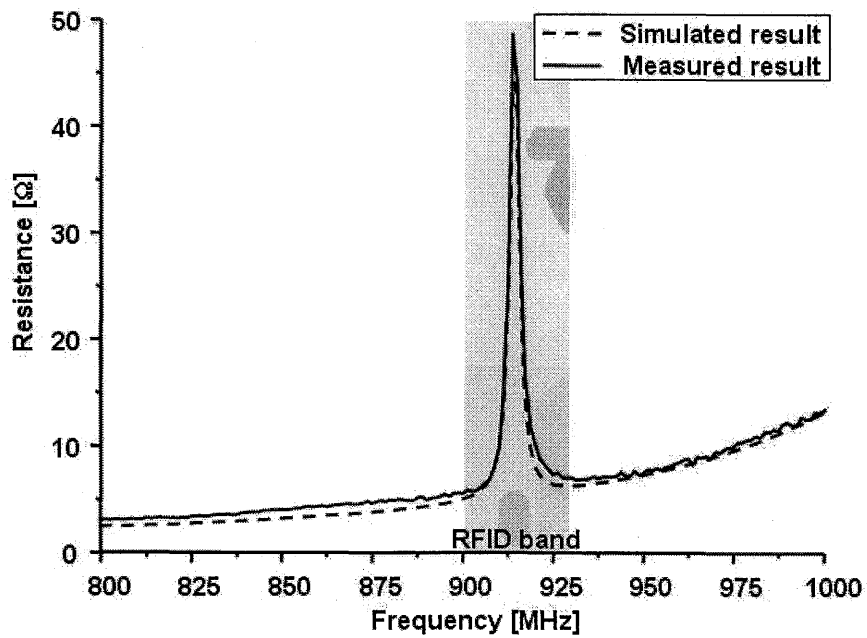


Figure 5. Simulated and measured real part of the impedance of the proposed antenna

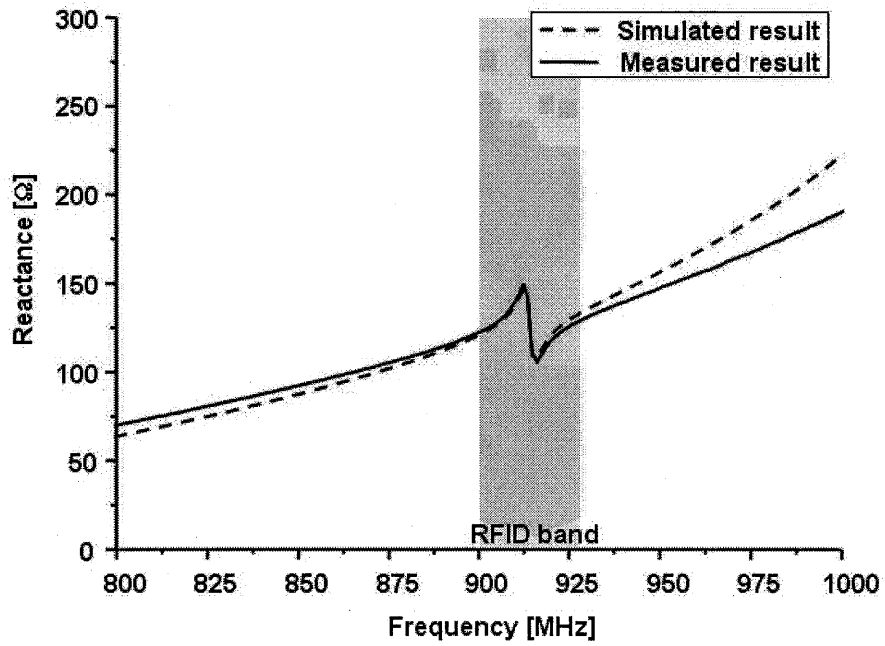


Figure 6. Simulated and measured imaginary part of the impedance of the proposed antenna

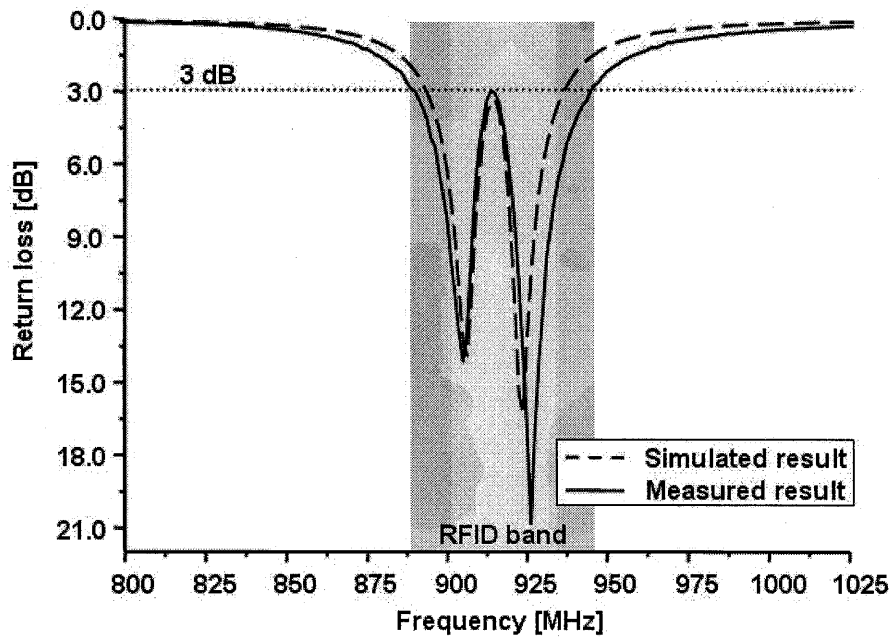


Figure 7. Normalized return loss between the antenna and the tag chip

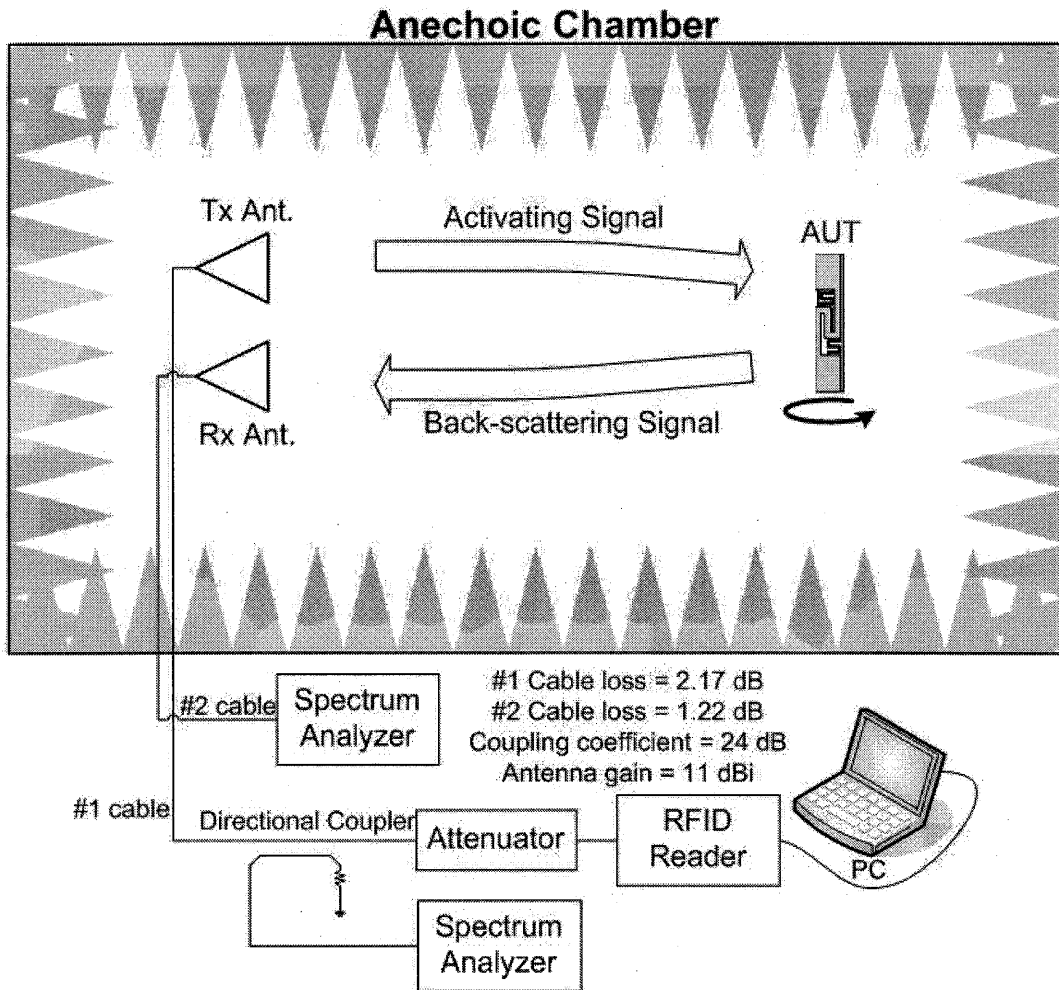


Figure 8. Setup of measurement system using the commercial RFID reader

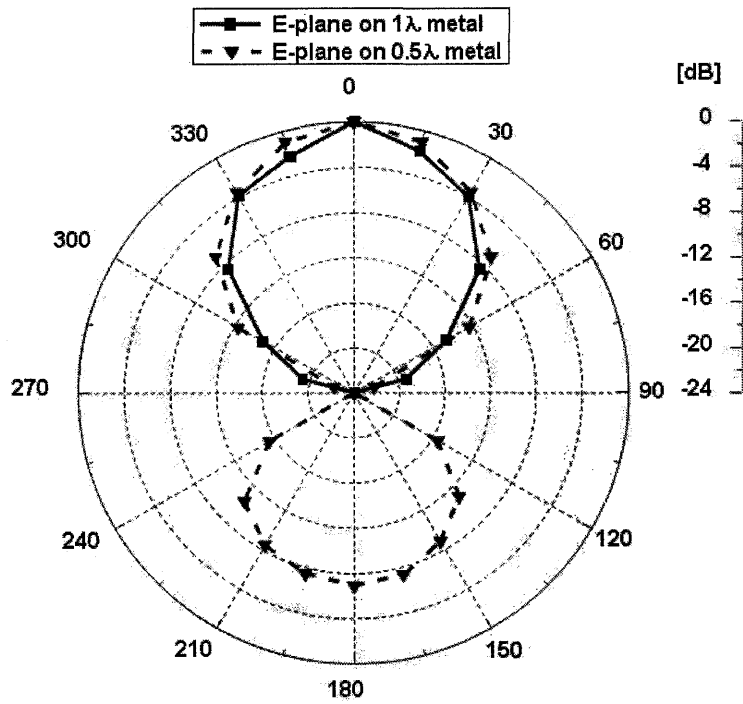


Figure 9. Measured E-plane(y-z plane) radiation pattern

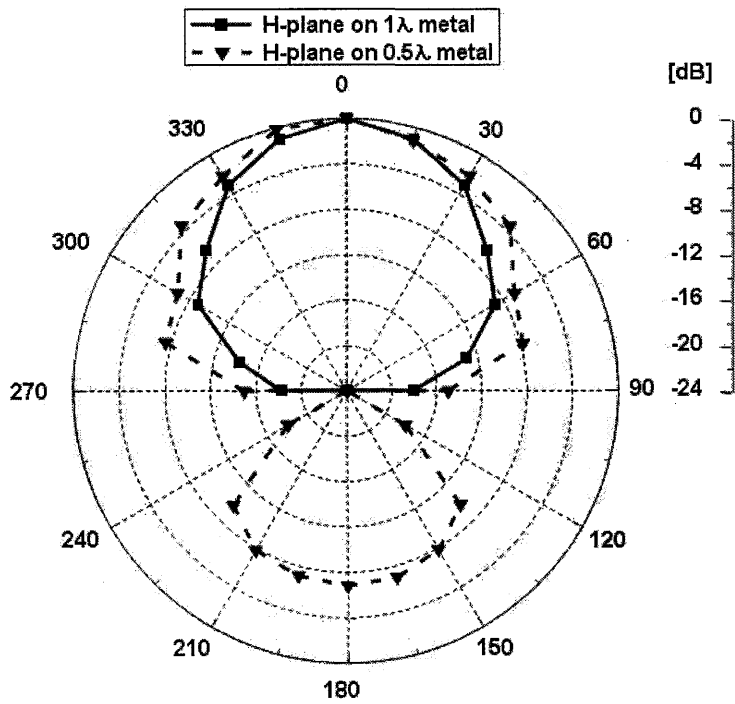


Figure 10. Measured H-plane(z-x plane) radiation pattern

# Small Antennas and Arrays for Wireless Communications

Yuanxun Ethan Wang  
Electrical Engineering Department,  
University of California at Los Angeles  
420 Westwood Plaza, Los Angeles, CA90095

**Abstract:** This paper addresses two fundamental topics regarding electrically small antennas and electrically oversampled antenna arrays. It is well known that electrically small antennas suffers the fundamental limit of high Q and can not be used for broadband radiation in conventional cases. However, it is found that by integrating high-speed switch devices on the antenna, the bandwidth limit on the radiation can be overcome. This is because the high-Q value associated with electrically small antennas no longer limits the bandwidth of radiation in such a time-varying system. On antenna arrays, it is commonly believed that the array spacing among the antennas has to be greater than  $\lambda/2$  to avoid mutual coupling. For an electrically oversampled array, the mutual coupling creates impedance mismatch so that the array gain will drop even if the antenna array's radiation pattern is "superdirective". Here, it is proposed to decompose the orthogonal radiation modes existing in the array into different excitation ports. Those ports can be matched individually as they are isolated from each other, a property resulting from the array symmetry and the orthogonality of the modes. The multiple modes can be used separately from diversity gain in a MIMO system or combined coherently for super array gain.

## 1. Introduction

Described by Moore's law, the breakthroughs in semiconductor integrated circuits have revolutionized the design concept of wireless communication systems. Modern wireless communication devices are of magnitudes of higher speed and more functions comparing to their predecessors, yet operated in a much smaller platform. Contrary to this main stream, antennas and antenna arrays in wireless transceivers, however, remain as the last components to be miniaturized. This is because of the fundamental physical limits regarding the bandwidth of electrically small antennas [1,2] and the gain of the array for a given aperture size. On the other hand, small antennas and arrays, if made without sacrificing the system performance, can become ever sought with the convenience of handheld or palm size wireless platforms. The fundamental physical limit in an electrically small antenna is the high energy storage in the near field of the antenna that prevents the antenna from radiating a broadband signal. Here, it is proposed to use high-speed switches to control the energy storage and release in the antennas in a real-time



fashion. As it will be demonstrated later, this can overcome the limit of the high  $Q$  to the antenna radiation bandwidth. With this technique, even Ultra-Wide Band (UWB) pulses can be efficiently radiated from an electrically small dipole antenna. For antenna arrays, the array gain is typically determined by the physical aperture size, which is called aperture limit. Even though the concept of “superdirective” antennas with densely packed antenna elements have existed for at least 5 decades, it is still commonly believed that the array spacing should be kept more than half of the wavelength to avoid mutual coupling. The conventional “superdirective” antenna can not offer substantial increase in antenna gain as severe impedance mismatch emerges when antenna elements are pushed to be closer than  $\lambda/2$  to each other. One exception is parasitic antennas like a Yagi-Uda antenna that can realize truly super gain than the aperture limit. However, the design of Yagi-Uda antennas is mainly through optimization and can thus not be generalized. Neither does it offer the beamforming flexibility and electronic scanning capability of a full array. In this paper, the proposed approach is to separate the orthogonal radiation modes of the array through a mode-decomposition network. The modes, instead of the individual antennas, are used to carry independent information channels. Those channels can be used separately for diversity gain in system capacity in Multiple-Input-Multiple-Output (MIMO) communications systems [3-5], or combined coherently through beamforming for supergain and electronic beam steering. Practical super gain antennas and super diversity antennas can be realized in this way. As another fundamental limitation of the supergain antenna is the reduction of the bandwidth and the increase of  $Q$ , it is expected that the aforementioned two techniques can be eventually combined to realize broadband radiations with supergain.

## **2. Switched Electrically Small Antennas**

Many researches have tackled the fundamental limitation on size reduction of antennas. It has been well recognized that the antenna’s radiation  $Q$  is physically limited by its volume. The Chu’s limitation describes such relationship [1]. Although antenna’s  $Q$  value is an important parameter, the final criterion for evaluating the performance of the antenna should be the efficiency-bandwidth product (EB). By re-examining how Chu’s limitation is derived, it is found that there is a possible way to boost EB beyond the original limit, even though the constraint on  $Q$  can not be violated. This is realized by introducing time-variance into the system through switching. To validate the approach, the paper presents the theoretical analysis and full-wave simulation results for electrically small antennas.

As a review, Chu’s limitation and extended work on the radiation  $Q$  of electrically small antenna is summarized as following. First, Chu imagines that the antenna is enclosed by a sphere with smallest possible radius  $a$ . Then, the field outside the sphere can be expanded by spherical wave modes. To calculate the  $Q$  value for each mode, Chu came up with the equivalent circuit model and derived the formulas. Finally, minimum  $Q$  can be obtained when only the lowest order mode exists. Since this  $Q$  takes into account only the stored

energy outside the sphere, any stored energy inside the sphere would increase its value. Later work shows mathematic form of the minimum Q is [2]

$$Q = \frac{1}{(ka)^3} \quad \text{when } ka \ll 1 \quad (1)$$

In conclusion, Chu's limitation is essentially the limitation on antenna's Q subject to its size. High Q indicates large stored energy compared to the radiation energy per cycle. The large stored energy makes it difficult to match the antenna in a wide frequency range, thus limiting EB of traditional antennas. However, it's only in a linear time-invariant system that a high Q would definitely lead to a low EB. This implies the possibility of obtaining larger EB from a small antenna if time variance of the electromagnetic boundary condition is introduced into the system. One approach is to integrate the switches with the antenna and turn on and off the radiation in time domain. In this way, controlling the transient stored and radiated energy of the antenna becomes the key for high efficiency. This is called direct-antenna modulation (DAM) technique [6-10], where it has been applied to increase the radiation bandwidth of resonant patch antennas [6-9]. Similarly, the transmission from a switched electrically small antenna is directly modulated by the switching signal [10]. The on and off stage of a short dipole is shown in Fig.1. The dipole is center driven by a RF source with an inductor and a switch. When the switch is on, the radiation is turned on. Fig.1 (a) shows the propagating electrical field lines. In this stage, the source forces the charge movement and thus producing current and radiation. When the switch is off, the radiation is turned off. The antenna enters into the static stage and charges on the antenna store electrostatic energy with the field lines depicted in Fig.1 (b). The off stage maintains the stored energy and prepares the antenna for radiation in the next cycle.

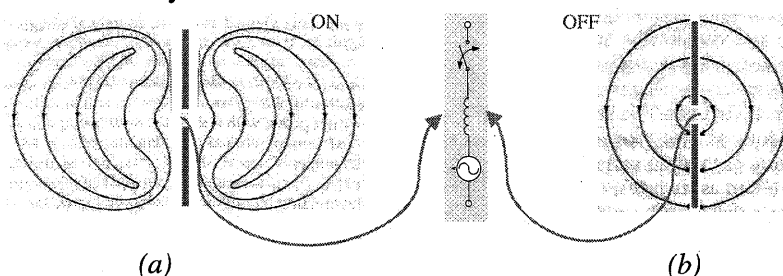


Fig. 1 Electric Field Lines of a short dipole for (a)on and (b)off stage

The concept can also be explained from the view of the equivalent circuit of the antenna. It is well known that an electrically small dipole can be roughly characterized by a series capacitor and resistor. As shown Fig. 2, when the switch is on, the power is transmitted from the source to radiation resistance  $R_a$ , and the stored energy is resonating between the inductor and capacitor. At the moment that the current through the inductor is passing zero, the voltage across the capacitor should be maximum. This means the maximum amount of energy is stored in electric field in the near field. If the switching occurs exactly at this moment, the capacitor, or the near field would maintain this

maximum amount of energy after the switch is off. Therefore, no energy loss will occur because in the transition between the two stages. In addition, assuming the charges “freezes” when the switch is off, the current flow will stop and no radiation will be generated. When the switch is turned on again, the resonator with the maximum amount stored energy in the capacitor is ready to take the input energy to the space and a new cycle of radiation can start immediately.

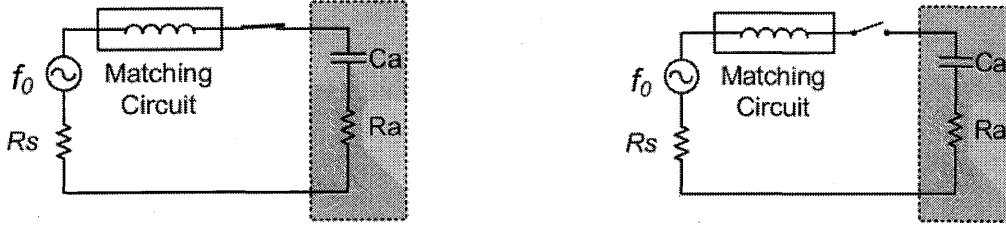


Fig. 2 Equivalent circuit for on and off stage

However, the equivalent circuit in a series capacitor and resistor does not represent the full physics of the antenna radiation. Neither does the more complicated broadband circuit models proposed for an electrically small dipole [4], as the transient radiation effect is missing in the circuit model. Therefore, an insight of how electromagnetic wave behaves in time-domain is necessary. From the energy efficiency perspective, the first possible side-effect due to switching in a finite-size electrically small antenna is the spurious radiation. As the switching speed of the device is required to be much faster than the carrier frequency, the force imposed by the source on the charges disappears as soon as the switch is turned off. The antenna is disconnected from source and the charges left on the antenna could redistribute themselves and forms a natural radiation response. This can cause undesired radiation at the self-resonance frequency of the antenna, which will dissipate part of the stored energy. However, since the antenna size is small, the charge redistribution effect is expected to be small. The FDTD simulation result has also proven this prediction later. An extreme case is an infinitesimal dipole. The charge movement will “freeze” immediately caused by the turning off of the switch, as the current flow path is cut off. Therefore, the spurious radiation of an ideal dipole under such switching should tend to zero. The efficiency calculations can be carried out in time-domain analysis. A comparison is made between the stored energy before and after the switching. The switching action is selected to occur exactly at the zero current instant. As the antenna radiates as usual before switching, the stored energy before the switching instant is derived to be

$$E_{stored,on} = E_{total} - E_{radiation} = \frac{\mu J_0^2}{3\pi k^2 a}, \text{ when } a \rightarrow 0 \quad (2)$$

The stored energy in off stage is derived to be

$$E_{stored,off} = \frac{\epsilon q^2}{3\pi a}, \text{ when } a \rightarrow 0 \quad (3)$$

where  $a$  is the size of the antenna,  $J_0$  is the current amplitude in the radiation mode, and  $q$  is charge amount in the non-radiation mode. By setting the relationship between  $J_0$  and  $q$  based on continuity equation

$$J_0 = \omega q \quad (4)$$

One can prove that

$$E_{on} = E_{off} \quad (5)$$

Therefore, no energy would be lost during the transition of on and off stage in an ideal dipole. This is the key for potential high efficiency operation of switched electrically

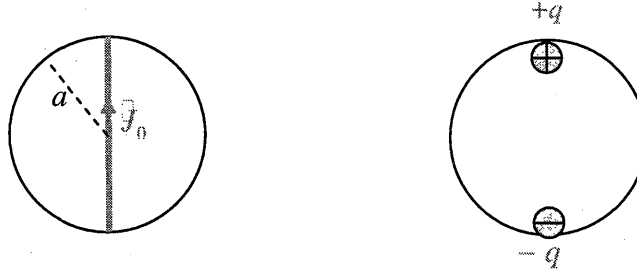


Fig.3 Continuity relationship between charge and current on the dipole

small antenna. For practical electrically small antennas with finite sizes, however, there will be energy loss caused by several non-ideal effects. The most fundamental one is the energy loss caused by the spurious radiation as stated in (1). However, as the analysis and simulation results have shown, it is a small amount compared to the radiated energy. The major loss would be the switching loss, which is caused by the non-zero resistance, finite off isolation and finite switching speed of the switches. In addition, the Ohmic loss of the antenna and the matching network will also contribute to the efficiency loss. With the advancement of switch device technology and the antenna integration technology, those factors can be minimize, which will result in a promising pulse transmitting scheme utilizing electrically small antennas. To confirm the concept, FDTD simulation is carried out for a  $\lambda/10$  planar dipole with the excitation frequency at  $100 \text{ MHz}$ . Fig. 4 shows the simulation setup. The switch is modeled as a variable resistor with three parameters: on resistance  $R_{on} = 5\Omega$ , off resistance  $R_{off} = 10M\Omega$ , and transition time  $t_{tran} = 0.6ns$  during which the resistance varies exponentially. To simplify the simulation, the inductor is not included because it only improves the matching but would not effect the spurious radiation or switching loss of the antenna.

Fig. 5 shows the simulated pulse waveform of the voltage and current across the antenna excitation port and the radiated far field.  $V_{ctrl}$  is the controlling signal of the switch. After the switch is turned off, undesired radiation appears at the self resonance frequency of the antenna. This is caused by the charge redistribution effect. It is observed that the energy carried by the undesired radiation is much smaller than that of useful radiation. To further check this effect, numerical calculation is carried out. Fig.6 shows the normalized charge distribution at the instant before switching and the instant when antenna enters static stage after the switch is off. The stored energy difference before and after is calculated to be 0.86% only, which is under the numerical noise floor of the FDTD simulation. Since the charge redistribution effect is the only fundamental physical limitation of this approach, the theoretical limit on the efficiency of this antenna would be very high.

To estimate the efficiency of the antenna with practical switches, the energy loss for each switching is calculated to be 4.76% stored energy with the above parameter. The radiated energy per pulse is

$$\frac{\text{Stored Energy}}{Q} \times 2 \approx 1\% \times \text{Stored Energy}, \text{ when } Q \approx 200$$

The efficiency is

$$\frac{\text{Radiated Energy}}{\text{Radiated Energy} + \text{Lost Energy}} = 18.76\%$$

Therefore, the EB is

$$EB = \text{efficiency} \times \text{bandwidth} = 18.76\% * 50\% = 9.38\%$$

Compared to a conventional antenna with  $Q \approx 200$ ,  $EB \approx 1/Q \approx 0.5\%$ , the proposed approach dramatically improves the EB provided good switches are available.

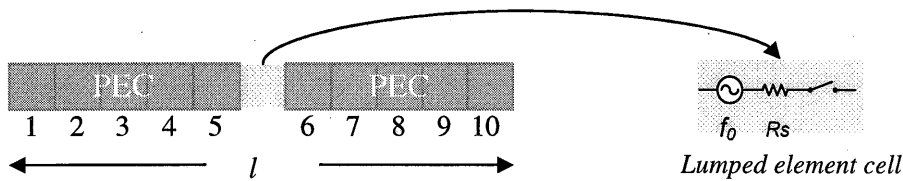


Fig. 4 FDTD simulation setup: cell size=3cm×3cm×3cm,time step=57.7 ps, $f_0=100\text{MHz}$ , $l=\lambda/10$

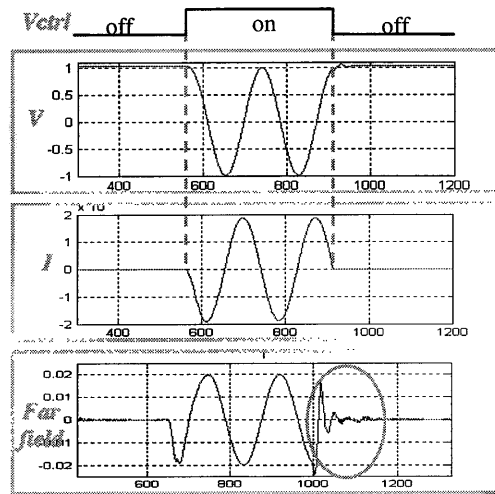


Fig.5 Voltage, current and far field pulses

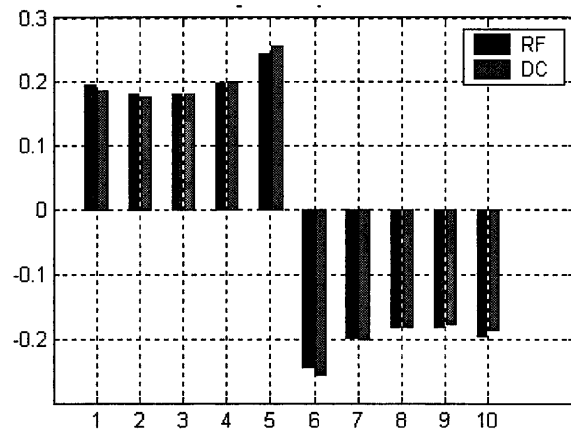


Fig. 6 Normalized charge distribution before and after switching

### 3. Electrically Oversampled Antenna Arrays

In the past, various researches have been carried out regarding the capacity limit of a MIMO system for a given physical boundary of a wireless platform, from the utilization of polarization diversity and pattern diversity [11-13]. For example, it has been proposed in [11] to use three electric dipoles and three magnetic dipoles that are perpendicularly co-located, to obtain six times the capacity of a single antenna system. However, the works are mostly theoretical as the practical issues regarding antenna excitations and mutual couplings are not considered. Mutual coupling and spatial correlation effects and their impacts on the MIMO system performance have been studied in [14-20]. It is common knowledge that these effects will degrade the system capacity when the antennas are placed closely together. Possible ways to combat the mutual coupling and correlation effects have also been studied [21-34]. Some have presented signal processing approaches [21, 22] to decouple the signals actually received by antennas. Though the signal errors due to the coupling can be eliminated this way, it does not enhance the system capacity performance as no improvements were made on the system signal to noise ratio. Others have proposed hardware approaches to reduce the mutual coupling [23-27]. However, the mutual coupling through free space is related to the non-orthogonality of the radiation patterns of the antennas, unlike the mutual coupling through the circuit board or the feed lines. It is part of the intrinsic property of the radiation physics and can not be simply removed. On the other hand, Anderson etc. proposed an approach to decouple the antennas in the excitation ports through a multi-port network [28]. In his pioneering work [28], a crossing transmission line is used to decouple two antennas with purely imaginary mutual impedances. Several recent papers further advanced this approach by presenting a more complete way of designing the transmission line decoupler for a pair of coupled dipoles based on its even and odd mode impedance characteristics [29-32]. Decorrelations between two dipole antennas in a

multi-path environment are also observed in those works [29-32]. Based on the network theory, Wallace etc. has proven [33, 34] the capacity performance of a multi-antenna system with the mutual coupling and correlation effects can be optimized with an optimum, lossless multiport matching network, defined by its S parameters. This is achieved through the maximization the signal power received by the coupled antennas and decorrelation of the received signals at the outputs of the network. However, there are no clues on how such a network can be implemented in practice. Others have demonstrated the mutual coupling can be used to build so-called supergain antennas through the optimization of the parasitic effects [35]. However, the physical mechanism of mutual coupling remains unclear and an explicit design rule of achieving supergain in arrays does not exist.

The proposed work is to explore the full potential of the closely coupled antenna system in terms of its diversity and gain performance. Instead of separating coupled antennas into individual ones, the antennas are treated as a whole. It focuses on the fundamental physics of the orthogonal radiation modes in the antenna system and explores how the modes are related to the mutual coupling and contributing to the antenna gain and system capacity. The orthogonal modes, in many cases, can be separated from the antennas to different output ports with a mode decomposition network (MDN). The mode-dependent impedance behavior of the closely coupled antennas can be observed, leading to a clear physical explanation of the coupling mechanism. In comparison with the transmission line decoupler approach used in [28-31], the proposed MDN based on 180 degree hybrids exhibits a clearer physical meaning as it can separate the modes completely at the outputs. It is a more general way of decoupling the antennas by offering the following several advantages. First, unlike the decoupler [28-31], the MDN does not need to be specifically designed for different antenna elements as long as the symmetry of the array configuration is satisfied. Furthermore, in contrast to the intrinsic narrowband isolation in the transmission line decoupling network, the isolation between the decoupled ports through the MDN is naturally broadband as defined by the bandwidth of the hybrid. As the impedance matching can be performed for each mode separately, the addition of active or tunable impedance matching for the higher order modes with high Q values is possible. The MDN for 2-elements can be used as a building block to construct a larger scale MDN for arrays having more than 2-elements, as will be demonstrated later. The orthogonal radiation modes, once separated, can be utilized for MIMO diversity and supergain applications. In rich scattering scenarios, one can use those modes to transmit or receive different channels of information, which is the concept of pattern diversity [13]. On the other hand, a supergain beamforming array may be obtained if those modes are excited in a coherent way and their radiation patterns are constructive in certain directions. Since the Q factor of the radiation is associated with the order of the mode, separating the modes also offers the most natural way of trading off between the supergain and the Q value. The Q value is usually inversely proportional to the radiation bandwidth in a linear, time invariant antenna system.

To illustrate the concept and the research method, the property of a closely coupled dipole pair is first studied as the simplest example. By separating the common mode and the difference mode in such a dipole pair, it will be demonstrated that double the capacity and three times the antenna gain in comparison to a single dipole antenna can be realized [38]. The mode decomposition network based on 180 degree hybrids is described. The performance of the resulted “supergain” antenna is proven experimentally in the study. On the other hand, the concept of mode decompositions can be directly applied in any N-element closely coupled circular array. It is proposed to simultaneously combine a number of spatial harmonic modes of circular array for a supergain beam with electronic scanning capability. It is also expected that the mode-based beamforming concept can be extended for other configurations of array such as linear arrays or parasitic antennas. Lastly, the implementation challenges and the fundamental limit of Q factors of higher order modes in tightly coupled antennas are discussed.

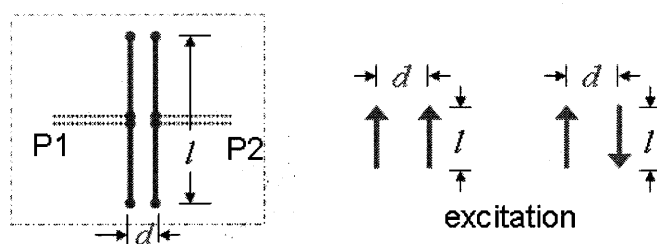


*Fig.7 Closely coupled dipole pair and common mode, difference mode excitation*

Consider two Hertzian dipoles of length  $l$  that are parallel to each other along the  $z$ -axis and excited by two independent sources. The spacing between the two antennas  $d$  is assumed to be small compared to the wavelength to allow for tight coupling. It is well known that this 2-element array supports two radiation modes, e.g. the common mode and the difference mode, as shown in Fig.7. If strong mutual coupling exists between the antennas, the radiation resistance of the difference mode can be much smaller than that of the common mode. The conventional one-to-one conjugate match to the single antenna impedance is no longer optimal as the energy of the difference modes is lost because of mismatch. In order to maximize the received power, these two modes have to be separated into different output ports and independently matched, which requires the aforementioned 180 degree hybrid as a mode decomposition network. From the network theory, the orthogonality between the common mode and difference mode can be related to the property of the characteristic modes in any symmetric antenna systems in a more general view of the mutual coupling mechanism. The radiation far field patterns of the  $z$ -axis oriented dipoles are drawn in Fig.8.



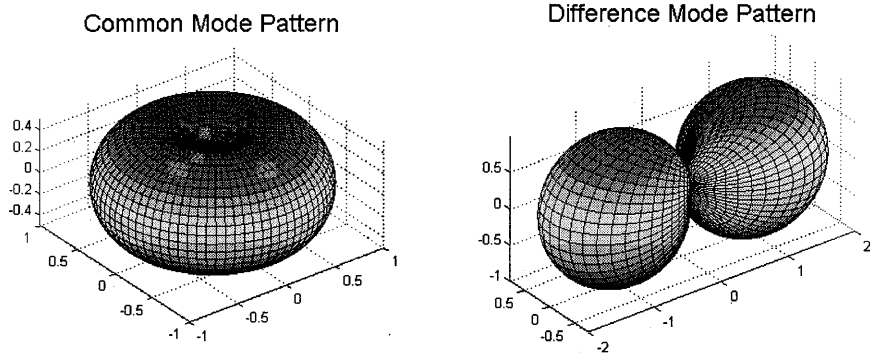


Fig.8 Common mode and difference mode radiation patterns of  $\hat{z}$  directed dipole antennas

The orthogonality can be analytically verified between any two modes or polarizations, which is in the form:

$$\oiint (\overrightarrow{Pat}_{CM,z} \bullet \overrightarrow{Pat}_{DM,z}^*) d\Omega = 0 \quad (6)$$

where  $\Omega$  is the solid angle. The property of pattern orthogonality is a necessary condition required to ensure that the channels are independent for the closely coupled antennas. The radiation resistances for both modes can thus be calculated by integrating the radiation patterns over all the angles, which yields:

$$\begin{cases} R_{CM} = \frac{2\pi\eta}{3} \left(\frac{l}{\lambda}\right)^2 \\ R_{DM} = \frac{8\pi^2\eta}{3} \left(\frac{ld}{\lambda^2}\right)^2 \end{cases} \quad (7)$$

The above formulas show that when the antenna spacing  $d$  reduces, the radiation resistance also reduces according to a square relationship for the difference mode, while the common mode radiation resistance remains the same. However, for legitimately small antenna spacing in the order of  $0.1\lambda$ , the radiation resistance of the difference mode is not outrageously small compared to that of the common mode and may be made of good use. For example, in the case  $l=d=0.1\lambda$ , the radiation resistance is  $7.9\Omega$  for the common mode and  $1.0\Omega$  for the difference mode. The orthogonal patterns of the two modes can be used for pattern diversity in a straightforward way if they are driven independently. Considering a rich scattering environment with uniform distribution in full angular spread, both modes carry the same amount of power through the scattering after integrating over all the spherical angles. The correlation coefficient between the two receiving modes can be derived as [20],

$$\rho = \frac{\iint (\overrightarrow{Pat}_{CM,z} \cdot \overrightarrow{Pat}_{DM,z}^*) d\Omega}{\sqrt{\iint |\overrightarrow{Pat}_{CM,z}|^2 d\Omega \iint |\overrightarrow{Pat}_{DM,z}|^2 d\Omega}} = 0 \quad (8)$$

In this case, the common mode and the difference mode offer equally good information channels within the pass band of both modes, which can maximize the capacity of the MIMO system. For limited angular spread, the integration boundary in (8) is modified and the received signals from the two modes are no longer perfectly uncorrelated. Yet the system capacity degrades gracefully, if two of such arrays are aligned in the end-fire direction. To examine the performance under different angular spreads, simulations are carried out for a MIMO link. The receiver is assumed to be surrounded by scatterers uniformly distributed on a spherical surface. The transmitter illuminates the sphere with a certain angular spread. Both the transmitter and the receiver are coupled,  $0.1\lambda$  long dipole pairs aligned in the end-fire direction, but there is no line of sight propagation. The spacing between the coupled dipoles is  $0.1\lambda$ . With the assumption of equal power excitation between the two modes, Fig.9 shows two comparable eigenvalues in the normalized channel matrix which corresponds to the contributions from the two-mode pattern diversity. In a typical MIMO system, there is no direct one-to-one relationship between the eigenvalues of the channel matrix to the modes because the propagation paths are mixed together in space. The two eigenvalues in Fig.9 approach each other as expected when the angular spread increases, which implies an increase in the system capacity. As shown in Fig.10, the system capacity at the 74 degree angular spread almost reaches that of a 2x2 Rayleigh fading channel, which is the optimal case in a rich

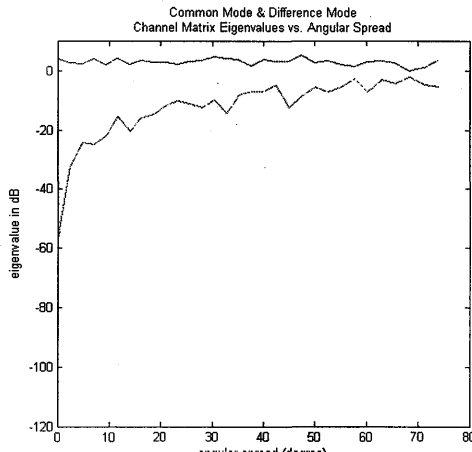


Fig.9 Eigenvalues of the channel matrix for the MIMO link consisting of coupled dipole pairs at  $0.1\lambda$  spacing and length

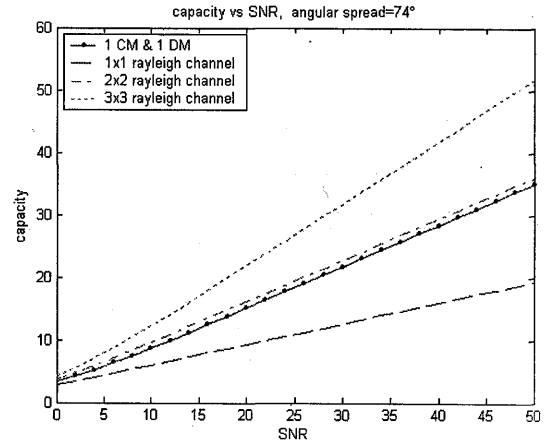


Fig.10 Capacity plot for the MIMO link consisting of coupled dipole pairs at  $0.1\lambda$  spacing and length

scattering environment. It should be noted that though the simulations are carried out for coupled dipoles with  $0.1\lambda$  spacing and length, the single-frequency capacity results should be independent of the spacing and the length of the antennas, if they are small and close enough together. However, the impedance matching bandwidth will reduce as a

consequence of increased Q value in the radiation. In the latter section, it will be shown that the impedance matching bandwidth of the difference mode is reduced to 1/20 of that of the common mode when a pair of parallel half-wave dipoles at  $0.1\lambda$  spacing is used. Therefore, the total system capacity over all the frequencies will reduce accordingly.

The crucial step in utilizing the parallel channels provided by the coupled antennas is a passive mode decomposition network (MDN) that can drive the different radiation modes independently. In fact, multiple radiation modes always exist in almost any N-element arrays, regardless coupled or not. However, there may not be a simple and easy way to separate them like those in multipoles or in circular arrays. Particularly for the coupled dipole pair, a 3dB 180 degree hybrid can separate the common and difference mode and match them respectively [40]. The 180 degree couplers can be realized in many ways such as rat-race couplers, magic Ts, coupled line couplers, baluns and transformers. In order to verify the mode separation capability of the hybrid, an equivalent T network can be derived from method of moments to represent the general coupling behavior of the antennas, which is shown in Fig.11. By performing the even and odd mode analysis, the impedance matrix of the antenna  $[Z_{ant}]$  can be defined as follows,

$$[Z_{ant}] = \begin{bmatrix} Z_{11} & Z_{12} \\ Z_{21} & Z_{22} \end{bmatrix} = \begin{bmatrix} R_{CM} + R_{DM} & R_{CM} - R_{DM} \\ R_{CM} - R_{DM} & R_{CM} + R_{DM} \end{bmatrix} \quad (9)$$

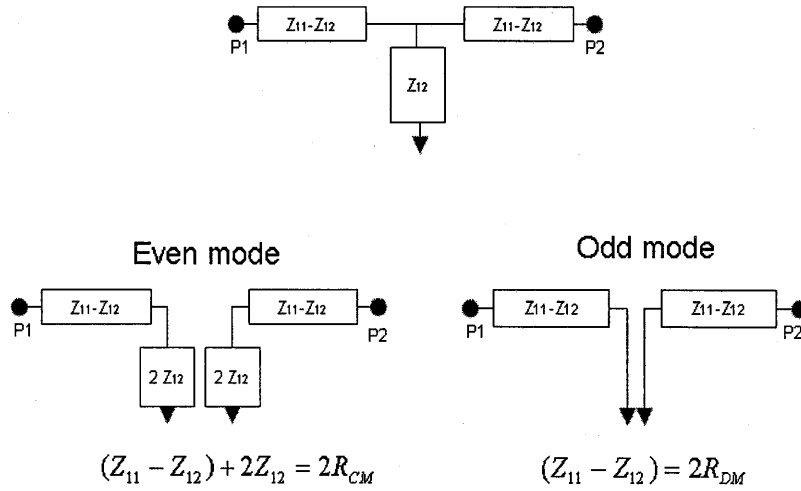


Fig.11 Equivalent T network and even and odd-mode analysis for two-port antenna

where  $R_{CM}$ ,  $R_{DM}$  are the common-mode and difference mode radiation resistance. In a non-coupling case,  $R_{CM}=R_{DM}$ , the non-diagonal terms in the matrix will become zero. From (7) and (9), it is evident that the difference in radiation resistances between the two

modes is the manifestation of the mutual coupling effect. A larger difference indicates a stronger coupling. The two-port impedance matrix can be transformed to two-port S parameters  $[S_{ant}]$ . The matching network realized by a 3dB 180 degree hybrid has the following scattering parameters:

$$\begin{bmatrix} V_{\Sigma}^- \\ V_A^- \\ V_B^- \\ V_{\Delta}^- \end{bmatrix} = \frac{-j}{\sqrt{2}} \begin{bmatrix} 0 & 1 & 1 & 0 \\ 1 & 0 & 0 & -1 \\ 1 & 0 & 0 & 1 \\ 0 & -1 & 1 & 0 \end{bmatrix} \begin{bmatrix} V_{\Sigma}^+ \\ V_A^+ \\ V_B^+ \\ V_{\Delta}^+ \end{bmatrix} \quad (10)$$

If the two power splitting ports are connected to the antenna ports like in Fig.12, one can obtain the common mode and difference mode separately from the sum and difference ports of the hybrid. This can be proven by decomposing the above four-port hybrid matrix into two 2x2 matrix equations

$$\begin{cases} \begin{bmatrix} V_A^- \\ V_B^- \end{bmatrix} = \frac{-j}{\sqrt{2}} \begin{bmatrix} 1 & -1 \\ 1 & 1 \end{bmatrix} \begin{bmatrix} V_{\Sigma}^+ \\ V_{\Delta}^+ \end{bmatrix} \\ \begin{bmatrix} V_{\Sigma}^- \\ V_{\Delta}^- \end{bmatrix} = \frac{-j}{\sqrt{2}} \begin{bmatrix} 1 & 1 \\ -1 & 1 \end{bmatrix} \begin{bmatrix} V_A^+ \\ V_B^+ \end{bmatrix} \end{cases} \quad (11)$$

At the same time, the S-parameters  $[S_{ant}]$  of the antenna is defined as,

$$\begin{bmatrix} V_A^+ \\ V_B^+ \end{bmatrix} = \begin{bmatrix} S_{11} & S_{12} \\ S_{21} & S_{22} \end{bmatrix} \begin{bmatrix} V_A^- \\ V_B^- \end{bmatrix} \quad (12)$$

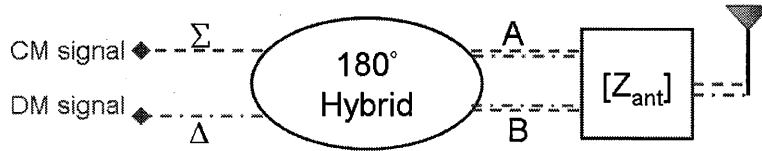


Fig.12 Block diagram for the antenna excitation through a 180 degree hybrid

The two-port S-parameters for  $\Sigma$  port and  $\Delta$  port can now be derived from the following matrix equation.

$$\begin{bmatrix} V_{\Sigma}^- \\ V_{\Delta}^- \end{bmatrix} = \left( \frac{-j}{\sqrt{2}} \begin{bmatrix} 1 & 1 \\ -1 & 1 \end{bmatrix} \right) [S_{ant}] \left( \frac{-j}{\sqrt{2}} \begin{bmatrix} 1 & -1 \\ 1 & 1 \end{bmatrix} \right) \begin{bmatrix} V_{\Sigma}^+ \\ V_{\Delta}^+ \end{bmatrix} \quad (13)$$

From (13), one can see that the original coupled  $[S_{ant}]$  matrix is actually diagonalized through the linear transformations defined by the two hybrid coupler matrices. Therefore, the impedance matrix of two driving ports are finally obtained in a diagonal form,

$$\begin{bmatrix} V_{\Sigma} \\ V_{\Delta} \end{bmatrix} = \begin{bmatrix} Z_{\Sigma\Sigma} & 0 \\ 0 & Z_{\Delta\Delta} \end{bmatrix} \begin{bmatrix} I_{\Sigma} \\ I_{\Delta} \end{bmatrix} \quad (14)$$

where  $Z_{\Sigma\Sigma} = \frac{Z_0^2}{2R_{CM}}$ , and  $Z_{\Delta\Delta} = \frac{Z_0^2}{2R_{DM}}$ .

From the above derivation, one can see that the 180 degree hybrid indeed decomposes the signal received from the antenna ports into the common mode and the difference mode through a process of diagonalizing the impedance matrix. This is also consistent with the orthogonality of the radiated power of these two modes. Now if the two driving ports are conjugately matched to different port impedances, there will be no mismatch in the system. More significantly, the 180 degree hybrid can be used not only as the MDN for a pair of coupled antennas, but also as a basic unit to build up the MDN for a large number of elements with many modes. This extendibility offers significant advantages of the proposed MDN over existing antenna specific decouplers [28-32] as it allows the proposed concept to be applied in a much greater scope.

Superdirective arrays have been studied for the past half century. Although people have concluded that any directivity can be realized in theory with a densely spaced linear array [41], little or virtually no improvements in antenna gain can be obtained mainly because the mutual coupling effects in those closely spaced antennas eventually corrupt the impedance matching and degrade the efficiency [42,43]. There are also disadvantages of extremely high current requirements and high sensitivities in conventional superdirective antennas [41, 43]. It should be noted the traditional superdirective array synthesis techniques assume a constant impedance termination for every antenna [44] and the mutual coupling effect is not included in their models. This, in fact, diminishes the contributions of higher order radiation modes and overestimates the difficulty of realizing a true supergain antenna. On the other hand, it is not surprising that supergain antennas can be realized with tightly coupled antennas, with the Yagi-Uda antenna serving as a perfect example [45]. However, only with the understanding of the mutual coupling and its relationship to the modes can the potential of achieving superdirectivity be fully exploited. Compared to traditional superdirective antennas that suffer serious impedance mismatch and gain loss [42, 43], the proposed antenna concept is truly “supergain” as there is no impedance mismatch in the system. We proposed to use a closely coupled half-wave dipole pair to demonstrate the supergain antenna concept. The only factor affects the efficiency is the ohmic loss of the antenna and the driving circuit. Similar to the short dipoles, the coupled half-wave dipoles can also be decomposed into the common mode and the difference mode. One may notice from the radiation patterns that the two radiation modes can be added coherently in the endfire direction. From the

analysis of the above coupled half-wave dipoles at  $d=0.1\lambda$ , the directivity of the sum pattern and the difference pattern are calculated to be  $D_{CM}=1.54(1.88\text{dBi})$  and  $D_{DM}=3.91(5.92\text{dBi})$  in the endfire direction. As these two modes can be independently driven with the 180 degree hybrid, the optimal directivity or gain can be achieved through a certain ratio of power and phase matching between these two modes, like that in a beamforming antenna. Based on the power orthogonality, the end-fire directivity from the combination of the common and difference modes can be characterized by the following equation,

$$D = \frac{(\sqrt{P_{CM}D_{CM}} + \sqrt{P_{DM}D_{DM}})^2}{P_{CM} + P_{DM}} = \frac{D_{CM} + 2\sqrt{D_{CM}D_{DM}\eta} + D_{DM}\eta}{1 + \eta} \quad (15)$$

where  $P_{CM}$ ,  $P_{DM}$  are the radiated power of the common mode and difference mode, and  $\eta$  is the ratio of radiated power between two modes, e.g.  $\eta=P_{DM}/P_{CM}$ . The maximum directivity  $D_{max}=D_{CM}+D_{DM}=5.45(7.48\text{dBi})$  is achieved when  $\eta=D_{DM}/D_{CM}=2.54$ . This corresponds to a current amplitude ratio of approximately 1:8 between the common mode and the difference mode.. Compared to the directivity of a single half-wave dipole antenna that is 1.64 (2.15dBi), the directivity of the proposed closely-coupled dipole pair is about 3.32 times of that or 5.2dB higher. It is also 1.66 times of (or 2.2dB higher than) that of a two-element uncoupled end-fire array at  $0.4\lambda$  spacing, with just a quarter of that spacing.

To verify the concept, a pair of monopoles operating at 2GHz is built on top of a microstrip substrate at  $0.1\lambda$  spacing, as shown in Fig.13. The MDN is a rat-race coupler that is fabricated on the same circuit board and connected to the antenna pair. After the common mode and difference mode are separated by the MDN, a microstrip open or short stub is inserted for each port to match the impedance of that mode. The complete antenna structure including the rat-race and the matching circuit is simulated by IE3D. The measured S-parameters for the sum and difference ports are plotted in Fig.14 along with the simulated S-parameters. It can be seen that the measured result agrees very well with the simulation result. The S-parameters show that both ports are well matched at around the operating frequency of 2GHz. The minimum return loss is about -20dB and the isolation between two ports is more than 30dB for at least 800MHz bandwidth. However, it is also noticed that the impedance matching bandwidth of the difference mode is much smaller than that of the common mode. It has only about 50MHz 3dB matching bandwidth in contrast to over 1GHz matching bandwidth of the common mode. This is related to the high Q behavior of the higher order mode, caused by the strong mutual coupling in the antennas. Even so, the bandwidth may already be sufficient for many narrow band applications.

The supergain experiment is carried out by measuring the absolute gain of the array in the transmitting mode in reference to a standard horn antenna. The circuit board is mounted on the center of a larger ground plane with size of 50cm by 50cm, to approximate the

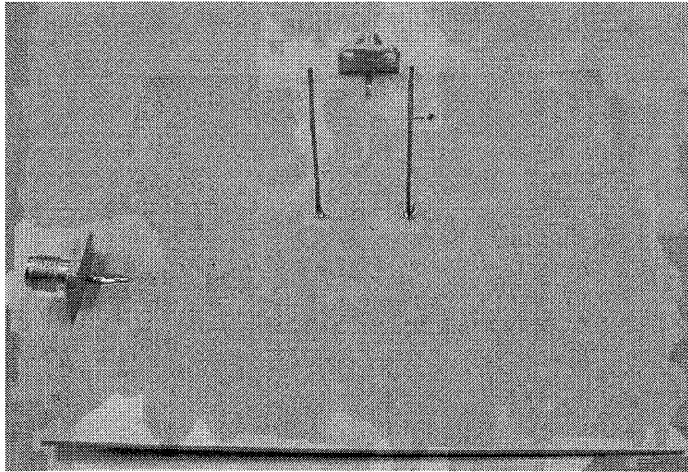


Fig.13 Picture of a fabricated two-element monopole at  $0.1\lambda$  spacing, connected to a rat-race coupler on board.

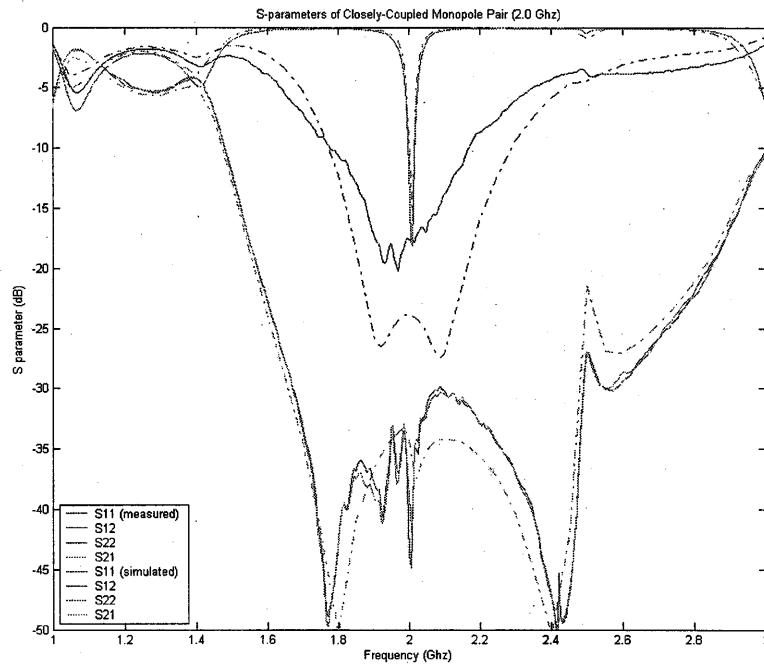


Fig.14 The simulated and measured S-parameters for the sum and difference ports in Fig.13. (Dashed line ----: simulation results, Solid line \_\_\_\_: measured results) results

monopole pattern. A power splitter, a variable attenuator and a variable phase shifter is used to adjust the amplitude ratio and the phase difference between the two modes until the maximum gain is achieved in the horizontal plane. The azimuth radiation pattern in

the horizontal plane is shown in Fig. 15(a). At the maximum azimuth, the antenna is then scanned in the elevation for observation of the elevation pattern, which is shown in Fig.

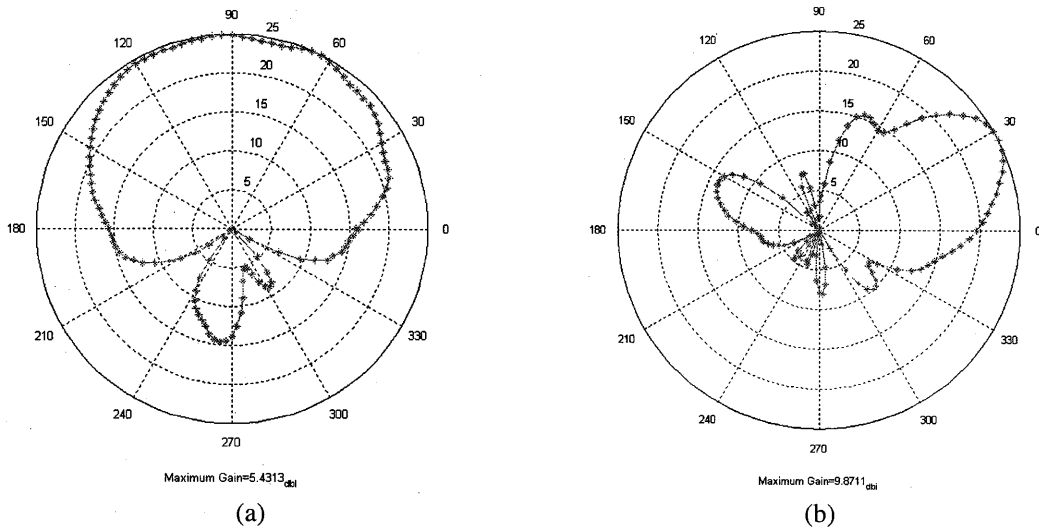


Fig.15 (a) Azimuth pattern of the array in the horizontal plane (b) Elevation pattern with the maximum beam tilted up by approximately 30 degrees

15(b). It can be seen that the maximum radiation is tilted up by approximately 30 degrees because of the finite size of the ground plane. The overall maximum gain of 9.87dBi is achieved with this two-element monopole array, which is only 0.5dB lower than the maximum synthesizable directivity of 10.37dBi in an ideal two-element monopole array. The realized gain of this 2-element array is also 4.72dB higher than the gain of an ideal monopole antenna, which is 5.15dBi.

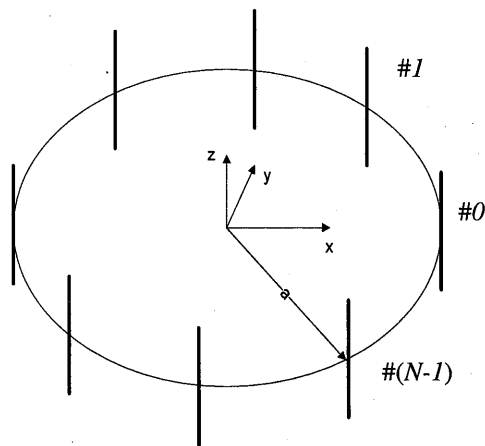


Fig.16 Configuration of an equally spaced N-element circular dipole array

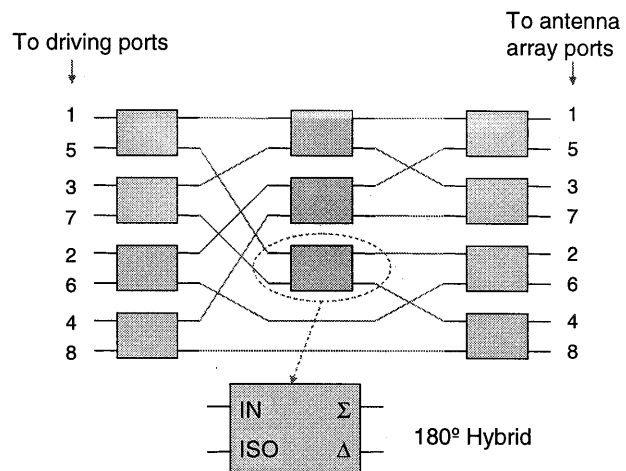


Fig.17 The 180 degree hybrid based MDN for an 8-element equally spaced circular array.



The result of a 2-element supergain array can be further generalized to a circular array with a large number of equally spaced dipole elements, as shown in Fig.16. Due to the symmetry of the array structure, a simple way of deriving the characteristic modes should exist. In the following, it will be illustrated that the fundamental spatial harmonic radiations are such modes that can be easily constructed. These modes can be combined coherently to realize supergain or in a complementary way so that the antenna beam can be scanned continuously like that in a conventional phased array. In general, the far field radiation from a N-element circular array of dipole elements is given by:

$$E_{\theta} = -j\omega \frac{\mu_0 e^{-jkr}}{4\pi r} F(\theta)G(\theta, \varphi) \quad (16)$$

where the element factor is  $F(\theta) = \frac{\cos(kL/2 \sin \theta) - \cos(kL/2)}{\sin \theta}$  and the array factor is  $G(\theta, \varphi) = \sum_{i=0}^{N-1} \left( I_{0i} \exp \left( jka \sin \theta \cos \left( \varphi - \frac{2\pi}{N} i \right) \right) \right)$ .  $L$  is the length of the dipole and  $I_{0i}$  is the current excitation at the  $i$ th antenna element. The array factor can be expanded in terms of Bessel functions as follows,

$$G(\theta, \varphi) = \sum_n j^n J_n(ka \sin \theta) \left( \cos n\varphi \sum_{i=0}^{N-1} I_{0i} \cos \left( n \frac{2\pi}{N} i \right) + \sin n\varphi \sum_{i=0}^{N-1} I_{0i} \sin \left( n \frac{2\pi}{N} i \right) \right) \quad (17)$$

For closely spaced circular arrays, the higher spatial harmonics of  $n > N/2$  can usually be ignored. By observing (17), one may notice the fundamental spatial harmonic terms of  $\cos n\varphi$  or  $\sin n\varphi$  for any  $n \leq N/2$  can be individually excited with a current distribution of  $I_{0i} = \cos \left( n \frac{2\pi}{N} i \right)$  or  $I_{0i} = \sin \left( n \frac{2\pi}{N} i \right)$ . For an example of an 8-element array, there are 8 modes, whose array factors are described in the following according to the order of the spatial harmonics  $n$ ,

$$0^{\text{th}} \text{ order:} \quad G^{(1)} = 4J_0(ka \sin \theta), \quad (18)$$

$$1^{\text{st}} \text{ order:} \quad G^{(2)} = 2\sqrt{2}J_1(ka \sin \theta) \sin(\varphi), G^{(8)} = 2\sqrt{2}J_1(ka \sin \theta) \cos(\varphi) \quad (19)$$

$$2^{\text{nd}} \text{ order:} \quad G^{(3)} = 2\sqrt{2}J_2(ka \sin \theta) \sin(2\varphi), G^{(7)} = 2\sqrt{2}J_2(ka \sin \theta) \cos(2\varphi) \quad (20)$$

$$3^{\text{rd}} \text{ order:} \quad G^{(4)} = 2\sqrt{2}J_3(ka \sin \theta) \sin(3\varphi), G^{(6)} = 2\sqrt{2}J_3(ka \sin \theta) \cos(3\varphi) \quad (21)$$

$$4^{\text{th}} \text{ order} \quad G^{(5)} = 2\sqrt{2}J_4(ka \sin \theta) \cos(4\varphi) \quad (22)$$

Observing the above spatial harmonic modes, one may notice each of them forms multiple sinusoidal lobes in the azimuth. The number of the lobes is twice of the order number  $n$ . Furthermore, the two modes in the same order from the 1<sup>st</sup> to the 3<sup>rd</sup> order have orthogonal sinusoidal patterns. They can be linearly combined to realize pattern rotations in any angles. For example, shown in Fig.18 (a) is a rotated pattern of the second order

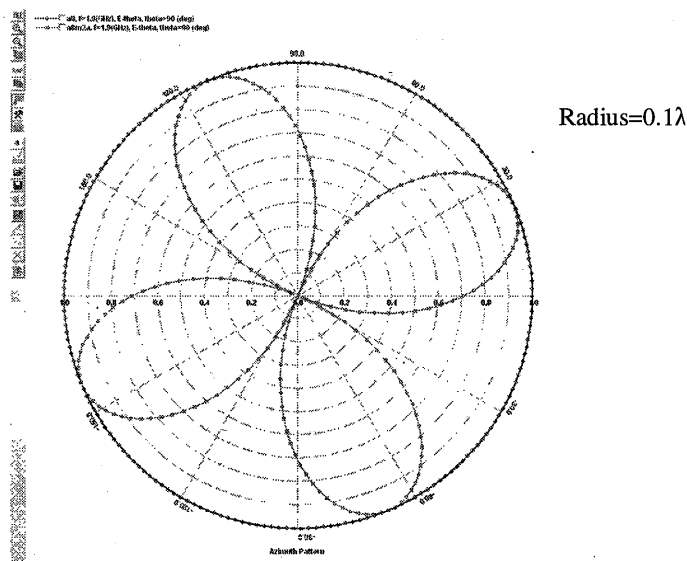


Fig.18 (a) Array pattern for a second-order mode ( $N=8$ ,  $\theta=90^\circ$ ,  $\varphi=0-360^\circ$ )

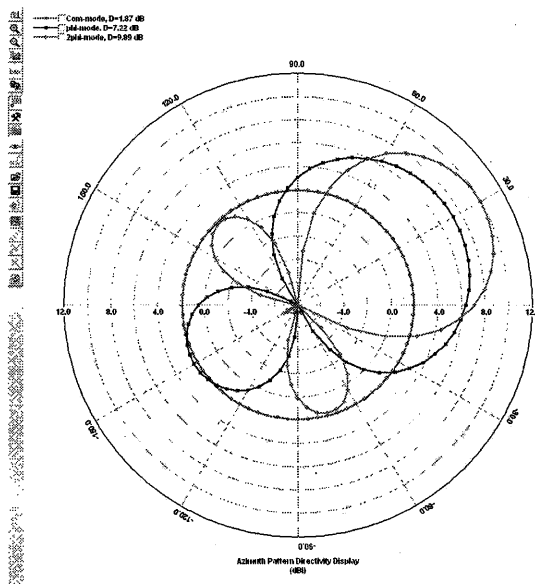


Fig.18 (b) Beamforming pattern with combinations of spatial harmonic modes for up to zero order, first order and second order respectively.

spatial harmonic mode. For 8-element arrays, a MDN based on 11 hybrids is proposed, as shown in Fig.17. One can prove that the above 8 modes or their rotated versions can be obtained with the MDN. After the modes are separated, they can be individually matched. In this way, the mismatch caused by the mutual coupling between adjacent antennas can be eliminated. On the other hand, if each order of mode is aligned with its maximum radiation direction in a particular azimuth angle  $\phi_0$ , a supergain beam can be formed in that angle by combining the different order of modes with an optimal set of weights. Considering the example of an 8-element circular array with an aperture diameter of  $0.25\lambda$ , the 3<sup>rd</sup> and the 4<sup>th</sup> order modes incur impractically high Q values and are usually not used. Fig.18 (b) shows the pattern of the zero order mode, the patterns resulting from supergain beamforming with up to the 1<sup>st</sup> order and up to the 2<sup>nd</sup> order. It shows that the maximum gain of 1.85dBi, 7.34dBi and 9.98dBi can be achieved respectively for these three cases. A general procedure of arbitrary pattern synthesis can also be carried out with the spatial harmonic modes, as any azimuth pattern with constant phase can be expanded into the summation of  $\cos(n\phi)$  or  $\sin(n\phi)$  series through Fourier transform. The resulted coefficients, after the normalization with equations (18)-(22), is the magnitude of the mode that needs to be excited at each modal port. Another system advantage of the proposed mode based beamforming approach is that, as the combination of  $\cos(n\phi)$  and  $\sin(n\phi)$  modes with a certain amplitude weights are enough to steer a beam to any direction, there is no need to change the phase ratios among the modes for the purpose of continuous electronic beam scanning.. This greatly simplifies the complexity of the beamforming network by removing the need of expensive and bulky variable phase shifters in the RF front-end. The separation of the modes in the excitation ports also offers the most natural way of trading off between the supergain and the bandwidth. A spatial and frequency “zooming in” system can thus be built by simply selecting which mode one wishes to drive.

#### 4. Acknowledgement

This work is partially supported by the Army Research Office through award No.911NF-05-1-0408.

#### 5. References

- [1] L. J. Chu, “Physical limitations on omni-directional antennas”, *J. Appl. Phys.*, vol. 19, pp. 1163-1175, Dec. 1948
- [2] J. S. Mclean, “A re-examination of the fundamental limits on the radiation Q of electrically small antennas”, *IEEE Trans. on Antennas and Propagation*, vol. 44, NO. 5, May 1996
- [3] W. C. Jakes, *Microwave Mobile Communications*. New York: Wiley, 1974, pp. 60-65.
- [4] G. J. Foschini and M. J. Gans, “On limits of wireless communication in a fading environment when using multiple antennas,” *Wireless Personal Commun.*, vol. 6, no. 3, Mar. 1998, pp. 311-335.

- [5] M. A. Jensen, M.A.; J. W. Wallace, "A review of antennas and propagation for MIMO wireless communications," *IEEE Trans. on Antennas and Propagation*, vol. 52, issue 11, Nov. 2004, pp. 2810-2824.
- [6] W. Yao; Y. Wang, "Direct antenna modulation - a promise for ultra-wideband (UWB) transmitting", *Microwave Symposium Digest, IEEE MTT-S International*, Vol.2, pp1273 - 1276 June 2004.
- [7] S. B. Tang, et al., "Modeling omnidirectional small antennas for UWB applications", *IEEE Antennas and Propagation Society International Symposium*, vol. 2, pp. 1295 – 1298, June 2004.
- [8] W. Yao and Y. E. Wang, "Direct antenna modulation for pulse transmitting through resonant antennas," accepted by *International Journal on Wireless and Optical Communications*, May, 2006.
- [9] H. C. Jing and Y. E. Wang, "Efficient Monocycle Pulse Transmitting from Patch Antennas" 2006 IEEE Antenna and Propagation Symposium, pp.905-908, July, 2006
- [10] X. Xu, H. C. Jing and Y. E. Wang, "High speed pulse radiation from switched electrically small antennas", 2006 IEEE Antenna and Propagation Symposium, pp.167-170, July, 2006.
- [11] M. R. Andrews, P. P. Mitra, and R. de Carvalho, "Tripling the capacity of wireless communications using electromagnetic polarization," *Nature*, vol. 409, pp. 316–318, Jan. 2001.
- [12] T. Svantesson, "Correlation and channel capacity of MIMO systems employing multimode antennas," *IEEE Trans. Vehicular Tech.*, Vol. 51, No. 6, Nov. 2002.
- [13] A. Forenza and R. W. Heath, Jr., "Benefit of pattern diversity via two-element array of circular patch antennas in indoor clustered MIMO Channels," *IEEE Trans. Comm.*, Vol.54, No. 5, May 2006.
- [14] D. S. Shui, G. J. Foschini, M. J. Gans, and J. M. Kahn, "Fading correlation and its effect on the capacity of multielement antenna systems," *IEEE Trans. Commun.*, vol. 48, Mar. 2000, pp. 502-513.
- [15] W. C.-Y. Lee, "Effects on correlation between two mobile radio base station antennas," *IEEE Trans. Commun.*, vol. COM-21, Nov. 1974, pp. 1214-1224.
- [16] C. N. Chuah, D. Tse, J. M. Kahn, and R. A. Valenzuela, "Capacity scaling in MIMO wireless systems under correlated fading," *IEEE Trans. Inform. Theory*, vol. 48, Mar. 2002, pp. 637-651.
- [17] T. Svantesson and A. Ranheim, "Mutual coupling effects on the capacity of multiple antenna systems," *Proc. IEEE Int. Conf. Acoustic, Speech, and Signal Processing (ICASSP)'01*, vol. 4, Salt Lake City, UT, May 2001, pp.2485-2488.
- [18] R. Janaswamy, "Effect of element mutual coupling on the capacity of fixed length linear arrays," *IEEE Antennas and Wireless Propagation Letters*, vol. 1, issue 8, 2002, pp.157-160.
- [19] B. N. Getu, R. Janaswamy, "The effect of mutual coupling on the capacity of the MIMO cube," *Antennas and Wireless Propagation Letters*, vol.4, 2005, pp. 240-244.
- [20] P.-S. Kildal, K. Rosengren, "Correlation and capacity of MIMO systems and mutual coupling, radiation efficiency, and diversity gain of their antennas: simulations and

- measurements in a reverberation chamber,” *IEEE Communications Magazine*, vol. 42, issue 12, Dec. 2004 pp. 104-112.
- [21] H. Steyskal, J. S. Herd, “Mutual coupling compensation in small array antennas,” *IEEE Trans. Antennas and Propagation*, actions, vol. 38, issue 12, Dec. 1990, pp. 1971-1975.
- [22] R. S. Adve, T. K. Sarkar, “Compensation for the effects of mutual coupling on direct data domain adaptive algorithms,” *IEEE Trans. Antennas and Propagation*, vol. 48, issue 1, Jan. 2000, pp. 86-94.
- [23] R. Mailloux, “Reduction of mutual coupling using perfectly conducting fences,” *IEEE Trans. Antennas and Propagation*, vol. 19, issue 2, Mar 1971, pp. 166-173.
- [24] J.-P. Daniel, “Reduction of mutual coupling between active monopoles: Application to superdirective receiving arrays,” *IEEE Trans. Antennas and Propagation*, vol. 25, issue 6, Nov 1977, pp. 737-741.
- [25] Fan Yang, Y. Rahmat-Samii, “Mutual coupling reduction of microstrip antennas using electromagnetic band-gap structure,” *IEEE Antennas and Propagation Society International Symposium*, 2001. vol. 2, 8-13 July 2001, pp. 478-481.
- [26] J. D. Fredrick, Yuanxun Wang, T. Itoh, “Smart antennas based on spatial multiplexing of local elements (SMILE) for mutual coupling reduction,” *IEEE Trans. Antennas and Propagation*, vol. 52, issue 1, Jan. 2004 pp. 106-114.
- [27] T. Brauner, R. Vogt, W. Bachtold, “Reduction of mutual coupling in active antenna arrays by optimized interfacing between antennas and amplifiers”, *IEEE MTT-S International Microwave Symposium Digest*, 12-17 June 2005 pp. 4.
- [28] J. B. Anderson and H. H. Rasmussen, “Decoupling and Descattering Networks for Antennas”, *IEEE Trans. on Antennas and Propagat.*, vol.24, pp. 841-846, Nov., 1976
- [29] S. Dossche, S. Blanch, and J. Romeu, ‘Optimum antenna matching to minimize signal correlation on a two port antenna diversity system’, *Electronics Lett.*, vol. 40, no. 19, pp. 1164-1165, 16 Sep. 2004.
- [30] H. J. Chaloupka and X. Wang, “Novel Approach for Diversity and MIMO Antennas at Small Mobile Platforms” *IEEE International Symposium on Personal, Indoor, and Mobile Radio Communications*, Vol. 1, Page 637-642, Sep. 2004.
- [31] H. J. Chaloupka and X. Wang, ‘On the properties of small arrays with closely spaced antenna elements’, *Proc. IEEE Antennas and Propagation Society International Symposium*, vol. 3, pp. 2699-2702, Monterey, CA, 2004.
- [32] S. Dossche et al, “Three Different Ways to Decorrelate Two Closely Spaced Monopoles for MIMO Applications” *IEEE International Conference on Wireless Communications and Applied Computational Electromagnetics*, Page 849-852, Apr. 2005.
- [33] J. W. Wallace, M. A. Jensen, “Mutual coupling in MIMO wireless systems: a rigorous network theory analysis,” *IEEE Trans. Wireless Communications*, vol. 3, issue 4, July 2004, pp. 1317-1325.

- [34] J. W. Wallace, M. A. Jensen, "Termination-dependent diversity performance of coupled antennas: network theory analysis," *IEEE Trans. Antennas and Propagation*, vol. 52, issue 1, Jan. 2004. pp. 98-105.
- [35] T. H. O'Donnell and A. D. Yaghjian, "Electrically small superdirective arrays using parasitic elements," 2006 IEEE Antenna and Propagation Symposium, pp.3111-3114, July, 2006.
- [36] B. N. Getu and J. B. Anderson, "The MIMO cube—a compact MIMO antenna," *IEEE Trans. Wireless Comm.* Vol.4, No. 3, May 2005.
- [37] C. H. Papas, *Theory of Electromagnetic Wave Propagation*, McGraw-Hill Inc., 1965.
- [38] T.-I. Lee and Y. E. Wang, "Parallel information channels in closely coupled dipole pairs," submitted to *IEEE Trans. Antennas and Propagation*, March, 2006
- [39] L. J. Chu, "Physical limitations of omni-directional antenna," *J. Appl. Phys.*, vol. 19, 1948. pp. 1163-1175.
- [40] D. M. Pozar, *Microwave Engineering*, Wiley, 2005.
- [41] C. A. Balanis, *Antenna Theory: Analysis and Design*: Wiley, 1997.
- [42] A. Ludwig, "Mutual coupling, gain and directivity of an array of two identical antennas," *IEEE Trans. Antennas and Propagation*, vol. 24, issue 6, Nov. 1976, pp. 837-841.
- [43] E. Altshuler, T. H. O'Donnell, A. D. Yaghjian and S. R. Best, "A monopole superdirective array," *IEEE Trans Antennas Propagat.* Vol. 53, No. 8, pp. 2653-2661, Aug. 2005.
- [44] M. Dawoud, A. Anderson, "Design of superdirective arrays with high radiation efficiency," *IEEE Trans. Antennas and Propagation*, vol. 26, issue 6, Nov. 1978, pp. 819-823.
- [45] W. Stutzman, *Antenna Theory and Design, 2<sup>nd</sup> Edition*, New York, Wiley, 1998.
- [46] H. Bach, "Directivity of Basic Linear Arrays" *IEEE Trans. on Antennas and Propagation*, Vol. 18, Page 107-110, Jan. 1970.

# **DEVELOPMENT OF A SLOTTED SUBSTRATE INTEGRATED WAVEGUIDE (SIW) ARRAY ANTENNAS FOR MOBILE DBS APPLICATIONS**

Songnan Yang, Aly E. Fathy  
Department of Electrical and Computer Engineering,  
University of Tennessee, Knoxville, TN, 37996

Shady H. Suleiman  
Winegard Company,  
Burlington, IA, 52601

**Abstract:** Substrate integrated waveguide slot arrays (SIWs) have been fabricated using printed circuit boards. The radiating slot elements are etched on the metalized top surface of a RT/duroid substrate, while the bottom surface is blank coated. The waveguide side-walls have been emulated using rows of closely spaced metalized via holes. The feed structure is comprised of SIW elements too to minimize insertion loss, thus achieving overall relatively high antenna efficiency. The developed slot arrays are designed to produce circularly polarized main beams radiating at  $\approx 45^\circ$  off broadside in the elevation plane to reduce the steering volume requirements from ( $20^\circ$  to  $70^\circ$ ) measured off horizon, to  $\pm 25^\circ$  in compliant with mobile DBS reception requirements in USA. Another important advantage is that the fabrication cost of the printed slot array antenna is definitely much lower than that of the slotted metallic waveguide array antenna. However, the SIW antenna has a relatively higher insertion loss due to the dielectric substrate. Nevertheless, SIW antennas, if integrated with LNAs, would sustain comparable performance to the all-metallic slot array structures. Preliminary simulated and measured results for a sub-array of  $12 \times 16$  and a larger full array of  $12 \times 64$  elements will be presented here.

## **1. Introduction:**

Currently, there is a need for a low profile steerable antenna design approach to adequately cover the US mobile DBS market. Antenna requirements for mobile DBS reception in the US include the following:

- 1) Dual circular polarization.
- 2) Full steering in two planes to track the satellite. The steering range is  $360^\circ$  in the azimuth, and in the elevation from  $20^\circ$  to  $70^\circ$  above horizon.
- 3) A gain of  $\approx 32$  dBi.

If we are going to use a flat plate phased array antenna structure, then its gain will drop significantly and its cross-polarization level, in addition, will become extremely and unacceptably high upon tilting the beam to  $20^\circ$  relative to horizon to accommodate the

full steering range requirements. Hence, we have investigated a mechanical steering concept, as an alternative to this phased array approach, where antennas, with a fixed broadside beam, are mechanically tilted/rotated in both the elevation and azimuth planes to provide the required beam steering. These mechanically steered antenna systems, in general, should be relatively inexpensive compared to the phased array ones, but would lead to an unacceptable overall antenna height-- due to their large scanning volume.

To enhance and render a low profile structure; a leaky wave antenna concept has been proposed here. The antenna will radiate at an inherent tilt angle, thus reducing the scan volume requirements significantly. In our case, the utilized leaky wave slot array has been designed to have an inherent  $45^\circ$  beam-tilt angle to lower the physical steering requirements in the elevation plane from  $20^\circ$  to  $70^\circ$  above horizon, to only  $\pm 25^\circ$  degrees from its horizontal position (as shown in Fig.1). Such feature reduces considerably the overall height of the mobile antenna to about  $\approx 3$ in., and renders a low profile antenna structure suitable for mobile reception.

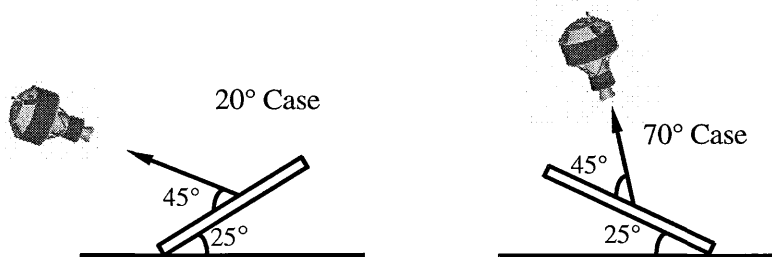


Fig.1. Mechanical steering range of leaky wave slotted waveguide array antennas with  $45^\circ$  off broadside beam

Previously, a single waveguide slot array comprised of 6 radiating waveguides has been designed and prototyped by the authors [1]. The prototypes are fabricated using CNC machining and their measured results were very encouraging. However, these designs suffered from the prohibiting cost of manufacturing, as well their heavy weight. Recently, the substrate integrated waveguide (SIW) technology has been introduced as a low cost solution for microwave systems [2], where waveguide components can be fabricated using standard PCB processes on dielectric substrates for mm-wave applications. However, the techniques can be also suitable for antenna array developments at microwave frequencies.

In this paper, a direct “translation” of the same leaky wave antenna idea onto printed circuit substrates using SIW technology will be introduced. Where in section two, the relationship between SIWs and regular dielectric waveguides will be studied to simplify propagation constant and loss factor evaluation. In section three, waveguide components for antenna feeding networks, such as junctions and transitions, will be developed in SIW using previously design equations that will be generalized. In section four, a  $12 \times 16$  element sub-array design of the leaky wave antenna on SIW will be discussed. Comparison will be made between the sub-array on SIW and the previously developed all



solid metallic waveguide sub-array. Finally, the design of the 12x64 SIW elements full array will be presented, along with its measurement results.

## 2. Substrate Integrated Waveguides:

Conventionally, metallic waveguides are utilized to fabricate both the slotted array antennas and their associated feed networks for their extremely low loss performance. However, they are bulky, heavy, and expensive to fabricate. Hence for consumer type applications, we propose a lower cost alternative technology -- substrate integrated waveguides (SIWs) structures fabricated on printed circuit boards. Where SIW sidewalls are constructed from lined via holes, as shown in Fig.2, rather than solid fences. This technology is simple, less expensive, and renders light structures.

In an effort to extend the well-known design rules of the metallic waveguide slot arrays to SIW designs, we have carried out extensive full parametric study of the SIW structures. The study is based on a full wave 3D analysis using Ansoft HFSS to develop an equivalent conventional dielectrically loaded waveguide to represent the SIW structure. The developed equivalent structure can then be used to estimate the complex propagation characteristics of the SIW guides using the known waveguide expressions. Design charts have been developed here and will be great asset in greatly facilitating the selection of the dielectric material, as well as the SIW dimensions in the system's level design step.

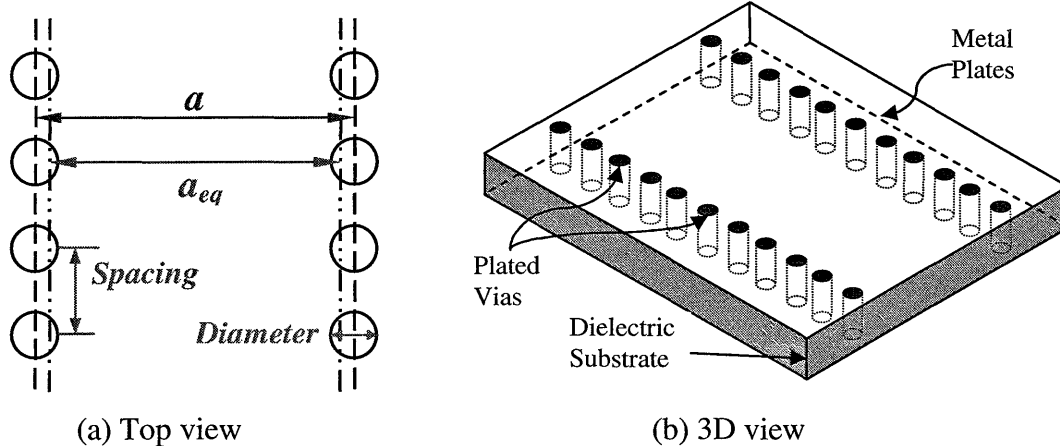


Fig.2. Substrate integrated waveguide defined on dielectric substrates.

### 2.1. Equivalent Waveguide Width “a”

To develop an equivalent width “a” for the SIW width dimension, as a function of the diameter and spacing of the vias, an extensive 3D EM simulation has been carried out, where the top and bottom walls, and the lined vias are assumed to be perfect conductors. In addition, absorbing boundary conditions have been applied along the SIW walls to allow energy to leak through the gaps between the lined vias, i.e. posts. The dielectric in

this step, is assumed lossless, and has  $\epsilon_r=2.2$  to carry out this simulation as most of the low loss dielectric printed circuit board materials are close to this value. The waveguide “a” dimension is selected in our design to be 13.5mm, such that the center frequency of our operating band is 12.45GHz with a single waveguide mode operation. Meanwhile, we have used a thickness of 3.175mm to ensure only TE<sub>10</sub> mode propagation.

The propagation constants of each diameter/spacing combination of these posts are theoretically estimated. Where the phase of the scattering matrix was extracted and compared to that of the regular dielectrically loaded waveguide, given that the propagation constant of the conventional waveguide is calculated based on the well know expression:

$$\beta_z = \beta \sqrt{1 - \left(\frac{\lambda}{2a}\right)^2} = \frac{2\pi}{\lambda} \sqrt{1 - \left(\frac{\lambda}{2a}\right)^2}, \quad (1)$$

Where  $\lambda = \lambda_0 / \sqrt{\epsilon_r}$  and  $\lambda_0$  is the wavelength in free space.

The extracted equivalent waveguide width ( $a_{eq}$ ) is plotted as shown below in Fig.3:

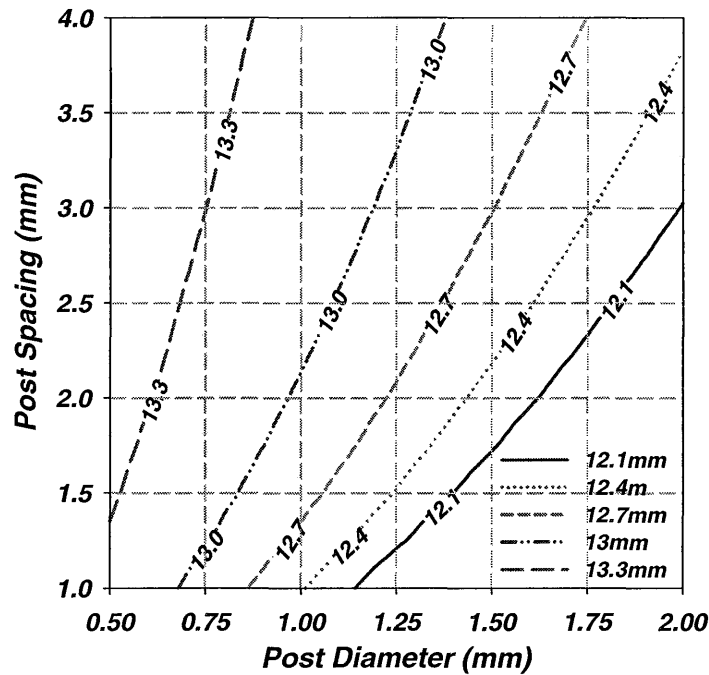


Fig.3. Equivalent waveguide “ $a_{eq}$ ” dimensions of SIW with different post parameters

Based on these previous simulations, the equivalent waveguide “ $a_{eq}$ ” dimension is smaller than the actual lateral spacing of the posts due to the reactive loading. However, its value tends to increase whenever thinner or widely spaced posts are used. But, the wider the spacing between the posts, the higher the leakage losses are, as will be

indicated in the next Section. The SIW then can no longer be used to build a feeding network for the antenna arrays due to its excessive leakage loss.

## 2.2. Leakage Loss

The side walls of the SIW structure can be represented by a lossy reactive load, obviously the losses are due to the leakage through the openings between the posts. This leakage loss " $L_{leakage}$ " together with the dielectric " $L_{dielectric}$ ", and the conductor's loss " $L_{conductor}$ " contribute to the total losses of the SIW feeding structure. To estimate the leakage coefficient, we have predicted the transmitted power of the lossless SIW structure, and the calculated drop in the transmitted power has been related to the leakage loss. A contour map has been generated as a function of the post parameters (as shown in Fig. 4).

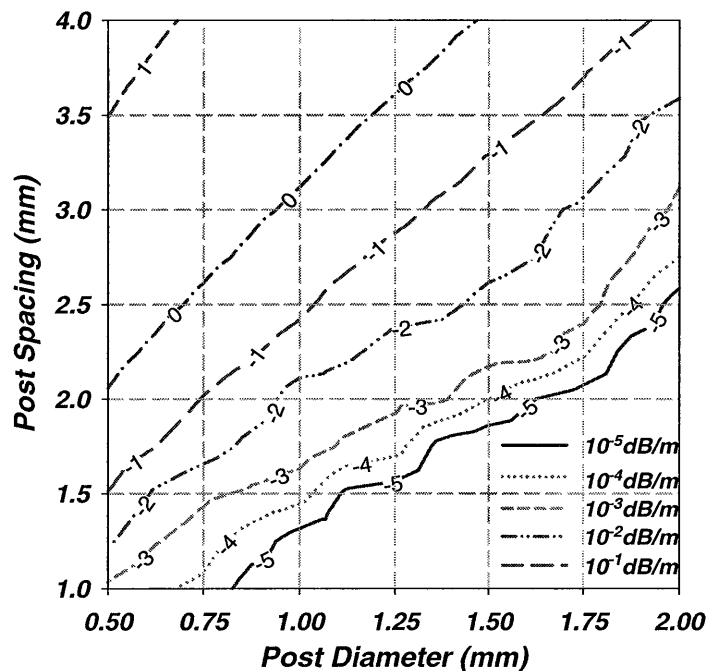


Fig.4. Contour plot of the unit loss of the SIW in logarithmic scale

It is important to recognize here that it is not practical to massively load the SIW structure with closely-spaced vias to minimize leakage. On the other hand, when the post spacing is moderately large, the leakage effects are rather high and could be unacceptable. In fact, a good leaky wave antenna could be designed using this high leakage feature of the SIW structure. However, a compromise between lowering the loss and lowering the fabrication cost can be achieved.

### 2.3. Dielectric Loss

To estimate the SIW dielectric loss, we have also utilized the well known dielectric loss formulas of a dielectrically loaded waveguide in association with the equivalent width where the losses are given by [3]:

$$L_{dielectric} \cong \frac{\epsilon'' \pi}{\epsilon' \lambda^2} \frac{\lambda}{\sqrt{1 - \left(\frac{f_c}{f}\right)^2}} = \tan \delta \frac{\pi}{\lambda} \left(\frac{\lambda_g}{\lambda}\right) \text{ Np/m}, \quad (2)$$

Where  $\epsilon'$  and  $\epsilon''$  are the real and imaginary parts of the complex dielectric constant of the lossy dielectric loading,  $\lambda$  and  $\lambda_g$  are the wavelength and guided-wavelength in a dielectric media and  $\tan \delta$  represents the dielectric loss tangent. A contour plot has been generated for the dielectric loss for a set of different materials and shown in Fig. 5(a). The same structure has been simulated using HFSS too, and extracted results are shown in Fig. 5(b). These results validate our assumptions of using Eq. (2) to predict SIW dielectric losses.

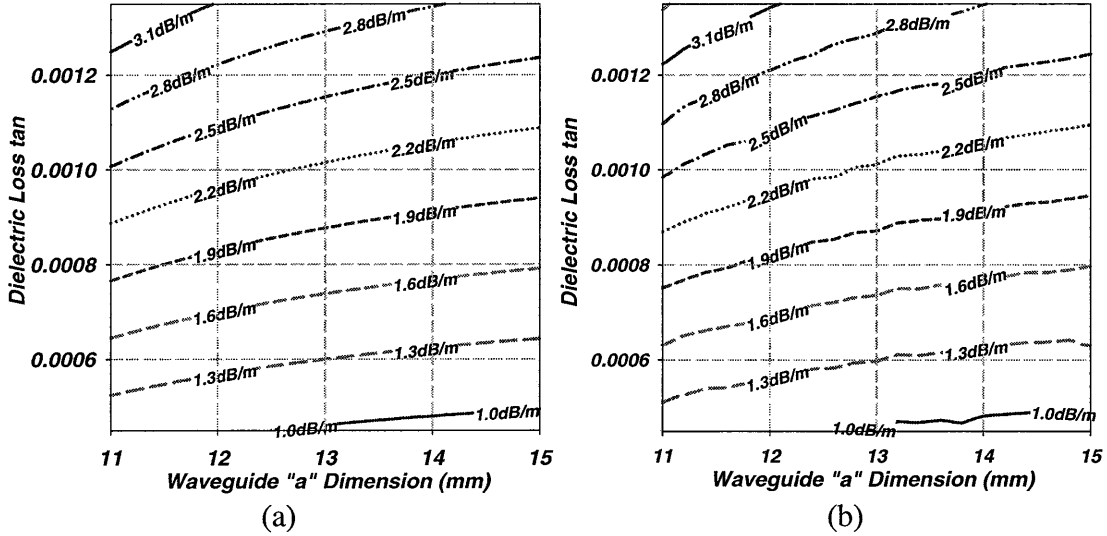


Fig.5. Contour of dielectric loss as a function of dielectric loss tangent and the waveguide “a” dimension. (a) Calculated from Eq.2, (b) HFSS simulation results.

The selection of the dielectric material is extremely important step when designing large arrays. The dielectric loss could be relatively high (as a 1dB/m) even for a substrate dielectric loss tangent as low as 0.00045. Hence, it is recognized that for regular high frequency laminate materials ( $\tan \delta \sim 0.0009$  and up), the dielectric losses can be prohibitively large if the antenna array is large, especially when long feed lines are required.

## 2.4. Conductor Loss

Similar to the dielectric loss, the conductor loss can be approximately evaluated using the rectangular waveguide equations after accounting for sidewalls extra loss, given that they are made of plated via-holes. In addition, the surface roughness of the plated metal layers (usually copper) degrades the conductivity of the equivalent waveguide walls. The conduction loss of TE<sub>10</sub> wave propagating in a single mode rectangular waveguide given by [3]:

$$L_{conductor} = L_{sidewalls} + L_{top\&bottom} = \frac{2R_{s1}}{\eta a} \frac{\left(\frac{f_c}{f}\right)^2}{\sqrt{1-\left(\frac{f_c}{f}\right)^2}} + \frac{R_{s2}}{\eta b} \frac{1}{\sqrt{1-\left(\frac{f_c}{f}\right)^2}} \text{ (Np/m)}, \quad (3)$$

Where  $R_{s1}$  and  $R_{s2}$  represent the real part of the complex surface impedances of the sidewalls and top/bottom conductors respectively, which can be approximated as:

$$R_s = \Re \left\{ \sqrt{\frac{j\omega\mu}{\sigma + j\omega\epsilon}} \right\} \cong \sqrt{\frac{\omega\mu}{2\sigma}} \text{ (Ohm)} \text{ and } \eta = \sqrt{\mu_0/\epsilon_0\epsilon_r}, \quad (4)$$

From the previous equations, we can see that the conductor losses are function of the physical dimensions of the waveguide and the conduction losses contributed by sidewalls are independent of the substrate thickness. A set of curves of losses per unit length at 12.45GHz is plotted below in Fig.6 according to equation (3-4), where a lossless dielectric with  $\epsilon_r=2.2$  is used and the waveguide “b” dimensions are selected to be standard PCB board thicknesses, also, the conductivity of copper ( $5.8e7$  S/m) is used for all conductive surfaces.

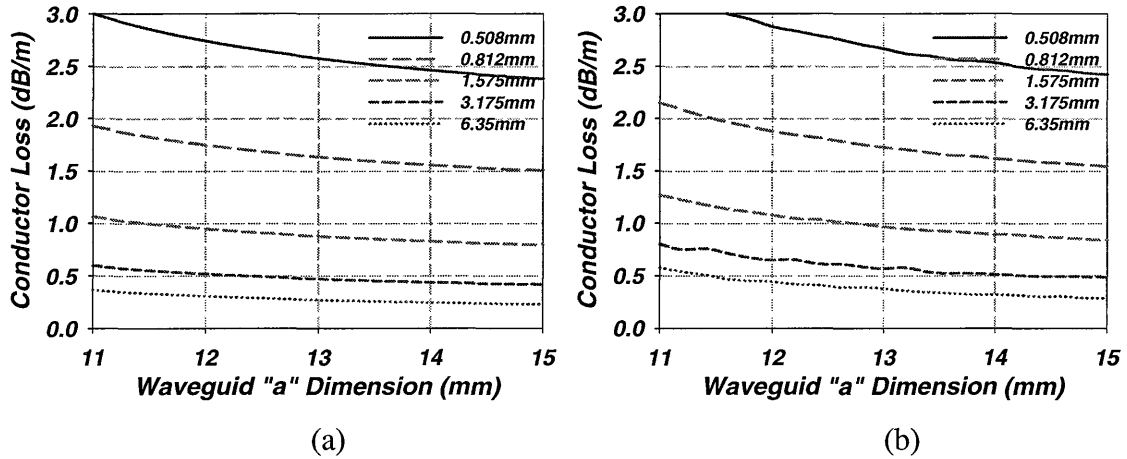


Fig.6. Conductor loss for different substrate thickness and waveguide “a” dimension (a) calculated using Eq.3, (b) Simulated results.

As can be seen from the plot, the conductor loss can not be neglected. It is quite comparable to the dielectric loss; even for the case when using large “a” and “b” dimensions. Significant conductor loss reduction can be achieved upon using thicker substrates as indicated from the second term of Eq.3’s dependence on b.

Moreover, it is obvious that there is a significant difference between the HFSS simulated results, and closed-form expressions calculated results. We believe the difference is due to the extra sidewall losses of the SIW structure. To account for this additional sidewall losses, the first term of Eq.3, could be multiplied by some fudge factor. In a regular waveguide the ratio between  $R_{s1}$  and  $R_{s2}$  should be the same. In our calculations here we will adjust this ratio to account for the extra side wall loss. Meanwhile, the ratio between  $R_{s1}$  and  $R_{s2}$  varies according to the spacing and diameter of the via defining these sidewalls, and as shown in Fig.7, the HFSS-simulated data can be fitted very well with  $R_{s1}/R_{s2}$  ranges from 1.45 to 1.7 for three different cases with via spacing/diameter values of 1.6, 2.0, and 2.4 respectively.

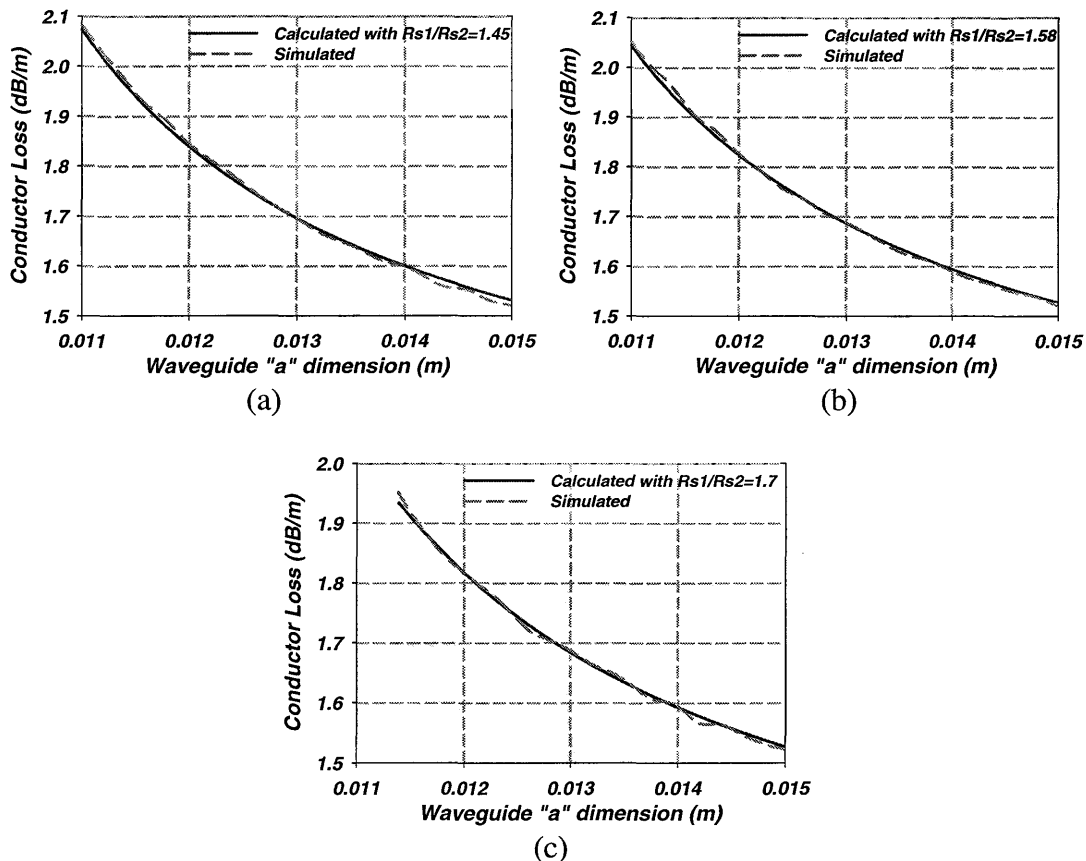


Fig.7, Sidewall conductor loss factor for different via spacing, (a) Spacing/Diameter=1.6, (b) Spacing/Diameter=2, (c) Spacing/Diameter=2.4

## 2.5. Design parameters Selection and Overall Performance Prediction:

According to the previous loss analysis of the SIW, the minimum insertion loss of antenna array feed network can be achieved upon using thick low loss dielectric substrates. In addition, the leakage loss can be reduced several orders of magnitude less than the dielectric and conductor losses by carefully selecting the spacing and diameter of the posts, e.g. close to 0.01dB/m line as shown in Fig.4. Extensive use of posts to the point that the spacing between the posts is less than twice of the post's diameter should be avoided too, to reduce the overall fabrication cost.

In our design, dielectrics with  $\epsilon_r \sim 2.2$  and a thickness of 125mil (the maximum available standard thickness is 3.175mm=125mil) is used to provide  $\sim 0.6$ dB/m conductor loss for a SIW with an equivalent width of 12.8mm. The dielectric loss tangent is presumed to be less than 0.001, which still accounts for about 2.0dB/m dielectric loss. The posts diameter is selected to be 1.25mm and the spacing is twice the post diameter to stay away from “overloading” the substrate with plated vias. According to these dimensions, a leakage loss factor of around 0.01dB/m is predicted, which is insignificant, when compared to either conductor or dielectric losses. Based on Fig.5, the overall loss is estimated to be in the range of 2.4 to 3dB/m, which is function of the “a” dimension, which is also defined by the antenna array structure.

## 2.6. Experimental results

In order to experimentally evaluate the overall insertion loss per unit length of the SIW antenna and verify previous simulated results, we have fabricated two test fixtures using a 125mil thick Rogers RT Duroid 5880 material with  $\epsilon_r=2.2$  and dielectric loss tangent of 0.0009. As shown in Fig.8 below, the “a” dimension of these two SIWs are 13.5mm and they are designed to have 2 inch difference in lengths.

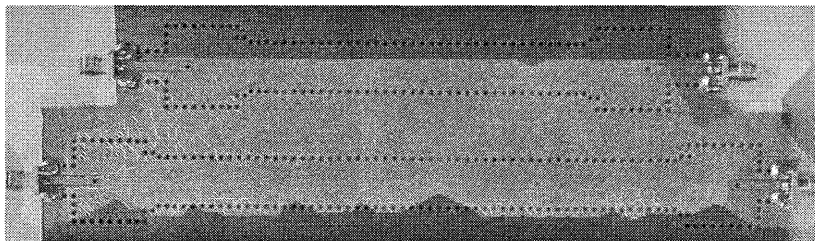


Fig.8. Back to back transitions with different waveguide lengths for insertion loss measurements.

Back-to-back measurements were carried out to measure the differential insertion loss between the two fixtures and results are shown in Fig.9. Based on these measurements, it is estimated that the loss of the SIW is 0.07dB/in, which translates to 2.75dB/m. The measured losses are higher than predicted based on perfect copper conductivity. A factor of 2 should be used in our metal loss calculations to account for the lower plated metal surface conductivity of the vias.

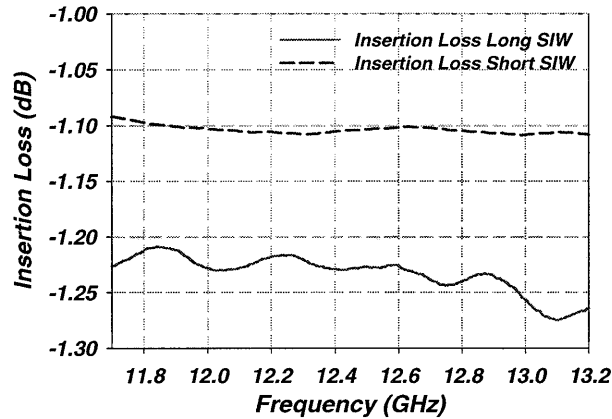


Fig.9. Measured insertion losses of two SIW lines with 2 inch difference in length

### 3. Development of SIW Basic Antenna Components

The basic building blocks to construct the slotted SIW array include:

- 1) Substrate integrated waveguides with low loss to construct the feed network.
- 2) Binary feed network based on waveguide T-junctions to achieve adequate bandwidth and good phase balance at the inputs of all radiating waveguides.
- 3) Smooth coaxial line to SIW transition through a grounded CPW.
- 4) X-Slotted radiating SIWs with properly spaced slots to create circularly polarized beams at 45° off broadside.

In the following sections, each block and its associated design/synthesis procedure will be discussed in details.

#### 3.1. Synthesis of the SIW T-Junctions

Waveguide T-junctions are key component for the antenna array feed network construction. Feed network can be either a serial or parallel network. Parallel feed (i.e. the binary feed) generally requires more stages, hence real estate. But it is proven to achieve the widest bandwidth for in-phase excitation.

Extensive studies have already carried out to develop different T-junctions power dividers in metallic waveguides [4]. These designs have included a post placed inside the junction (as shown in Fig. 10(a)), to enhance the operating bandwidth. However, the manufacturing of such isolated posts inside the junction is a fundamental difficulty for mass production, especially when the design is dimensionally sensitive. Alternatively, the authors have previously developed a synthesis procedure for waveguide T-junctions power divider to achieve arbitrary power split ratio [5]; while keeping a balanced phase between the output ports. Where a wedge and diaphragms have been placed inside the junction and the input ports respectively, as shown in Fig. 10(b). Neither the wedge nor



the diaphragms are separated from the junction body, so it is relatively easy to fabricate these structures including cast fabrication.

Similarly, SIWs are defined by vias on the dielectric substrate. Hence, there is no additional difficulty to introduce a matching post in the junction, as long as, it is the same size. So, according to the equivalent concept developed in section 2, we have extended our previous T-junction designs to the SIW after replacing the wedge by posts with same size. The equivalent structure renders a T-junction structure suitable for SIW fabrication.

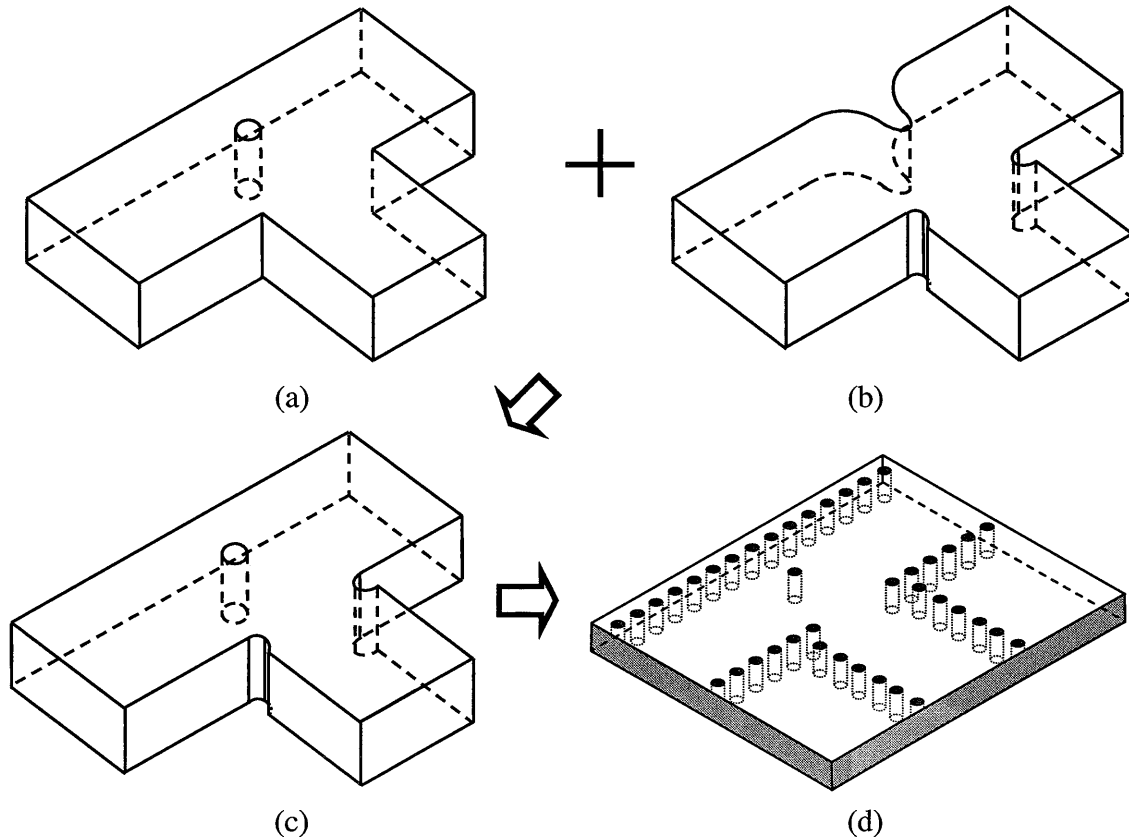


Fig.10. Waveguide T-junctions with (a) Matching post only, (b) Wedge and diaphragms, (c) Combination of a and b, a T-junction with matching post and diaphragms, (d) The SIW counterparts of the waveguide T-junction (c)

In addition, we have developed a set of design charts for the SIW T-junction design parameters based on extensive HFSS numerical simulations. This set of curves can be used to design the post-diaphragm configuration. As shown in Fig.11, both the  $L_p$  (offset/distance of post in the junction from the common sidewall of two outputs) and the  $L_d$  (offset/indent of the vias forming the diaphragms from sidewalls of the input SIW) have been optimized to achieve a return loss better than -50dB at the center frequency.

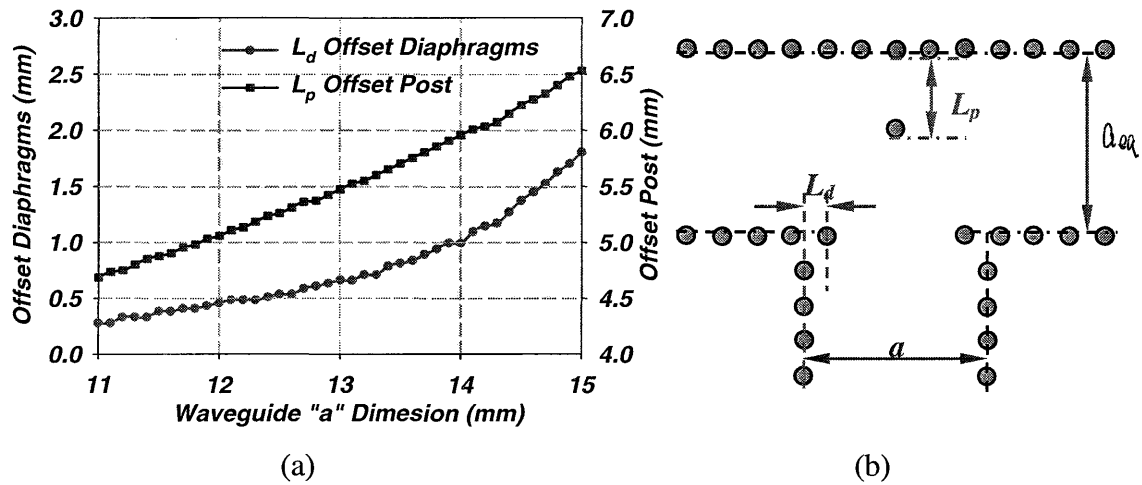


Fig.11. Design (a) charts and (b) parameters of the post-diaphragms configuration SIW T-junction

### 3.2. Synthesis of the SIW Y-Junctions

The previous analysis has been extended here to include a special case of the T-junction, the Y-junction. This is usually used at the input of the binary feeding network. In a similar fashion, the Y-junction can also be compensated by introducing the diaphragms and the offset of the common sidewall of two outputs as shown in Fig.12. Following the same method described in the previous section, a set of design curves, as shown in Fig.13, have been generated for the SIW Y-junction using the SIW dimensions and material.

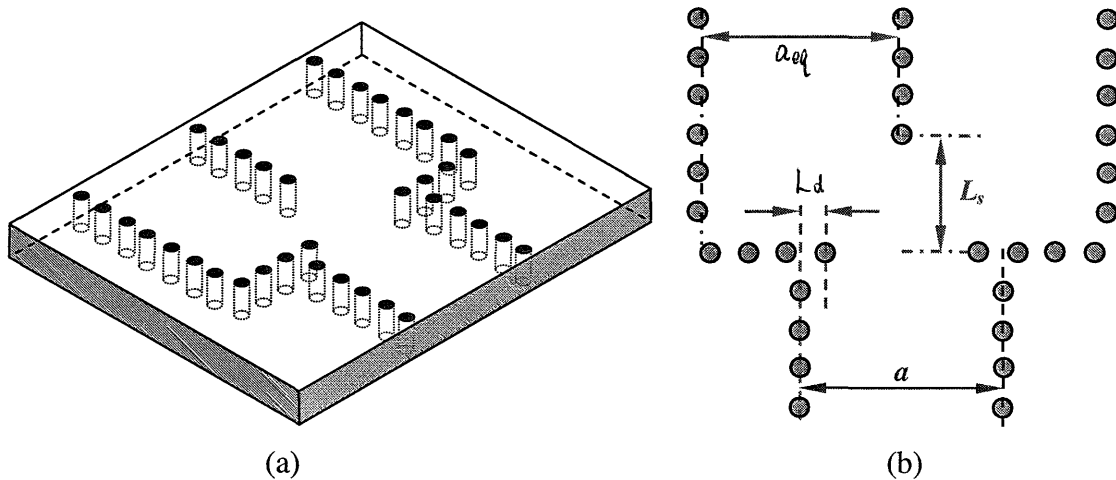


Fig.12. SIW Y-junction (a) structure and (b) design parameters

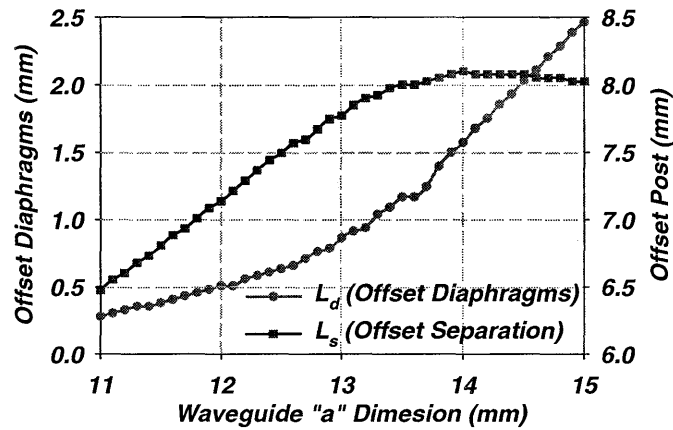


Fig.13. Design charts of the SIW Y-junction.

### 3.3. Feed Waveguide Design

The basic dimensions of the SIW have been discussed in section 2.5, where the feed guide “a” dimension is designed to minimize the insertion loss. Obviously, increasing the a dimension would lead to further conductor loss reduction, however this dimensions is limited by the maximum allowable space requirements of the feed network. In addition, the developed designs for both the T and Y-junctions should cover at least 500 MHz, i.e. the DBS bandwidth in USA.

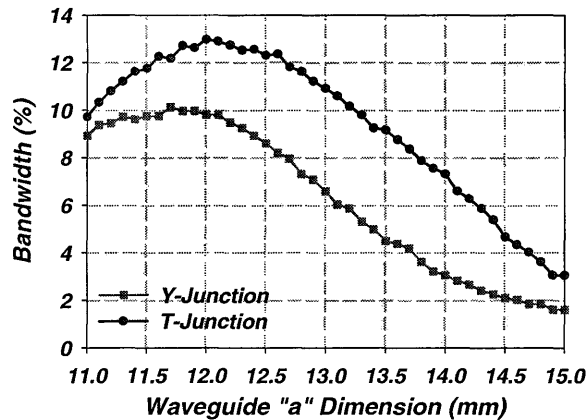


Fig.14. Bandwidth of SIW T and Y junctions

As shown in Fig.14, the simulated bandwidth (for return loss <math><-30\text{dB}</math>) of both the SIW T and Y junctions discussed in section 3.1~2 are shown as function of the waveguide “a” dimension. It can be seen that both structures provide a fairly wide operating bandwidth. It was noticed that when the SIW is narrow, the bandwidth peaks at 13% and 10% for the T- and the Y-junctions respectively. Along the diaphragms offsets, the quality factor of the junction becomes higher and higher, so the bandwidth continues to drop as the width of SIW increases. However, for both of the junctions, it is very easy

to achieve 500MHz at 12.45GHz (~4%) bandwidth, therefore, in order to sufficiently minimize the feed network loss we have utilized an optimum value for the SIW waveguide width  $a$ , where  $a=14.2$  mm was selected.

### 3.4. Coaxial to SIW transition

A current probe transition from grounded coplanar waveguide (GCPW) to SIW [6] is used to transform the transmission line from waveguide to a planar structure, which can be easily integrated with active devices in a later stage. As shown in Fig.15a, a plated through hole is placed in the junction to operate as a current coupling probe. To insure full energy propagation in one direction, a back short for the current probe is provided where the GCPW is terminated by an open circuit right next to the coupling post. In addition, via holes are strategically placed along the GCPW to cancel the parallel plate mode in the GCPW line, and to cut off the waveguide modes entering the GCPW from the SIW. In order to allow easy connection to coaxial connectors, a characteristic impedance of  $50\Omega$  is selected for both the GCPW and the SIW lines. In this design, a minimum manufacturable slot width has been used in the GCPW structure, and the SIW has been widened in this junction area. Based on simulated return and insertion loss of a back to back transitions (shown in Fig.15b), It is anticipate to achieve excellent input transitions.

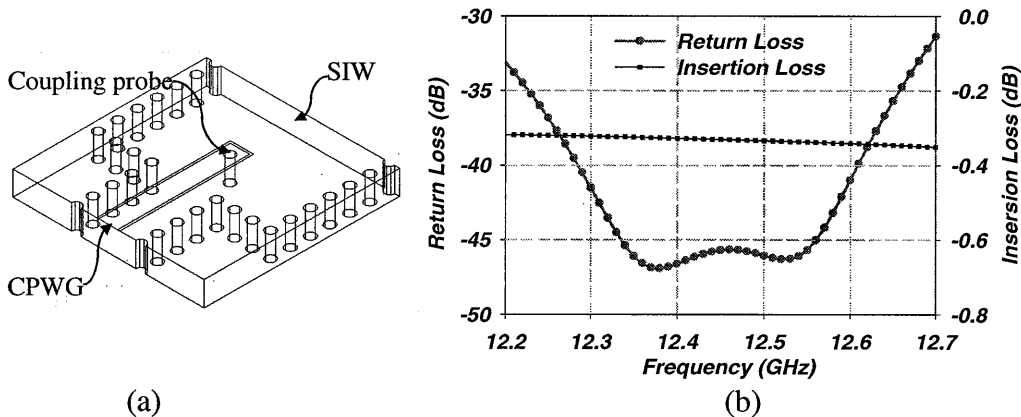


Fig.15. (a) CPWG to SIW transition, (b) simulated result of back to back transitions

### 3.5. Concept of Dual CP Operation:

The concept of dual circular polarization is the same as the previously developed metallic waveguide slot array. As shown in Fig.16, “X-shaped” slots are densely arranged on the broad wall of the radiating SIW structures, where the leaky waveguide radiates a circular polarization at the main beam, and already has a large tilt angle (about  $45^\circ$  degrees from zenith)[7]. As can be seen in Fig.16, when the cross-slots are excited by a mode propagating from Port1 to Port2, the slots radiate left-hand circular polarization together with a tilt of  $45^\circ$ . On the other hand, when the same slots are excited by a mode traveling from Port2 to Port1, a right-hand circularly polarized beam is generated with a tilt angle of  $-45^\circ$ .

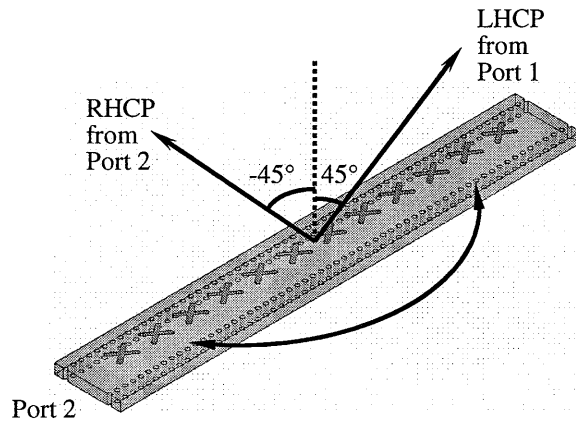


Fig.16. Dual Circular Polarization realization

### 3.6 Single Element Design:

A single element is first designed utilizing SIW with the previously selected dimensions ( $a=14.2\text{mm}$ ,  $b=3.175\text{mm}$ ). A 12 “X” slots etched on the top metallization of the SIW are utilized to obtain circular polarization. As seen in Fig.17 (a), the total length of each cell  $L_1$  is 11.18mm, and the slot width  $S_2$  is 1.27mm. While offset of the shape “X” from the centerline of waveguide broadside  $OO'$   $S_1$  is 2.29mm, and slot length  $L_2$  is 9.65mm. The cross-angle  $\theta$  is  $75^\circ$ . All these parameters are chosen to minimize the transmission between the two ports, maximize the gain of main lobe, and maintain a good axial ratio at  $45^\circ$  degrees. As shown in Fig.17 (b), excellent axial ratio has been achieved at peak of RHCP radiation, which is approximately  $45^\circ$  off broadside.

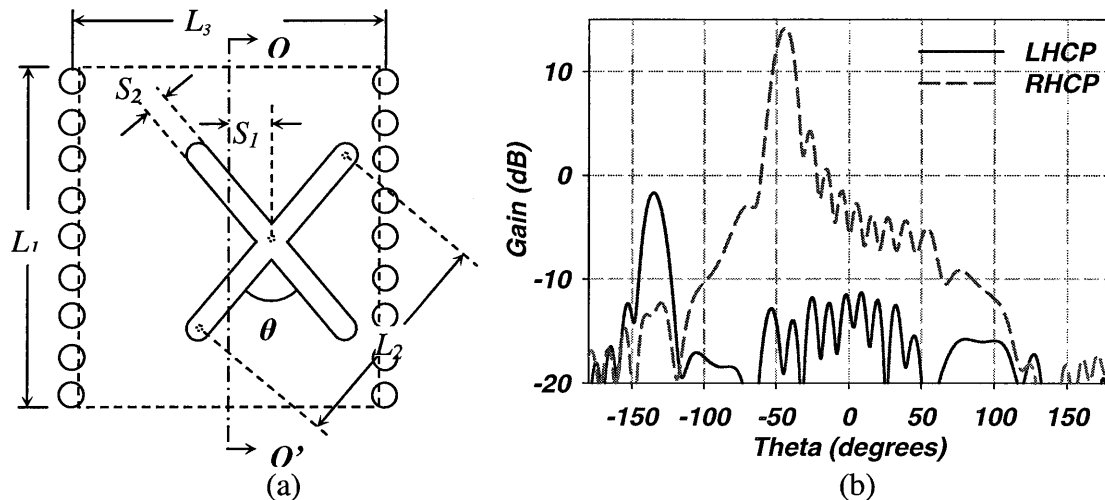


Fig.17. (a) Unit element dimensions and (b) predicted single SIW slot array performance

### 4. 12x16 Elements Sub-Array Development

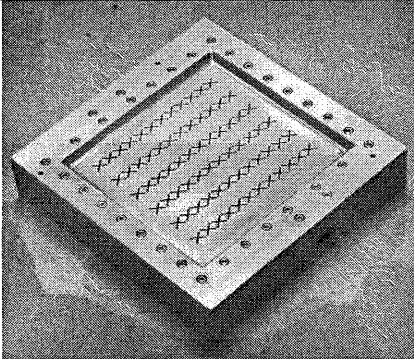
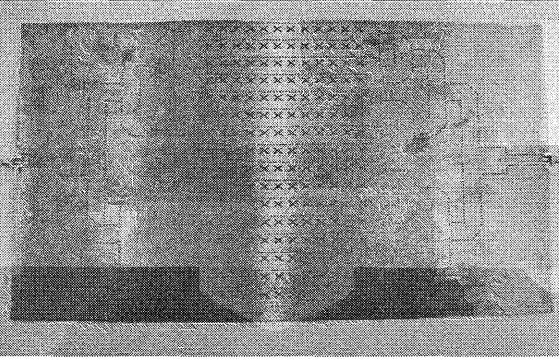
The sub-array structure is comprised of a 12x16 slot array defined on the surface of the SIWs as depicted in Fig.19. A 1 to 16 binary feed network (shown in Fig.21) has been

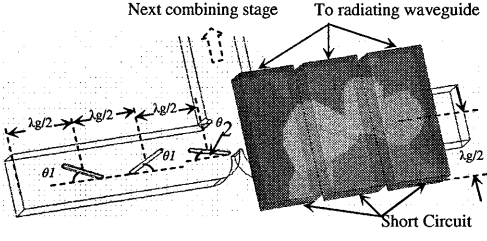
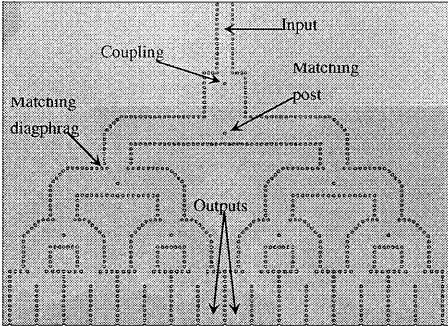
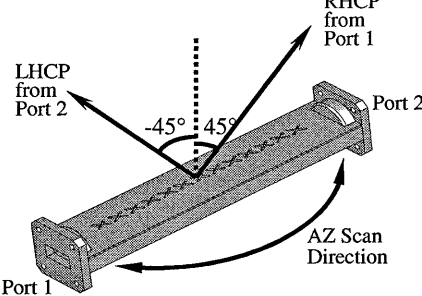
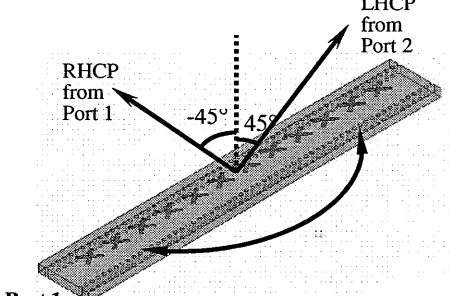
utilized, the design of which is based on the SIW T- and Y- junction synthesis procedure developed in the previous section. The fabricated parts include a coaxial line to SIW transition through GCPW at the input and output ports.

#### 4.1. Metallic vs. SIW Array

Design steps of the printed slot array are very similar to the all-metallic version. For the SIW, the utilized substrate (RT/duroid 5880) is 3.175mm-thick with a dielectric constant of 2.2, and a loss tangent of 0.0009. The radiating slot elements were defined using chemical photo-etching process and the reduced height waveguide sidewalls were emulated using metalized via holes. A full comparison of the slotted waveguide array antennas fabricated using both CNC machine [1], and the SIW printed circuit technology is shown in Table I.

**TABLE I**  
COMPARISON BETWEEN THE METALLIC AND THE SUBSTRATE INTEGRATED WAVEGUIDE SLOT ARRAYS

	Metallic Waveguide Slot Array	SIW Slot Array
Fabricated Slotted Waveguide Sub-Arrays	 Fig.18. 12x6 metallic waveguide slot sub-array	 Fig.19. 12x16 SIW slot sub-array
Cost	Very high, requires CNC machining, and high precision manufacturing	Low, slots are $\pm 0.001$ in. accurate using conventional printed circuit board technology
Loss	$< 0.025$ dB/in for WR62 with a 0.280in reduced height waveguide	$< 0.07$ dB/in, for a 0.125in. thick Duroid 5880 substrate

<p style="writing-mode: vertical-rl; transform: rotate(180deg);">Feed Mechanism</p>	 <p>Fig. 20. Two layer metallic waveguide feeding network</p>	 <p>Fig. 21. Planar feeding network</p>
<p>Beam Tilt</p>	<p>Metallic waveguide leaks forward</p>	<p>Dielectrically loaded SIW leaks backward</p>
<p>Feed Height</p>	<p>Requires different layers for feeding network. More than 0.75 inch for two layer feeding networks</p>	<p>Feeds could be easily integrated using coplanar structures. Less than 0.25 inch for two layer feeding networks</p>
<p>Weight</p>	<p>Bulky, heavy</p>	<p>Light, and low profile</p>
<p style="writing-mode: vertical-rl; transform: rotate(180deg);">Radiation Scheme</p>	 <p>Fig. 22. Single metallic waveguide slot array</p>	 <p>Fig. 23. Single SIW slot array</p>

The radiating beam is designed to have a 45° tilt angle from elevation. As shown in both Figs. 22 and 23, in order to produce circular polarization, the “X-shaped” slots are densely arranged on the broad wall of the radiating SIW structures. The traveling waves in these waveguides radiate (leak) at a certain angle, which is a function of the electrical spacing between the slots along the radiating waveguide. It has been designed here for a 45° tilt angle at the operating frequency. As can be seen from Fig. 22, when the cross-slots are excited by the dominant mode propagating in the metallic guide from Port1 to Port2, these slots radiate right-hand circular polarization at a tilt angle of 45°. On the other hand, when the same slots are excited by a mode traveling from Port2 to Port1, a left-hand circularly polarized beam is generated with a tilt angle of -45°. Consequently, Ports1 and 2 would correspond to RHCP and LHCP in +45° and -45° respectively. However, a frequency beam squint is expected over the frequency range of 12.2 to 12.7 GHz.

Similarly, the SIW sub array is comprised of 16 radiating waveguides that are lined up next to each other (as shown in Fig. 19). Although both metallic and SIW solutions are designed to have the same main beam tilt angle, the directions of their main beams are opposite due to the dielectric loading. Inside the air filled metallic waveguide, the wave is traveling faster than the speed of light, while waves in the dielectrically loaded waveguide travel slower. So, the metallic waveguide slot array has a beam pointing forward, but the SIW has a beam pointing backward as demonstrated in Figs. 22 and 23. For both cases, it is not possible to provide simultaneous dual polarization reception. But, the two circularly polarized beams received from the same satellite can be addressed one at a time by mechanically rotating the whole antenna  $180^\circ$  in azimuth.

#### 4.2. Sub-Array Measurement Results

We have carried out extensive S-parameter evaluation of the 12x16 sub-array using HP8510C network analyzer. The measured return loss is better than -18 dB, and the transmission (termination) loss is less than -15 dB. The measured return and transmission loss of the SIW sub-array are shown in Fig.24. The -20dB bandwidth of the sub array is relatively narrow, which is due to the narrow band performance of SIW T- and Y-junctions at the selected SIW width.

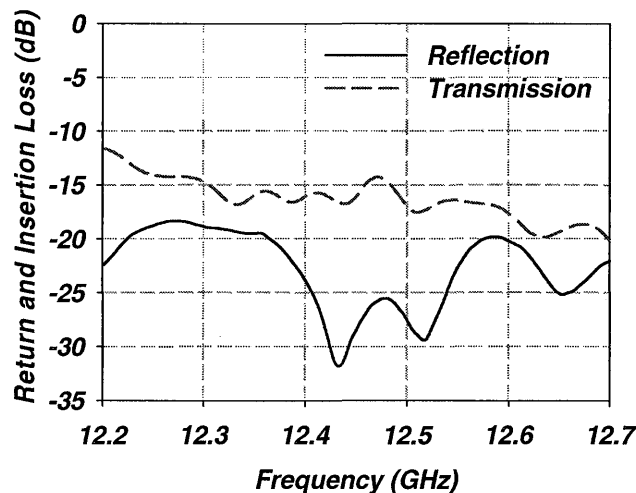
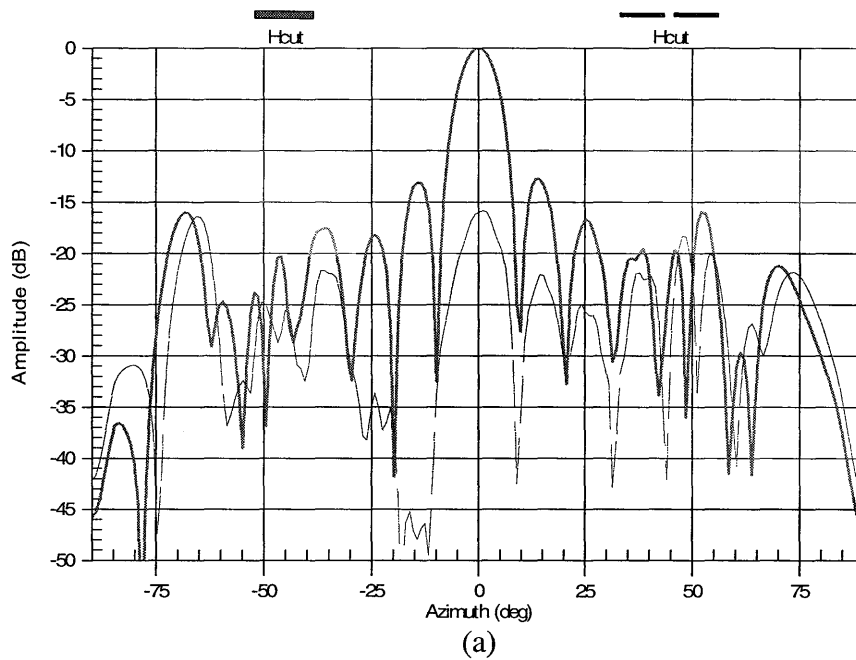


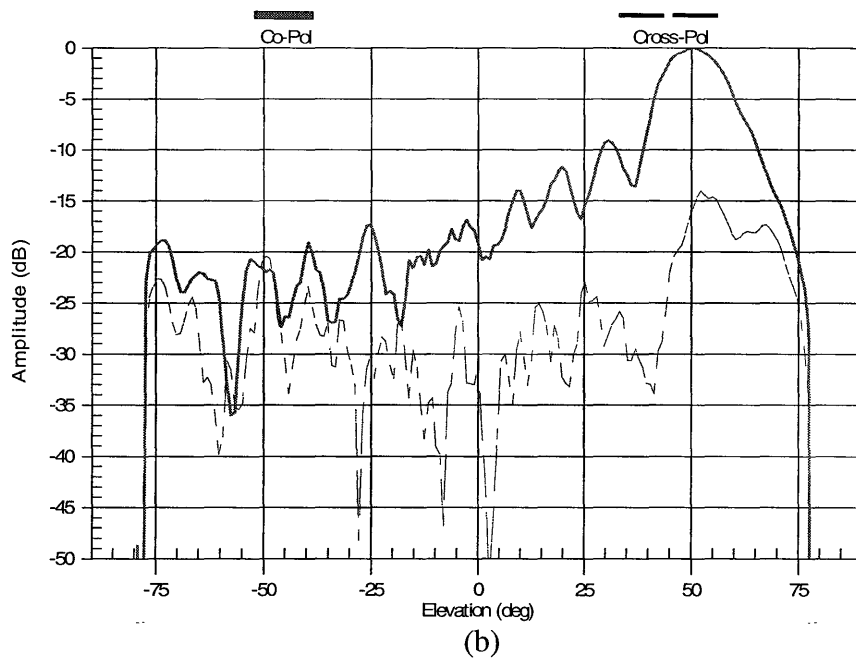
Fig.24. Measured results of 12x16 elements slot array

Additionally, we have evaluated their radiation patterns using both far- and near field measurement setups [8]. The measured radiation patterns were close to the simulated results over the 12.2 GHz to 12.7 GHz. Two orthogonal cuts across the main beam are shown in Fig. 25, 26 and 27 respectively for 12.2GHz, 12.45 GHz 12.7GHz. Note that over 24.7 dBi gain has been measured. This is equivalent to over 65% efficiency. Furthermore, cross polarization levels were also measured, and were always better than 20dB down from the peak of the main beam which indicates a good axial ratio.



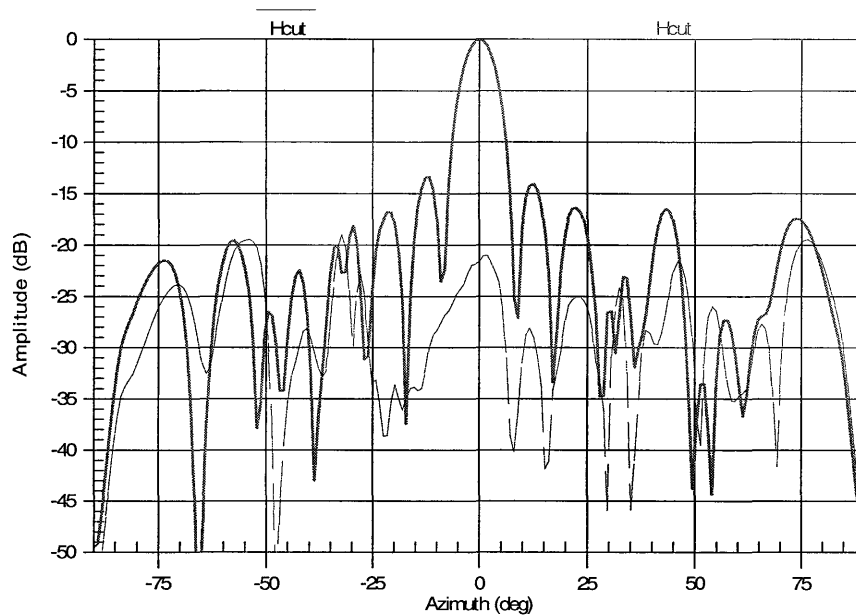


Polarization = LHCP, -3dB AZ BW = 8.5 deg, Peak Gain = 23.29 dBi,  
 AZ Peak = 0.036 deg, Left Sidelobe: -13.08 dB, Right Sidelobe: -12.70 dB



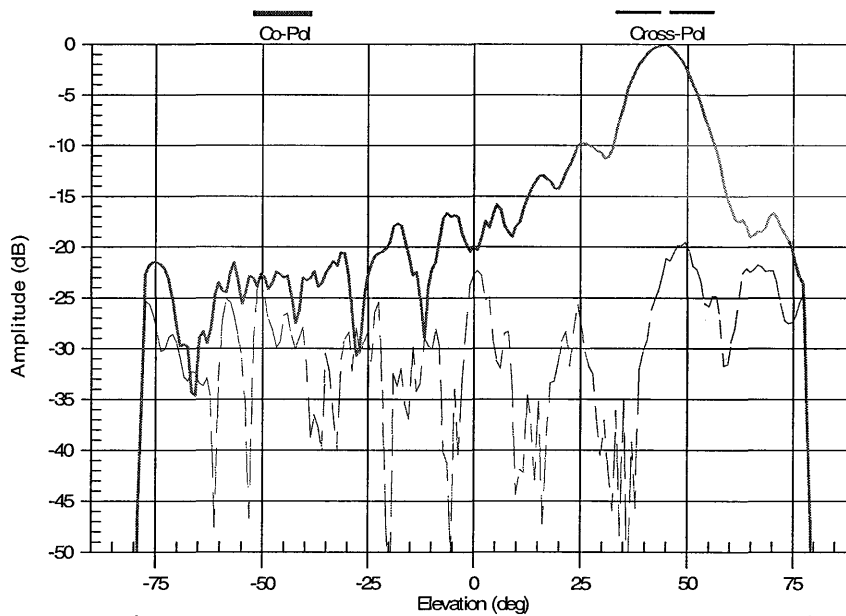
Polarization = LHCP, -3dB EL BW = 15.23 deg, EL Peak = 50.19 deg  
 Left Sidelobe: -9.08 dB, Right Sidelobe: -52.95 dB

Fig.25. Radiation patterns of the sub-array at 12.2GHz (a) Azimuth and (b) Elevation cuts



(a)

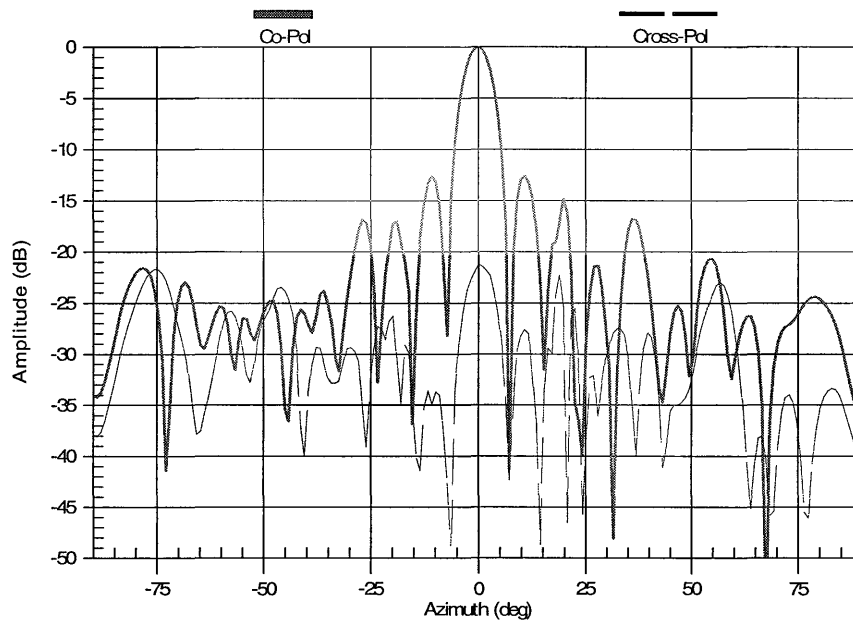
Polarization = LHCP, 3dB AZ BW = 7.56 deg, Peak Gain = 24.72 dBi,  
 AZ Peak = -0.33 deg, Left Sidelobe: -13.40 dB, Right Sidelobe: -14.06 dB



(b)

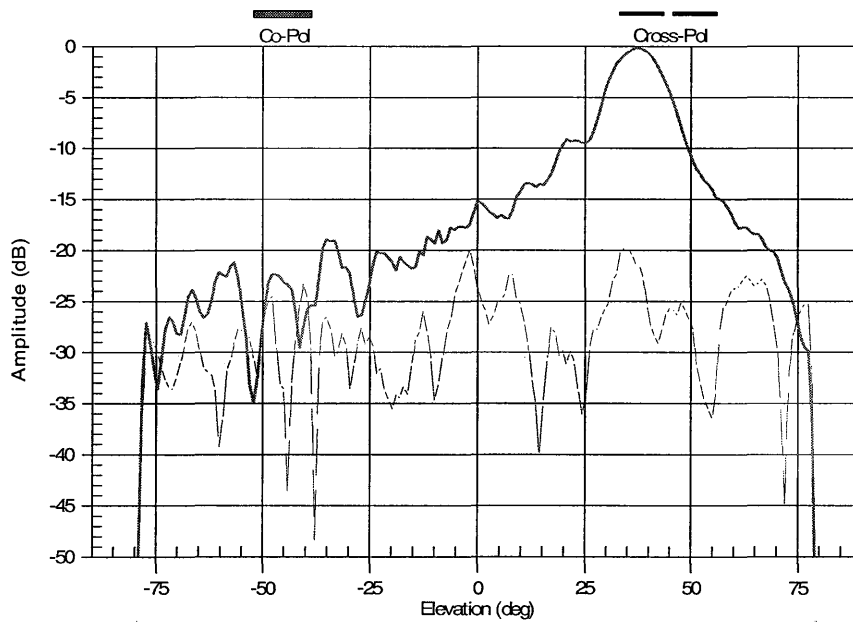
Polarization = LHCP, 3dB EL BW = 13.04 deg, EL Peak = 44.68 deg  
 Left Sidelobe: -9.73 dB, Right Sidelobe: -16.58 dB

Fig.26. Radiation patterns of the sub-array at 12.45GHz (a) Azimuth and (b) Elevation cuts



(a)

Polarization = LHCP, 3dB AZ BW = 6.46 deg, Peak Gain = 25.51 dBi,  
 AZ Peak = -0.74 deg, Left Sidelobe: -12.63 dB, Right Sidelobe: -12.59 dB



(b)

Polarization = LHCP, 3dB EL BW = 12.86 deg, EL Peak = 36.87 deg  
 Left Sidelobe: -15.02 dB, Right Sidelobe: None

Fig.27. Radiation patterns of the sub-array at 12.7GHz (a) Azimuth and (b) Elevation cuts

As shown in the measured radiation patterns, at the center frequency, the beam points exactly to  $45^\circ$ . However, it has a pronounced frequency dependent beam squint. As the main beam moves from  $51^\circ$  from horizon at  $f = 12.7\text{GHz}$  to  $39^\circ$  from horizon at  $f = 12.2\text{GHz}$ . This beam squint can be easily corrected by introducing a look up table in the tracking system, and then the antenna tilt angle can be adjusted based on the channel number selected.

For this sub array design, we have optimized the structure for the lowest loss, but still, the efficiency of the SIW is slightly lower than that for all-metallic version due to the loss of the dielectric substrate material. However, the loss of the former is still relatively small, and would allow increasing the number of radiating waveguides, which should result in an acceptable performance as will be investigated in the next section.

## 5. Full Array Design

### 5.1. Compact Feed Network Development:

A binary feed network has been used to implement a full array design. Binary feeds achieve excellent match, bandwidth, and output phase balance. In this design, compact waveguide T and  $\pi$  junctions [9-10] designs have been “translated” into SIW, and implemented here to minimize the size of the feed network. For instance, a 1:8 power divider (shown in Fig. 28), is noticeably compact. Its simulated amplitude and phase balance are shown in Fig. 29.

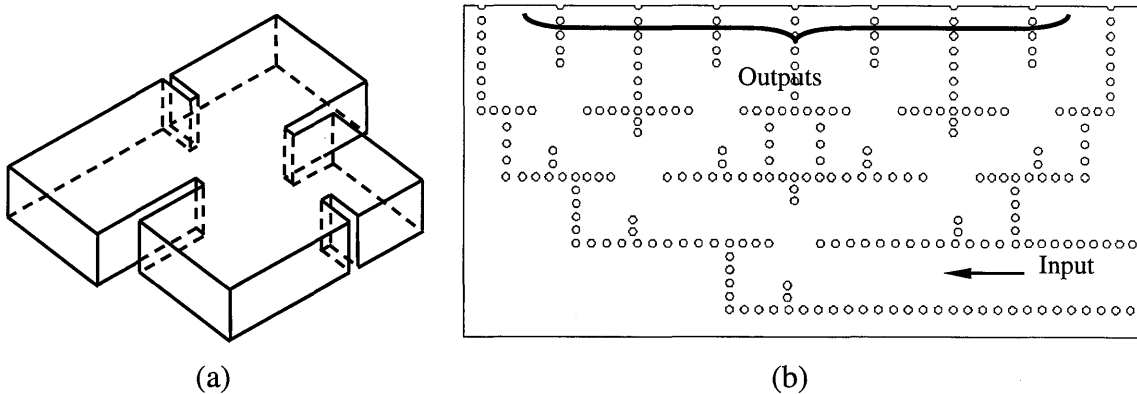


Fig.28. Compact (a) Waveguide T-junction, (b) 1 to 8 binary power divider structure

This feed network will be eventually folded to the back of the radiating elements to provide further size reduction. However, in order to do that, the width of the feed SIW guides need to be reduced to as narrow as 11.2mm. According to the design guide lines given in section 2, both conductor loss and dielectric loss increase upon reducing the width of the SIW guide. Hence, it is anticipated to incur extra loss by as much as 0.45dB/m, which will account for a total of 2.95dB/m. In addition, when adding two

more combining stages to feed the 64 radiating SIWs, the overall feed lines will become as long as 1m, and will cause antenna efficiency degradation even further.

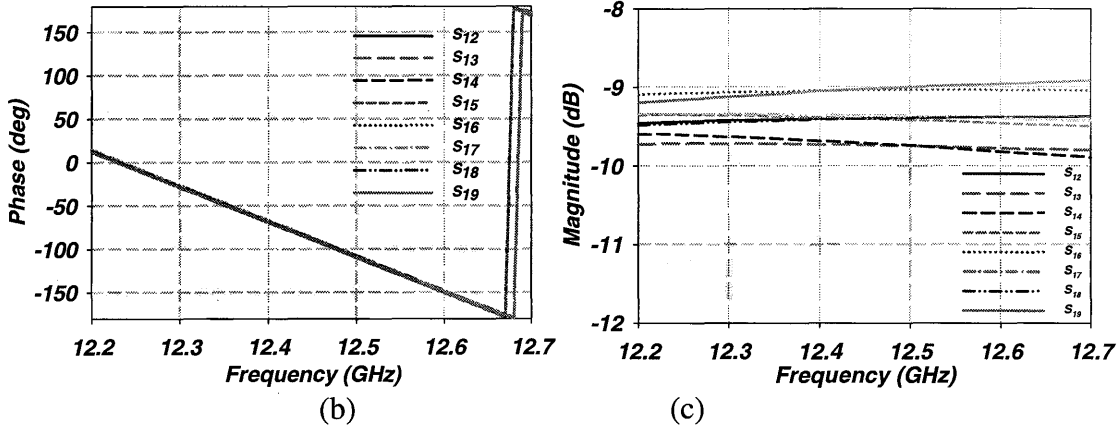


Fig.29. (a) Simulated phase (b) and amplitudes at output ports of the compact 1:8 power divider

Finally, a 12x64 SIW slot array structure has been fabricated (shown in Fig.30), and when compared to the sub array design (shown in Fig.19), the number of radiating elements are four times more. But in this case, the size of feed network is greatly reduced due to the utilization of compact junctions and narrower SIWs. However, after increasing the number of radiating waveguides to 64, the loss of the feed network has significantly increased to a point that further lateral expansion of the array size will give marginal gain increments. Then to compensate for the feed loss and to establish the noise figure of the receiving antenna, it is required to add LNAs before combining the outputs of more sub-arrays.

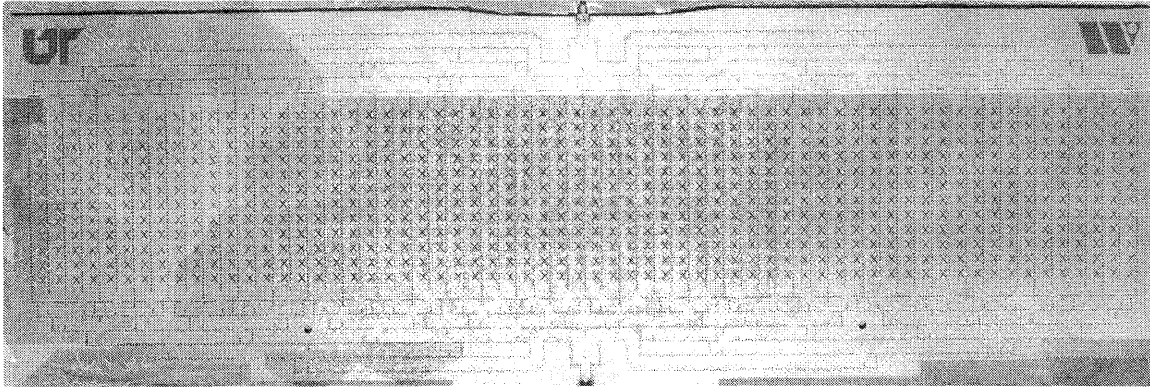


Fig.30. Fabricated 12x64 elements slotted SIW full antenna array.

## 5.2. Measurement Results:

The measured return loss and termination losses are shown in Fig. 31. It is recognized from these measurements that a wide bandwidth has been achieved, when using SIW junctions with narrower “a” dimensions. In addition, the radiation patterns of these fabricated full arrays have been evaluated using near-field measurements. The measured LHCP radiation patterns at 12.2, 12.45 and 12.7GHz are shown in Fig.32, 33 and 34 respectively, demonstrating excellent axial ratio performance at the center frequency. Comparing their performance to that of a standard gain horn, approximately 28 dBi gain has been achieved. The loss of the feed network is around 3dB, which is very close to the predicted insertion loss values according to the design charts detailed in section 2. Similar results were measured for the RHCP case as well.

In the azimuth cut, a very narrow beam with a relatively high side lobe levels are measured, which can be reduced by tapering the feed for each radiating SIW. In the elevation cut, however, fewer elements are used and as expected a wider beam has been measured. Meanwhile, due to the tapering of the radiating slots’ size, a much lower side lobe level (<-18dB down) has been achieved here, when compared to that of the previously built sub array design shown in Figs.25-27. At the center frequency, the beam points exactly to 45° (Fig.32 (b), 33(b) and 34(b) are centered at the beam location angle). Similar to the measured results of the sub-array, a frequency dependent beam squint has been observed here as well for the full array.

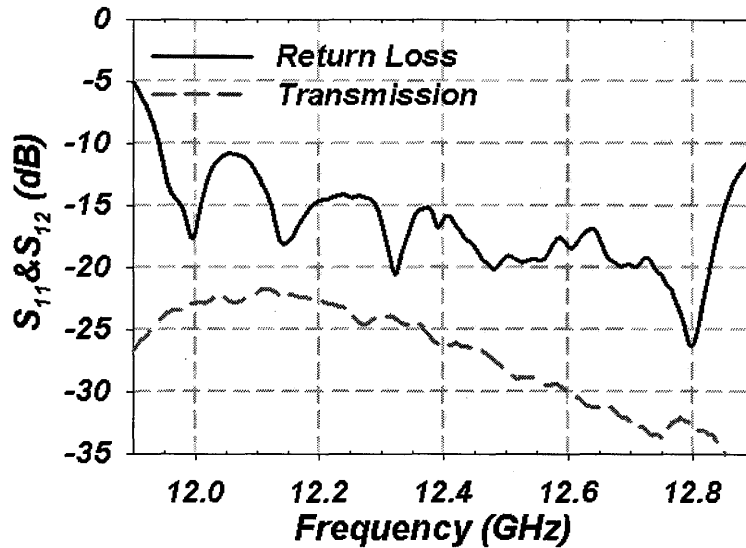
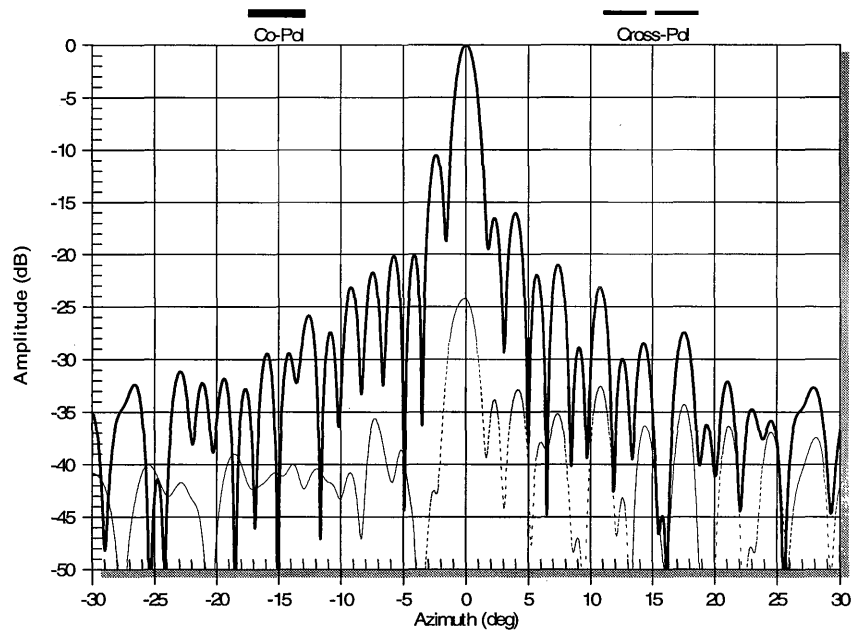
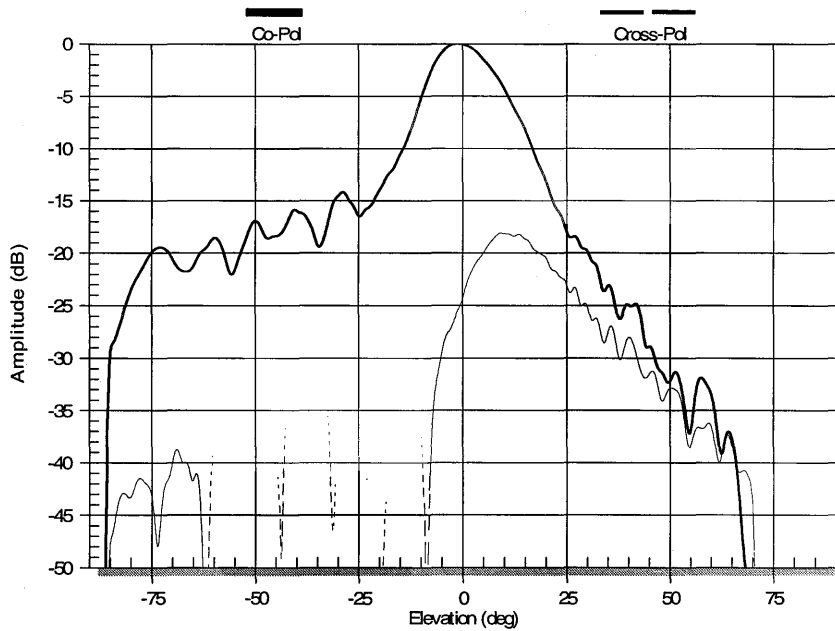


Fig.30. Measured return and termination losses of the 12x64 full SIW slot array



(a)

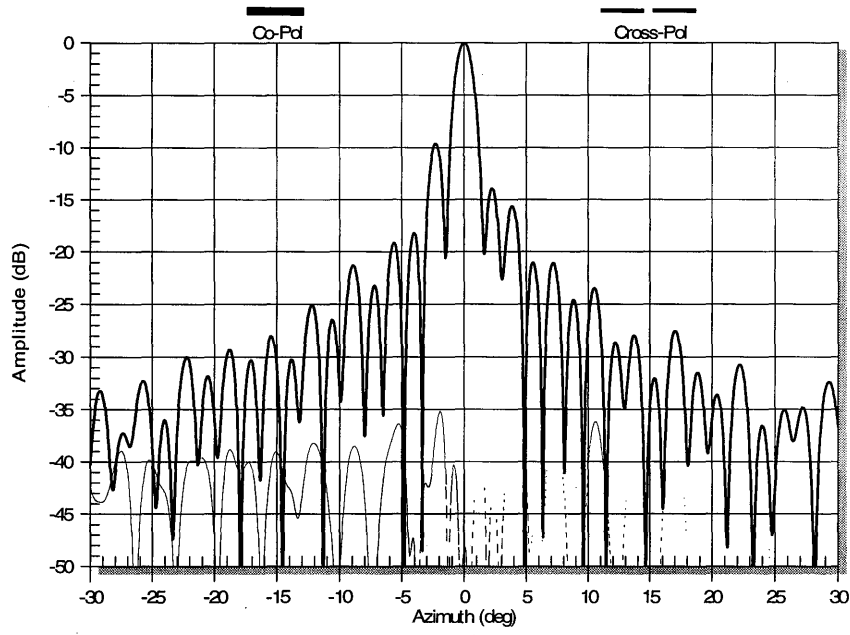
Polarization = **LHCP**, Peak Gain = **27.27 dBi**, Directivity = 30.75 dB  
 3 dB Az BW = 1.51°, 3 dB El BW = 16.06°, Cross-Pol Level = -24.28 dB



(b)

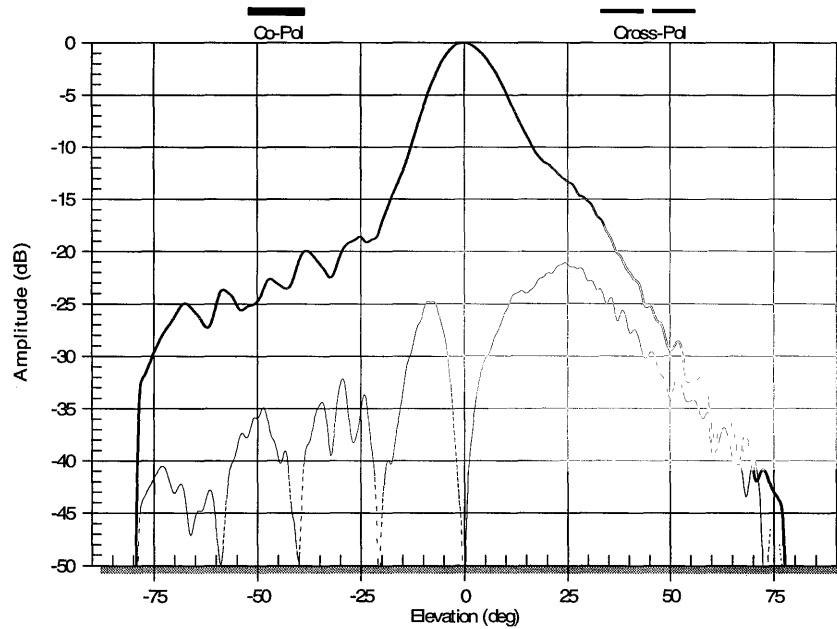
Polarization = **LHCP**, Peak Gain = **27.27 dBi**, Directivity = 30.75 dB  
 3 dB Az BW = 1.51°, 3 dB El BW = 16.06°, Cross-Pol Level = -24.28 dB

Fig.32. Radiation patterns of the full array at 12.2GHz (a) Azimuth and (b) Elevation cuts



(a)

Polarization = **LHCP**, Peak Gain = **27.98 dBi**, Directivity = 31.20 dB  
 3 dB Az BW = 1.39°, 3 dB El BW = 14.75°, Cross-Pol Level = -56.15 dB

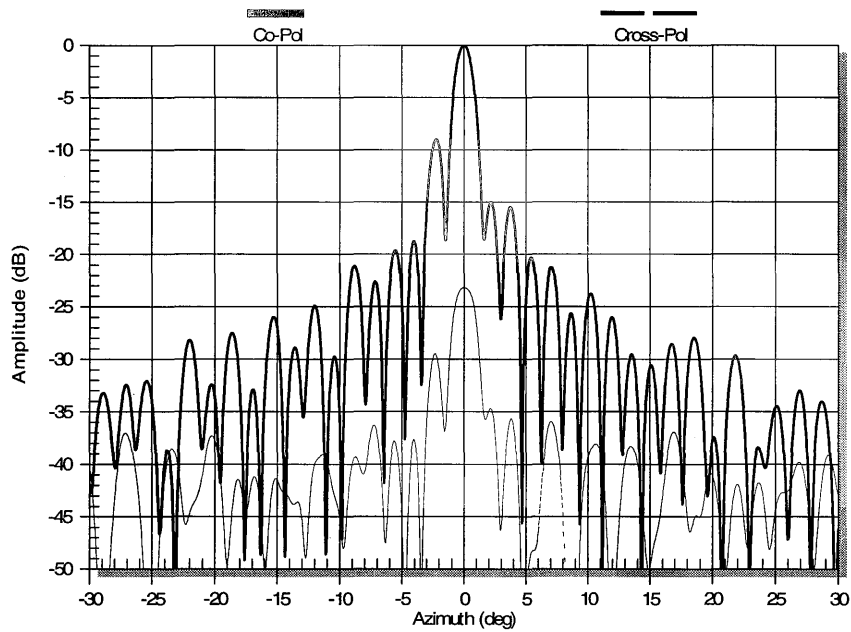


(b)

Polarization = **LHCP**, Peak Gain = **27.98 dBi**, Directivity = 31.20 dB  
 3 dB Az BW = 1.39°, 3 dB El BW = 14.75°, Cross-Pol Level = -56.15 dB

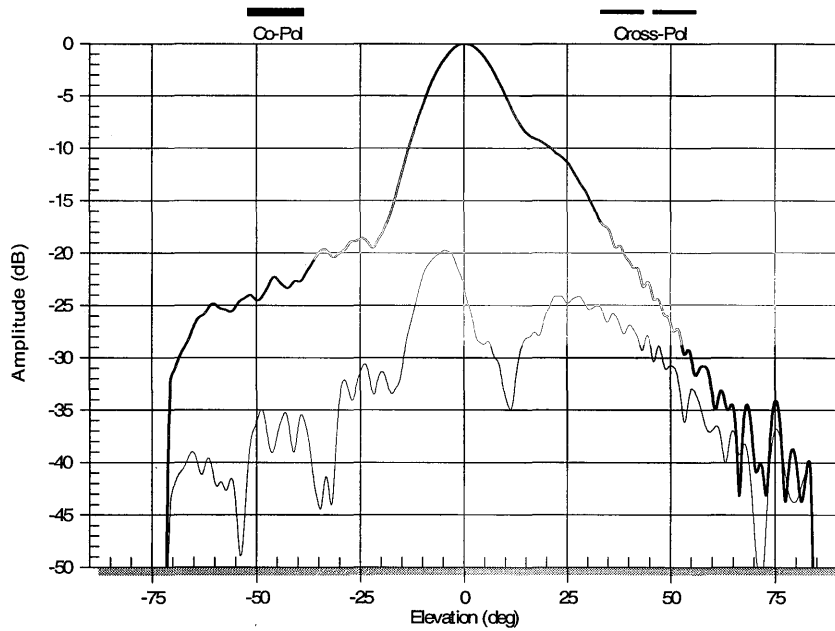
Fig.33. Radiation patterns of the full array at 12.45GHz (a) Azimuth (b) Elevation cuts





(a)

Polarization = **LHCP**, Peak Gain = **28.13 dBi**, Directivity = 31.09 dB  
 3 dB Az BW = 1.42°, 3 dB El BW = 14.58°, Cross-Pol Level = -23.17 dB



(b)

Polarization = **LHCP**, Peak Gain = **28.13 dBi**, Directivity = 31.09 dB  
 3 dB Az BW = 1.42°, 3 dB El BW = 14.58°, Cross-Pol Level = -23.17 dB

Fig.34. Radiation patterns of the full array at 12.7GHz (a) Azimuth and (b) Elevation cuts

## 6. Conclusion:

Slotted SIW array antennas utilizing emulated waveguide feed structures should have lower insertion loss when compared to planar printed antennas. They are easy to manufacture, have light weight, and their use should lead to a lower cost product as well. While its' alternative, the all-metal version, requires high manufacturing tolerances, bulky, heavy in weight, and expensive. SIW array antennas require conventional printed circuit board processing with a  $\pm 0.001$ " tolerance, that could be easily achieved when using conventional circuit board chemical etching processes. These fabricated SIWs have demonstrated less than 0.07dB/in loss at 12.45 GHz, when utilizing a 3.175mm thick RT-duriod 5880 substrate.

X-slotted arrays produce circularly polarized radiation, and have been designed to produce an inherent tilt angle of  $45^\circ$ . In this case, scan volume requirements in the elevation plane then could be significantly reduced due to the inherent tilt angle of these leaky wave antennas. As an advantage too, mechanical steering circumvents typical phased array gain drop, and X-pol degradation upon steering. Meanwhile, measured results have shown about 3dB overall insertion loss due to the feed network for the full array design, which indicates that we should double the aperture area by combining two parallel apertures and embed LNAs after each sub-array to minimize noise figures. Hence, the reported antenna design could lead to a low profile antenna ( $< 3$ in height) upon folding the feed structure, and will surmount to over 30 dB gain when splitting apertures (i.e. combining parallel apertures) as indicated in [11].

## References

- [1] Songnan Yang and Aly E. Fathy, "Slotted Arrays for Mobile DBS Antennas," *Proceedings of the 2005 Antenna Applications Symposium*, pp. 496 - 509, 21-23 September 2005, Monticello, IL
- [2] D.Deslandes and K. Wu," Integrate microstrip and rectangular waveguide in planar form." *IEEE Microw. Guided Wave Lett.*, vol.11, no.2, pp. 68-70, Feb. 2001
- [3] C. A. Balanis, *Advanced Engineering Electromagnetics*, New York: Wiley, pp. 376-283.
- [4] J. Hirokawa, K. Sakural, M. Ando, and N. Goto, "An analysis of a waveguide T junction with an inductive post," *IEEE Trans. Microwave Theory and Tech.*, vol. MTT-39, pp. 563-566, March 1991
- [5] Songnan Yang and Aly E. Fathy, "Synthesis of a Compound T-junction for a Two-Way Splitter with Arbitrary Power Ratio," *2005 IEEE MTT-S Int. Symp. Dig.*, pp 985-988, June 2005.

- [6] Dominic Deslandes and Ke Wu, "Analysis and Design of Current Probe Transition From Grounded Coplanar to Substrate Integrated Rectangular Waveguides," *IEEE Trans. Microwave Theory & Tech.*, vol. 53, no. 8, pp. 2487-2495, August 2005.
- [7] W. J. Getsinger, "Elliptically Polarized Leaky-Wave Array", *IRE Trans. Antennas and Propagation*, vol. 10, pp. 165-171, Mar. 1962
- [8] S. Suleiman, S. Yang and A. E. Fathy, "Evaluation of a Ku Band Slotted Array Antenna Using Planar Near-Field Measurements," *2006 IEEE AP-S Int. Symposium on Antennas and Propagation*, Albuquerque, NM, USA. July 13-17.
- [9] T. Takahashi, J. Hirokawa, M. Ando and N. Goto, "A single-layer power divider for a slotted waveguide array using  $\pi$ -junction with an inductive wall," *IEICE Trans. Commun.*, vol. E79-B, no. 1, pp. 57-62, Jan. 1996.
- [10] K. Fukazawa, J. Hirokawa, M. Ando and N. Goto, "Two-way power divider for partially parallel feed in single layer slotted waveguide arrays," *IEICE Trans. Commun.*, vol. E81-B, no. 6, pp. 1248-1253, June. 1998.
- [11] S. Yang and A. E. Fathy, "Cavity-Backed Patch Shared Aperture Antenna Array Approach for Mobile DBS Applications", *2006 IEEE AP-S Int. Symposium on Antennas and Propagation*, Albuquerque, NM, USA. July 13-17.

# DIRECT MODULATION OF AN L-BAND MICROSTRIP PATCH ANTENNA USING INTEGRATED PIN DIODES

Steven D. Keller<sup>(1)</sup>, W. Devereux Palmer<sup>(2)</sup>, and William T. Joines<sup>(1)</sup>

(1) Duke University Electrical and Computer Engineering, Durham, NC, 27708

(2) U.S. Army Research Office, Research Triangle Park, NC, 27709

**Abstract:** Army mobile ground communication systems typically require an antenna that provides large bandwidth, optimized power efficiency, and a small visual signature. A technique known as direct antenna modulation is a promising candidate to provide all three of these characteristics. By utilizing high-speed semiconductor switching components to directly modulate an antenna with a baseband pulse-modulated signal, the information bandwidth of the antenna may be decoupled from its resonant bandpass limitations. The direct modulation of an L-band microstrip patch antenna with fast-switching PIN diodes is described in this paper, as well as an introduction to the direct antenna modulation concept and a brief discussion of future research plans.

## 1. Introduction

When antenna structures are designed for Army ground communication systems, research efforts are typically focused on maximizing the information bandwidth and achieving high radiation efficiency with an antenna of the smallest physical size. Tradeoffs between these desired characteristics are often necessary during antenna design since antenna size and geometry generally control the resonant frequency, and since an antenna operating linearly at resonance with high radiation efficiency is intrinsically narrowband.

The standard rectangular patch antenna is an excellent example of a narrowband radiating element. The interactions between the energy that excites the patch at the feedpoint and the magnetic walls of the rectangular cavity geometry yield an input impedance that is highly frequency-dependent. This produces a resonant bandwidth that is dependent upon both the feedpoint impedance matching, represented in the following equation by the voltage standing wave ratio (VSWR), and the quality factor,  $Q_t$ , of the structure, [1]

$$BW = \frac{\Delta f}{f_0} = \frac{VSWR - 1}{Q_t \cdot \sqrt{VSWR}} \quad (1)$$

The quality factor of the patch is proportional to the summation of a wide variety of antenna losses, including radiation losses,  $Q_{rad}$ , conduction losses,  $Q_c$ , dielectric losses,  $Q_d$ , and surface wave losses,  $Q_{sw}$ , [1]

$$\frac{1}{Q_t} = \frac{1}{Q_{rad}} + \frac{1}{Q_c} + \frac{1}{Q_d} + \frac{1}{Q_{sw}} \quad (2)$$

Typically,  $Q_{rad}$  dominates the above expression for thin-substrate patch antennas while  $Q_{sw}$  dominates for thick-substrate structures. Since  $Q_{rad}$  is inversely proportional to power lost or radiated, and the power radiated is directly proportional to substrate thickness, then  $Q_{rad}$  is inversely proportional to substrate thickness. On the other hand, surface wave losses increase significantly if the substrate thickness is too large. [1] Thus, design compromises must be made regarding the substrate thickness to optimize both  $Q_{rad}$  and  $Q_{sw}$  and consequently optimize the antenna bandwidth and radiation efficiency. In this way, the bandwidth of the commonly-used patch antenna is significantly limited by both its resonant impedance feed matching and the losses associated with its quality factor components.

When traditional antenna modulation techniques are applied to a patch antenna in a communication system, the information bandwidth of the system will be significantly constrained by the bandpass nature of the antenna geometry. However, the system information bandwidth may be decoupled from the limits of the resonant antenna bandwidth by employing direct antenna modulation [2], a novel modulation technique that has only begun to be explored.

## 2. Background

Direct antenna modulation involves the incorporation of high-speed semiconductor switching technology with a radiating element in order to decouple the information bandwidth and radiation efficiency from the limiting bandpass nature of a resonant antenna and to eliminate the reliance of antenna size and geometry on the desired information signal frequency. By applying semiconductor switching techniques similar to those described in a US patent on synthesizer radiating systems [3] and those utilized for high-efficiency Class-D amplifiers [4], a unique antenna modulation system can be employed. A basic implementation of direct antenna modulation that is being employed in this research is shown in Figure 1.

After an antenna is designed and constructed to operate at a desired resonant frequency, one or more high-speed semiconductor switches, such as Schottky or PIN diodes, are connected between the antenna and the ground plane. An RF carrier wave at the resonant frequency of the patch antenna passes through a bias tee circuit and drives the antenna at

resonance through a feedpoint. Simultaneously, a lower-frequency baseband information signal, in digital pulse train format, passes through the bias tee circuit to the feedpoint and controls the diode switch. When the baseband signal has a value below that of the diode junction voltage,  $V_d$ , the switch displays high impedance to the carrier wave-generated oscillating charges on the patch antenna and the antenna efficiently radiates the carrier wave. When the baseband signal has a value close to or higher than that of  $V_d$ , the switch closes and provides a direct path for the oscillating charges on the patch antenna to flow to ground, causing antenna radiation to effectively cease. [2], [5] In this way, the digital baseband information signal is directly modulated onto the carrier wave. The antenna always radiates at or near its resonant frequency, producing high radiation efficiency. Also, the antenna geometry and size are no longer dependent upon the baseband information signal frequency, but are mainly dependent upon the desired carrier wave frequency. The information bandwidth of the system is also decoupled from the resonant bandwidth of the antenna and is mainly limited by the switching characteristics of the incorporated diode. This should result in a significant increase in the available information bandwidth, well beyond that which is provided by a linearly-operating resonant antenna that is inherently limited by its bandpass effect.

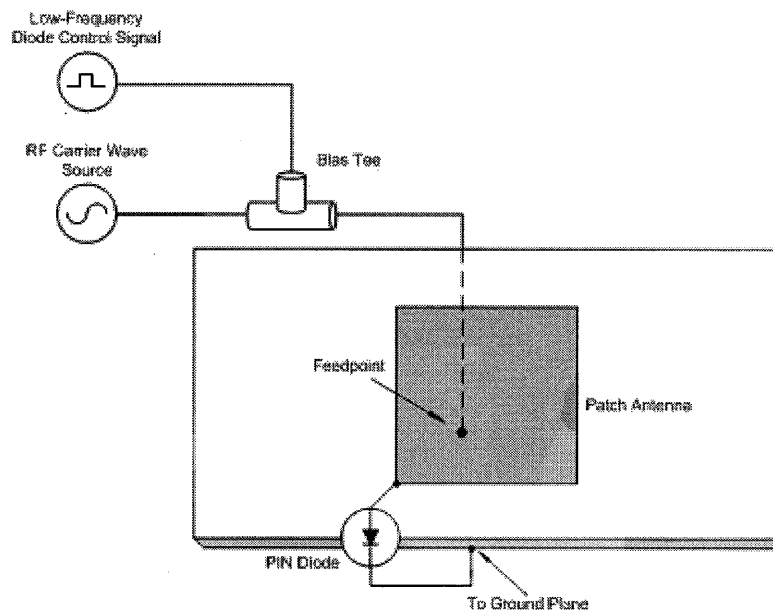


Figure 1. Basic implementation of direct antenna modulation.

Because 80% of the Army's mobile ground communications occurs below 1 GHz with dipole antennas that can be several meters in length [6], the reduction in visual signature resulting from the implementation of direct antenna modulation could be immense. With the incentive of compact antenna geometry and an increase in information bandwidth beyond that of a linearly-operating resonant antenna, further investigation of this promising antenna modulation technique is conducted and documented in this paper.

### 3. Analysis and Design

A symmetrical 1.5 GHz patch antenna was designed, simulated, and constructed to be the radiating element in the direct antenna modulation experiment. With a narrow resonant bandwidth of ~16 MHz for 15 dB or better return loss ( $VSWR = 1.43$ ), there is significant room for improvement that direct antenna modulation may offer to the information bandwidth of the system. By driving the antenna at resonance and directly modulating it with an integrated high-speed diode switch being biased by an external pulse train, the frequency of this external modulating signal is predicted to far exceed the resonant bandwidth of the antenna and still produce a clear demodulated waveform at the receiving end of a communication system.

When direct antenna modulation is implemented with this patch antenna design, the diodes should be placed between the antenna and the ground plane at locations where the volume current density (and consequently the electric field) is at its highest value. This will maximize the switching effect of the integrated diodes and consequently yield the cleanest modulation effect.  $J_{vol}$  and E-field magnitude and vector plots from an HFSS [7] simulation of the symmetrical patch antenna were used to find these points.

A model of the microstrip patch antenna was constructed in HFSS, as shown in Figure 2. The copper ground plane on the bottom surface of the substrate was approximated as an infinite perfect electric conducting (PEC) ground plane, while the patch antenna above the substrate was approximated as an actual copper tape slab, with a thickness of 88  $\mu\text{m}$ . The substrate was modeled after a 7.6 x 15.2 cm G-10 epoxy glass board with a thickness of 1/16" and relative dielectric constant of 4.24 at 1.5 GHz. The dimensions of the symmetric patch antenna model were set to 4.76 x 4.76 cm, with a feedpoint ~2.38 cm along the patch diagonal.

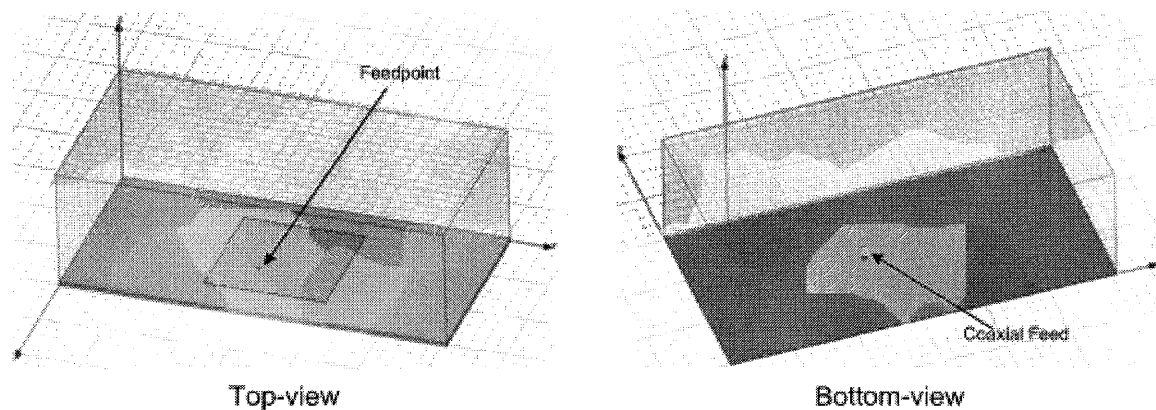


Figure 2. HFSS model of symmetric microstrip patch antenna.

The resulting  $J_{vol}$  magnitude and vector plots of this simulation are shown in Figure 3. The highest points of the volume current density appear to occur near two of the corners of the square patch, along the feedpoint diagonal. These points were confirmed by the E-

field plots (not shown in this paper). When diodes are integrated with the patch antenna in the direct antenna modulation experiment, they should be placed at or around these locations to maximize the diode switching effect.

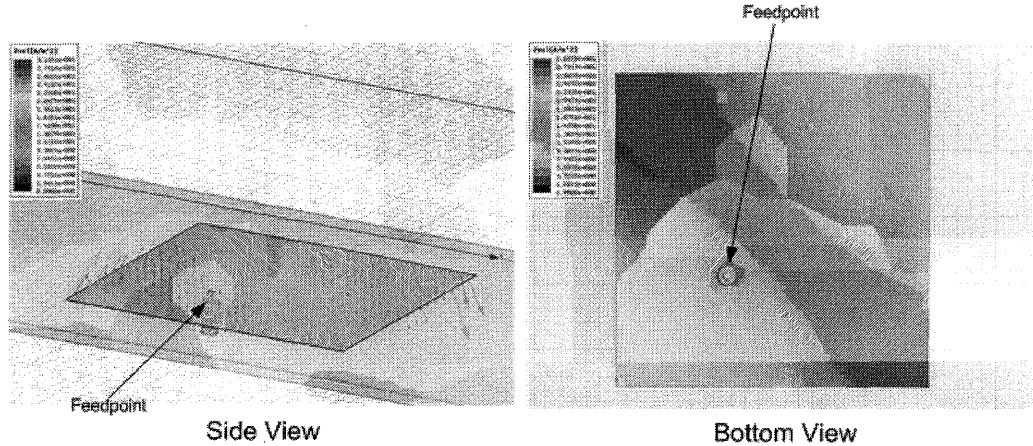


Figure 3.  $J_{vol}$  magnitude and vector overlay for HFSS simulation of patch antenna.

A number of semiconductor device characteristics must be considered when a Schottky or PIN diode is incorporated into a direct antenna modulation system as a switching element. The diode must be able to switch ‘on’ and ‘off’ fast enough to accommodate the baseband information signal that controls the diode bias. In previous direct antenna modulation research efforts, the switching “turn-off” period seemed to be significantly affected by the carrier lifetime of the semiconductor device. [2], [5] By using a diode with a very small carrier lifetime, the upper limit to the directly-modulated antenna’s information bandwidth should be significantly increased. Another important diode characteristic pertaining to direct antenna modulation is the junction capacitance. Since the diode must effectively function as an open circuit at 0 V bias, it is important to minimize its junction capacitance and consequently maximize its 0 V bias impedance value as a carrier wave passes across it.

For this direct antenna modulation experiment, the *Skyworks Solutions* SMP1340 PIN diode [8] was selected as the switching element. The carrier lifetime of the SMP1340 is specified as ~100ns, making it a suitable fast-switching device. The junction capacitance of this diode was also suitably low, being 0.3pF at 0 V bias. With a carrier wave frequency of 1.5 GHz passing across the diode, the resulting impedance is,

$$Z = \frac{1}{j\omega C} = \frac{1}{j \cdot 2\pi \cdot 1.5 \cdot 10^9 \cdot 0.3 pF} = j354\Omega \quad (3)$$



Thus, at 0 V bias, the diode will still function as a “closed” switch – not quite a true open circuit but possessing a reasonably high impedance value to be deemed an effective open circuit.

#### 4. Experiment

Two functional 1.5 GHz patch antennas were constructed according to the specifications detailed above to serve as the transmit/receive devices of a direct antenna modulation communication system. The experimental resonant frequency was measured as ~1.56 GHz. This difference between the designed and measured resonant frequencies is attributed to the difference in the initially assumed  $\epsilon_r = 4.8$  and the later measured  $\epsilon_r = 4.4$  dielectric constant of the G-10 epoxy glass substrate of the patch antenna. A microstrip bias tee circuit was then designed and fabricated to isolate the RF port and the baseband diode bias control signal port from one another and to provide a common output port to the transmit antenna’s feedpoint. Finally, two *Skyworks Solutions* SMP1340 PIN diodes were soldered between the patch antenna and the ground plane of the G-10 epoxy glass board, as shown in Figure 4, to serve as the switching devices for the implementation of direct antenna modulation.

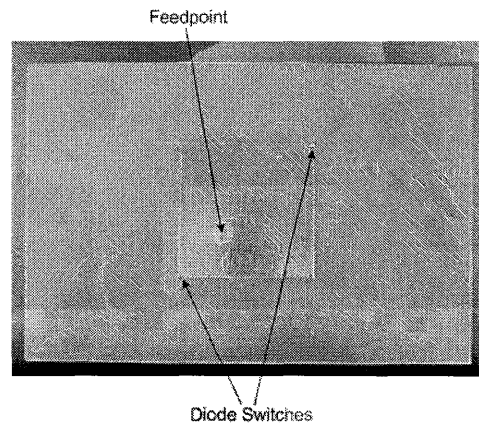


Figure 4. 1.56 GHz patch antenna with integrated PIN diodes.

With these components completed and fully integrated, the direct antenna modulation technique was then tested. A diode bias control signal with peak-to-peak voltage amplitude of ~0.8 V was produced by the *Wavetek* Model 145 function generator and sent into the low-frequency signal input port of the bias tee circuit, while a 1.56 GHz carrier wave was produced by the *Hewlett-Packard* 8614A signal generator and sent into the high-frequency signal input port. The 0.8 V amplitude for the diode bias control signal corresponded to the optimal SMP1340 forward bias voltage range of ~0.7 to 0.9 V. The frequency of this signal was varied from 100 kHz to the function generator limit of 20 MHz. The output port of the bias tee circuit was connected to the feedpoint of the transmit patch antenna and the feedpoint of the receive patch antenna was connected to

the Tektronix DSA 602A digitizing signal analyzer. This experimental setup is shown as a block diagram in Figure 5.

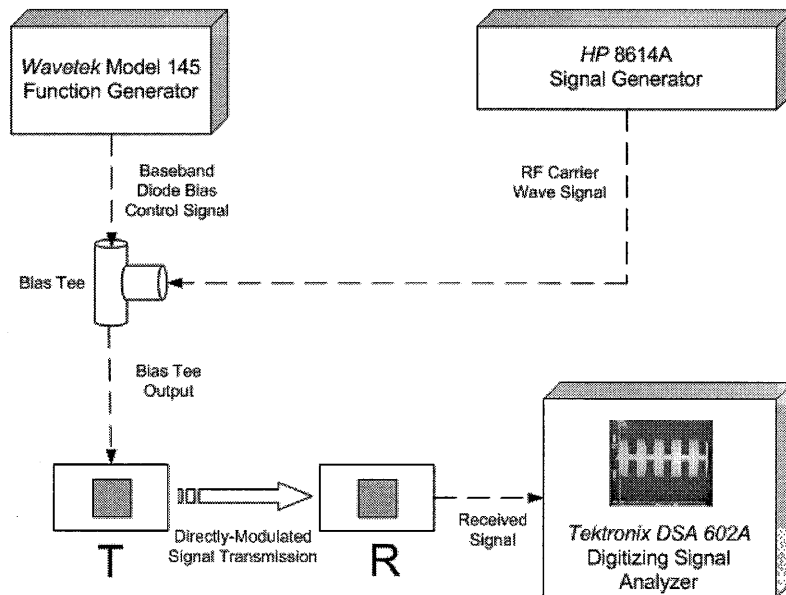


Figure 5. Block diagram of direct antenna modulation experiment.

The modulation effect of the baseband signal-controlled diode switch on the radiated 1.56 GHz carrier wave was examined by displaying the received carrier wave on the signal analyzer. The direct pulse modulation of the radiated carrier wave by the pulse-train biasing of the diode switches could clearly be seen, as shown in Figure 6. When the diode bias control signal had a value of 0 V (diode switch open), the carrier wave radiation was maximized and the received signal amplitude averaged  $\sim 40$  mV. When the diode bias control signal had a value of  $\sim 0.8$  V (diode switch closed, in forward bias), the carrier wave radiation was significantly reduced and the received signal amplitude averaged  $\sim 5$  mV.

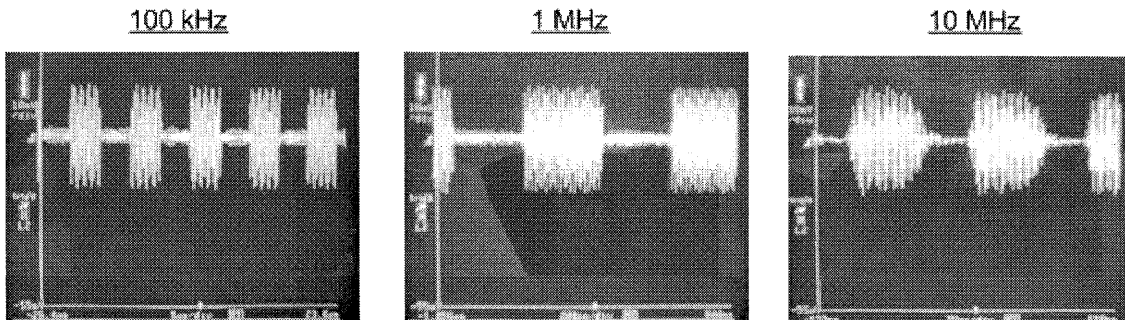


Figure 6. Directly-modulated carrier wave (viewed on signal analyzer).

For the majority of the 100 kHz – 20 MHz modulation frequency range that was tested, the pulse shape of the input diode bias control signal was well-preserved in the received directly-modulated carrier waveform. It should be noted that the received waveform did seem to become increasingly distorted in shape for frequencies between 10 MHz and 20 MHz, yet it still maintained a reasonably clear pulse shape.

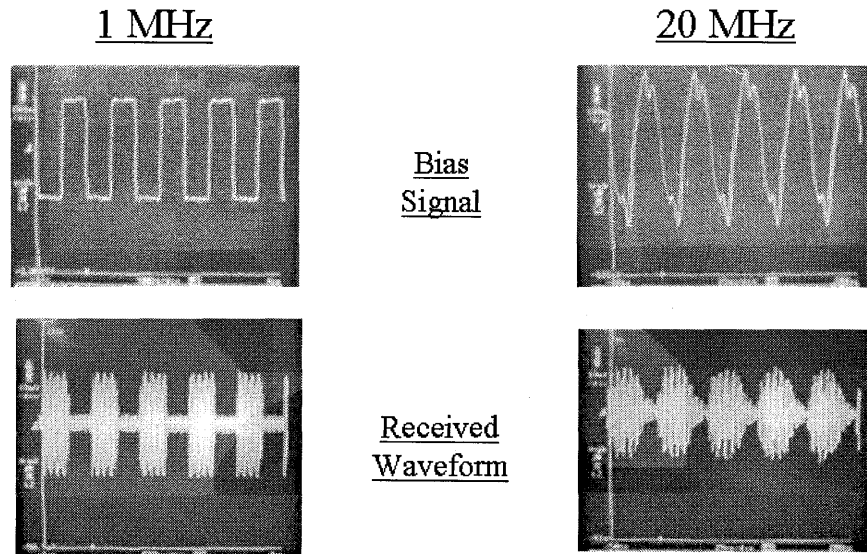


Figure 7. Effects of distorted function generator signal on modulated waveform.

This small distortion was most likely caused by the 20 MHz upper frequency limit of the function generator, as opposed to limitations related to the direct antenna modulation technique. A comparison of the function generator output and the received signal waveform is shown in Figure 7 and clearly supports this theory. With a function generator that can provide a clean 20+ MHz pulse train, the direct antenna modulation technique should produce a clean pulse-modulated carrier waveform for modulating frequencies well above the established narrowband antenna bandwidth.

## 5. Conclusion

The direct antenna modulation technique was successfully demonstrated by this experiment. The 20 MHz upper frequency limit on the available function generator restricted the extent to which the potential increase in system bandwidth could be explored. However, it was promising that the received pulse-modulated carrier waveform still retained a clear pulse shape (albeit the increasingly distorted pulses of the function generator output), even as the modulating signal frequency surpassed the resonant antenna bandwidth of ~16 MHz. Further experiments involving the direct antenna modulation technique are encouraged by these results and will be conducted in the near future. Such experiments will include a full investigation of the bandwidth

increase potential with a higher-frequency function generator and an examination of the bit error rate as the modulation frequency increases. The next step will be to explore ways to computationally model direct antenna modulation, which will allow for a deeper understanding of the underlying mechanisms of this technique and may spur improved methods of its implementation. The long-term goal of direct antenna modulation research is its application to Army communication systems, with a focus on increasing system bandwidth and reducing the visual signature of the Army's mobile ground communication system antennas.

## 6. Acknowledgements

We would like to thank the Army Research Office for their past and continued support of this project under Agreement Number W911NF-04-D-0001, Delivery Order 0003. We would also like to thank Dr. Ethan Wang of UCLA for ongoing constructive discussions about this research.

## 7. References

- [1] C. A. Balanis, *Antenna Theory: Analysis and Design*, 2nd Edition, pp. 760 – 764, John Wiley and Sons, Inc., 1997.
- [2] W. Yao and Y.E. Wang, "An Integrated Antenna for Pulse Modulation and Radiation," *Conf. Rec. 2004 IEEE Radio and Wireless Conference*, pp. 427–429, 2004.
- [3] J.T. Merenda (to Hazeltine Corporation), "Synthesizer Radiating Systems and Methods" US Patent 5,402,133, March 28, 1995.
- [4] T.-P. Hung, A.G. Metzger, P.J. Zampardi, M. Iwamoto, and P.M. Asbeck, "Design of high-efficiency current-mode class-D amplifiers for wireless handsets," *IEEE Trans. Microwave Theory and Techniques*, vol.53, no.1, pp. 144–151, January 2005.
- [5] V.F. Fusco and Q. Chen, "Direct-signal modulation using a silicon microstrip patch antenna," *IEEE Trans. Antennas and Propagation*, vol.47, no.6, pp. 1025–1028, June 1999.
- [6] Joint Tactical Radio System (JTRS) Operational Requirements Document (ORD), Version 3.2 JROC Approved, JROCM 087-03, pp E1–E6, 09 April 2003.
- [7] Ansoft Corporation. (2005, July 14). "Ansoft Corporation – HFSS" [Online], 2005.
- [8] Skyworks Solutions, Inc. "SMP1340 Series: Fast Switching Speed, Low Capacitance Plastic Packaged PIN Diodes Datasheet"[Online], 2005.

# Tri-band Reconfigurable Antenna for Active RFID

Wonbin Hong, Nader Behdad, and Kamal Sarabandi

Department of Electrical Engineering and Computer Science

University of Michigan, Ann Arbor, MI, 48109-2122

{wonbin, behdad, saraband}@umich.edu

## ABSTRACT

A compact multifunctional antenna with electronic tuning capability is designed and measured. Due to its operational frequency and miniaturized dimension, the antenna can be used as an active RFID antenna. Operating at the 400 MHz, 900 MHz, and 2.4 GHz band, the antenna displays a wide operational bandwidth using capacitive loading and fictitious short circuit technique. Resonant frequency of the antennas can be controlled by varying the DC bias voltage of the varactor diode. The antenna consists of three sub level antennas with separate connectors making it feasible for frequency bands to be easily selected through a switching network. The measured tri-band reconfigurable antenna has very low input VSWR, low cross-polarization levels with acceptable efficiency.

## 1. INTRODUCTION

Whether it is recognized or not, radio frequency identification (RFID) has become an essential element in our daily life. Nowadays, and more in the future, as we shop merchandises, get on a highway, or gain entrance to buildings, RFID technology is deeply involved. RFID systems fall into two categories, passive and active, depending on their source of electrical power. Passive RFID tags receive power from the signal of a RFID reader through inductive coupling and therefore are limited to short ranges comparable to the size of the antenna. Active RFID tags contain both the radio transceiver and source of power. These systems use radiative coupling and therefore has higher read range and does not require line-of-sight access. Due to their on-board power source, active RFID tags operate at microwave frequencies – commonly 433 MHz, 915 MHz, and 2.45 GHz. As for most long range wireless communication devices, antennas then become an important component in enabling the active RFID tags to communicate effectively and efficiently. Research and development of antennas for RFID application has been extensively studied by various authors [1]-[3].

However, since RFID technologies are widely used in the ISM band, frequency allocation and interference with other signals become an important issue. In addition, spectral allocation by governments varies from one country to another. This can result in the RFID device being confined to a certain region, which can often be a fatal problem. Also, operating frequencies affect the radiation characteristics of resulting radiated fields. For locating large objects, low frequencies such as 433 MHz are more applicable to avoid obstacle blockage, whereas higher frequencies can be used when a clear line-of-sight is assured. Therefore, a multifunctional antenna capable of operating at all major frequencies used for RFID technology can alleviate and compensate the short comings that a single band antenna will experience. Recently, reconfigurable antennas with

various electronic tuning capabilities have been extensively studied [4]-[6]. Since typical dimensions of antennas for RFID devices operating at 900 MHz range from 10 cm to 30 cm, size reduction of the antenna can enable the RFID system to be more mobile and versatile. A number of studies have shown the dimension of the antenna can be reduced through capacitive loading using PIN diodes or varactors. [7]-[8].

In this paper, a compact multifunctional antenna capable of operating at three separate frequency band is presented. Three sub level antennas are designed on the same ground plane layer and additional techniques are applied to achieve a wide band operation for each frequency band. In what follows, the antenna design process is first described and then the measurement results are presented and discussed.

## 2. ANTENNA DESIGN

For easy control in selecting the frequency band of interest, three different antennas are designed on a  $50 \times 50 \text{ mm}^2$  ground plane. Each antenna is designed to be connected to SMA connectors which can be connected to a switching network. A slot antenna topology is used for both the 400 MHz and 900 MHz frequency band due to its omni-directional behavior, ease of miniaturization, and higher radiation efficiency. To achieve further versatility, the antennas are designed to be reconfigurable using identical varactor diodes. A  $\lambda/4$  slot antenna at first resonance can be considered a transmission line of equivalent length. Loading such structure with capacitors increases the line capacitance and therefore, reduces the resonant frequencies. The line capacitance can be tuned electronically using varactor diodes to achieve reconfigurability. Here, the lumped capacitor is replaced with a MTV4030 varactor diode from MicroMetrics. The varactor's capacitance varies from 1.36 pF to 0.32 pF as the bias voltage increases from 0 V to 30 V. The location of the varactor is determined by a series of full wave simulation based on method of moments [9] to achieve a linear tuning ability throughout the band of interest. Then, the location of the varactor is slightly adjusted so that maximum frequency tuning range can be achieved with relatively low voltage levels. This enables the antenna to be ultimately powered by small, light-weighted batteries, and therefore increasing its portability and mobility. The schematic of the proposed Tri-band antenna is shown in Figure 1. The 400 MHz and the 900 MHz antenna are located in the lower and mid portion of the figure respectively. The antennas are fed with open-stub microstrip lines with an impedance of  $50 \Omega$ . Matching is achieved by adjusting the location ( $L_s$ ) of the microstrip feed and the length of the open-circuit stub ( $L_m$ ) to compensate the reactance of the feed. Low-pass filters are implemented on the DC feed networks for both antennas to achieve RF-DC isolation. Two separate DC feed networks are designed for each reconfigurable antenna.

Due to its relatively high operating frequency and therefore, less need for miniaturization, a notch antenna is used for the 2.4 GHz frequency band, as shown in the upper portion of Figure 1. The antenna is matched to a line impedance of  $50 \Omega$  by choosing the appropriate location ( $L_s$ ) and the length of the stub ( $L_m$ ). The location of the microstrip feed introduces two resonance behaviors. The first resonance is the normal resonance which is inversely proportional to the length of the antenna. The second resonance occurs when the electric field along the slot is manipulated by the microstrip

feed from the edge of the slot antenna. Basically, the electric field of the slot excited by the return current on the ground plane of the microstrip line is canceled out by the tangential component of the electric field created by the microstrip line, introducing a fictitious short circuit with a resonant frequency slight higher than the first resonance. Therefore, by adjusting the location of the microstrip feed, a dual-band or wideband behavior can be achieved. In this case,  $L_m$  is optimized for wideband operation. The slot antenna is then transformed into a notch antenna, which resembles a quarter wave slot antenna. The final topology of the notch antenna is obtained by removing the excess ground plane around the antenna as shown in Figure 2.

### 3. RESULTS AND DISCUSSION

The tri-band antenna is simulated using IE3D and fabricated on a 0.5 mm thick RO4003 substrate from Rogers Corp with a dielectric constant of 3.4. The input reflection coefficients  $S_{11}$  are measured for the reconfigurable antennas and the notch antenna and the results are shown in Figure 3, 4 and 5 respectively. For the reconfigurable antennas, it can be seen from their respective figures that the antennas are well matched throughout the frequency of interest, displaying a tuning range of more than 40 MHz and 140 MHz, respectively. The DC voltage ranges remains relatively small with the maximum range being less than 4 V. Although the DC-RF isolation is measured to be less than 20 dB for both reconfigurable antennas, when the DC voltage exceeds 4 V, the resonant frequency begins to saturate and ultimately displays very limited change. The 2.4 GHz notch antenna is also well matched, displaying more than 8% 2:1 VSWR bandwidth from 2.4 GHz to 2.6 GHz.

The far field radiation patterns were measured in the anechoic chamber at the University of Michigan. A log periodic antenna was used as the reference antenna for the reconfigurable antennas whereas a double ridged horn antenna was used as the reference antenna for the notch antenna operating at the higher frequency band. The co- and cross polarized E and H planes of the different types of antennas are presented in Figure 6, 7 and 8. The reconfigurable antennas display a similar radiation pattern as the bias voltage is changed. The cross polarization levels are relatively small for both frequency bands. Cross polarizations are mostly caused by the close proximity of SMA connectors and cables to the antenna. When the ground plane is small compared to the wavelength, the radiated field is capable of inducing currents on the feeding cables and re-radiating. In addition, the contribution of the anechoic chamber gives rise to cross polarizations at the low 400 MHz band. It can be noted that nulls are observed in the E-plane radiation pattern in Figure 6, which is unusual for electrically small antennas. This is due to the close proximity of the connectors to the edge of the quarter wave slot antenna. The open circuit boundary at the edge of the slot antenna results in maximum voltage, inducing the currents on the connectors and cable and ultimately distorting the far field radiation pattern. Rearranging the antennas and the connector feeds can significantly reduce the induction and improve the radiation pattern results.

**TABLE I**  
MEASURED GAIN VALUES OF THE RECONFIGURABLE ANTENNAS

Frequency	DC voltage	Gain	Frequency	DC voltage	Gain
415 MHz	0 V	-2.72 dBi	800.5 MHz	0 V	-0.23 dBi
425 MHz	0.6 V	-2.73 dBi	865 MHz	0.6 V	-0.43 dBi
445 MHz	1.8 V	-2.43 dBi	895 MHz	1.8 V	-0.75 dBi
460 MHz	3.3 V	-2.54 dBi	930 MHz	3.0 V	-0.33 dBi

The gains of the antennas are also measured and presented in Table I. and Table II. The relatively lower gains of the reconfigurable antenna are a result of the small electrical dimensions of the antenna at this band. Another major factor that contributes to the reduced gain of the antenna is the additional size reduction that occurs as a result of capacitive loading. The finite ground plane size compared to the wavelength results in significant back radiation. Finally, strong edge currents on the boundary of small ground planes cause an ohmic loss which also decreases the gain of the antenna. Nevertheless, the gain can be improved by increasing the ground plane size.

**TABLE II**  
MEASURED GAIN VALUES OF THE NOTCH ANTENNA

	2.45 GHz	2.51 GHz	2.58 GHz
Gain (dBi)	0.73 dBi	0.87 dBi	0.81 dBi

#### 4. CONCLUSIONS

An antenna operating at three bands of frequency is built and presented. The antenna is based on two different topologies, both designed to achieve maximum bandwidth and tunability at the corresponding frequencies. Due to the nature of the frequencies of operation, the antenna is capable of being used as an active RFID tag. The antenna topology also enables feasible frequency selection through a switching network and reconfiguring ability through digital interface. It is found that radiation patterns remain similar for each different frequency with relatively low cross polarization levels.

#### 5. REFERENCES

- [1] S.K. Padhi, N.C. Karmakar, C.L. Law, and S. Aditya, "A dual polarized aperture coupled circular patch antenna using a C-shaped coupling slot" *IEEE Transactions on Antennas and Propagation*, Vol 51, 2003 pp. 3295-3298.
- [2] S.S.Basat, K. Lim, J. Laskar, and M.M. Tentzeris, "Design and modeling of embedded 13.56 MHz RFID antennas", in *Proc. IEEE Antennas and Propagation Society Int. Symp.*, vol. 4, Jul. 2005, pp. 64-67.
- [3] R.L. Li, G. DeJean, M.M Tentzeris, and J. Laskar, "Integrable miniaturized folded antennas for RFID applications", in *Proc. IEEE Antennas and Propagation Society Int. Symp.*, vol. 2, June 2004, pp. 1431-1432.



- [4] N. Behdad and K. Sarabandi, "Dual-band reconfigurable antenna with a very wide tunability range", *IEEE Transactions on Antennas and Propagation*, Vol. 54, 2006 pp. 409-416.
- [5] S. Nikolaou, R. Bairavasubramanian, C. Lugo. Jr., I. Carrasquilli, D.C. Thompson, G.E. Ponchack, J. Papapolymerou, and M.M. Tentzeris, "Pattern and frequency reconfigurable annular slot antenna using PIN diodes" *IEEE Transactions on Antennas and Propagation*, Vol 54, 2006 pp. 439-448.
- [6] M.K. Fries, M. Grani, and R. Vahldieck, "A reconfigurable slot antenna with switchable polarization", *IEEE Microwave and Wireless Components Letters*, vol. 13, no.11, Nov. 2003 pp. 490-492.
- [7] D. Peroulis, K. Sarabandi and L.P.B. Katehi, "Design of reconfigurable slot antennas", *IEEE Transactions on Antennas and Propagation*, Vol. 53, 2005 pp. 645-654.
- [8] N. Behdad and K. Sarabandi, "A varactor-tuned dual-band slot antenna", *IEEE Transactions on Antennas and Propagation*, Vol. 54, 2006 pp. 401-408.
- [9] IE3D *Electromagnetic Simulation and Optimization Software*, Zeland Software, Inc.

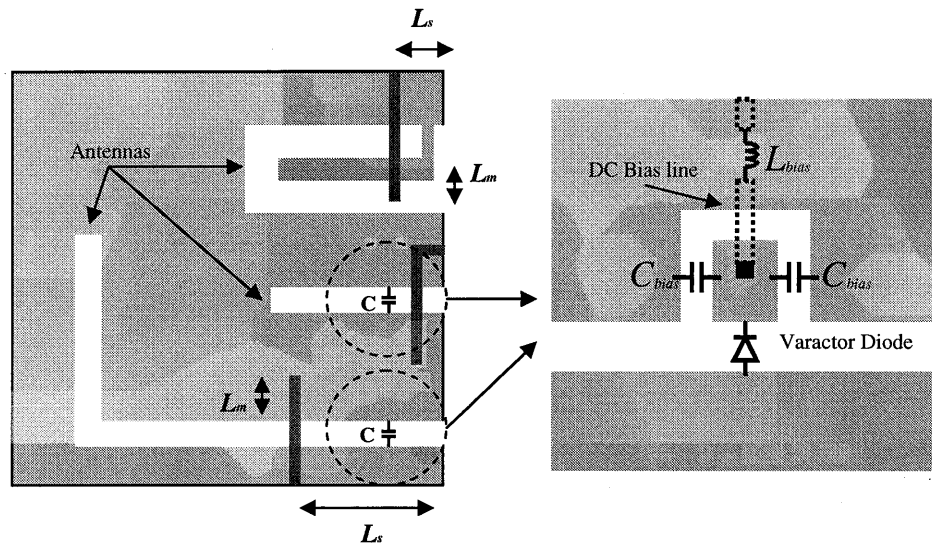


Figure 1: Topology of the Tri-band antenna (Left) and the biasing network (Right).

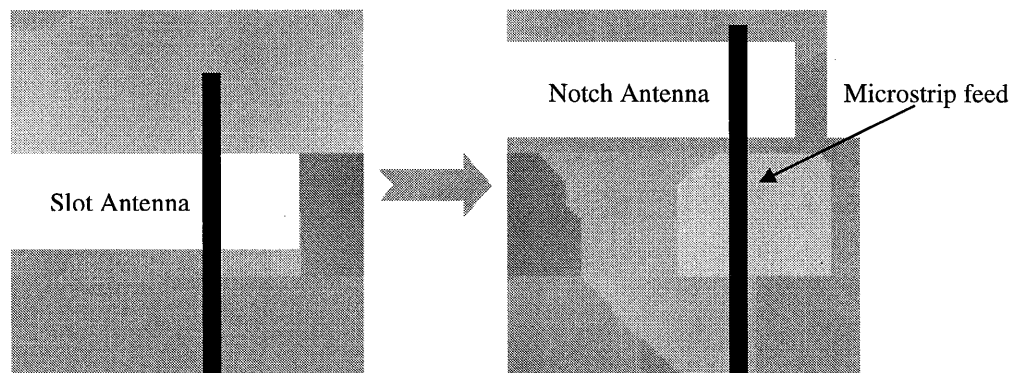


Figure 2: Transformation of a quarter wave slot antenna to the proposed antenna.

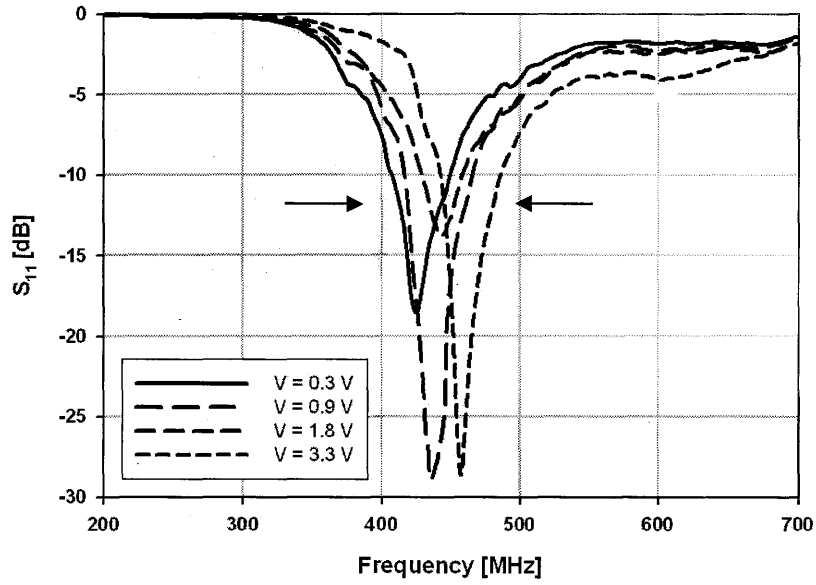


Figure 3: Measured  $S_{11}$  of the reconfigurable antenna at 400 MHz band.

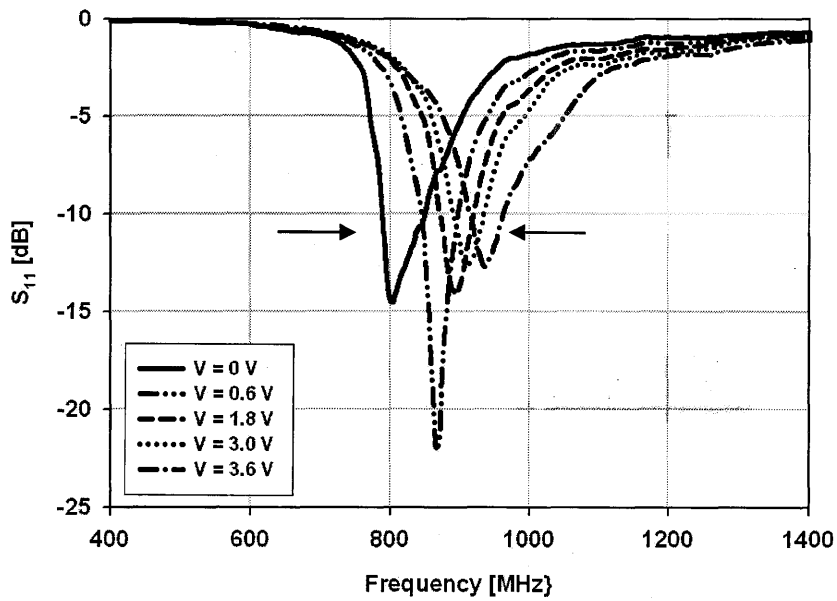


Figure 4: Measured  $S_{11}$  of the reconfigurable antenna at 900 MHz band.

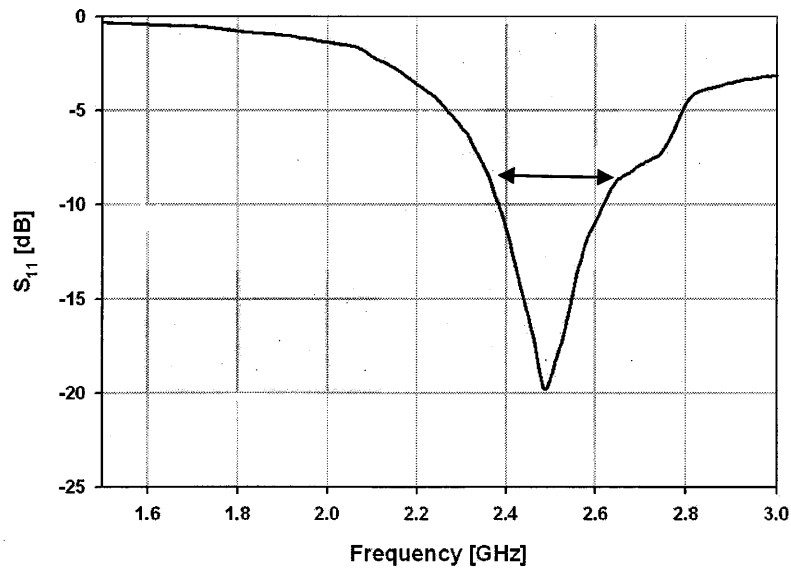


Figure 5: Measured  $S_{11}$  of the notch antenna operating at the 2.4GHz band.

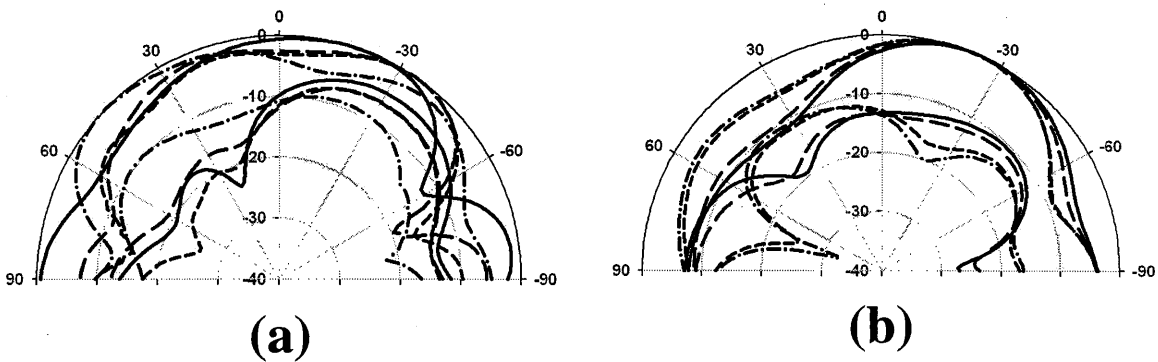


Figure 6: Far field CO-POL and X-POL radiation patterns of the reconfigurable slot antenna at 400 MHz band (a) E-plane and (b) H-plane. Solid line:  $V_{dc} = 0$  V, Long dash:  $V_{dc} = 0.9$  V, Short dash:  $V_{dc} = 1.8$  V, Dash-dot:  $V_{dc} = 3.3$  V

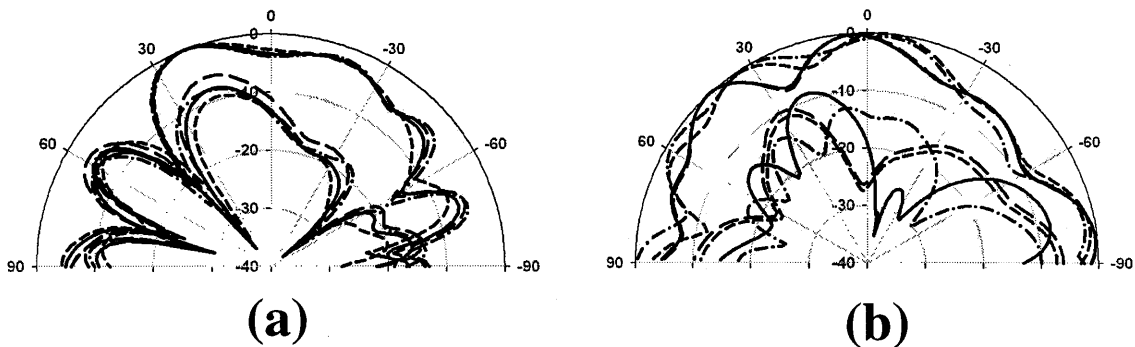


Figure 7: Far field CO-POL and X-POL radiation patterns of the reconfigurable slot antenna at 900 MHz band (a) E-plane and (b) H-plane. Solid line:  $V_{dc} = 0$  V, Long dash:  $V_{dc} = 0.6$  V, Short dash:  $V_{dc} = 1.8$  V, Dash-dot:  $V_{dc} = 3.6$  V

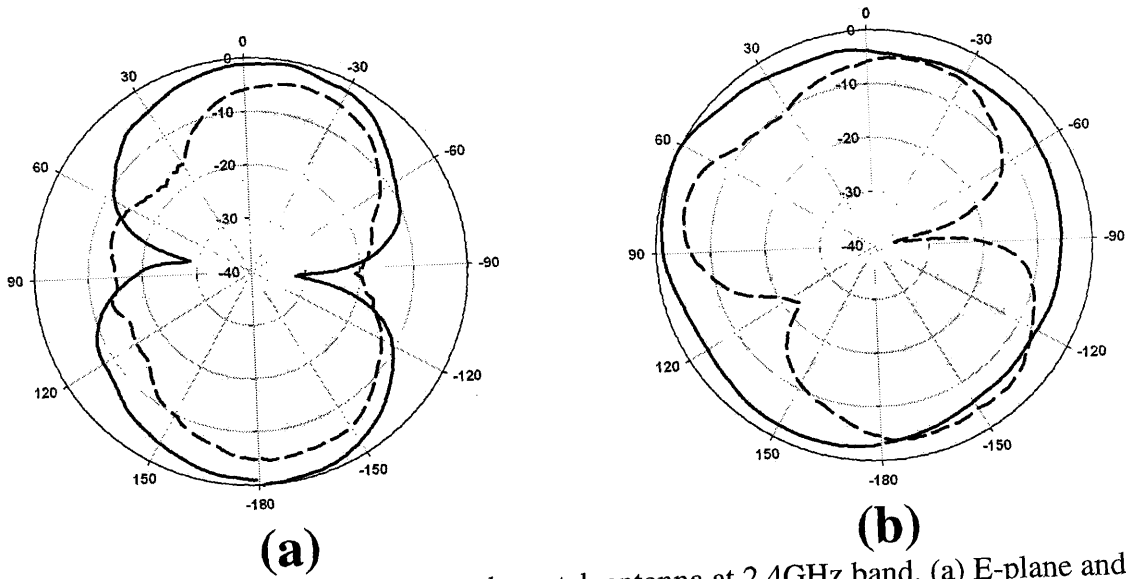


Figure 8: Far field radiation patterns the notch antenna at 2.4GHz band. (a) E-plane and (b) H-plane (dotted line – X-POL, solid line-CO-POL )

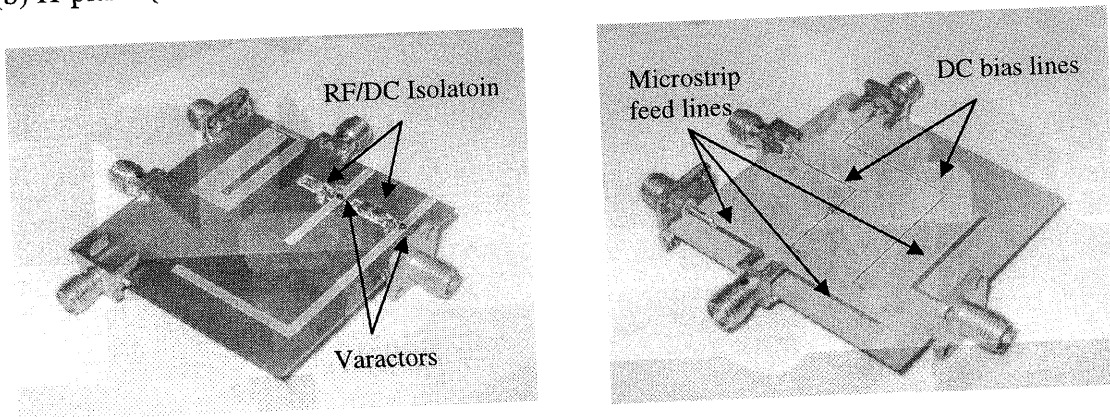


Figure 9: Photograph of the top view (Left) and bottom view (Right) of the fabricated Tri-band antenna.

# A WIDE BAND, LOW PROFILE ARRAY OF END LOADED DIPOLES WITH DIELECTRIC SLAB COMPENSATION

**Ben A. Munk**  
*ElectroScience Laboratory*  
*Ohio State University*  
*1320 Kinnear Rd.*  
*Columbus, Ohio USA*  
*Email: munk.2@osu.edu*

## ABSTRACT

This paper considers an array of dipoles mounted in front of an electric groundplane. To avoid onset of grating lobes, the interelement spacings are kept to less than  $\lambda/2$  at the highest frequency. Thus, the length of the dipoles is considerably shorter than normal which necessitates the use of capacitors between adjacent dipole tips. Adjustment of these end capacitors allows us to manipulate the dipole array impedance. When we add the groundplane impedance it can be designed to partly compensate for the frequency variation of the array impedance and thereby increase the bandwidth. Placing a dielectric slab of proper thickness and dielectric constant in front of the dipole elements provides further improvement. In addition to increasing the bandwidth we can also reduce the variation of the impedance with scan angle in the E- as well as the H- plane.

## 1. INTRODUCTION

In Figure 1 we show a picture of an array of dipoles placed in front of a ground-plane (not shown). By using two orthogonal sets of dipoles we are able to obtain arbitrary polarization. To avoid onset of grating lobes the interelement spacings  $D_x = D_z < \lambda/2$  at the highest frequency. Thus, the lengths of the dipoles are shorter than normal which often is expected to lead to poor impedance properties. However, two factors enable us to overcome this dilemma, namely capacitive end-loading of the individual elements and a very strong mutual coupling that dominates the self-impedance. The capacitors shown in Figure 1 are of the interdigital type but lumped elements can be used just as well.

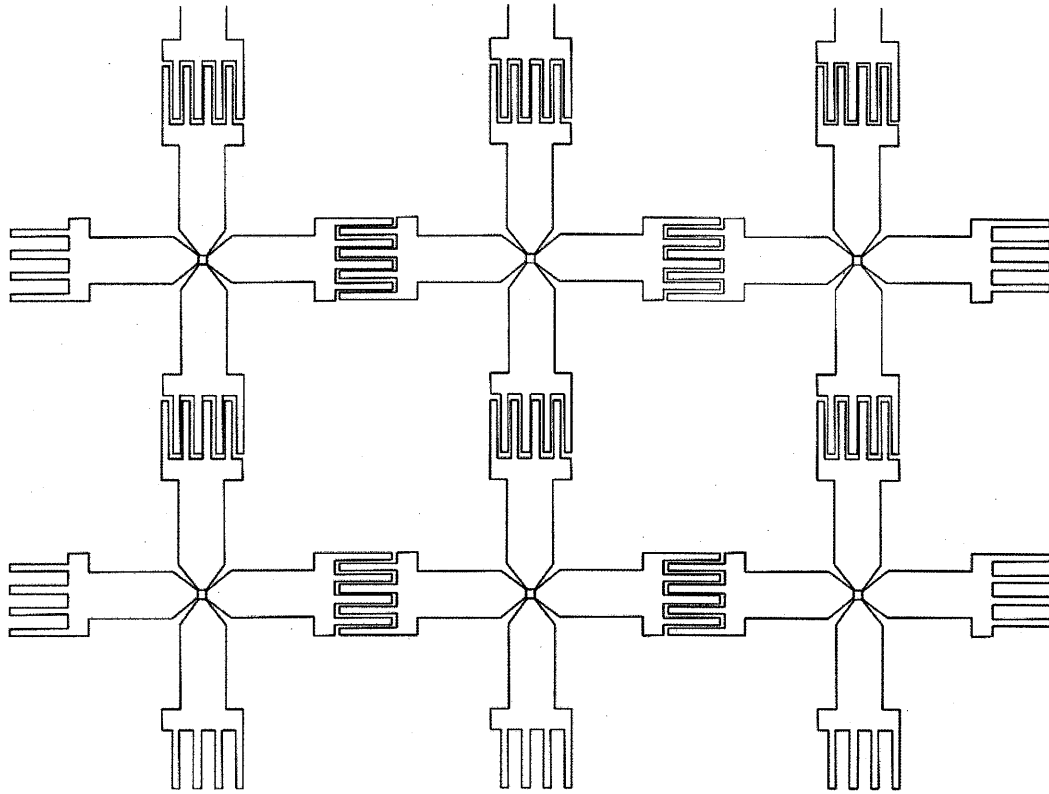


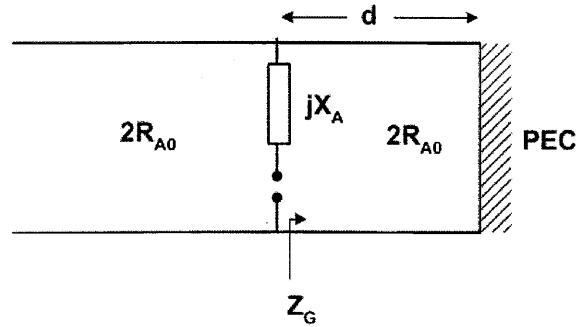
**Figure 1. Two orthogonal arrays of capacitively end-loaded dipoles. The ground plane is not shown.**

## 2. EQUIVALENT CIRCUIT

The key to understanding the workings of this array is the equivalent circuit given in Figure 2 left [1,2]. To the far right we observe a short circuit representing the perfectly conducting groundplane at a distance,  $d$ , behind the array elements with the input terminals. We denote the impedance as seen from here toward the ground plane by  $Z_G$  (groundplane impedance). It will be purely imaginary and thus be located on the rim of the Smith chart spanning from the low frequency  $f_L$  to the high  $f_H$  as shown in Figure 2, right. Also shown is the imaginary part,  $jX_A$ , of the antenna impedance without the groundplane. Finally, the real part of the array impedance without groundplane is denoted  $2R_{A0}$ . It is given as the input impedance of an infinitely long transmission line with characteristic impedance  $2R_{A0}$  and is located at the center of the Smith chart. For details see [1].

We first connect the impedances  $2R_{A0}$  and  $Z_G$  in parallel and obtain the curve denoted  $2R_{A0} \parallel Z_G$  as shown in Figure 2, right. We finally add to this the impedance  $jX_A$  in series

### Equivalent Circuit — Typical Wire Array



and obtain the curve denoted  $2R_{A0} \parallel Z_G + jX_A$ . We observe that this curve when properly normalized has potential for large bandwidth in spite of the fact that the groundplane impedance  $Z_G$  has a considerable span on the rim of the Smith chart.

### Impedance Smith Chart — Typical Wire Array

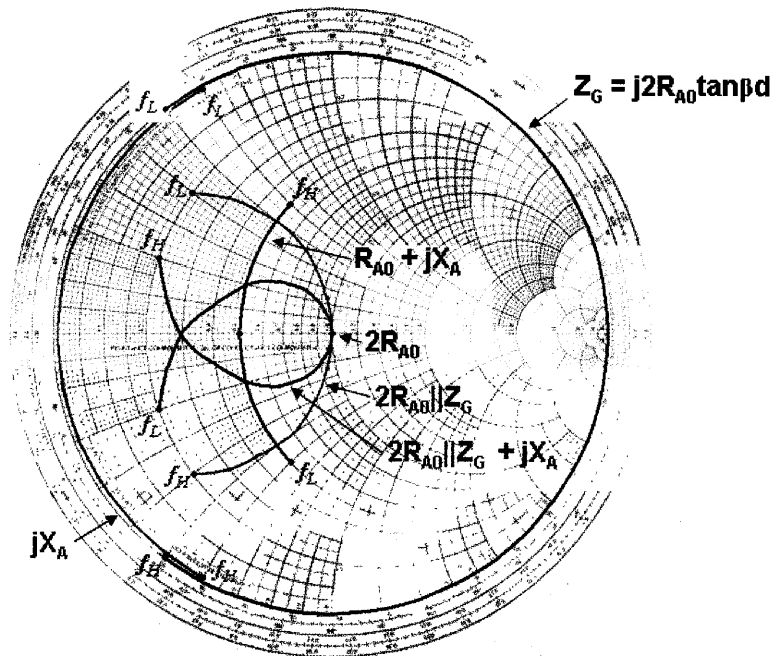


Figure 2. Equivalent circuit and Smith chart of a typical wire array.

We emphasize that the equivalent circuit only serves the purpose of guiding us in the development of our design concepts. The actual calculations shown next are obtained from the computer program PMM.

### 3. THE EFFECT OF THE END CAPACITORS

In Figure 3 we show the array impedances without groundplane for three different values of the end capacitors  $C$ . First at the top we show the case for  $C = \infty$ , i.e. just infinitely long wires fed periodically as shown in the schematic to the left, top. Next at the bottom we show the cases  $C = 0.20$  pF and  $C = 0.05$  pF to the left and right, respectively. We observe that as we reduce  $C$  the impedance curve is rotated counter clockwise in the Smith chart. This enables us for example for  $C = 0.05$  pF to obtain an impedance curve that from  $\sim 6$  to  $\sim 14$  GHz runs in the opposite direction of the groundplane impedance  $Z_G$  also shown on the rim of the Smith chart in Figure 3. Playing these two components out against each other is precisely what enable us to increase the bandwidth as illustrated in Figure 4. We further show in Figure 5 the same case ( $C = 0.05$ pF) for scan angles  $0^\circ$ ,  $30^\circ$  and  $60^\circ$  in the H-planes.



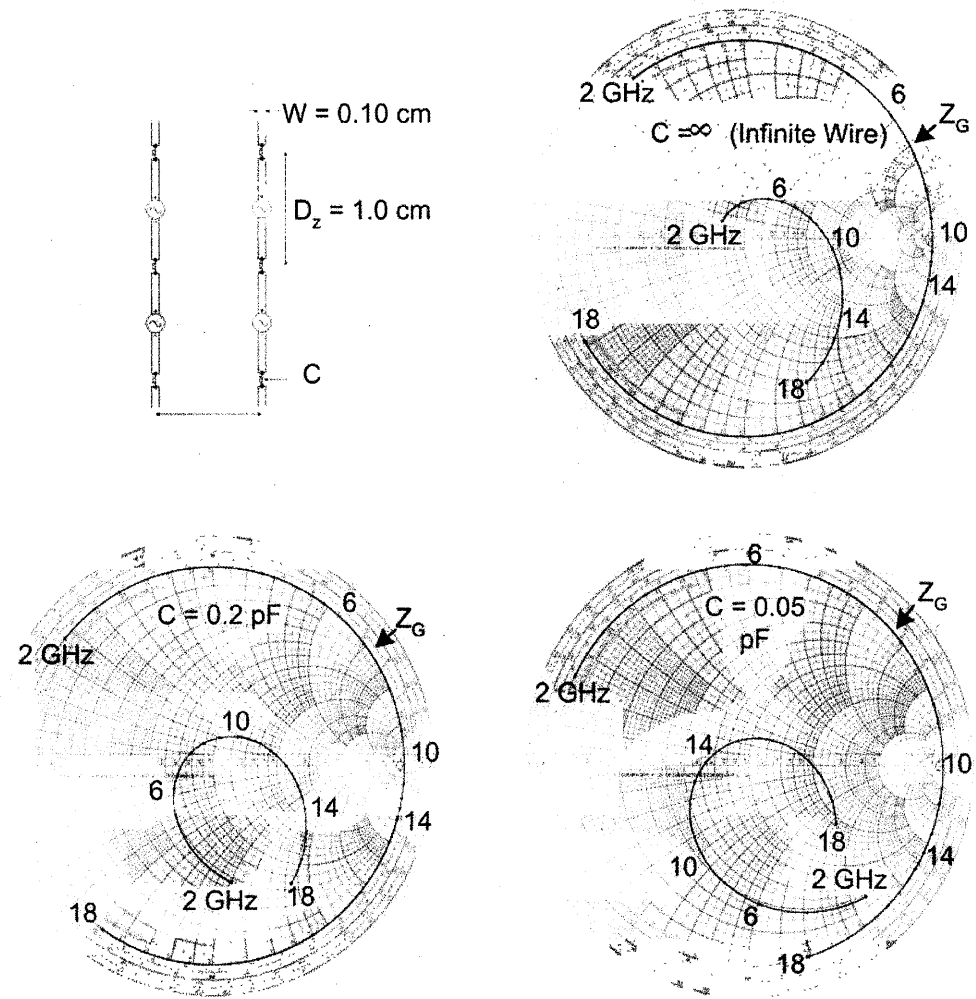


**Figure 3. Schematic and impedance Smith charts of wire dipole array with no groundplane and three values of capacitive end-loading.  $0^\circ$  scan angle. Normalized to  $Z_0 = 250 \Omega$ .**

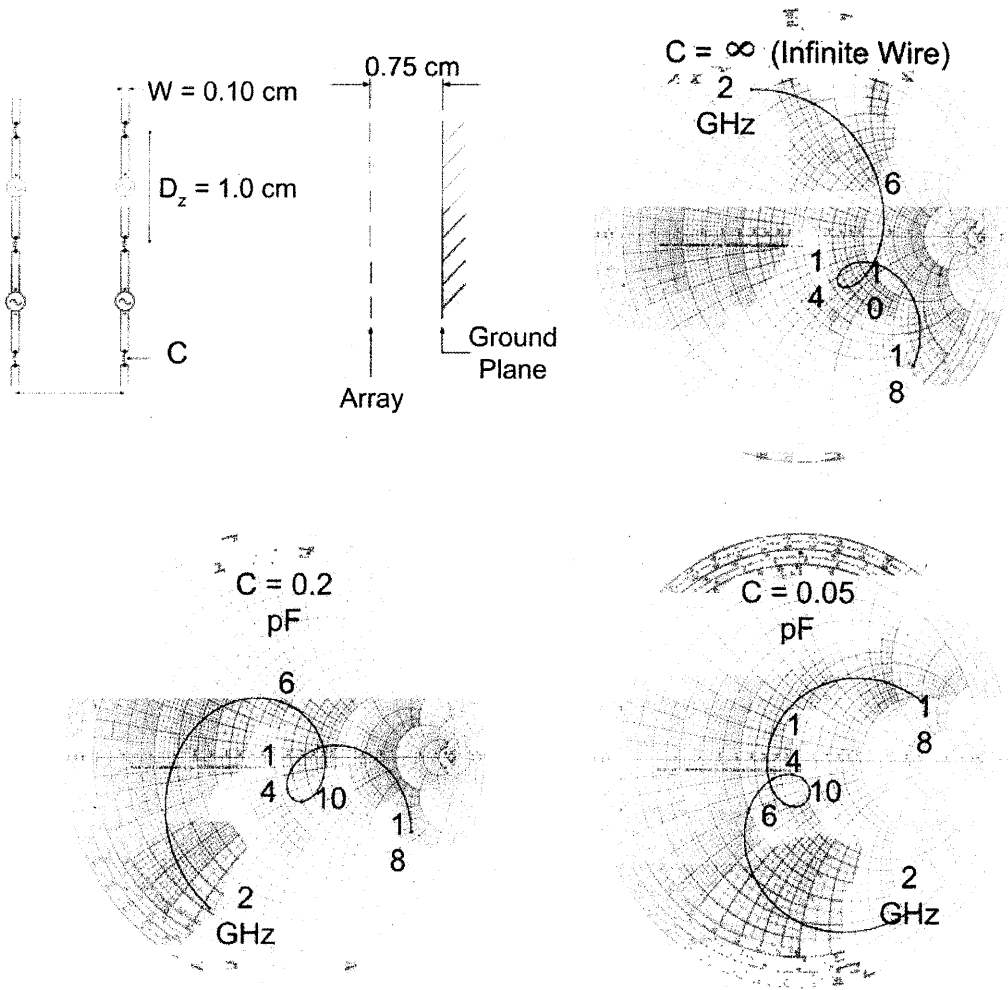


**Figure 4. Schematic and impedance Smith charts of wire dipole array with groundplane ant three values of capacitive end-loading.  $0^\circ$  scan angle.  $Z_0 = 250\ \Omega$ .**

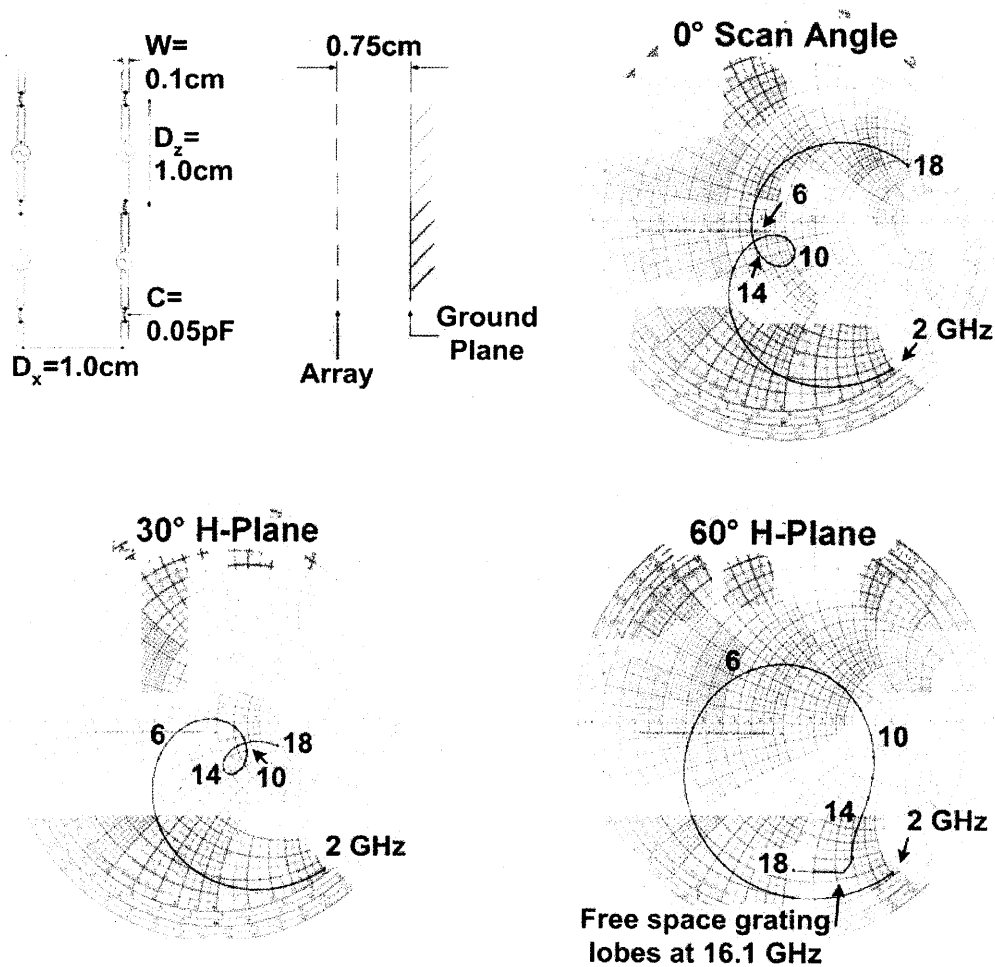


Figure 5. Schematic and impedance Smith charts of wire dipole array with groundplane and 0.05 pF capacitance at 0°, 30° and 60° scan angles in the H-plane.

#### 4. EFFECT OF THIN DIELECTRIC SLABS ADJACENT TO THE ARRAY (“UNDERWEAR”)

We demonstrated above how the capacitive end loading can rotate the impedance curve as illustrated in Figures 3 and 4. A further adjustment can be obtained by placing thin dielectric slab(s) adjacent to the array as illustrated in Figure 6 for the case  $C = 0.05$  pF. It should be compared with the case in Figure 5 when the scan angles are also 0°, 30° and 60° in the H-plane. This effect is quite different from placing thick dielectric slabs in

front of the array as discussed next, where a transforming action takes place in addition to a rotating observed for “underwear”.

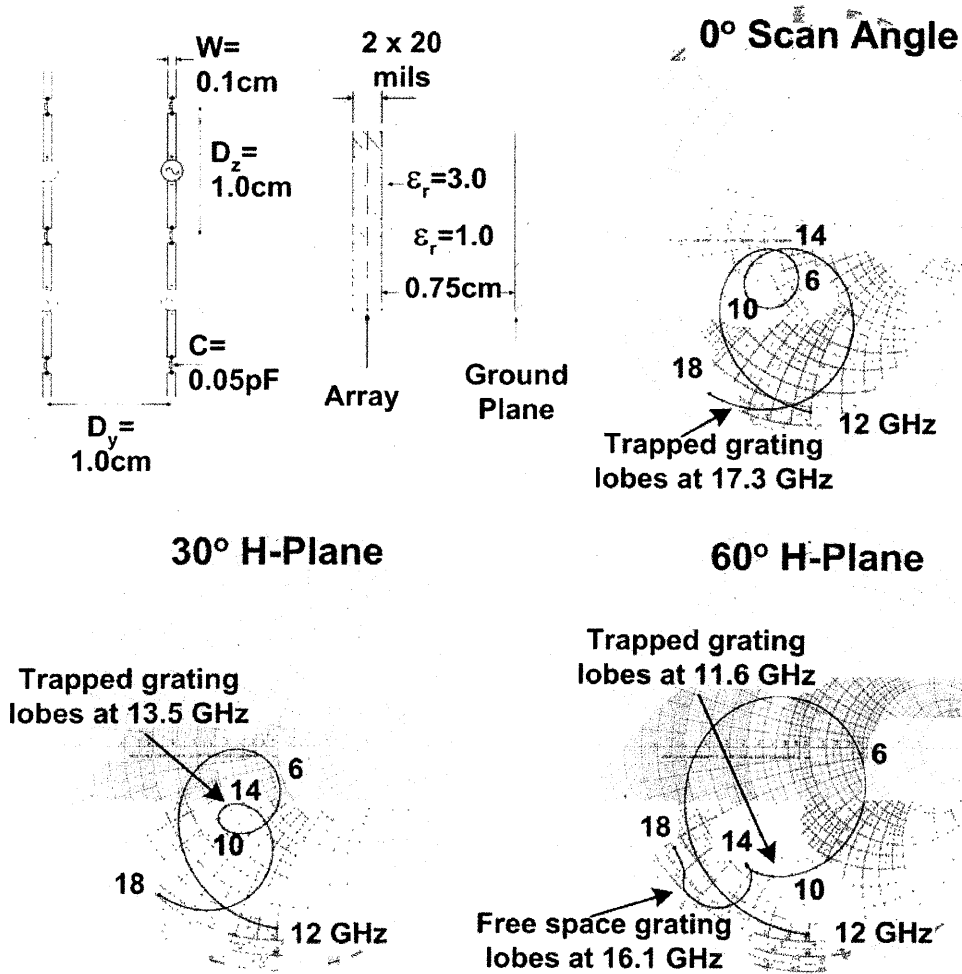


Figure 6. Schematic and impedance Smith charts of wire dipole array with adjacent dielectric slabs and a groundplane.  $C = 0.05\text{ pF}$ .  $0^\circ$ ,  $30^\circ$  and  $60^\circ$  scan angles in the H-plane.

## 5. EFFECT OF THE DIELECTRIC SLABS IN FRONT

The purpose of the dielectric slab in front of the dipoles is to act as a transformer in such a way that the bandwidth is increased and also to make the array impedance more

independent of scan angle. The equivalent circuit is shown in the insert of Figure 7, where we have used a rectangular coordinate system instead of the Smith chart.

More specifically, we start with the antenna resistance  $2R_{A0}$  given as the input impedance of an infinitely long transmission line going to the left in the insert and marked by  $2R_{A0}$  to the far right in Figure 7. We now transform this impedance through a dielectric slab with characteristic impedance  $2R_{A1}$ , where  $2R_{A1}$  is the radiation resistance of the array if placed in an infinite medium with dielectric constant  $\epsilon_1$ . It is easy to show that  $2R_{A1} < 2R_{A0}$ , i.e. the input impedance  $Z_{1-}$  of the slab looking left will follow a circle going through  $2R_{A0}$  and a point to the left, namely  $0.5 \cdot 2R_{A0}$  in our particular case. At the center frequency  $f_c$ , the slab thickness is typically  $\lambda/4$  (electrically) and  $2R_{A0}$  will at that frequency be transformed into the point marked  $f_c$  on the real axis. Similarly, at a lower frequency the electrical thickness of the slab is less than  $\lambda/4$ , i.e. the input impedance  $Z_{1-}$  will go through only part of the transformation circle, typically as indicated by the point  $Z_{1-}$  in the negative plane of Figure 7. We next add the groundplane impedance  $Z_{1+}$  in parallel with  $Z_{1-}$  similar to what we did earlier without a dielectric slab, i.e. this parallel combination  $Z_{1-} \parallel Z_{1+}$  will be located on a circle going through  $(0,0)$  and  $Z_{1-}$  as indicated in Figure 7 (remember  $Z_{1+}$  is purely imaginary). Finally, we add the impedance  $jX_A$  in series with  $Z_{1-} \parallel Z_{1+}$ . Since we are below the center frequency  $f_c$ ,  $jX_A$  is typically negative, i.e. the final curve gets compacted around the real axis resulting in a larger bandwidth than without the dielectric slab. This is simply because the imaginary part of  $Z_{1-}$  is  $< 0$  at frequencies below  $f_c$  like  $jX_A$  such that they add together and thereby cancel  $Z_{1+}$  more effectively. (The groundplane impedance is always the domineering part).

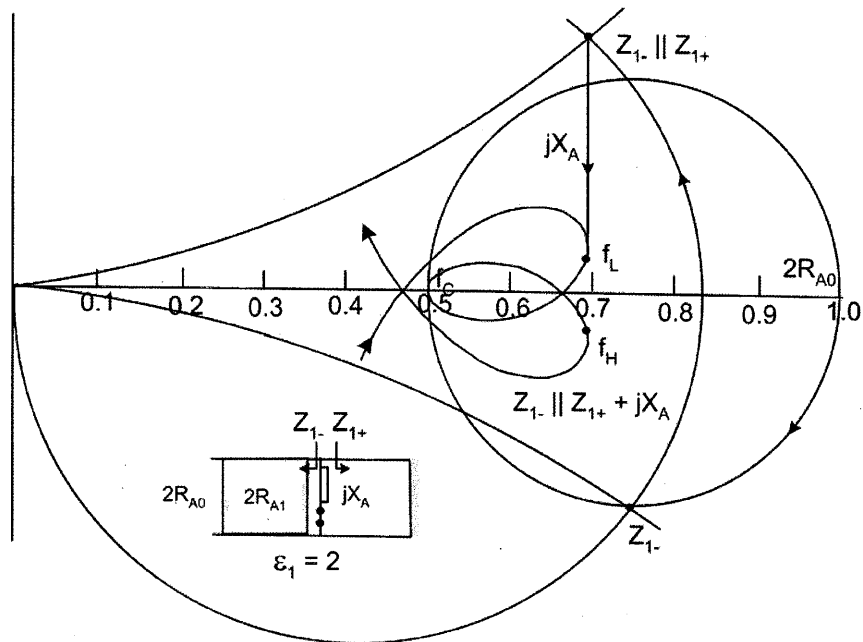


**Figure7. Equivalent circuit (inset) and impedances (in rectangular coordinate system) of dipole array with dielectric slab.**

## 6. THE CALCULATED TOTAL SCAN IMPEDANCE

We emphasize again that the graphical discussion above serves only the purpose of guiding us in the development of our design concepts. Once they are formulated, we use the PMM program to obtain the final results. A typical result is shown in Figure 8 where the schematic gives dimensions and lay out of the array in question. We show two curves: Curve a is the scan impedance obtained directly by the PMM program. Curve b shows a significant improvement by using a small matching section consisting of a transmission line with characteristic impedance  $\sim 200$  ohms and length  $\sim 2.5$  mm. The VSWR  $< \sim 2$  for  $\sim 3$  to  $\sim 19$  GHz.

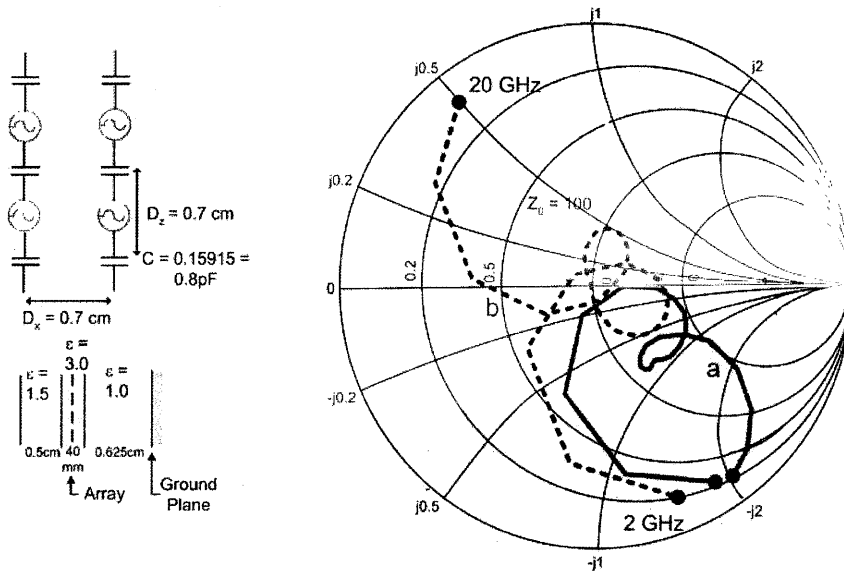


**Figure 8. Calculated terminal impedance at broadside obtained from the PMM code. The dotted curve includes a small matching section.**

It is interesting (and important) to point out that the PMM program originally was primarily developed for calculating FSS's, i.e. the dipoles terminals are Delta gaps with inherent high base capacitance. If, for example, the finite elements approach is used instead, the gap between the dipole terminals will realistically be wider leading to a smaller base capacity. To obtain the same superior matching as shown in Figure 8, it is advisable to add a base capacitance at the dipole terminals, either lumped or otherwise.

We further show in Figure 9 the scan impedances for  $30^\circ$ ,  $45^\circ$  and  $60^\circ$  for the H-plane. The E-plane impedances are shown in Figure 10.

One may finally ask: If one dielectric slab is beneficial, will two or more be better? Thus, in Figure 11 we show a case with two dielectric slabs where some improvement can be observed. Results for scan angle  $30^\circ$ ,  $45^\circ$  and  $60^\circ$  for H-plane is shown in Figure 12.

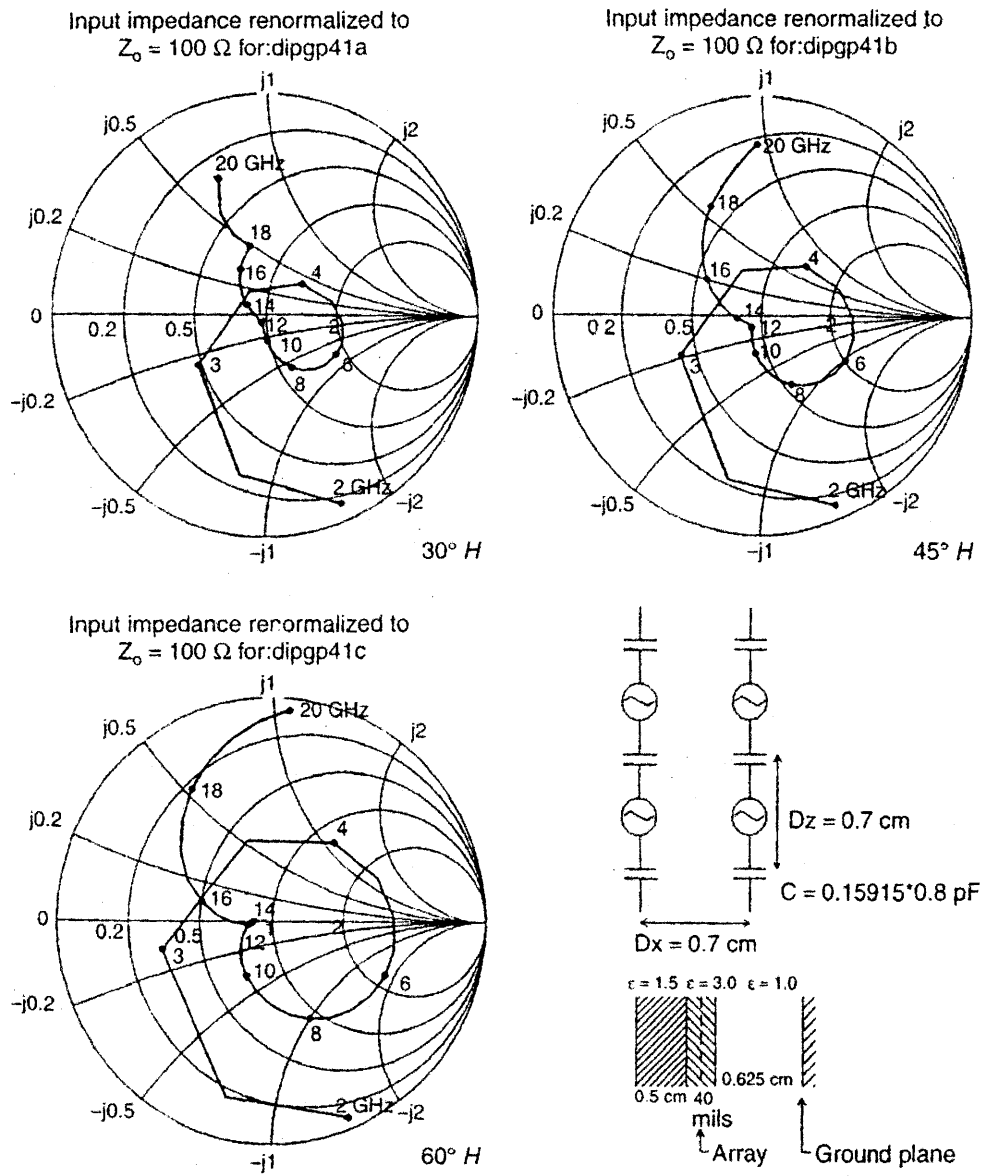


Figure 9. Scan impedances for  $30^\circ$  (top left),  $45^\circ$  (top right) and  $60^\circ$  (bottom left) of dipole array with groundplane (schematic, bottom right). H-plane.



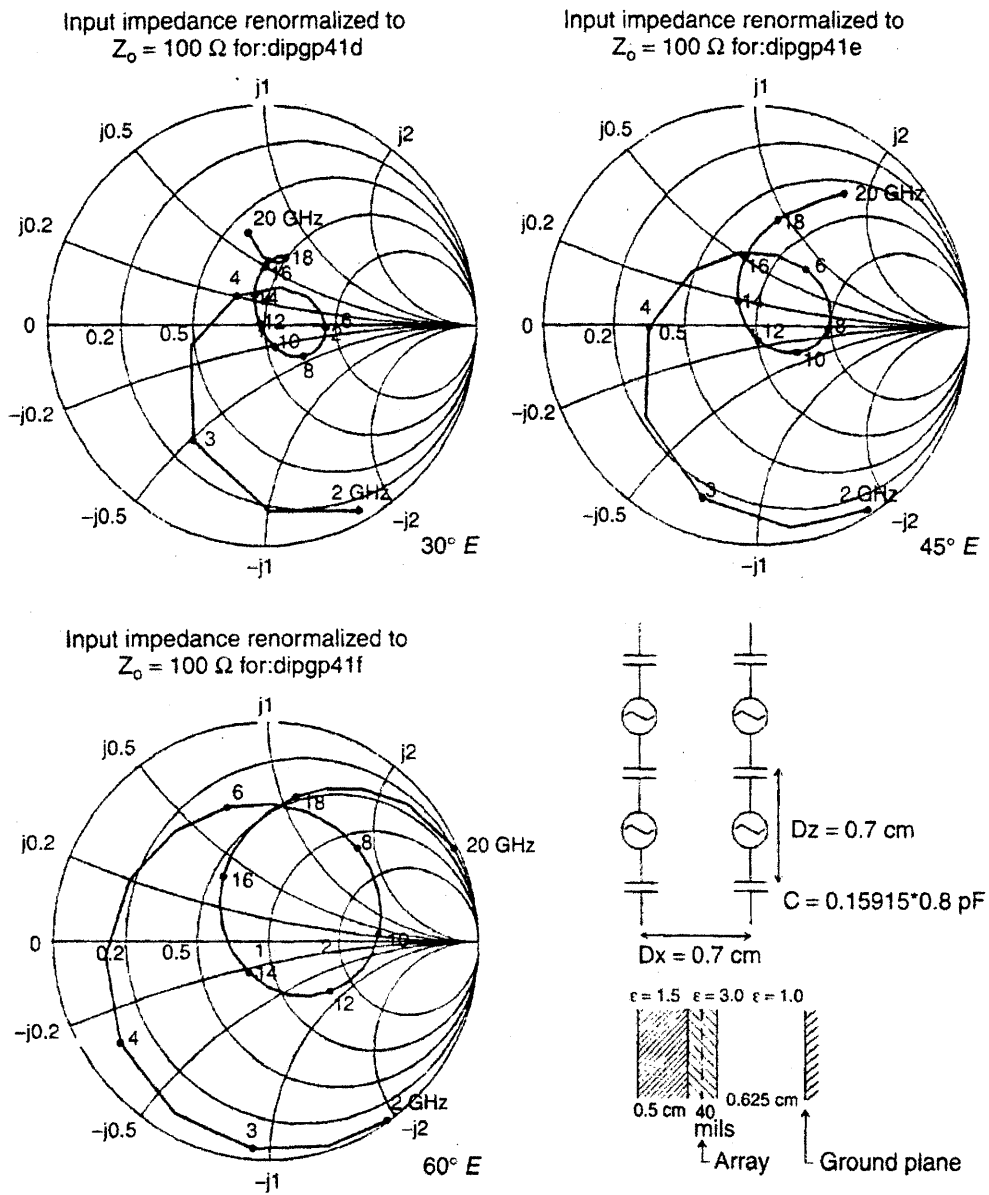


Figure 10. As in Figure 7, except for the E-plane.

Input impedance renormalized to  $Z_0 = 100 \Omega$  for:dipgp68o

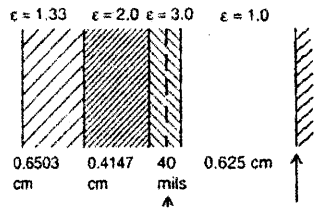
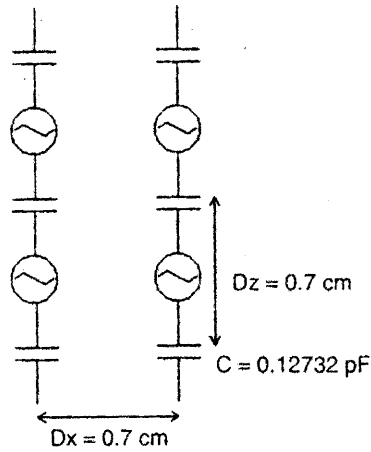
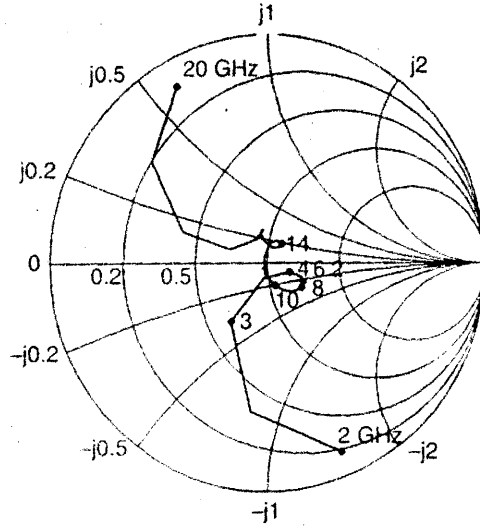


Figure 11. Scan impedance with second dielectric slab included.

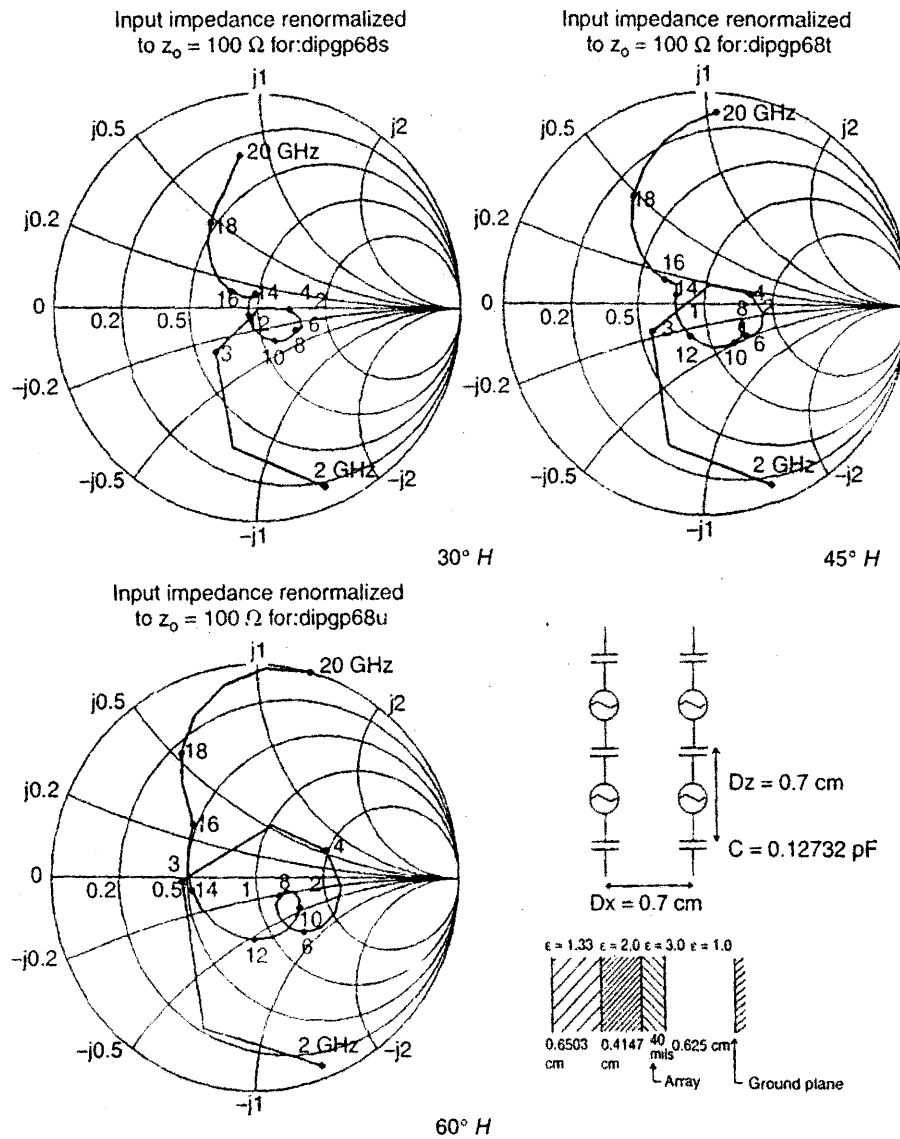


Figure 12. As in Figure 9 but for scan angles of  $30^\circ$ ,  $45^\circ$  and  $60^\circ$  in the H-plane.

For further details see ref [1,2,3].

## Acknowledgements

The contributions from two former students Jonathon Pryor and John McCann are greatly appreciated.

## 7. REFERENCES

- [1] B.A. Munk, *Frequency Selective Surfaces, Theory and Design*, John Wiley: New York, 2000, Chapters 4 and 5.
- [2] B. A. Munk, *Finite Antenna Arrays and FSS*, John Wiley: Hoboken, NJ, 2003, Chapter 6.
- [3] R. C. Hansen, "Non-Foster and connected planar arrays," *Radio Science*, vol. 39, 2004.

## 8. APPENDIX - WHY NOT USE A MAGNETIC GROUNDPLANE?

Magnetic or high impedance groundplanes all start with an electrically perfectly conducting groundplane. At a certain distance smaller than  $\lambda/4$  in front of this groundplane the input impedance is purely inductive. Thus, by placing a parallel capacitor at that distance, we can tune the input impedance to a very high value. This "trick" is well known among antenna engineers and so is the price: smaller bandwidth than if the spacing had been  $\lambda/4$  with no capacitor.

However, the most important reason for not using a magnetic groundplane is a misconception concerning dipoles placed in front of an electric conducting groundplane. It is well known that when the spacing between dipole and groundplane is  $\lambda/4$ , the signal radiated directly and the reflected signal will be in phase. Quite often it is implied that this is where the gain is maximum. This is just not true. In fact, the gain for a single column of dipoles is maximum for small spacing and tapers off until the spacing reaches  $\lambda/2$ . For details see [2]. For a two dimensional array the spacing is even less critical because the total pattern factor is dominated by the array factor. In short, the important point is simply the matching. And that was as shown above handled quite well by simply letting the dipole and groundplane impedances partly cancel each other. This approach would simply not have been as broad banded if we had used a magnetic groundplane.

I have just seen in a newly published book that magnetic groundplanes have many important applications. Frankly, I cannot think of one (except producing an endless stream of useless papers!). Certainly, if a truly magnetic groundplane was feasible it would be of interest even if its gain enhancement would be smaller than that of a perfectly conducting groundplane; for more details see [2].

Perhaps the most "famous" case showing maximum gain when array elements are slightly out of phase is the endfire array. It is called the "Hansen-Woodyard" Theorem and is illustrated in Figure 13. More details will be given during the presentation.

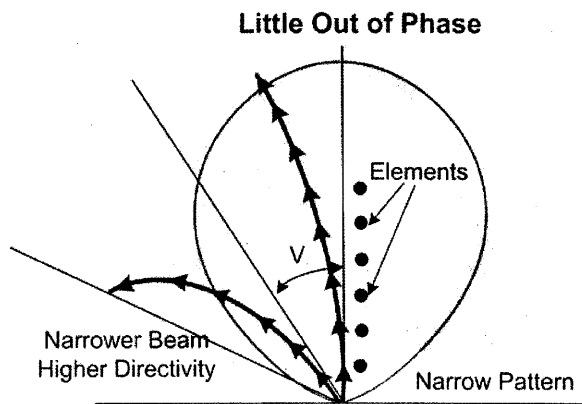
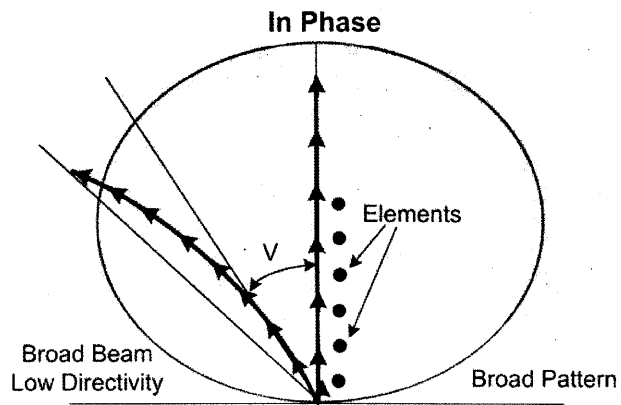


**Figure 13. Illustration explaining the Hansen-Woodyard Theorem.**

# On the Performance Trade-Offs Associated with Modular Element of Single- and Dual-Polarized DmBAVA

M. W. Elsallal<sup>(1,2)</sup> and D. H. Schaubert<sup>(1)</sup>

(1) Center for Advanced Sensor and Communications Antennas  
Department of Electrical and Computer Engineering  
University of Massachusetts, Amherst, MA 01003  
w.elsallal @ieee.org and schaubert @ecs.umass.edu

(2) Advanced Technology Center  
Rockwell Collins, Inc. Cedar Rapids, IA 52489  
waelsall @ rockwellcollins.com

**Abstract:** The Doubly-mirrored Balanced Antipodal Vivaldi Antenna (DmBAVA) appeared last year to be a promising technology to achieve an electrically short ( $\sim \lambda_{\text{Highest-Frequency}}/2$ ), broadband (3:1), and wide scan ( $\pm 45^\circ$ ) phased arrays. Its discovery is significant because it appears to be the only type of notch antenna that can operate over wide bandwidths when fabricated without electrical and mechanical contacts between adjoining elements. This paper discloses several recent results: (1) higher order Floquet mode evidence that grating lobes are not a significant problem in DmBAVA arrays, (2) further developments of single-polarized DmBAVA arrays as being fabricated based on modular element or subarray, and (3) extensions to dual-polarized DmBAVA arrays. As of now, achievable bandwidths are still not as great as obtained with arrays of contacting Vivaldi elements, but the investigations so far show somewhat more than 3.75:1 bandwidth and wide-angle scanning.

## 1. Introduction

In the past decade, Vivaldi antennas have been used for a variety of radar, electronic warfare (EW) and communication applications [1-2]. Many interesting features have been observed in the Vivaldi antennas such as being capable for wideband (10:1) and wide-scan angle phased array systems. However, these features are typically achievable when the radiating elements are fabricated on continuous metal plate structure along their E-plane direction for single polarized arrays, or with metallic posts at the intersections of dual-polarized arrays [3]. Inserting gaps between the elements or reducing their depths to less than two wavelengths at high frequency band's end produces severe impedance anomalies that disrupt the operating band of the array.

The Bunny Ear Antenna has been successfully realized in phased arrays without contiguous electrical contact between adjoining elements, and has shown an appreciable bandwidth in dual polarized arrays [4]. It was, however, necessary to connect film resistors in the gaps between antenna arms and the ground plane to suppress electromagnetic resonances caused by the gap. Installation of these lumped elements hinders future maintenance.

For phased array systems that require electrically small, wideband, and wide-scan angle operation based on modular elements, Doubly-mirrored Balanced Antipodal Vivaldi Antenna (DmBAVA) has been considered [5]. The elements are one-half wavelength long at the high end of the band. In an array, they can be inserted and removed individually, i.e. without electrical and mechanical contacts between adjoining elements, while maintaining a substantial portion of the operating frequency range with no apparent detrimental effects. This is expected to enable a low profile aperture and simplify the array's assembly and maintenance in the field.

When DmBAVA was introduced in last year symposium, there was an unresolved concern that since the effective unit cell size of the array (physical periodicity) has been doubled, a grating lobe could exist and cause undesirable power loss and impedance variation. This paper demonstrates that excitation of higher order Floquet modes is not significant at scan angles of interest. In addition, performance trade-offs associated with variation of air gap width between individual elements and subarrays of the single polarized DmBAVA are also presented. Finally, numerical simulations of dual-polarized (DP) DmBAVA arrays are discussed showing good performance over more than an octave bandwidth and wide scan angles.

## 2. Method of Analysis, and New Design Parameters

A fast and accurate computational electromagnetic code, PBFDTD [6], has been used to simulate infinite and finite arrays of DmBAVA. It computes the active scan impedance and radiation patterns when the elements are excited by a stripline port. The antenna and array's unit cell structure used in the simulations is shown in Figure 1. Most of the design parameters and equations were defined in [5]. In this paper, five new parameters are considered to thoroughly study the performance tradeoffs in DmBAVA as follows:

- Element's width,  $W$ . It helps to study the effect of filling the gap,  $G = (B-H_a)$ , completely with dielectric by extending substrate width beyond the aperture height,  $H_a$ . If  $G$  is partially filled, this creates another parameter equals to  $W_{ag} = (B-W)$ .
- Upper and bottom conductors' width,  $Fw_1$ , of the triline section is made different than that of the embedded conductor,  $Fw_2$ . When  $Fw_1 < Fw_2$ , the impedance match is significantly improved over wide-scan angle, as is depicted in Figure 2.
- Crosswalls height,  $H_{cw}$ , will be varied to study the scan blindness occurs in the E-plane of single polarized arrays.

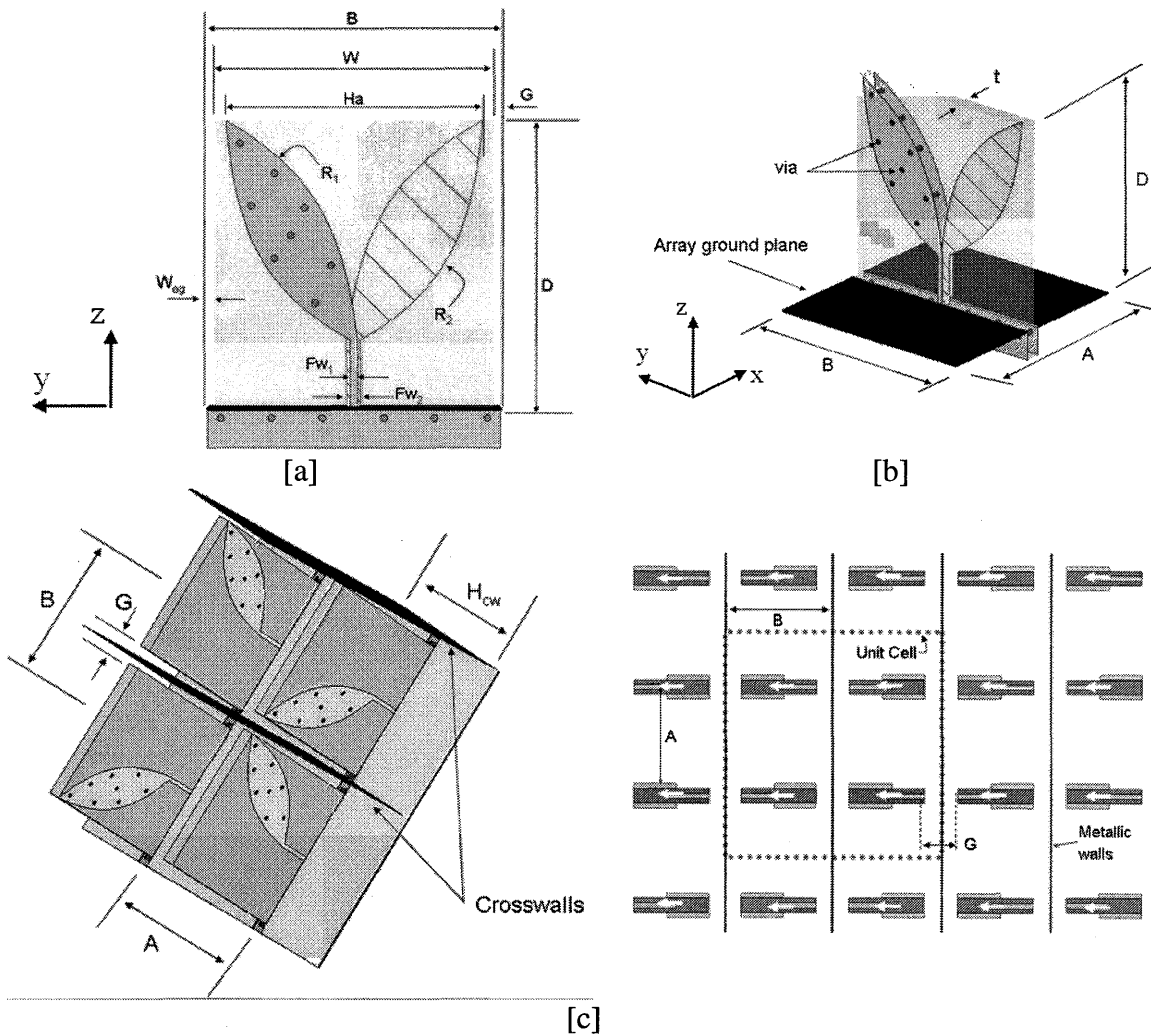


Figure 1: Structure of DmBAVA unit cell in array environments. [a] Front view of a single element of Balanced Antipodal Vivaldi Antenna (BAVA). [b] Isometric view of BAVA. The hatched area is a conductor embedded in the middle of the substrate forming a strip transmission line in the feed region. The solid and slightly shaded shapes are identical conductors forming the ground plane of the stripline on the upper and lower surfaces of the substrate. [c] DmBAVA array's unit cell, where only the outer conductors are shown.



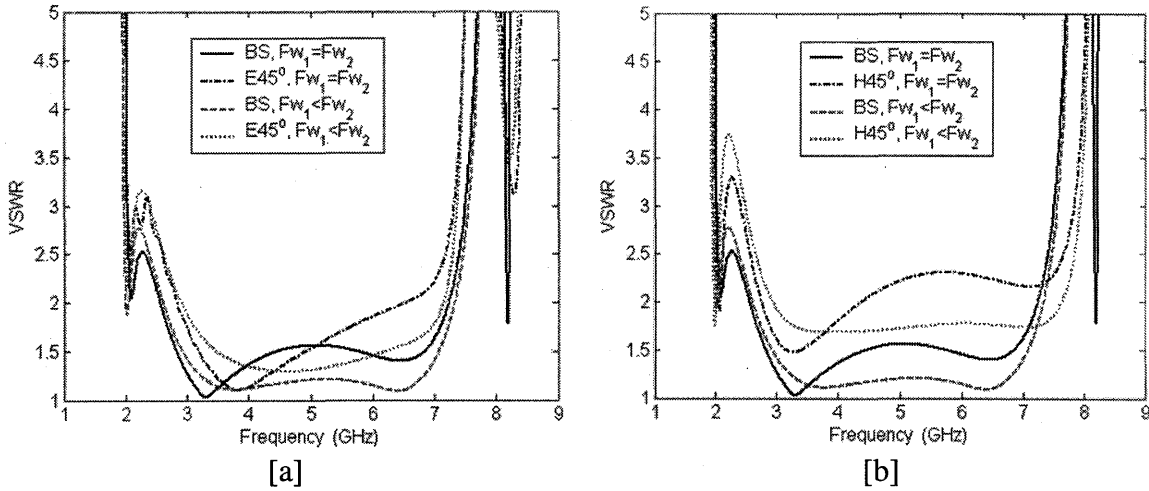


Figure 2: Improvement in the DmBAVA scan impedance when  $Fw_1 < Fw_2$ . [a] E-plane VSWR. [b] H-plane VSWR.  $D=2.17\text{cm}$ ,  $A=B=2.00\text{cm}$ ,  $H_a=1.80\text{cm}$ ,  $\epsilon_r=2.2$ ,  $\tan\delta=0.009$ ,  $t=60\text{mils}$ ,  $Fw_2=0.13\text{cm}$ ,  $Fw_1=0.10\text{cm}$  and  $W_{ag}=G=80\text{mils}$ .

### 3. Broadband Results for Infinite and Finite Arrays

The preliminary numerical studies in [5] of the (2.51:1) and (3:1) infinite DmBAVA arrays did not reveal any undesirable behavior in principal-plane scanning, i.e. E-plane ( $\phi=0^\circ, \theta$ ) and H-plane ( $\phi=90^\circ, \theta$ ). Three new numerical examinations of the (2.51:1) array performance are discussed in this section as follows:

#### a. Active Input Impedance at $\Phi = 45^\circ$

For an array with center-to-center spacing of the elements maintained at 1.51cm, its active input impedance in the intercardinal plane ( $\phi=45^\circ, \theta$ ) scanning is found to be approximately equal to the average value of that at the principle planes, as is shown in Figure 3. The array has low cross-polarization radiation in the principle planes, which has been confirmed when an array of 100 (10x10) elements was simulated in PBFDTD over an infinite ground plane, as shown in Figure 4. The Cx-Pol is found to be at least about -35dB in E plane scanning and -25dB in H plane scanning, as is depicted in Figures 5 - 7. The figures also show usual patterns of finite array with no grating lobe problems in the principal planes.

In Figure 5f, the computed directivity of the 100 elements array is slightly bigger than predicted by the area array. This is associated to the fact that the array is simulated over an infinite ground plane, and because of the edge effects of the finite number of elements.

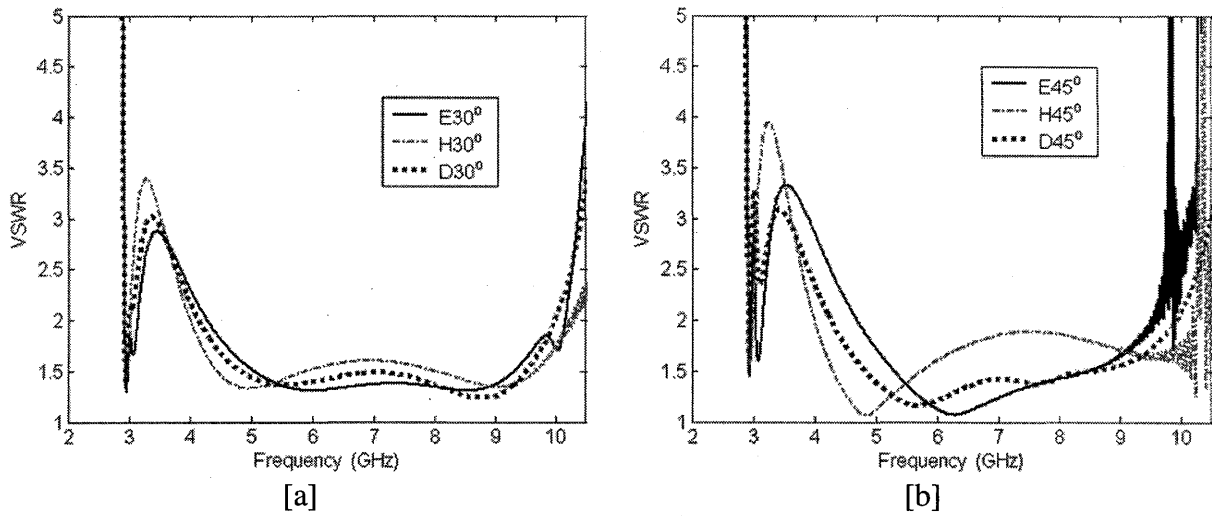


Figure 3: Infinite array of DmBAVA performance in the intercardinal plane scanning. [a] VSWR for  $(\phi, \theta = 30^\circ)$ . [b] VSWR for  $(\phi, \theta = 45^\circ)$ .  $D = H_{cw} = 1.5\text{cm}$ ,  $A = B = 1.51\text{cm}$ ,  $H_a = 1.26\text{cm}$ ,  $\epsilon_r = 3.0$ ,  $\tan\delta = 0.003$ ,  $t = 90\text{mils}$ ,  $Fw_3 = Fw_2 = 0.153\text{cm}$ ,  $G = W_{ag} = 98\text{mils}$ .

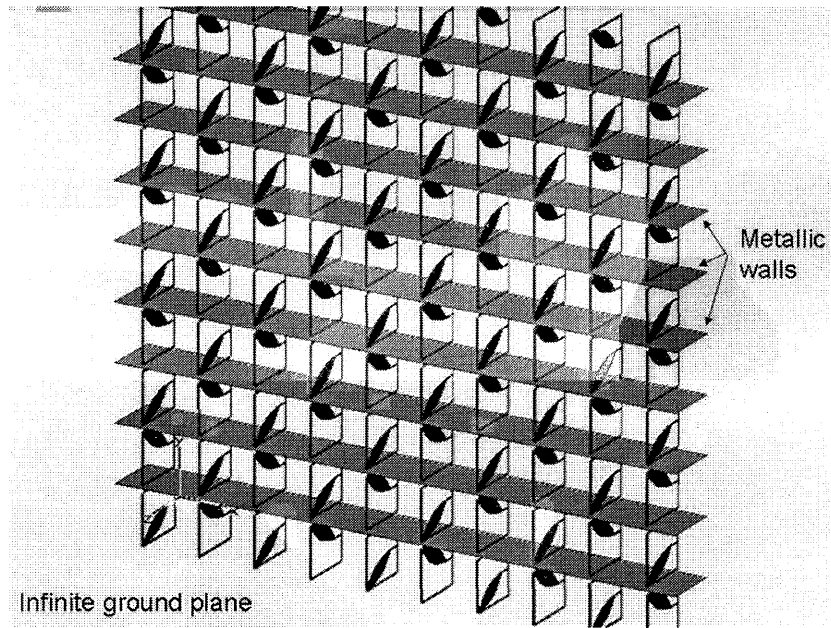
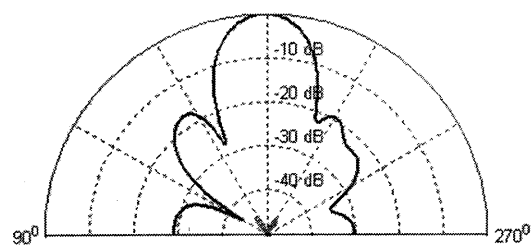
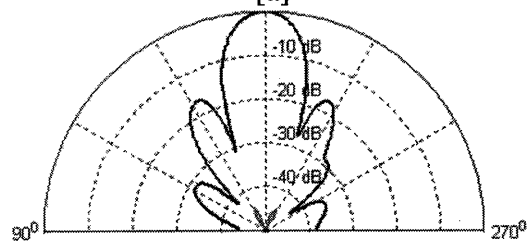


Figure 4: Sketch of a finite array of 100 elements DmBAVA over infinite ground plane.

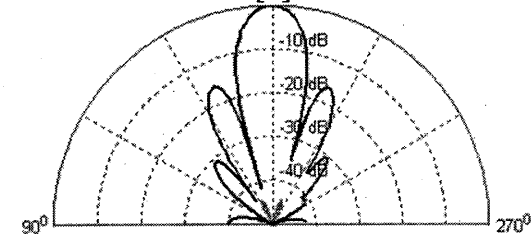
In Figure 5g, it is worth to be noted that the input match efficiency  $1 - |\Gamma(\vartheta, \varphi)|^2$  of the central elements in the finite array agrees very well with that computed based on the unit cell analysis of the infinite array study.



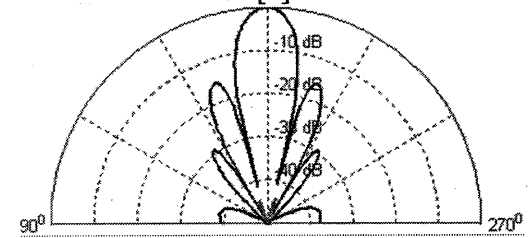
[a]



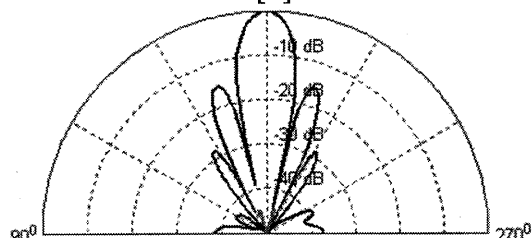
[b]



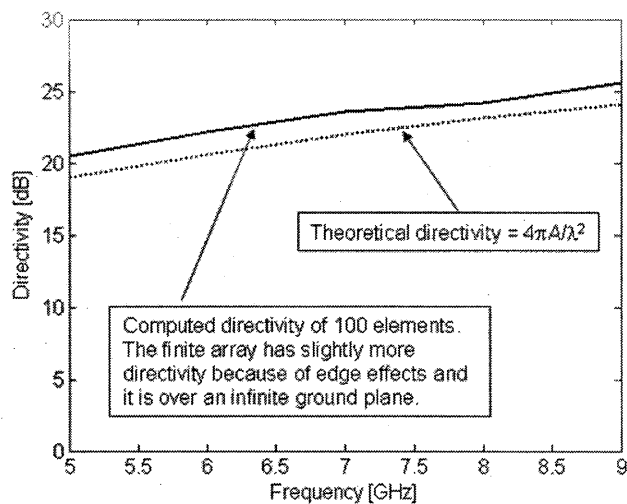
[c]



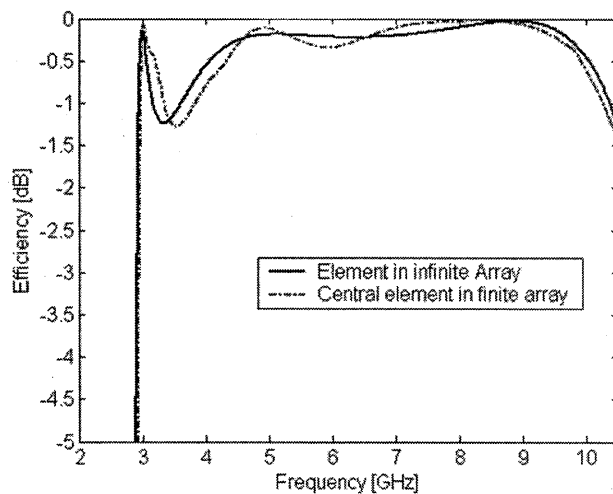
[d]



[e]



[f]



[g]

Figure 5: Radiation characteristic of finite 100 elements of DmBAVA at broadside. Normalized radiation patterns at: [a] Freq = 5GHz. [b] Freq = 6GHz. [c] Freq = 7GHz. [d] Freq = 8GHz. [e] Freq = 9GHz. The solid line is the Co-Pol whereas the dashed line is the Cx-Pol pattern. [f] Array directivity tracked and ideal curve. [g] Mismatch efficiency of central DmBAVA element in infinite and finite array.  $D=H_{cw}=1.5\text{cm}$ ,  $A=B=1.51\text{cm}$ ,  $H_a=1.26\text{cm}$ ,  $\epsilon_r=3.0$ ,  $\tan\delta=0.003$ ,  $t=90\text{mils}$ ,  $Fw_1=Fw_2=0.153\text{cm}$ ,  $G=W_{ag}=98\text{mils}$ .

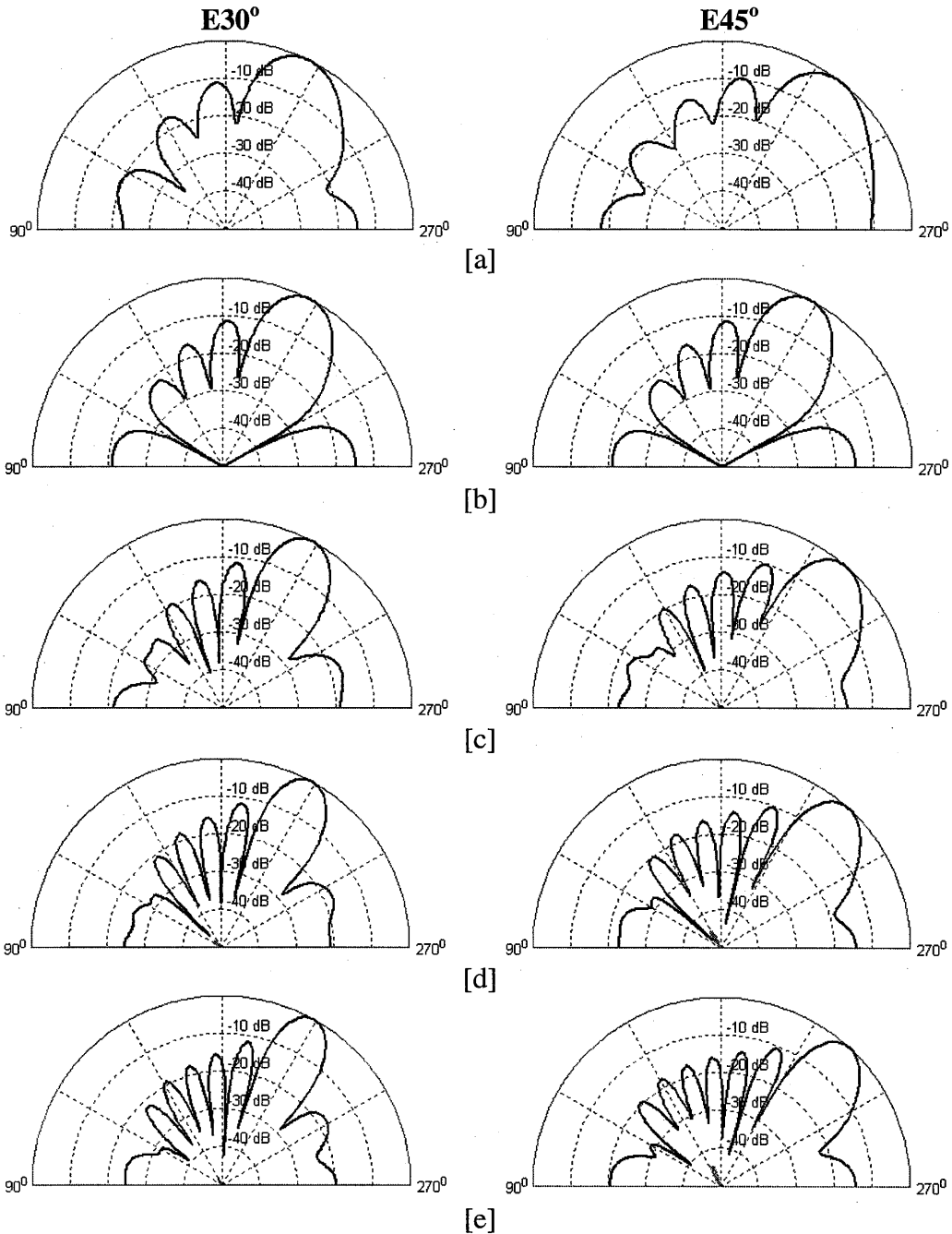


Figure 6: Normalized radiation pattern of finite 100 elements of DmBAVA for E-plane scan. The left column is for  $30^\circ$  scan while the right column is for  $45^\circ$  scan. [a] Freq = 5GHz. [b] Freq = 6GHz. [c] Freq = 7GHz. [d] Freq = 8GHz. [e] Freq = 9GHz. The solid line is the Co-Pol whereas the dashed line is the Cx-Pol pattern.  $D=H_{cw}=1.5\text{cm}$ ,  $A=B=1.51\text{cm}$ ,  $H_a=1.26\text{cm}$ ,  $\epsilon_r=3.0$ ,  $\tan\delta=0.003$ ,  $t=90\text{mils}$ ,  $Fw_1=Fw_2=0.153\text{cm}$ ,  $G=W_{ag}=98\text{mils}$ .

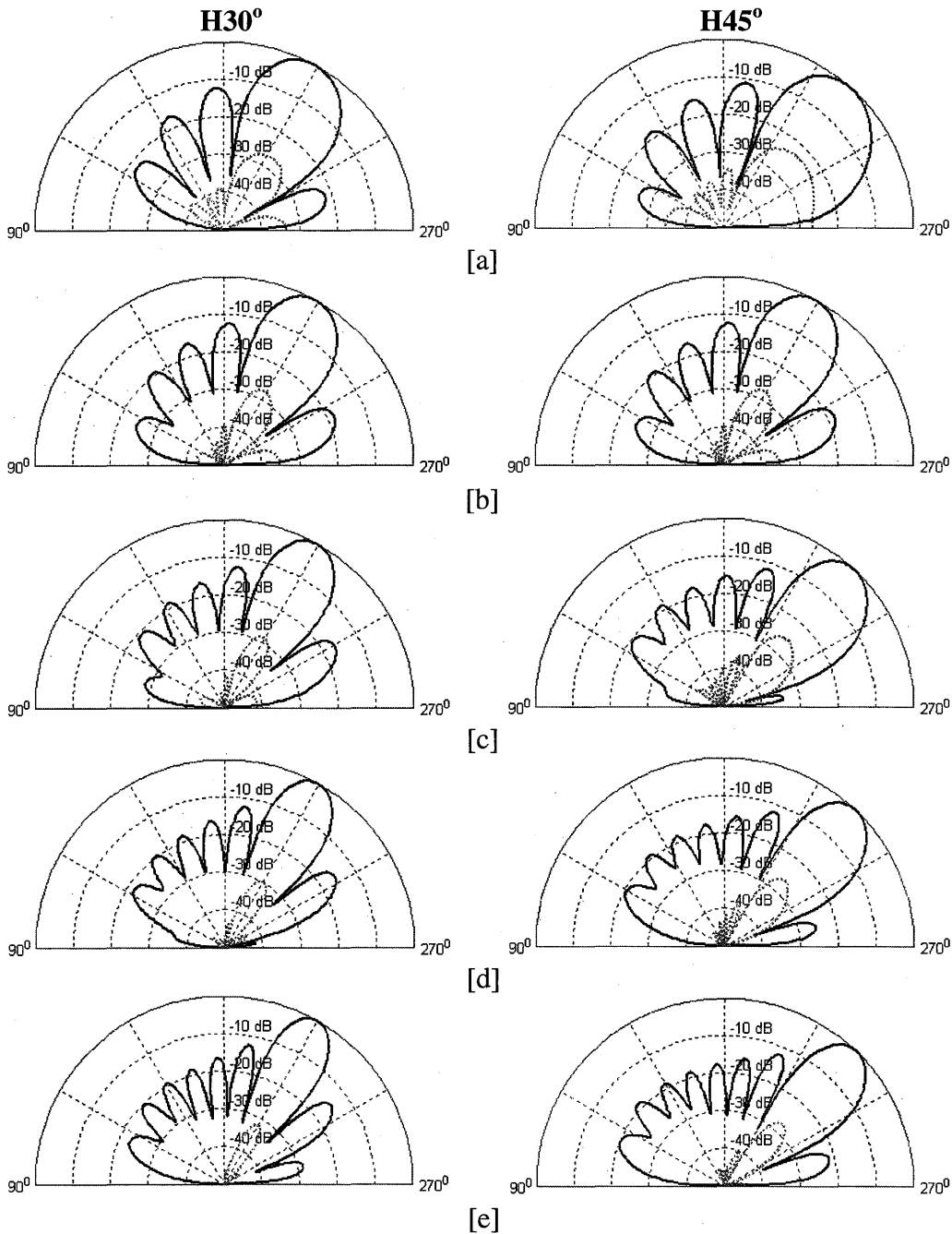


Figure 7: Normalized radiation pattern of finite 100 elements of DmBAVA for H-plane scan. The left column is for  $30^\circ$  scan while the right column is for  $45^\circ$  scan. [a] Freq = 5GHz. [b] Freq = 6GHz. [c] Freq = 7GHz. [d] Freq = 8GHz. [e] Freq = 9GHz. The solid line is the Co-Pol whereas the dashed line is the Cx-Pol pattern.  $D=H_{cw}=1.5\text{cm}$ ,  $A=B=1.51\text{cm}$ ,  $H_a=1.26\text{cm}$ ,  $\epsilon_r=3.0$ ,  $\tan\delta=0.003$ ,  $t=90\text{mils}$ ,  $Fw_1=Fw_2=0.153\text{cm}$ ,  $G=W_{ag}=98\text{mils}$ .

### b. Floquet Modal Analysis of an Infinite Array of DmBAVA

So far, the finite array's radiation patterns did not show grating lobe, or degradation in radiation efficiency associated with doubling the physical periodicity of the DmBAVA array. To further verify that the larger periodicity does not result in grating lobe problems, the radiation from an infinite array has been analyzed to determine its Floquet mode content.

At a surface slightly above the array aperture, the fields were decomposed in Floquet mode components. The strength of each Floquet mode was evaluated relative to the power input to the unit cell to define a transmission coefficient,  $T$ . In the plots that follow,  $T_x(m,n)$  is the strength of the  $(m,n)$  Floquet mode that is X polarized. Similarly,  $T_y(m,n)$  is the strength of the  $(m,n)$  Floquet mode that is Y polarized. A Y-polarized array should radiate all of its power in the Y-polarized  $(0,0)$  Floquet mode so that  $T_y(0,0) = 1$  and all other transmission coefficients should be zero.

The X- and Y- polarized transmission coefficient for a Y-polarized array are plotted in Figure 8 for several scan angles. These plots show that:

1. In the principal planes, where element spacing is 1.51 cm and the periodicity of the array is 3.02 cm, higher order Floquet modes have a maximum amplitude of approximately -35 dB across the operating band. The upper frequency of interest is 10 GHz because the 1.51-cm element spacing allows grating lobes above this frequency. Also, in the principal planes, the excitation of X-polarized fields is very low, indicating good linear polarization from the array.
2. In the diagonal plane, higher order Floquet modes begin to be excited for large scan angles and higher frequencies, but the level of excitation does not exceed approximately -25 dB for frequencies and scan angles of interest. Also, in the diagonal plane, there is noticeable excitation of cross-polarized fields. For scanning at 45° in the diagonal plane,  $T_x(0,0)$  is approximately -17dB over the operating band.

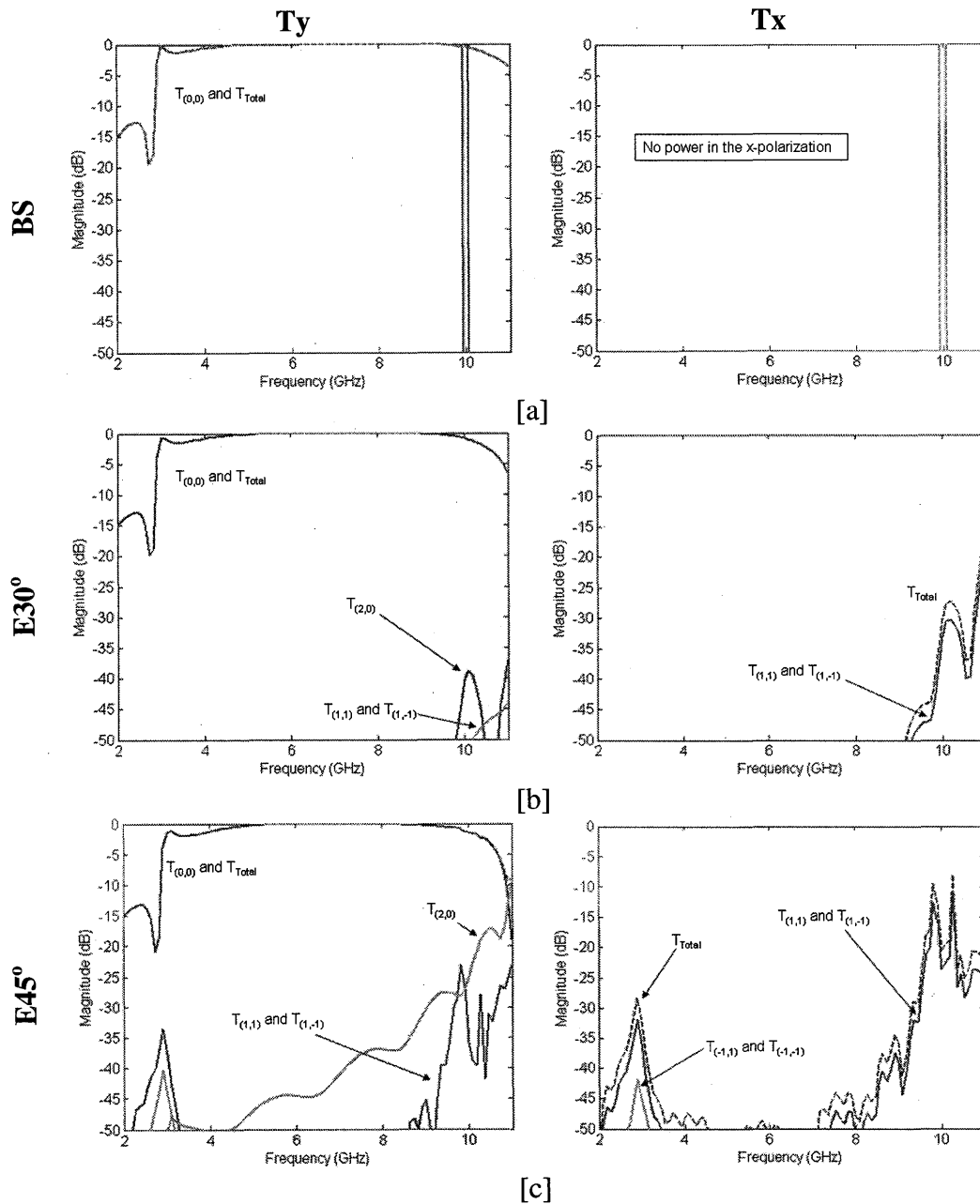


Figure 8: Floquet modal analysis of infinite DmBAVA array for [a] Broadside. [b] E-plane scanning at 30°. [c] E-plane scanning at 45°. The left column is for  $T_y$  coefficient while the right column is  $T_x$  coefficient.  $D=H_{CW}=1.5\text{cm}$ ,  $A=B=1.51\text{cm}$ ,  $H_a=1.26\text{cm}$ ,  $\epsilon_r=3.0$ ,  $\tan\delta=0.003$ ,  $t=90\text{mils}$ ,  $Fw_1=Fw_2=0.153\text{cm}$ ,  $G=W_{ag}=98\text{mils}$ .

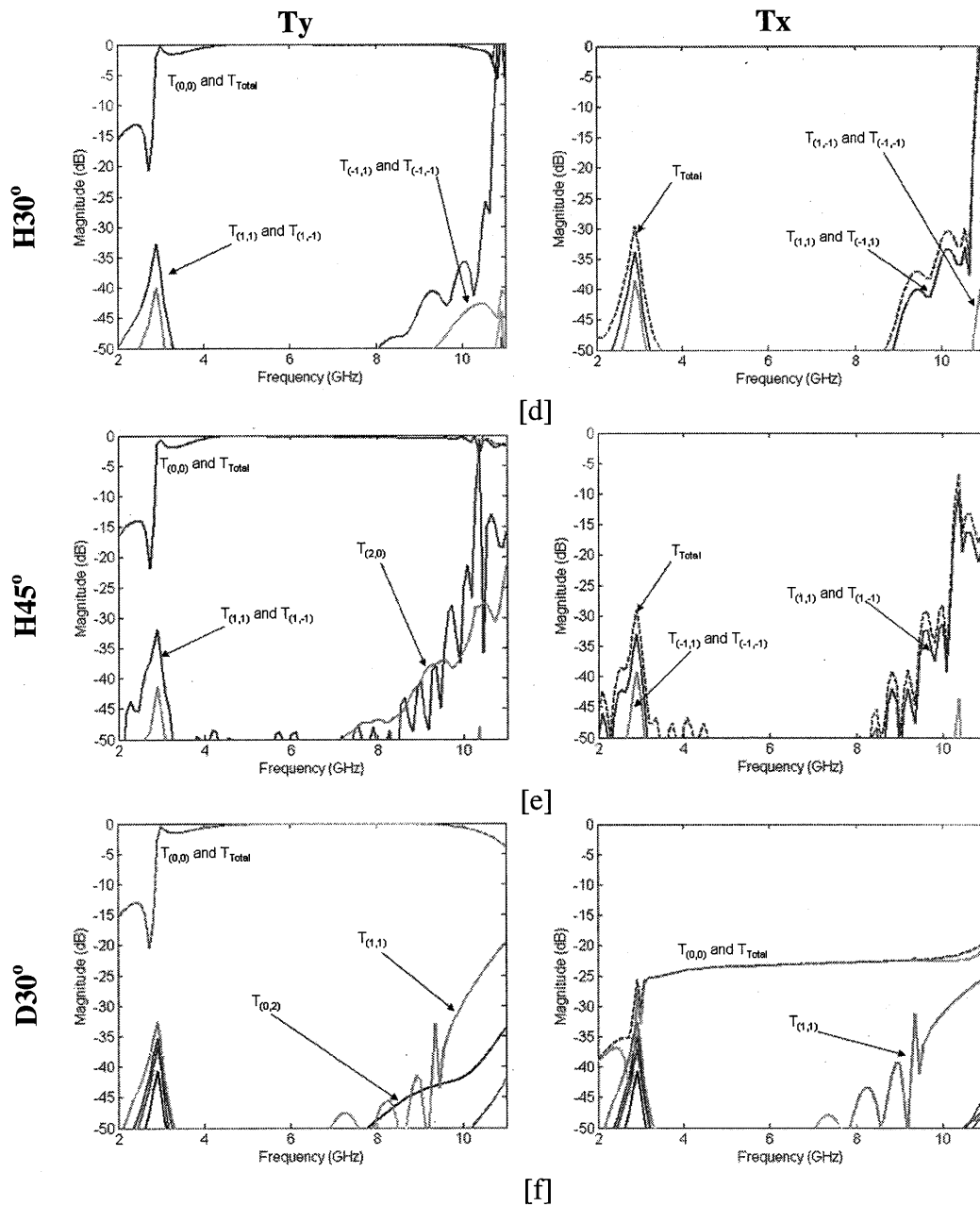
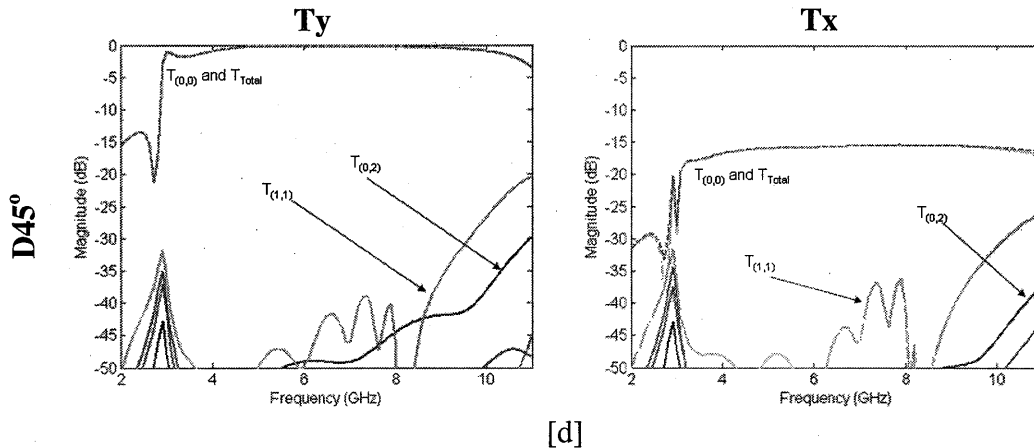


Figure 8 - continued: Floquet Modal analysis for [d] H-plane scanning at 30°. [e] H-plane scanning at 45°. [f] D-plane scanning at 30°. The left column is for  $T_y$  coefficient while the right column is  $T_x$  coefficient.  $D=H_{cw}=1.5\text{cm}$ ,  $A=B=1.51\text{cm}$ ,  $H_a=1.26\text{cm}$ ,  $\epsilon_r=3.0$ ,  $\tan\delta=0.003$ ,  $t=90\text{mils}$ ,  $Fw_1=Fw_2=0.153\text{cm}$ ,  $G=W_{ag}=98\text{mils}$ .





[d]  
 Figure 8 - continued: Floquet modal analysis for [g] D-plane scanning at  $45^\circ$ . The left column is for  $T_y$  coefficient while the right column is  $T_x$  coefficient.  $D=H_{cw}=1.5\text{cm}$ ,  $A=B=1.51\text{cm}$ ,  $H_a=1.26\text{cm}$ ,  $\epsilon_r=3.0$ ,  $\tan\delta=0.003$ ,  $t=90\text{mils}$ ,  $Fw_1=Fw_2=0.153\text{cm}$ ,  $G=W_{ag}=98\text{mils}$ .

#### 4. Preliminary Results on Performance Trade-Offs Study

Altering the environment of array elements has long been used to control scan impedance [8]. In this paper, the particular modification of interest to DmBAVA is the air gap width and its periodicity between the neighboring elements or subarrays. The following analysis is conducted on an antenna that is very similar to the (3:1) DmBAVA array described in [5] but the element depth and dielectric thickness has been changed to 1.8cm and 80mils, respectively.

Three configurations of the array are studied here (see Figure 9).

- *Case I:* The traditional way of modular element of DmBAVA where individual elements can be inserted or removed. This was introduced in [5].
- *Case II:* Modular subarray of DmBAVA, where every  $N$  elements are fabricated on the same substrate board. In this paper,  $N = 2$ .
- *Case III:* All the elements in one row are fabricated on the same substrate board. In other words, the air gap between the elements is filled with dielectric, i.e.  $W_{ag}=0$ . Although the elements of each row are fabricated on a contiguous board, there is no electrical connection between the elements.

The VSWR and radiation resistance for these three cases at several scan angles are shown in Figure 10.

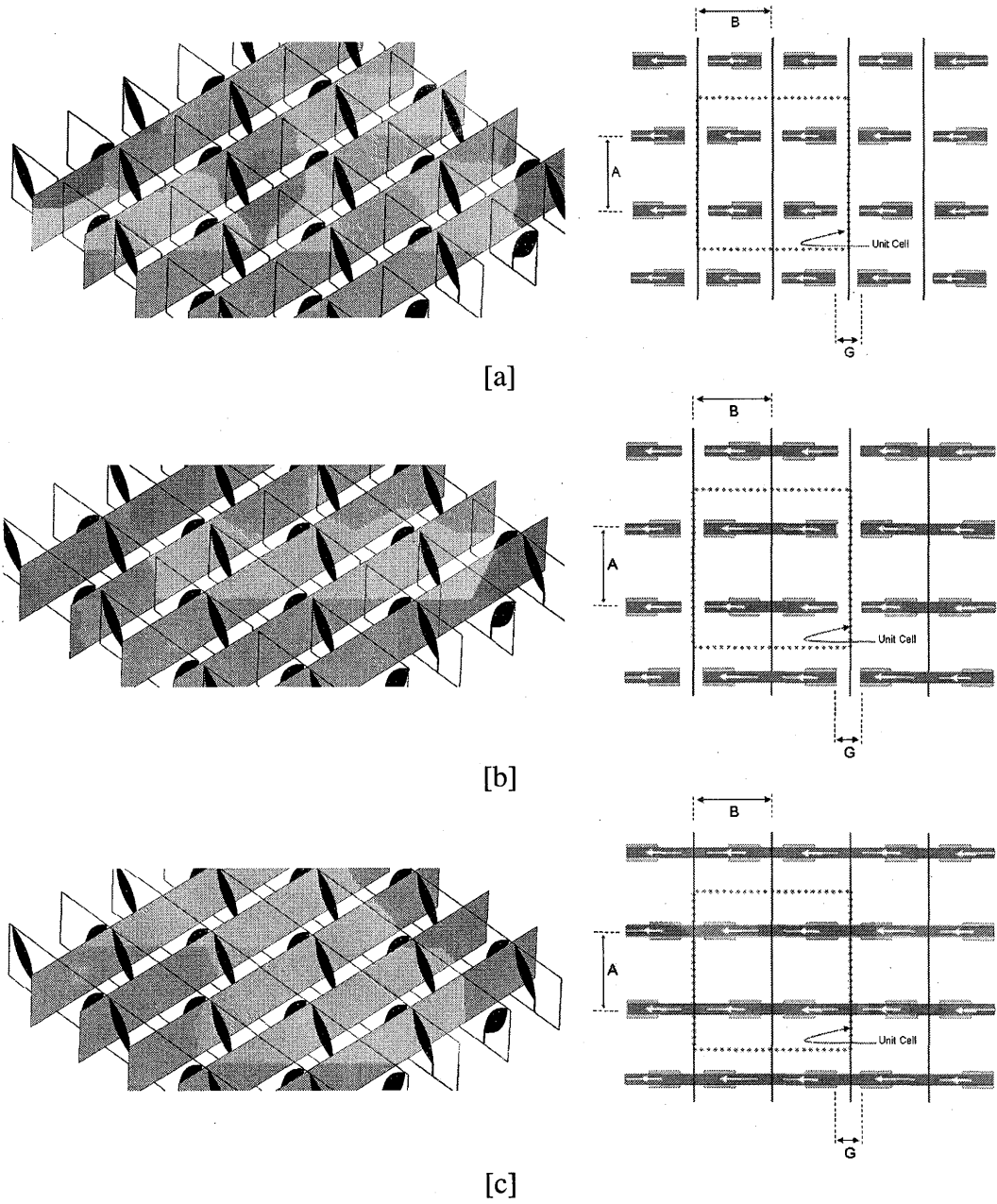


Figure 9: Infinite array configurations. [a] Case I: Modular elements of DmBAVA. [b] Case II: Modular subarray of 2x2 tiled elements. [c] Case III: No modularity, i.e. each row built on a single substrate board. In all of the three cases, there is no electrical connection between the elements or subarrays.

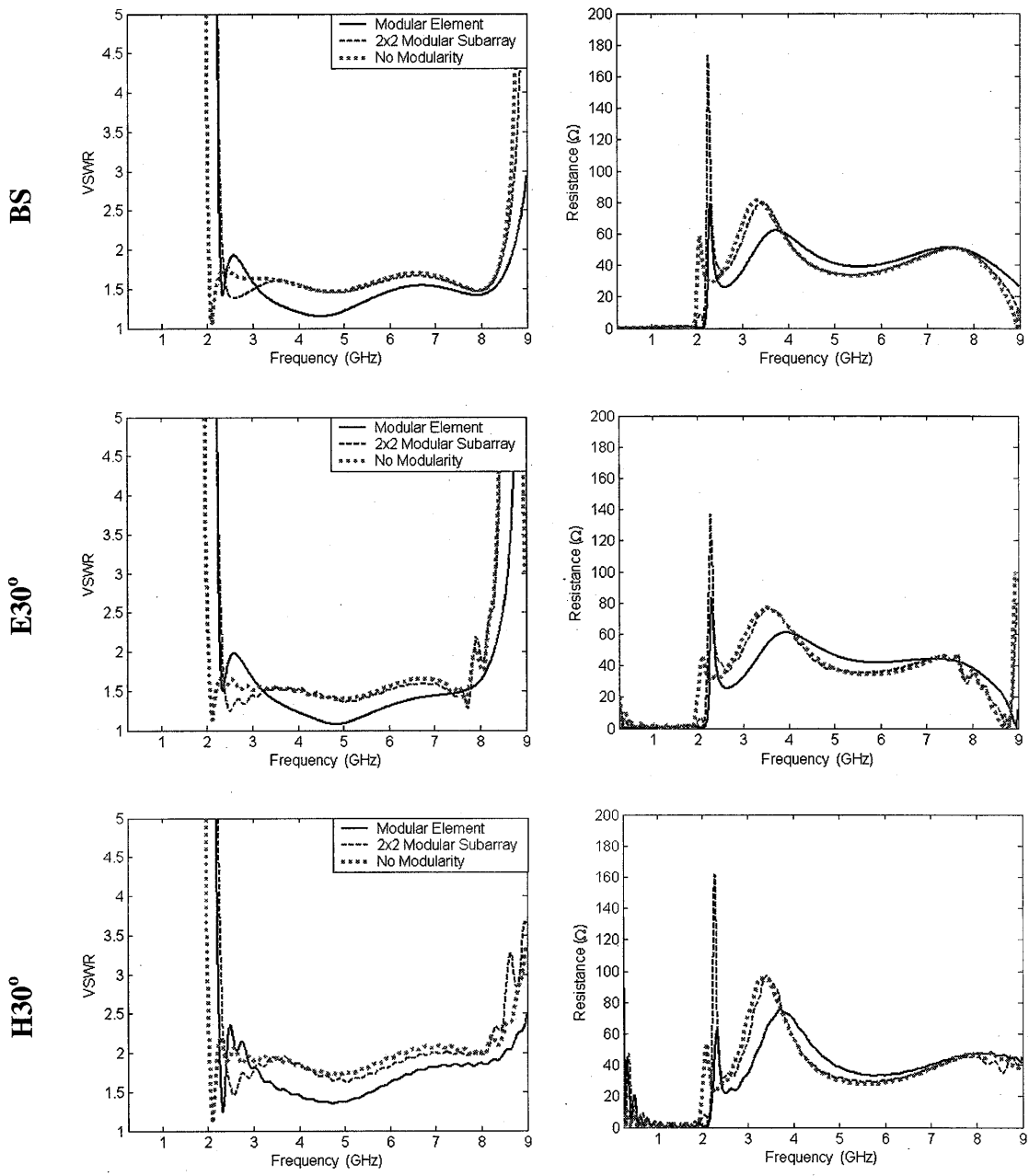


Figure 10: VSWR and resistance of infinite array configurations; modular element of DmBAVA, modular subarray 2x2 tiled elements and no modularity.  $D=1.8\text{cm}$ ,  $A=B=2.00\text{cm}$ ,  $H_a=1.80\text{cm}$ ,  $\epsilon_r=2.2$ ,  $\tan\delta=0.009$ ,  $t=80\text{mils}$ ,  $Fw_2= Fw_1=0.13\text{cm}$ , and  $G=80\text{mils}$

The key effects of filling the air gap between the elements with dielectric are:

1. The array has the operable bandwidth 3.75:1 below the grating lobe frequency of 7.5GHz, half-wavelength spacing. In this design, the element depth,  $D$ , is found to be equals to  $0.45\lambda_{\text{high-frequency}}$ .
2. For limited scan application, the array has a bandwidth of 4:1.
3. The anomaly at 8.9GHz seems is not very sensitive to how the medium between neighboring elements is manipulated. In [5], it was reported that this anomaly depends on the element's depth.
4. If the modularity is necessary for a phased array's mission, then the array configuration in case II (i.e. modular of subarray) has the best compromise between maximum operable bandwidth and the modularity.

Further improvement in the design can be achieved by changing the periodicity at which the air-gap occurs from rectangle lattice, shown in Figure 9b, to a triangle lattice. The latter has a better impedance match over a widescan volume, as is depicted in Figure 11.

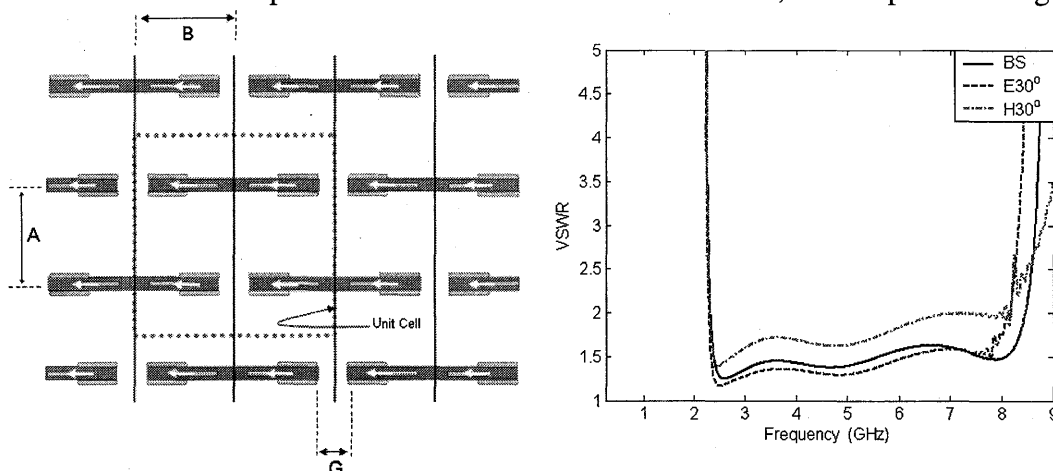


Figure 11: An infinite array configuration based on a 2x2 modular subarray with a triangular lattice for the air-gap periodicity.  $D=1.8\text{cm}$ ,  $A=B=2.00\text{cm}$ ,  $H_a=1.80\text{cm}$ ,  $\epsilon_r=2.2$ ,  $\tan\delta=0.009$ ,  $t=80\text{mils}$ ,  $Fw_2=Fw_1=0.13\text{cm}$ , and  $G=80\text{mils}$ .

## 5. Dual-Polarized (DP) DmBAVA

So far, several broadband single polarized DmBAVA elements were discussed. They all share metallic walls between neighboring elements. Assuming the 2.5:1 array as a framework in the following discussion, the addition of orthogonal elements to create a DP version of this array causes the orthogonal antennas to produce similar effects to the PEC walls, as is depicted in Figure 12.

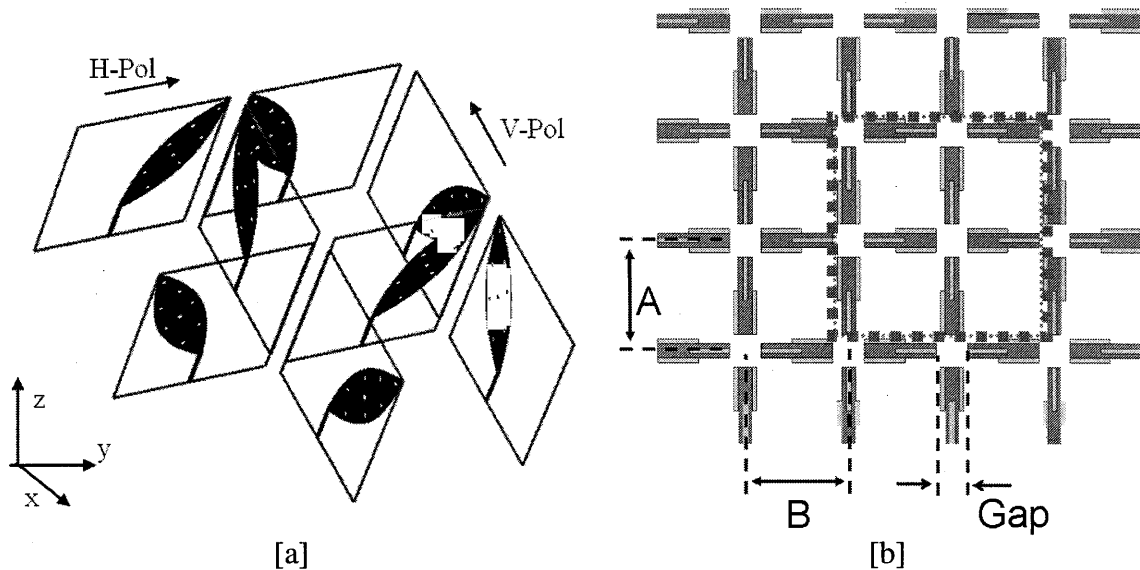


Figure 12 Dual-polarized version of DmBAVA. [a] Structure of a unit cell of DP-DmBAVA comprised of eight mirrored elements. This creates an array with two principle polarization: vertical (VP) and horizontal (HP). Only the outer conductors are shown. [b] Top view of a unit cell of DP-DmBAVA comprised of eight mirrored elements. Adjacent elements are excited  $0^\circ$  and  $180^\circ$  alternatively.

When the metallic crosswalls are replaced by the orthogonal DmBAVA elements, a lot of metal has been removed because of the shape of BAVA element. Therefore, the scan performance of the DP array is not identical to SP array as is shown in Figure 13. In fact, the scan volume has degraded between  $(\pm 30^\circ \sim \pm 45^\circ)$  with a 2.45:1 bandwidth.

In figure 12c, the scan impedance of intercardinal scanning plane at  $\theta=45^\circ$  has a weak anomaly appearing at approximately 7.77GHz. This 5-8 $\Omega$  impedance variation in the vicinity of the grating lobe onset is a result of increasing the symmetry cell size of the DP array to be equal to  $\sqrt{2} \times B = 2.26\text{cm}$  along the diagonal plane. This has been found to be consistent with the Floquet modal analysis of the DP array. When all the elements in the array are simultaneously excited and phased to scan to  $(\phi=45^\circ, \theta=45^\circ)$ , the power of the (1,1) Floquet mode increases to approximately -25dB (see Fig. 14e). Although this is approximately 10dB higher than the (1,1) mode power at  $30^\circ$  scan, it is still quite small and does not cause significant grating lobe problems.

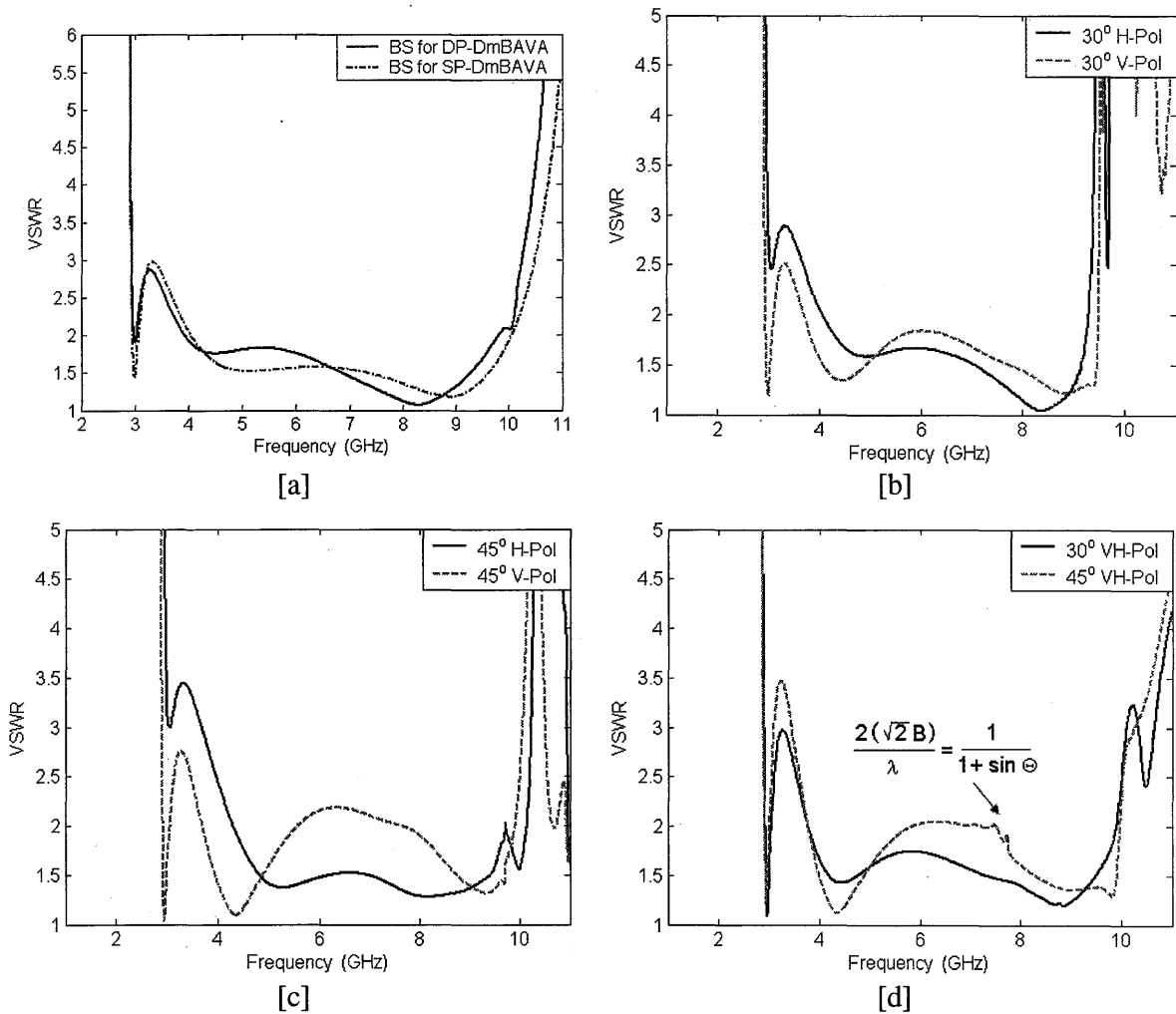


Figure 13: VSWR for the dual-polarized version of the array. [a] Broadside in Sp vs. DP array [b] 30° scan. [c] 45° scan. [d] Diagonal scan.  $D=H_{cw}=1.5\text{cm}$ ,  $A=B=1.51\text{cm}$ ,  $H_a=1.26\text{cm}$ ,  $\epsilon_r=3.0$ ,  $\tan\delta=0.003$ ,  $t=90\text{mils}$ ,  $FW_1=FW_2=0.153\text{cm}$ ,  $G=W_{ag}=98\text{mils}$ .

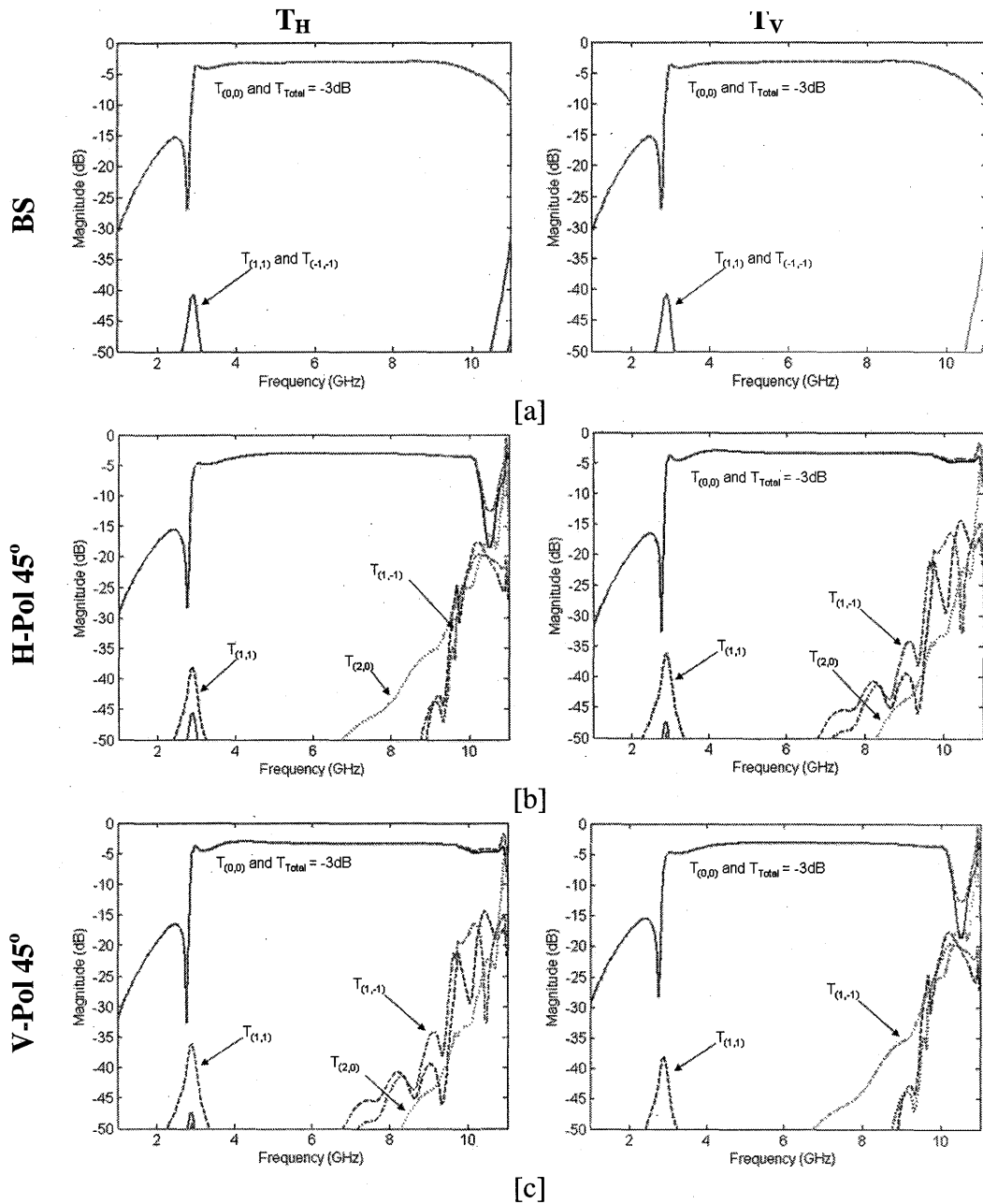


Figure 14: Floquet Modal Analysis for DP-DmBAVA that are simultaneously excited, i.e. slant polarization. [a] Broadside. The 3dB in transmission coefficient is because both polarizations are excited and half of the radiated power is associated with each polarization. [b] H Pol scanning at 45°. [c] V Pol scanning at 45°.  $D=H_{cw}=1.5cm$ ,  $A=B=1.51cm$ ,  $H_a=1.26cm$ ,  $\epsilon_r=3.0$ ,  $\tan\delta=0.003$ ,  $t=90mils$ ,  $Fw_1=Fw_2=0.153cm$ ,  $G=W_{ag}=98mils$ .

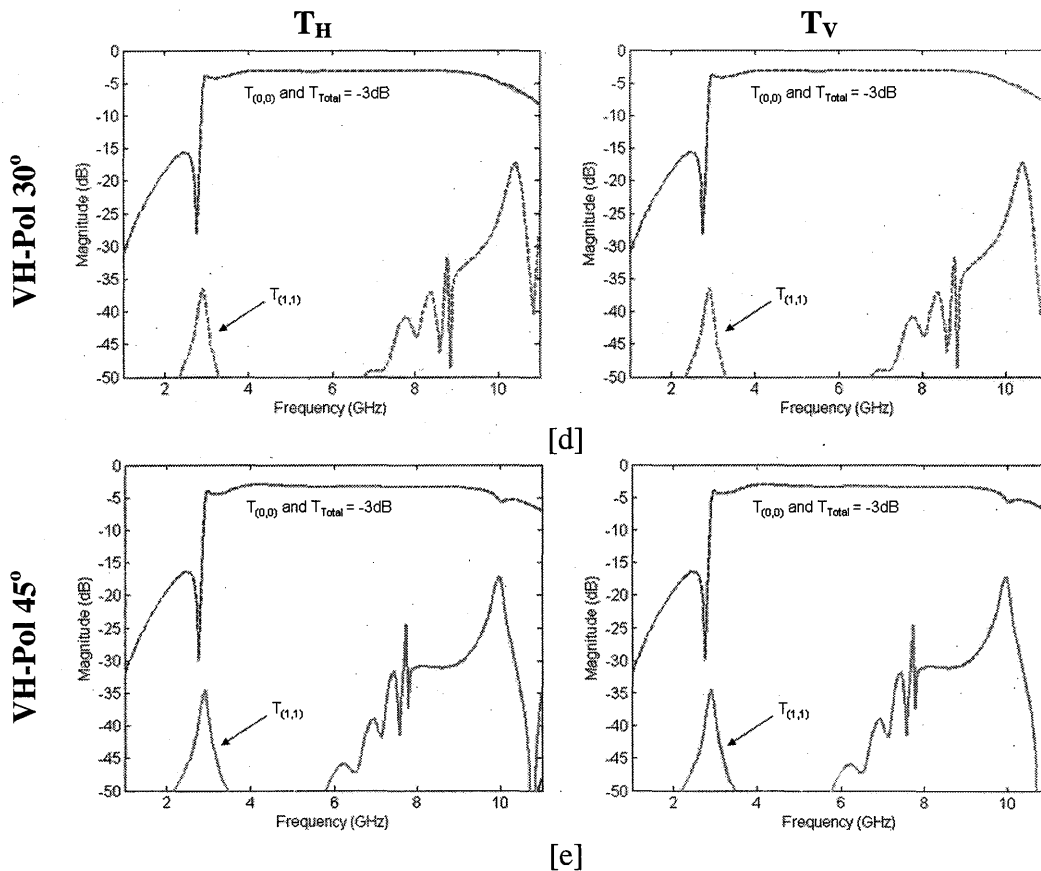


Figure 14 - continued: Floquet Modal Analysis for DP-DmBAVA that are simultaneously excited, i.e. slant polarization. The 3dB in transmission coefficient is because both polarizations are excited and half of the radiated power is associated with each polarization. [d] VH Pol scanning at 30°. [e] VH Pol scanning at 45°.  $D=H_{cw}=1.5\text{cm}$ ,  $A=B=1.51\text{cm}$ ,  $H_a=1.26\text{cm}$ ,  $\epsilon_r=3.0$ ,  $\tan\delta=0.003$ ,  $t=90\text{mils}$ ,  $Fw_1=Fw_2=0.153\text{cm}$ ,  $G=W_{ag}=98\text{mils}$ .

An array of 200 elements (10x10 V-Pol + 10x10 H-Pol) over infinite ground plane has been simulated. The array's radiation patterns have been examined for broadside and scanning 30° along the H-Pol axis. Figure 15 and 16 depict the performance of the finite array, and the key results are summarized as the following:

1. When all the elements in the DP array are excited, the peak of the patterns at each polarization is 3dB less than the total directivity. This is an evidence that all the maximum power occurs at the main beam of the array, and there is no power loss due to grating lobe onset.



2. Comparing the radiation pattern of the array when all elements are excited vs. only one set of polarized elements, the pattern follow the same trends of beamwidth, and positions of sidelobe and nulls.
3. As a result of replacing the crosswalls with orthogonal elements, the cross polarization of the case when only one set of polarized elements is excited, has risen from -50dB (see Fig. 6) to about -30dB. This is still an acceptable value.

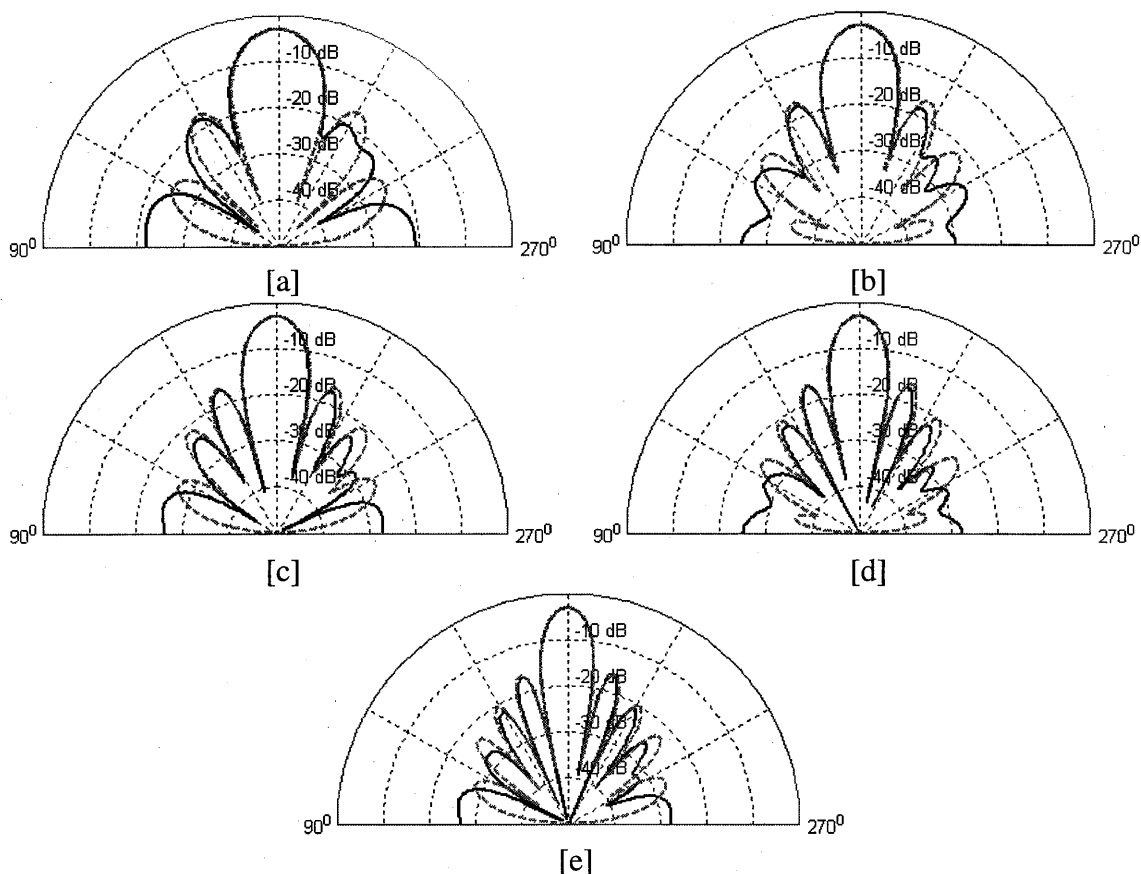


Figure 15: Radiation characteristic of 200 element DP-DmBAVA array at broadside. All elements are excited. The solid line is H-Pol, and dashed line is V-Pol. Normalized radiation patterns at: [a] Freq = 5GHz. [b] Freq = 6GHz. [c] Freq = 7GHz. [d] Freq = 8GHz. [e] Freq = 9GHz. The peak is 3dB at H and V Pol because all the elements are simultaneously excited. Thus, the array has slant polarization.  $D=H_{cw}=1.5\text{cm}$ ,  $A=B=1.51\text{cm}$ ,  $H_a=1.26\text{cm}$ ,  $\epsilon_r=3.0$ ,  $\tan\delta=0.003$ ,  $t=90\text{mils}$ ,  $Fw_1=Fw_2=0.153\text{cm}$ ,  $G=W_{ag}=98\text{mils}$ .

**H-Pol 30° – Slant Polarization  
(All elements are excited)**

**H-Pol 30° – Horizontal Polarized only.  
(vertical elements are terminated)**

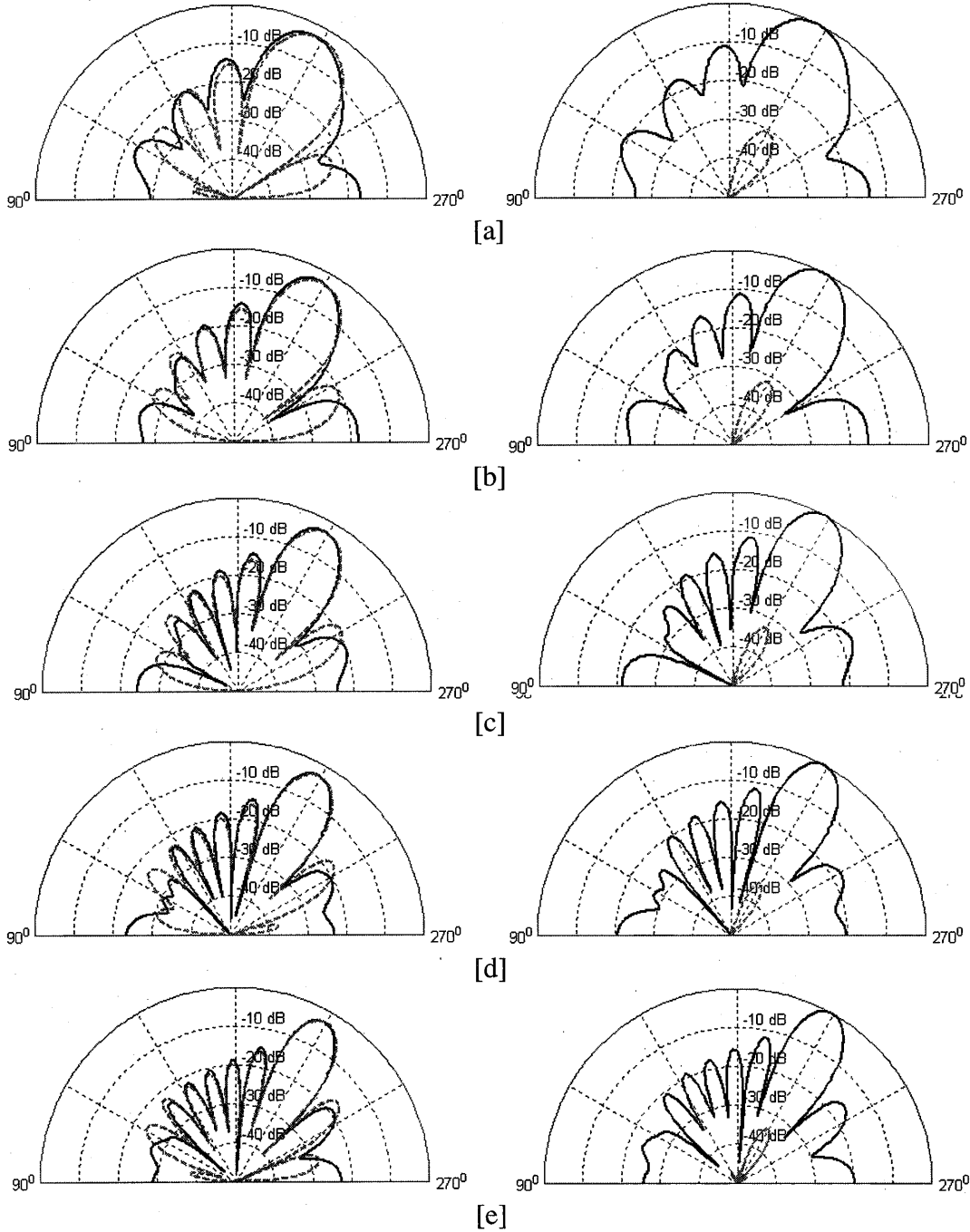


Figure 16: Radiation characteristic of 200 elements of DP-DmBAVA array along Horizontal-axis of the array. The solid line is H-Pol, and dashed line is V-Pol. Normalized radiation patterns at: [a] Freq = 5GHz. [b] Freq = 6GHz. [c] Freq = 7GHz. [d] Freq = 8GHz. [e] Freq = 9GHz.  $D=H_{cw}=1.5\text{cm}$ ,  $A=B=1.51\text{cm}$ ,  $H_a=1.26\text{cm}$ ,  $\epsilon_r=3.0$ ,  $\tan\delta=0.003$ ,  $t=90\text{mils}$ ,  $Fw_1=Fw_2=0.153\text{cm}$ ,  $G=W_{ag} = 98\text{mils}$ .

## 6. Summary

The weak impedance variation in the vicinity of grating lobe onset associated with doubling the physical periodicity of the array has been studied in Floquet modal analysis. It was found to be an insignificant problem. Several improvements to the previous design were discussed. A practical 2x2 modular subarray of DmBAVA element has been introduced. The array has a maximum bandwidth of (3.75:1) over more than 30° scan volume. The dual-polarized DmBAVA array doesn't perform as well as the single-polarized array with metallic walls, but the dual-polarized array maintain good performance over more than an octave of bandwidth and moderately wide scanning.

## 7. Acknowledgment

The authors thank several individuals whose contributions have been valuable in this work. Mr. James West and the Advanced Technology Center of Rockwell Collins provided financial support and access to computational resources. The contributions are greatly appreciated.

## References

1. P. J. Gibson, "The Vivaldi Aerial," Proc. 9<sup>th</sup> European Microwave Conference, 1979, pp. 101-105.
2. D. Norman, D. Schaubert, B. DeWitt and J. Putnam, "Design and Test Results for a Dual-Polarized Vivaldi Antenna Array," 2005 Antenna Applications Symposium, Monticello, IL, pp. 243 – 267 Sept. 2005
3. D. Schaubert, S. Kasturi, M.W. Elsallal and W Cappellen, "Wide bandwidth Vivaldi Antenna Arrays – Some Recent Developments," to appear at EuCAP 2006. Nov 06 – 10, 2006. Nice, France.
4. J. J. Lee, S Livingston and R. Koenig, "Perforamnce of a Wideband (3-14 GHz) Dual-pol Array," IEEE APS 2004 Symposium, pp. 551-554, 20-25 June 2004.
5. M.W. Elsallal and D. H. Schaubert, "Reduced-Height Array of BAVA with Greater Than Octave Bandwidth," 2005 Antenna Applications Symposium, pp. 226 – 242, 21-23 September, 2005
6. Periodic Boundary FDTD (PBFDTD) Program, written by Henrik Holter. Stockholm, Sweden.
7. M.W. Elsallal and D. H. Schaubert, "Parameter study of single isolated element and infinite arrays of balanced antipodal Vivaldi antennas," 2004 Antenna Applications Symposium, Allerton Park, Monticello, Illinois, pp. 45 – 69, 15-17 September, 2004.
8. Amitay, Galindo and Wu, "Theory and analysis of phased array antennas," 1972

## NEW RESULTS USING POLYOMINO-TILED SUBARRAYS FOR TIME-DELAY CONTROL OF WIDEBAND ARRAYS

\*R. J. Mailloux, \*\*S. G. Santarelli, and \*\*T. M. Roberts

\* Department of Electrical and Computer Engineering, University of Massachusetts,  
Amherst Massachusetts

\*\* Sensors Directorate, Air Force Research Laboratory  
Hanscom, AFB, Massachusetts

**Abstract:** This paper presents recent results describing the use of polyomino subarrays to introduce time delays into phased-array systems. Results for arrays of 8-element subarrays show suppression of peak quantization lobes to levels below -14 dB, relative to the quantization lobes of 8-element rectangular subarrays. Since algorithms for producing arbitrarily large arrays that tile rectangular areas are not available, we have combined smaller arrays chosen to be statistically independent. These have allowed the evaluation of ensemble averages of array gain, average and peak sidelobe levels.

### 1. Introduction

Time delay is most often introduced into phased-array systems by using phase shifters at the array face and time-delay units behind rectangular subarrays. As discussed in many texts and publications, this practice leads to significant quantization lobes in the radiated pattern. The locations of these quantization lobes in angle space correspond to the grating lobes one would see for an array with inter-element spacing equal to the subarray dimensions. Obviously, quantization lobes represent severe pattern degradation.

Various subarray techniques have been developed to reduce quantization lobes. These methods, which include interlacing or overlapping the subarrays, have been understood for years [1, 2] and have been demonstrated in practice; however, these approaches are relatively difficult and expensive to build. In addition, thinned array techniques may be used, but they can have significant residual "error sidelobes" even at center frequency.

In addition to earlier symposium presentations by the present authors, there have been several other recent papers describing the use of random or irregular subarrays or other techniques for randomizing the phase-center locations of the subarrays [3-6]. In this paper, we show that the use of irregular-shaped subarrays can provide suppression of quantization lobes and that the subarrays can be realized entirely in the control network that feeds the elements.

## 2. Polyomino Subarrays

This paper describes a practical technique for using polyomino-shaped subarrays to provide time delay for a large array. Polyominos are figures composed of elements on a square grid. Systematic study of polyominos, as the general figures are named, began in 1953 and now has a substantial literature in mathematical combinatorics [7-10]. Particular L-shaped tetromino and octomino subarrays seem practical for reasons mentioned in the introduction and the earlier publications [3, 4]. The words tetromino and octomino are an extrapolation of the familiar word domino. Dominos have 2 elements; tetrominos have 4; and octominos have 8.

There have been numerous publications in mathematical journals dealing with the perfect 'tiling' of rectangular areas using various similar or dissimilar polyominos. "Perfect" implies that the rectangular area is completely filled such that no part of any polyomino extends beyond the rectangular boundary. In our application, however, we are dealing with a rectangular grid of array elements. Thus, we do not worry about having the tiles end exactly at the edges, since we can choose to either load these edge elements or simply not excite them. The few that extend beyond the edges, as in Figure 1 (with data shown in Figure 2) are of little concern for a large array. (The results shown later in Figures 6 and 7 are computed with an available tiling program that produces perfect tiling).

All of the polyomino arrays discussed in this paper adhere to the following rules:

1. Each array is tiled with a single polyomino shape. This shape may be rotated through  $90^\circ$  increments and is sometimes allowed to flip. Therefore, if we allow the polyomino to flip, there are a total of 8 different subarray configurations, as illustrated in Figure 1.
2. We require that the aperture be completely 'tiled' or filled with subarrays, with no gaps. In this manner, the center-frequency pattern will be identical to the center-frequency pattern of the phase-shifted array, and there will be no reduction in aperture efficiency.
3. We choose the number of elements in each subarray to be  $2^n$  (for positive  $n$ ), such that a lossless power divider can be used to feed each subarray.

All results discussed in this paper are for the L-octomino and the corresponding rectangular subarrays they replace. Figure 1 shows an array of 2048 (64 x 32) elements grouped into 256 L-octomino subarrays.

Working by hand, we were unable to perfectly tile any large array using octominos, so all of our hand-made tilings have elements protruding beyond the rectangular boundaries of the array [3]. These hand-made arrays resulted in some of the lowest-sidelobe designs; however, they were extremely tedious to construct. Fortunately, the literature offers computer programs that perfectly tile rectangular areas [7-10]. During the course of this

project, we have generated tens of millions of tilings using [9], which came to our attention as a Linux screensaver.

For a rectangular array of equal but rotated polyomino shapes, one can envision using a single type of power-divider network. There is no need to assemble the subarrays and place them into the array individually, or to design the array with mechanical structures that separate the subarrays, because the subarrays will be formed entirely in the control network that feeds the elements.

The array of L-octominoes shown in Figure 1 was analyzed assuming that an amplitude taper was imposed at every element across the array, not just at the subarray ports. Parenthetically, we note that subarray amplitude quantization effects are usually much smaller than phase or time-delay quantization effects, especially in a large array; thus, we haven't studied them here.

The elements of each subarray are excited by a time-delayed signal, such that the time delay is exact for one of the elements (denoted as the phase-center element). Note that the phase-center element is the same for all  $90^\circ$  rotations of the subarray (both flipped and non-flipped). The phase shifters at the remaining elements in the subarray are chosen to produce a progressive phase across the subarray, and thus, a continuous phase progression across the entire array at center frequency.

The arrays are assumed to lie in the  $(x, y)$  plane of a spherical coordinate system radiating into the half space  $z \geq 0$ . Figure 2 shows pattern data plotted in direction cosine space ( $u = \sin \theta \cos \phi$  and  $v = \sin \theta \sin \phi$ ) for two arrays scanned to  $(u_0, v_0) = (0.5, 0.5)$ . The first array has 256 rectangular subarrays of eight elements arranged in a  $4 \times 2$  grid. The second array consists of 256 L-shaped octomino subarrays. The elements in both arrays are spaced  $0.5 \lambda$  apart at the highest frequency,  $r = f/f_0 = 1.2$ .

Figure 2a shows the periodic quantization lobes for the rectangular case. Figure 2b shows the pattern corresponding to the array of L-shaped octomino subarrays depicted in Figure 1. Figures 2c and 2d show the three dimensional patterns (2a and 2b, respectively) projected onto a plane so that sidelobe levels can be measured. For the array of rectangular subarrays, the largest quantization lobe is approximately  $-11.5$  dB below the broadside gain (Figure 2c). Results in Figure 2d for the array of octomino subarrays show lower peak sidelobes with the highest being approximately  $-25.9$  dB relative to broadside gain, or reduced by approximately  $-14.4$  dB relative to the rectangular subarray configuration. It should be noted that the difference in gain between the rectangular and octomino patterns is  $0.1$  dB based on pattern integration.

### 3. Dot-Product Metric

One of the goals of this project is to investigate peak and average sidelobe behavior as a function of array size; however, the tiling program that is used to generate the octomino

subarray configurations is limited to 32 x 32-element arrays. In order to generate larger arrays, we can combine any number of 32 x 32-element “unit cells.” For example, two adjacent unit cells form a 32 x 64 array, whereas four unit cells can be used to generate a 64 x 64 array, as illustrated in Figure 3.

When generating these larger arrays, however, the unit cells must be chosen such that the tilings are significantly “different” from one another. For example, consider a 64 x 64-element array (like the one shown in Figure 3), which consists of 4 unit cells. If the unit cells are identical, or nearly identical, then this periodicity will manifest as quantization lobes in the radiated pattern. If the unit cells are chosen such that the tilings are significantly different, however, the corresponding quantization lobes are suppressed.

In order to measure the “degree of similarity” between any two unit cells, we applied the *dot-product metric*. This metric is implemented in neural network theory for pattern classification problems [11]. Basically, each pattern (i.e., unit cell) is represented as a multi-dimensional vector. The angle between any two vectors (i.e., patterns) **A** and **B** can be computed using the following:

$$\theta_{AB} = \cos^{-1} \left[ \frac{\overline{\mathbf{A}} \cdot \overline{\mathbf{B}}}{\|\overline{\mathbf{A}}\| \|\overline{\mathbf{B}}\|} \right]. \quad (1)$$

Smaller values of  $\theta$  correspond to patterns that have a high degree of similarity, whereas larger values of  $\theta$  indicate dissimilar patterns.

To illustrate this point, consider the pattern classification problem of Figure 4. Here, a 3 x 5 grid is used to represent numerical values from 0 to 9 by blackening the appropriate blocks. The pattern which represents the number zero is shown at the top of the figure. If we assign each black box a value of -1 and each white box a value of 1, we can describe this pattern in vector format (by taking the values column-wise) as follows:  $V_0 = [-1, -1, -1, -1, -1, -1, 1, 1, 1, -1, -1, -1, -1, -1, -1]$ . The patterns representing the numerals one and eight are shown at the bottom of the figure. Applying equation (1), it can be shown that the dot-product angle between patterns zero and one,  $\theta_{01}$ , is 137.2°, whereas  $\theta_{08}$  is only 29.9°. These results are expected, since the “zero” pattern is very similar to the “eight” pattern (i.e., differs by only a single block-value), whereas the “zero” pattern is quite dissimilar to the “one” pattern (i.e., the two patterns have only two blocks in common).

For this project, we tile a unit cell using a single octomino shape, namely, the L-shaped octomino. There exist eight orientations for this octomino as shown in Figure 5. Each orientation is assigned a unique bipolar, binary representation; thus, every element within

a particular octomino is assigned the same binary number. Again, taking the array elements column-wise, a 384-element vector is formed (i.e., 128 octominos  $\times$  3-bit representation) for each unit cell. When the unit cell shown at the top of the figure is compared to the unit cell directly below, we see that the dot-product angle is only  $10.1^\circ$ . This result is expected, since these two unit cells differ only in the small area indicated by the circles; otherwise, these two tilings are identical. On the other hand, the dot-product angle between the top unit cell and the bottom-right unit cell is much larger, indicating that the two patterns are dissimilar, and this dissimilarity is easily recognized by a simple visual comparison.

#### 4. Statistics for octomino unit-cell arrays and arrays of unit cells

Using the polyomino tiling program described in [9], we generated 99 random tilings of L-shaped octominos. Each tiling consisted of 128 octominos and covered an area corresponding to a  $32 \times 32$ -element array or “unit cell” (as previously defined and as shown in Figure 3). We subsequently measured the dot-product angle,  $\theta$ , between each unit cell and every other one (i.e.,  $0.5 \times 99 \times 98 = 4,851$  dot-product computations). The values for  $\theta$  ranged from roughly  $75^\circ$  to  $105^\circ$ , indicating that there is a fairly high degree of dissimilarity across the entire set of tilings. As mentioned previously, it is desirable to use dissimilar unit cells when constructing larger arrays, since unwanted periodicities in the array structure often manifest as large quantization lobes in the radiated pattern.

We used 96 unit cells to construct twenty-four  $64 \times 64$  arrays. Then, we calculated the radiation pattern for each of the original ninety-nine  $32 \times 32$  arrays in addition to the newly constructed  $64 \times 64$  arrays. Figure 6 shows the average sidelobe levels for both sets of tilings as a function of frequency. The x-axis represents the ratio  $r = f / f_0$ , where  $f_0$  denotes center frequency. The y-axis represents amplitude in decibels. The average sidelobe levels for the entire set of  $32 \times 32$  *octomino* arrays are plotted vertically for each value of  $r$ . The small blue dots represent the individual values, whereas the large blue circle indicates the mean value at each frequency point. The average sidelobe level of the corresponding  $32 \times 32$  *rectangular* array (which consists of a grid of 128,  $2 \times 4$ -element subarrays) is also plotted as a function of  $r$  (red solid line) for comparison.

Similarly, the average sidelobe levels for the entire set of  $64 \times 64$  *octomino* arrays are plotted as a function of  $r$  denoted by blue triangles, and the corresponding  $64 \times 64$  *rectangular* array (which consists of a grid of 256,  $2 \times 4$ -element subarrays) is also plotted as a function of  $r$  (red dotted line).

As expected, there is a general trend for the average sidelobe level to increase as  $f$  departs from center frequency. It is also apparent that, for a given array size, the octomino curve tracks the corresponding rectangular curve rather closely. In most cases, there is less than 1 dB difference between the mean value of the octomino curve and the corresponding rectangular curve; however, the octomino curve tends to lie above the rectangular curve for almost all values of  $r$ . Thus, we can conclude that although the octomino array



structure is able to suppress the quantization lobes that manifest from the periodic structure of the rectangular array, the random phase errors introduced by the octomino array structure cause the average sidelobes to increase slightly.

If we look closely at the octomino curves for either array size (i.e.,  $32 \times 32$  or  $64 \times 64$ ), it is evident that for each value of  $r$ , the individual values vary from the mean by roughly 1 dB or less. This implies that the average sidelobe level does not change significantly as a function of array tiling. On the other hand, the difference between curves corresponding to different array sizes (i.e., the difference between the two rectangular curves or the difference between the two octomino curves) is a fairly constant 5 – 6 dB. This result is not surprising, since one would expect the average sidelobe level to be inversely proportional to the array size (i.e., the average sidelobe level itself is proportional to the phase-error variance and is independent of the array size, so doubling the array size reduces the average level by about 6 dB).

Figure 7 plots maximum sidelobe level as a function of tiling configuration for the set of  $64 \times 64$  octomino arrays for a constant frequency ratio of  $r = 0.7$ . The solid red line represents the maximum sidelobe level for the corresponding  $64 \times 64$  rectangular array. Note that even the worst of the octomino arrays (tiling #2) is roughly 8 – 9 dB below the rectangular value, and some of the octomino arrays (tilings #4 and #24) are as much as 15 dB below the rectangular value. Thus, the range of values is considerable – roughly 6.5 dB. Overall, these results suggest that, although the *average* sidelobe level does not depend heavily on tiling configuration, the *maximum* sidelobe level does. In addition, this wide range of values corresponding to the maximum sidelobe level illustrates the importance of array simulation and analysis as part of the design process. For example, the analysis presented in Figure 7 allows one to choose a “good” tiling (such as #4 or #24) rather than a “bad” tiling (such as #2). As a final note, the peak sidelobe performance of any given tiling varies very little with frequency, as illustrated in Figure 8. Here we see that tilings #4 and #24 consistently outperform tiling #2 at every frequency (except, of course, at center frequency where all three tilings become equivalent to the rectangular case).

## 5. Conclusion

This study has presented data from arrays of L-octomino shaped subarrays used to provide time-delay steering for a phase-steered array. The paper demonstrates elimination of the -11.5 dB quantization lobes that are radiated by an array of rectangular subarrays, and their replacement by lower sidelobes that are between -25 and -26 dB below the main-beam gain.

Acknowledgements: This work was supported by the Air Force Office of Scientific Research, Mathematics and Space Sciences Directorate, under Dr. A. Nachman.

References:

- [1] R. Tang, "Survey of time delayed beam steering techniques," in Phased Array Antennas: Proc. of the 1970 Phased Array Antenna Symposium, Artech House, Dedham, MA 1972, pp. 254-260.
- [2] R. J. Mailloux, Phased Array Antenna Handbook, 2<sup>nd</sup> Edition, Artech House Publishing Co., Dedham, MA, 2005.
- [3] R. J. Mailloux, S. G. Santarelli, T. M. Roberts, "Irregular shaped subarrays for time delay control of planar arrays," Proceedings of the 2004 Antenna Applications Symposium, Monticello, Illinois.
- [4] R. J. Mailloux, S. G. Santarelli, T. M. Roberts, "Polyomino shaped subarrays for limited field of view and time delay control of planar arrays," Proceedings of the 2005 Antenna Applications Symposium, Monticello, Illinois.
- [5] R. C. Hansen, and G. G. Charlton, "Subarray Quantization Lobe Decollimation," IEEE Trans. AP-47, No.8, August 1999, pp.1237-1239.
- [6] V. Pierro, V. Galdi, G. Castaldi, I. M. Pinto, and L. B. Felson, "Radiation properties of planar antenna arrays based on certain categories of aperiodic tilings," IEEE Trans. AP-53, No.2, February 2005, pp. 635-643.
- [7] S. W. Golomb, Polyominoes: Puzzles, Patterns, Problems, and Packings, Princeton University Press, Princeton, New Jersey, 2nd edn., 1994.
- [8] G. E. Martin, Polyominoes: A Guide to Puzzles and Problems in Tiling, Mathematical Association of America, Washington, DC, 1991.
- [9] S. Montgomery-Smith, "\polyomino-0.4," available online <http://www.math.missouri.edu/stephen/software/polyomino>.
- [10] G. Putter, "\Gerard's Universal Polyomino Solver," available online <http://www.xs4all.nl/gp/PolyominoSolver/Polyomino.html>.
- [11] M. T. Hagan, H. B. Demuth, M. H. Beale, Neural Network Design, Martin Hagan Publishing, 2002.

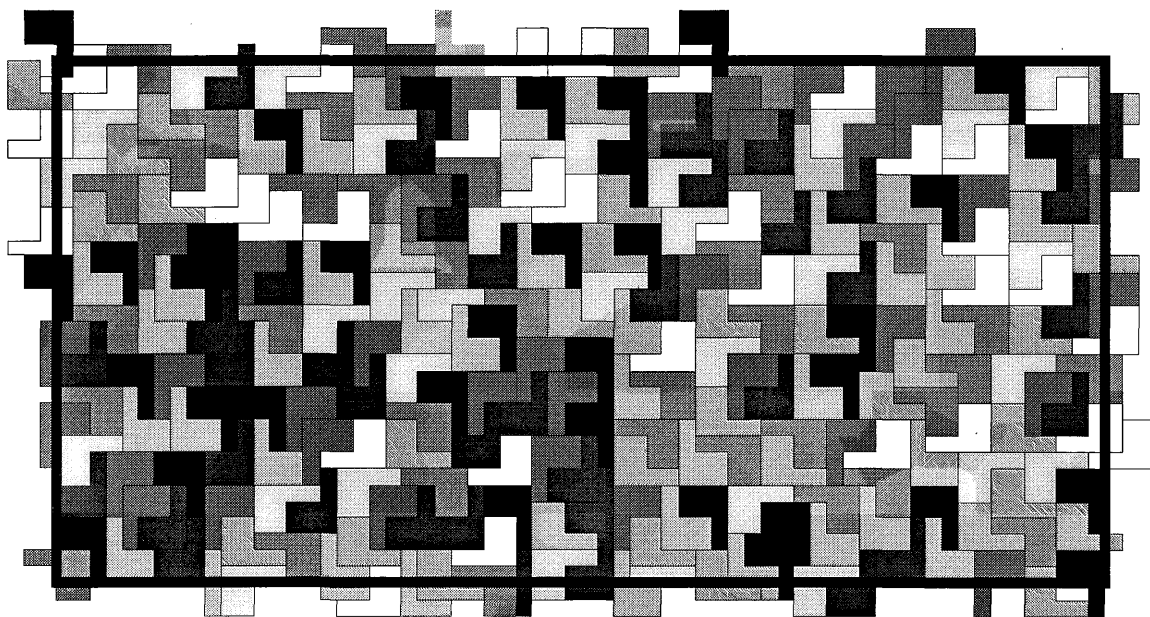


Figure 1. Array of 2048 elements consisting of 256 L-octomino subarrays).

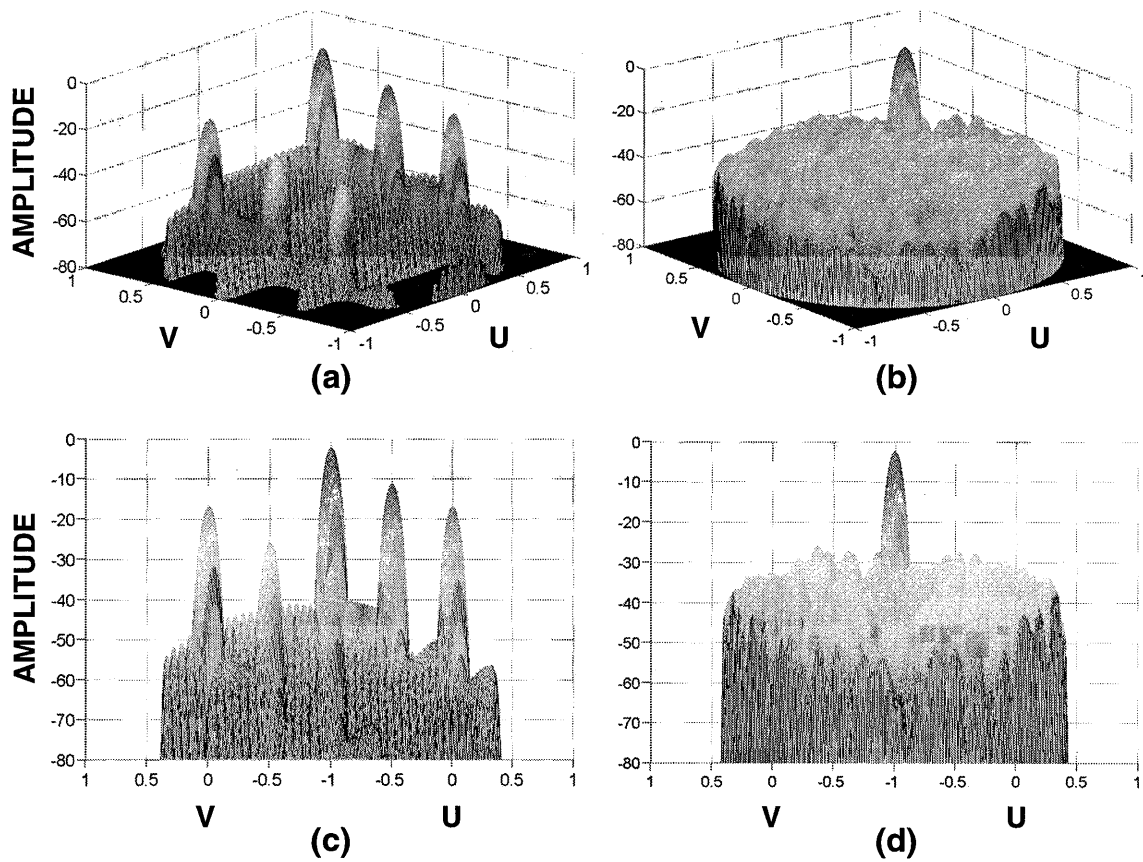


Figure 2. 3-D sidelobe profiles for arrays of rectangular and polyomino subarrays at a scanning angle of  $(u_0, v_0) = (0.5, 0.5)$ . (a) Array pattern of rectangular ( $2 \times 4$ ) subarrays. (b) Array pattern of L-octomino subarrays. (c) Projected pattern of rectangular subarrays. (d) Projected pattern of L-octomino subarrays.

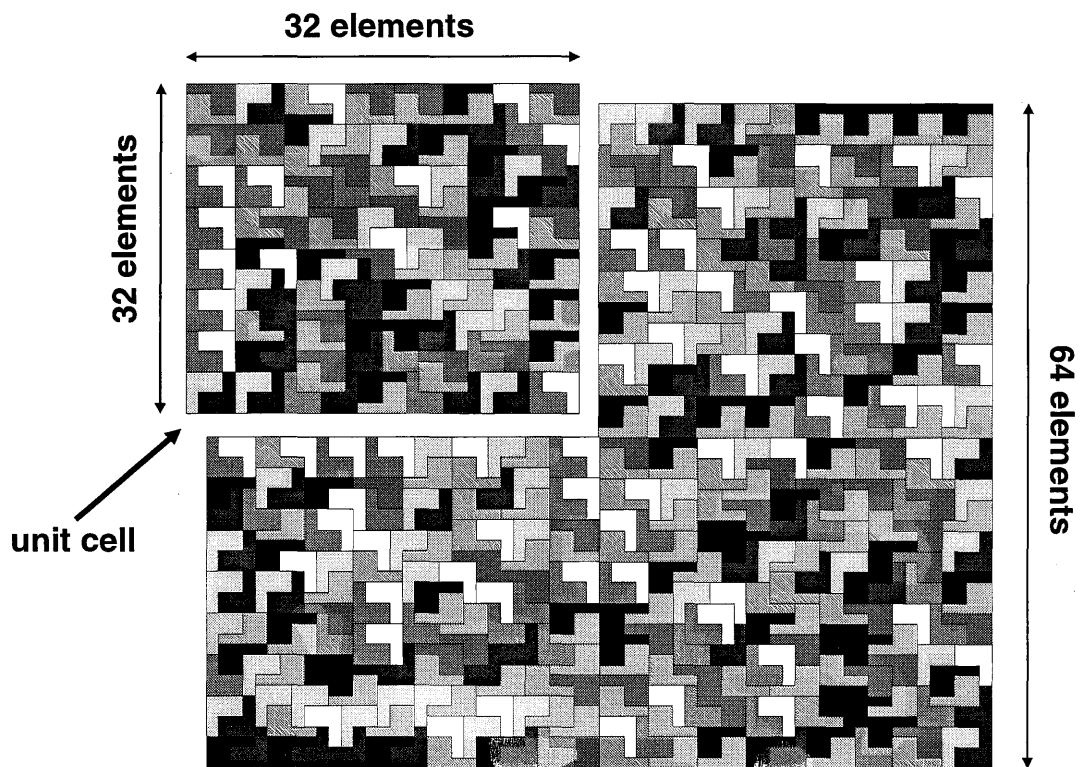
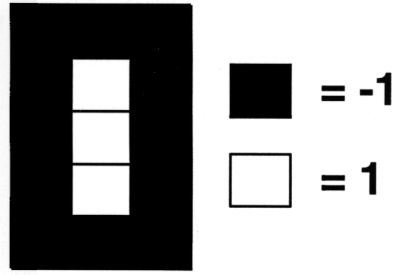
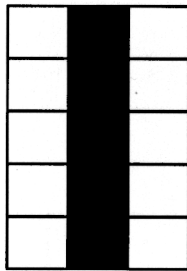


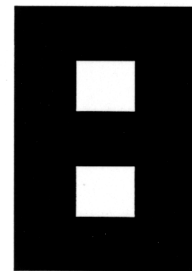
Figure 3. Definition of a "unit cell".



$$V_0 = [-1, -1, -1, -1, -1, -1, 1, 1, 1, -1, -1, -1, -1, -1]$$



$$\theta_{01} = 137.2^\circ$$



$$\theta_{08} = 29.9^\circ$$

Figure 4. Dot-product metric example.

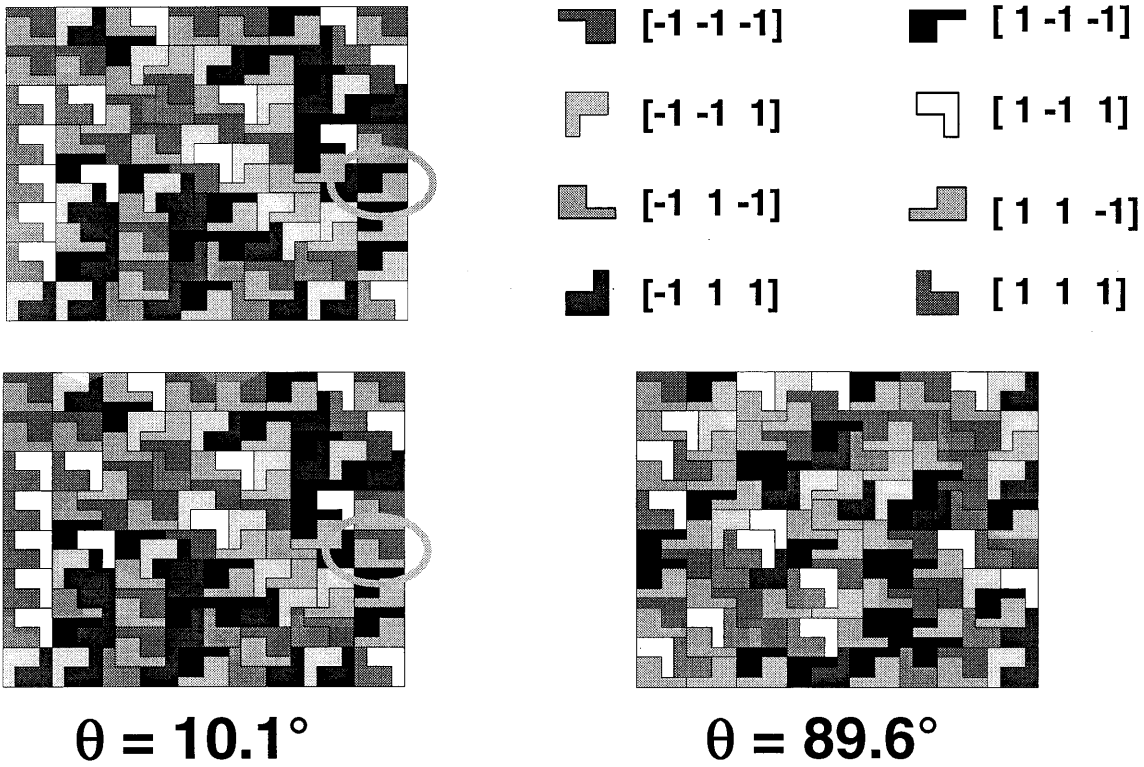


Figure 5. Dot-product metric applied to unit cells.

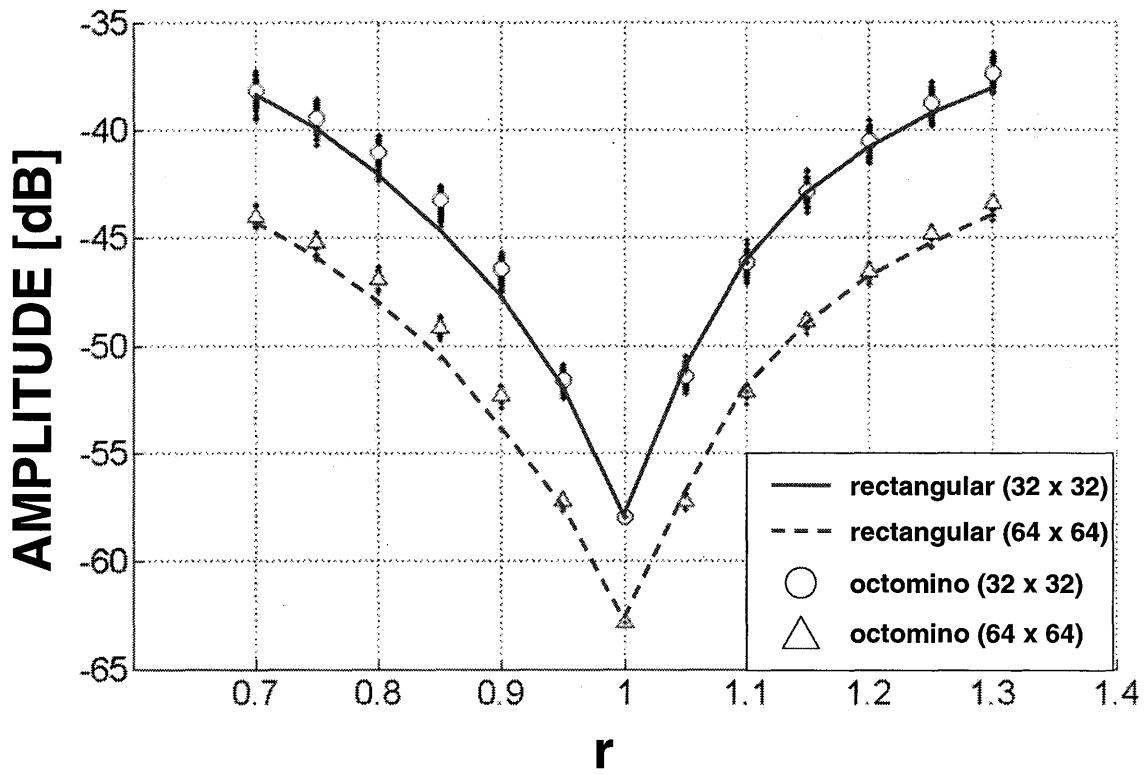


Figure 6. Statistical analysis of average sidelobe levels as a function of frequency for two array sizes: 32 x 32 and 64 x 64.



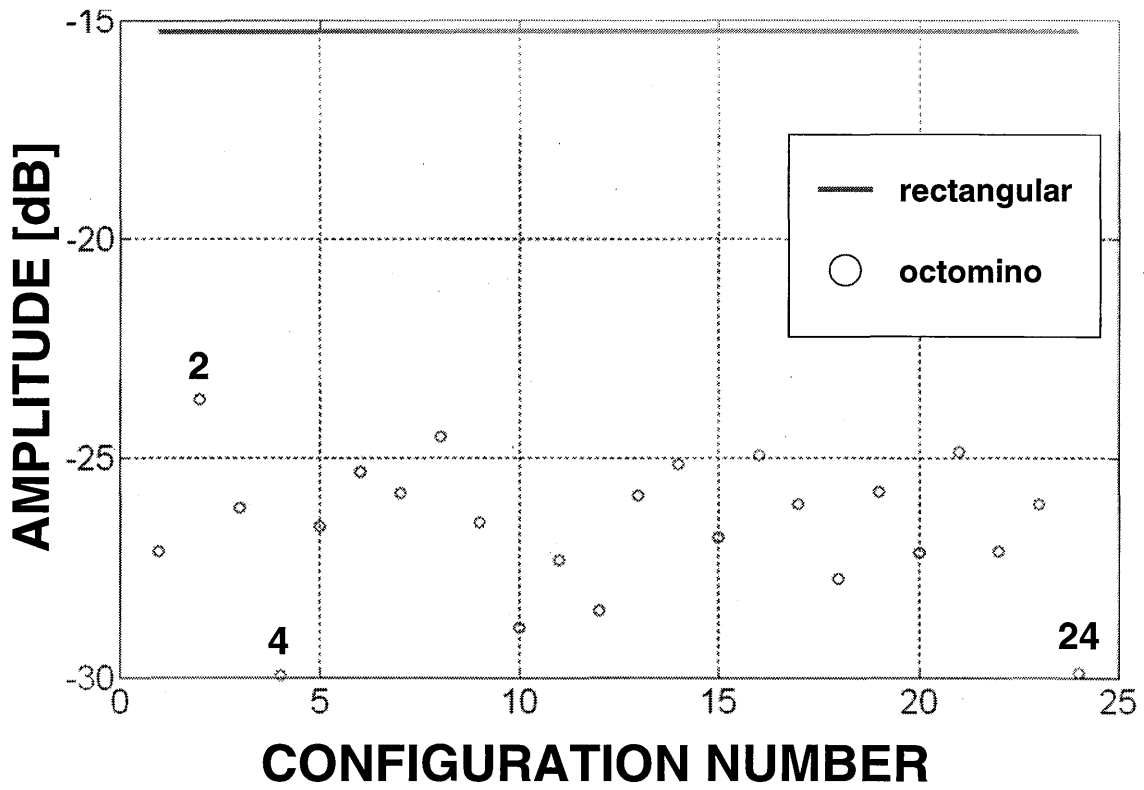


Figure 7. Comparison of maximum sidelobe level for rectangular (solid) and octomino (circles) arrays for  $r = 0.7$ .

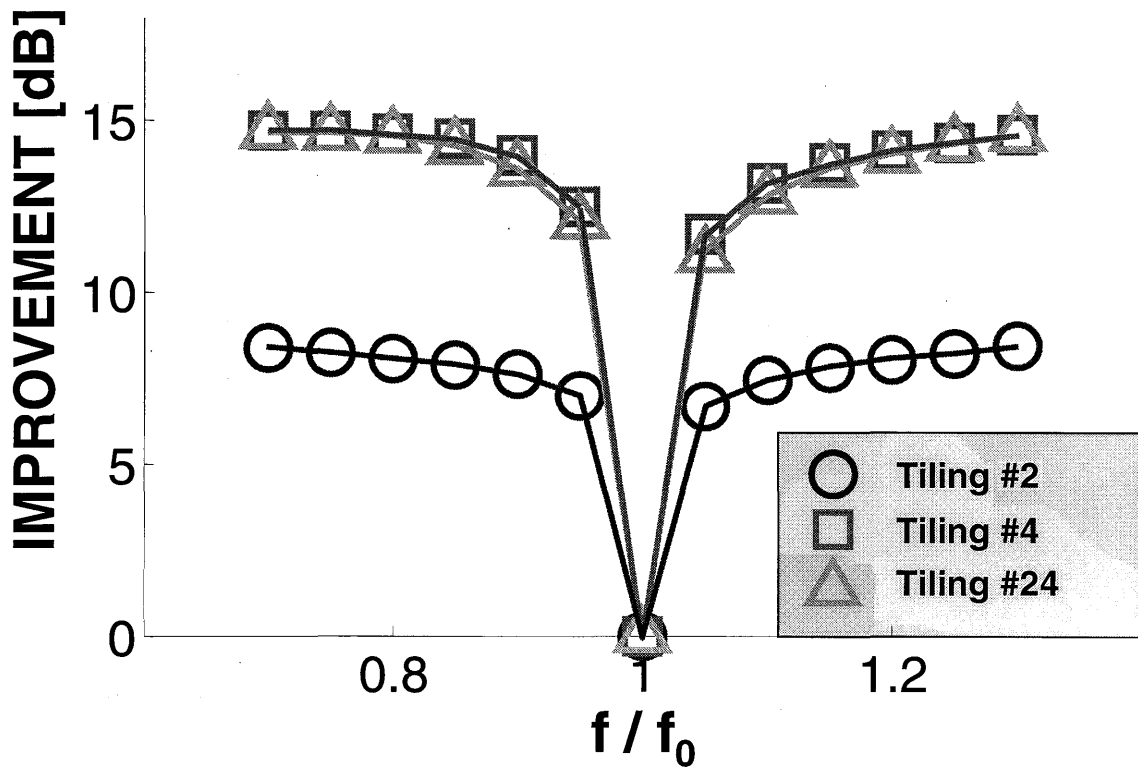


Figure 8. Peak sidelobe level (normalized to rectangular case) as a function of frequency for tilings #2 (circle), #4 (square), and #24 (triangle) of Figure 7.

# High Efficiency SATCOM and MILSTAR Solid State Power Amplifiers

Paul J. Oleski  
Air Force Research Laboratory/IFGE  
Rome, NY 13441-4505  
[Paul.Oleski@afrl.af.mil](mailto:Paul.Oleski@afrl.af.mil)

Sarjit S. Bharj  
Princeton Microwave Technology  
Princeton, NJ 08619  
[sarjit@princetonmicrowave.com](mailto:sarjit@princetonmicrowave.com)

## ABSTRACT

High Efficiency Solid State Amplifiers are required for mobile platforms that are used for satellite communications. High efficiency SSPAs have been developed for the SATCOM, 27.5 to 31 GHz frequency and MILSTAR, 43.5 to 45.5 GHz. The SATCOM amplifiers have been designed using binary combining methods using the Gysel in Phase combiner as well as a Four-way Waveguide combiner. Using the Binary power combining approach, power output in excess of 10 Watts has been achieved. Using waveguide combiners, power in excess of 20 Watts has been achieved with power efficiency greater than 20 %. The design and development of MILSTAR amplifier is based on radial combining power from 26 amplifier modules using 1 Watt MMIC devices using pHEMT technology. The linear amplifier is designed for a power output of 10 Watts over the full MILSTAR band. The measured insertion loss of the 26 way radial combiner is 0.5 dB. Each amplifier module of this amplifier is an independent amplifier. Both amplifiers consist of sequencing circuits for bias, bias stabilization and temperature compensation using MMIC based attenuators. Because the amplifier combiners power from 26 identical 1-watt modules, the format afford an amplifier with graceful degradation. This paper will present the results of the developments of both the SATCOM and MILSTAR amplifiers.

## Introduction

The limitation of output power of solid state devices can be partially overcome by combining several amplifiers or devices. A difficult aspect of designing a combiner is finding an efficient scheme that offers low loss, good amplitude tracking and phase balance and high power handling capability. Combining approaches can be separated into two groups, those that can combine two devices at a time (binary combiners) and those that can combine the output of multiple devices in one step. The most common types of binary combiners are 90 degree hybrids and in phase power dividers and 180 degree hybrids. The binary combiner losses increase substantially when more than eight devices are combined in parallel. The Wilkinson power divider can be extended from a binary to a radial combiner where the inputs are arranged in a circular pattern and connected together at the center. Radial combiners are used for combining more than eight devices in parallel. Air Force Research Laboratory Information Grid Division and Princeton Microwave Technology has developed a solid state amplifier using binary combiners for SATCOM band with a power output of 40 dBm and a radial combined solid state power amplifier for the MILSTAR application, using 26 1-Watt MMIC devices. This paper will present the concepts and measured results of the amplifiers.

## SATCOM AMPLIFIER:

The technical specifications for the 27.5-31 GHz SATCOM amplifier are detailed below. The amplifier has a power output and gain requirements of 40 dBm and 50 dB respectively. Other factors of importance are small size and high efficiency.

### 30 GHz Amplifiers

	Parameter	Unit	Specification
1.	Frequency	GHz	30 GHz
2.	Bandwidth	MHz	2000 MHz
3.	Gain	dB	50
4.	Power Output	dBm	40
5.	Noise Figure	dB	10
6.	Spurious	dBc	<-75
7.	Operating Temperature	C	-30 to 80
8.	Efficiency	%	>20
9.	Size	Inches	.65 x 8 x 6

The temperature performance of the amplifier demands a temperature compensation network. This network requires an analog attenuator and temperature sensor circuits in the pre-driver stages of the amplifier. The format of the amplifier has been divided into two modules which comprise the driver stages in conjunction with the temperature compensation network and the power stages. In order to achieve high efficiency and small size MMIC based amplifiers and attenuators were evaluated and implemented in the driver stages. The block diagram of the driver amplifier is shown below in Figure 1.

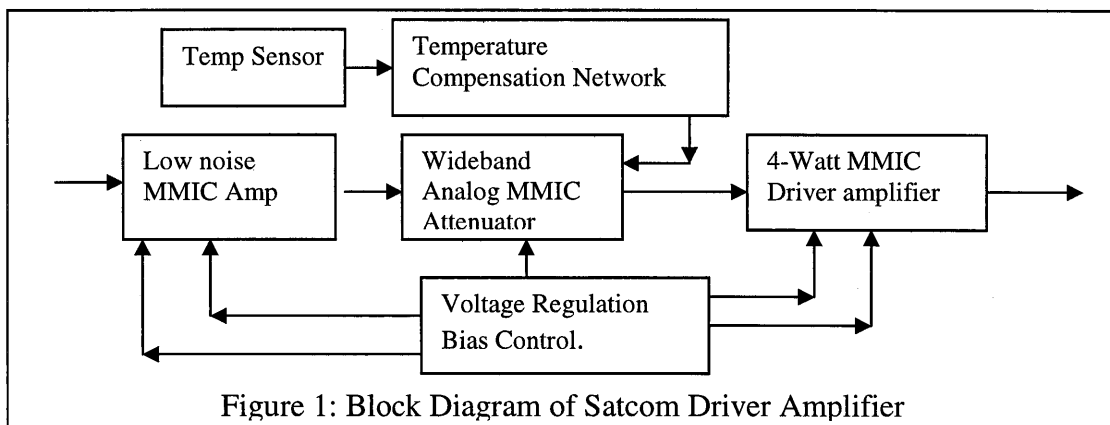
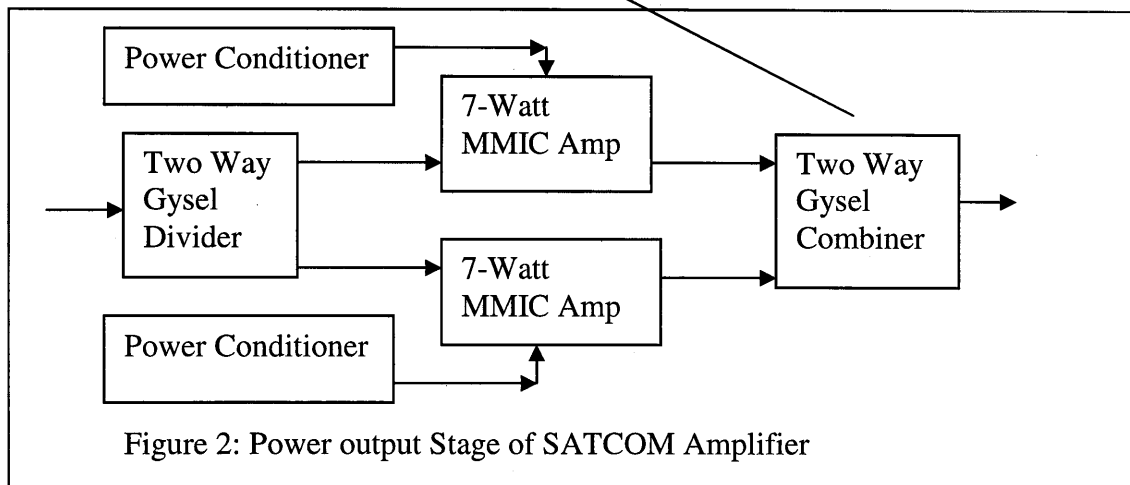
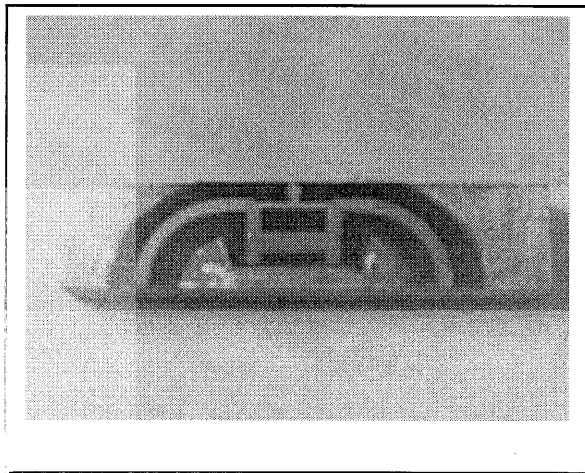


Figure 1: Block Diagram of Satcom Driver Amplifier

The driver amplifier exhibits an overall gain of 30 dB and a power output of 36 dBm at one dB of gain compression. The voltage regulation and bias control network provided positive and negative voltages to the MMIC amplifier and the attenuators.

The output of the driver amplifier drives the power output stages of the amplifier. The block diagram of the power stage is detailed in Figure 2. It consists of two 7-Watt MMIC power amplifiers that are combined in parallel using a low loss power combiner. The power combiner used, Gysel type, has demonstrated a low loss performance over a 20% bandwidth. The Gysel combiner is a modified Wilkinson power combiner, which has two resistors that are grounded. The main advantages of this structure are the use of external resistors that allow high power handling capability, easily realizable geometry and the capability of monitoring the imbalances at the output ports. However, Gysel power combiner/divider circuit has a narrower bandwidth as compared to the Wilkinson structure. In the design of this structure the resistors of the Wilkinson design are replaced by a network of two quarter wavelength 50-Ohm lines connected via a 35-Ohm transmission line. Only the breakdown voltage of the transmission line or heat dissipation capacity of the lines restricts the power handling capability of the divider. When used as a power combiner the termination resistors required power handling capability is determined from power rating of each resistor.



The power output stage gives a power output of 40 dBm with a Gain of 20 dB. Figure 3 shows a picture of the amplifier showing the integration of the driver amplifier and the power amplifier. Also shown is the temperature compensation circuit and bias network for the driver amplifier. The bias boards for the output stages are mounted under the housing. The power output stages consist of TGA-4915-EPU-CP packaged MMIC modules that are in production in Triquint. The amplifier is shown in Figure 4 and its performance shown in Figure 5. Detailed Amplifier performance will be presented.

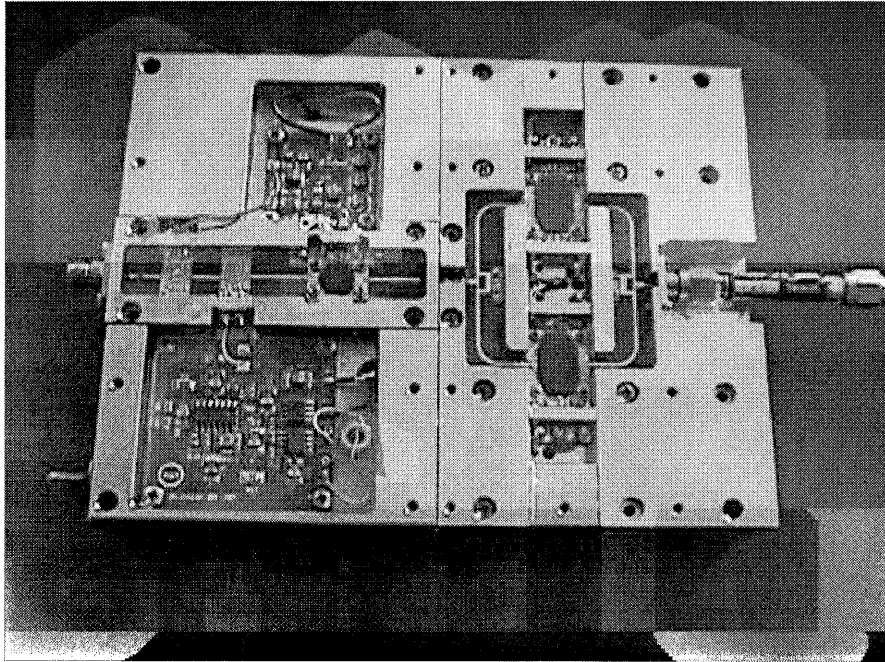
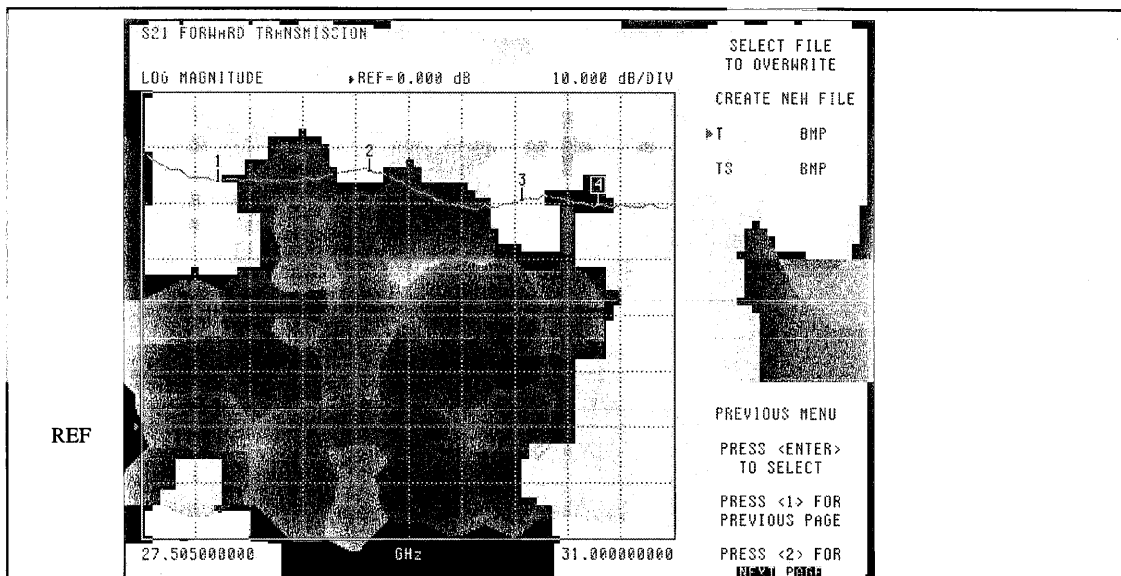


Figure 4: SATCOM Amplifier



Marker 1 28 GHz Markers 2: 29 GHz Markers 3: 30 GHz Markers 4: 30.5 GHz  
The data shows a minimum of 40 dB gain for the Amplifier

Figure 5: Measured Gain of 10-Watt SATCOM amplifier

### Milstar Amplifier

The technical specifications for the 43.5-45.5 GHz MILSTAR amplifier are detailed below. The amplifier has a power output and gain requirements of 40 dBm and 50 dB respectively. Other factors of importance are small size and high efficiency.

#### 44 GHz Amplifiers

	<b>Parameter</b>	<b>Unit</b>	<b>Specification</b>
1.	Frequency	<b>GHz</b>	44 GHz
2.	Bandwidth	<b>MHz</b>	2000 MHz
3.	Gain	<b>dB</b>	50
4.	Power Output	<b>dBm</b>	40
5.	Noise Figure	<b>dB</b>	10
6.	Spurious	<b>dBc</b>	<-75
7.	Operating Temperature	<b>C</b>	-30 to 80
8.	Efficiency	<b>%</b>	>20
9.	Size	<b>Inches</b>	TBD

### Radial Power Combiners

Binary combiners typically combine two devices at a time. Radial combiners are those, which combine the output of N devices in one step. The losses associated with the adders of the binary structure degrade the combining efficiency, as the number is increase. The N-way combining structures are designed to combine the output power of N devices per MMICs in one step. Therefore this scheme has the potential for higher power combining efficiency. A difficult aspect of designing a combiner is finding an efficient scheme that offers low loss, good amplitude and phase tracking and high power capability. A careful optimization of the physical structure is essential to obtain a high combining efficiency together with high isolation and broad bandwidth. We have selected the radial combiner for Milstar amplifier because it permits the placement of large number of ports very close to the central combining port. High combining efficiency results when the combiner path and corresponding loss are kept to a minimum. The design is based on a 26-way Waveguide combiner. The Waveguide input is transformed into a coaxial waveguide that is inserted into a radial cavity. The radial cavity has 26 TE 01 waveguide outputs at its periphery. The splitter combiner is shown in Figure 6 below. The measured insertion loss of 0.5 dB has been achieved over the entire band.

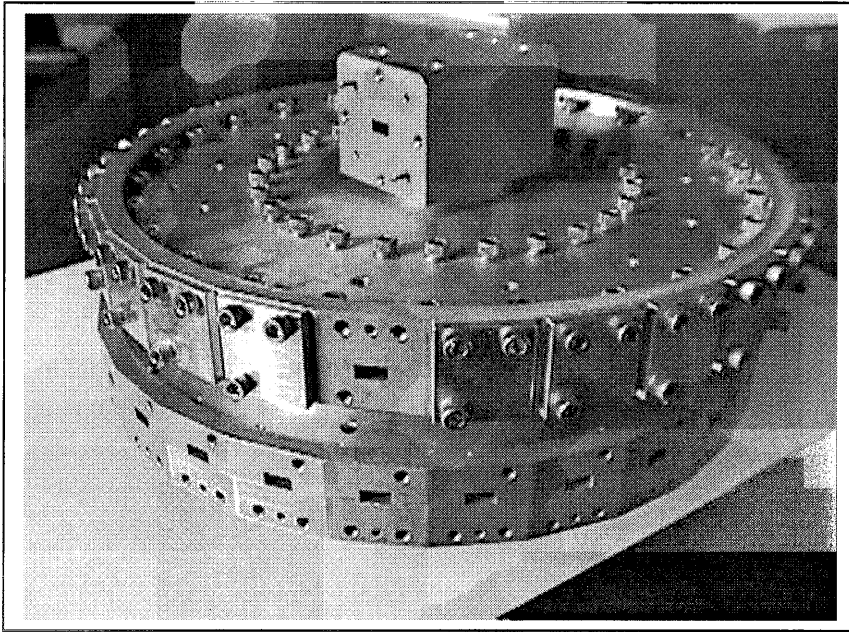
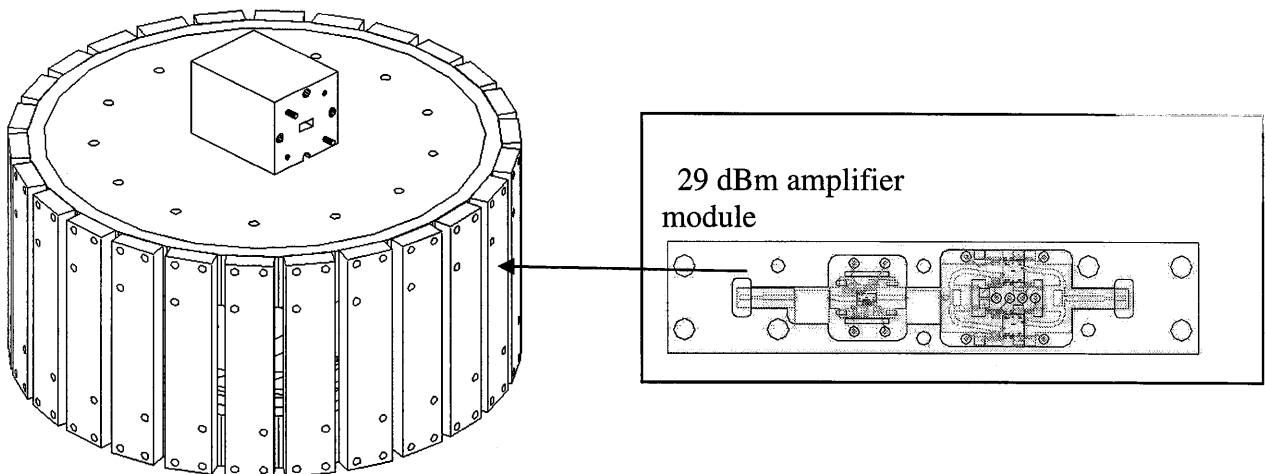


Figure 6: Radial power Splitter and Combiner

### Amplifier Format

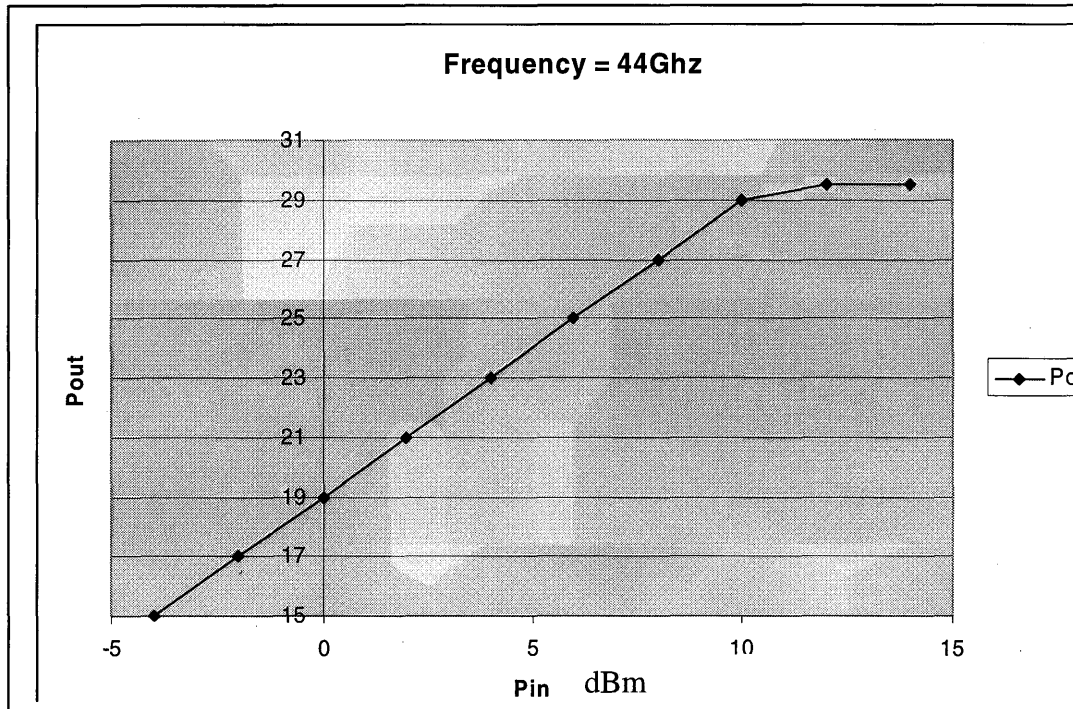
The amplifier consists of 26 modules that are attached to the radial combiner on the vertical periphery, as shown below. Each module consists of a driver amplifier followed by a 29 dBm power amplifier. The overall gain each module is 30 dB. In order to achieve the best performance from the radial combiner each MMIC amplifier that has been selected has an input return loss better than -15 dB. The assembly of the amplifier module is also detailed below. The voltage regulation and bias control id mounted between the two radial structures.





## Measured Results

The measured results of the 29 dBm module are shown in Figure 7. The driver amplifier consists of two MMIC amplifiers assembled in line. The PAE of the module is 11%



## Conclusion

Solid State Power amplifiers for 30 GHz SATCOM and 44 GHz MILSTAR have been designed and fabricated measurements have been conducted. The amplifier is powered from a single +12 Volt supply which has full sequencing and regulation. The measured performance of the amplifier showed a power output of 41 dBm with a power added efficiency of 9%. The format of the amplifier allows changing of the modules quickly and allows newer devices technology to be implemented without any major redesigns. The physical format agility of the amplifier configuration allows it to achieve higher output powers, by changing the modules, without much expense and redevelopment..

# A Constrained Pattern Synthesis Technique for a Circular IFF Array Antenna

Matthew S. Lasater and Herbert M. Aumann  
Lincoln Laboratory, Massachusetts Institute of Technology  
Lexington, MA 02420-9108

**Abstract:** This paper details two algorithms for synthesizing sum and difference patterns of a 108-element, L-band circular array built by the Office of Naval Research. The array is a candidate for the next generation Identification Friend or Foe (IFF) radar system on the U.S. Navy's airborne surveillance aircraft, the E-2C Hawkeye. The IFF system's performance depends on creating sum and difference patterns with widely separated power distributions in the patterns' sidelobe regions while maintaining the sum and difference pattern characteristics in the mainlobe region. Two constrained algorithms are presented for generating acceptable sum and difference patterns. One algorithm is based on solving a nonlinear optimization problem; one is based on solving a generalized eigenvalue problem. The pattern synthesis algorithms incorporate realism through using the measured amplitude and phase data from each of the 108 L-band elements of the prototype array. The paper summarizes the extraction of the individual element patterns from the experimental data, explains the two synthesis algorithms, and discusses several simulations to resolve the effectiveness of the algorithms when applied to realistic element patterns. While both algorithms compute similar array patterns for each simulation, the generalized-eigenvalue-based algorithm more efficiently calculates the desired electrical excitation for each element in the array.

## 1. Introduction

As a part of an ongoing modernization program, the U.S. Navy's E-2C Hawkeye aircraft, the airborne early warning aircraft employed in U.S. naval operations, is undergoing several technological upgrades. Replacing the present mechanically steered radar system will be one that is electronically steered, increasing the system's scanning rate while decreasing the aircraft's structural requirements for utilizing the radar. One candidate being considered for the new radar uses a combined UESA/IFF under development by the Office of Naval Research (ONR). The UHF electronically scanned array (UESA) is the primary radar and is a circular array comprised of 54 UHF elements while the Identification Friend or Foe (IFF) antenna, consisting of 108 L-band elements in a circular array, is a secondary surveillance radar for interrogating aircraft.

---

This work is sponsored by the Office of Naval Research under Air Force Contract #FA8721-05-C-0002. Opinions, interpretations, recommendations and conclusions are those of the authors and are not necessarily endorsed by the United States Government.

An IFF radar system [1] identifies aircrafts by emitting a directional beam of electromagnetic radiation with a frequency of 1030 MHz. If the aircraft has an IFF transponder that detects the beam, the transponder will transmit relevant information back, replying with an omnidirectional response at a frequency of 1090 MHz. To avoid confusion and minimize erroneous transmission from aircraft present in the sidelobes of the IFF radar's directional beam, the IFF's method of interrogation consists of three consecutive pulses:  $P_1$ ,  $P_2$ , and  $P_3$ . The pulses  $P_1$  and  $P_3$  are transmitted by the interrogation beam, the directional beam of radiation sent by the IFF radar. Pulse  $P_2$  is transmitted by the control beam. The control beam has a null in the direction of the interrogation beam and has more power in the sidelobes than the interrogation beam. Transponders determine whether or not to respond by comparing the received power from the  $P_1$  and  $P_3$  pulses with the received power from the  $P_2$  pulse. If the power in the  $P_1$  and  $P_3$  pulses is greater than some threshold value when compared to the power in the  $P_2$  pulse, the transponder answers. Otherwise, the transponder does not reply. The goal of this paper is to develop a way of computing the electrical excitations for the array elements in the prototype circular phased array to create these interrogation and control beams. Here, these beams are made with sum and difference beams, where the sum beam corresponds to the interrogation beam and the difference beam corresponds to the control beam.

For the sum and difference beams, the elements' excitations are symmetric about the direction of the interrogation. For this particular circular array, this means the excitations of the 54 elements at one side of the look direction are mirror images of the 54 element excitations at the other side of the look direction. The sum beam is effected by adding the contributions of all 108 elements, in hopes of producing a beam with low sidelobes, high gain, and narrow beamwidth. The difference beam is made by adding the contributions of the 54 elements on one side of the look direction while subtracting the contributions of the 54 elements on the other side of the look direction. This subtraction is performed by altering the phase of outgoing radiation from these 54 elements. Due to the symmetry in the excitations, this difference beam has a null in the look direction of the interrogation. The next section explains the data collection from the 108 L-band elements for deriving the individual element patterns. The incorporation of authentic element patterns into the pattern synthesis algorithms will allow for realistic computer simulations, leading to more accurately computed excitations.

## 2. Data Analysis

The IFF element data was collected from the UESA antenna located on Makaha Ridge at the Pacific Missile Range Facility on January 13-14, 2005. Figure 1 gives a diagram of the experimental set-up. The diagram shows an overhead view of the experiment where a horn antenna was placed 298 feet from the base of the 108 element, IFF array with the  $n$ -th element lying on a circumference of a circle with nominal radius of 106 inches at an azimuth angle  $\varphi_n$ . Each of the elements were numbered 1 through 108. The horn antenna illuminated the IFF elements which collected amplitude and phase data of the incoming radiation.

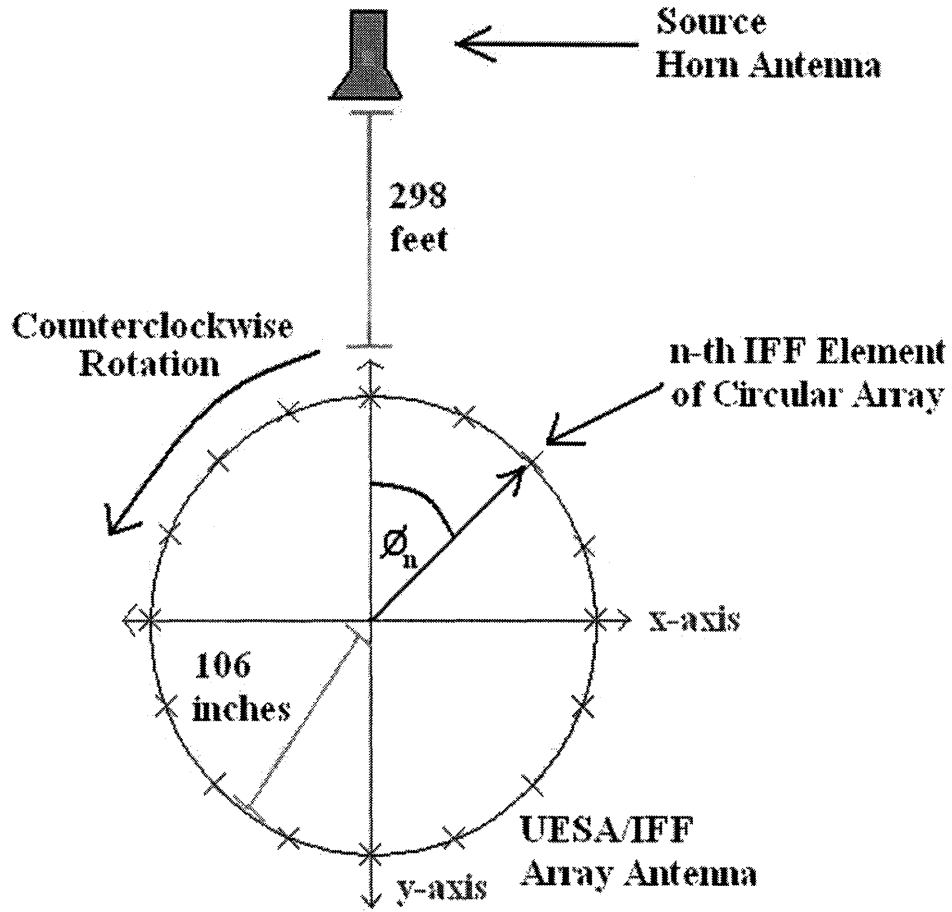


Figure 1. Experimental set-up

The frequency of the radiation ranged from 1000 MHz to 1100 MHz, taken in steps of 5 MHz, totaling 201 different frequencies. The array of elements was then rotated counterclockwise 2 degrees, and the amplitude and phase of the elements were measured. These steps were repeated until the array had rotated 360 degrees. Due to limitations in the measurement hardware, this collection process was performed twice in which 54 elements collected data each time.

With the collected data, we want to estimate the complex element pattern of each IFF element. For the  $n$ -th element, we denote the complex element pattern by

$$p_n(\theta) = M_n(\theta)e^{j\alpha_n(\theta)}, \quad (1)$$

where  $M_n(\theta)$  represents the amplitude variation of the  $n$ -th element pattern as a function of the azimuth angle  $\theta$ , and  $\alpha_n(\theta)$  represents the phase variation of the  $n$ -th element

pattern as a function of the azimuth angle  $\theta$ . Each element pattern's amplitude variation can be directly determined from the data while curve-fitting is required to determine the phase variation. Figure 2 shows representative amplitude data collected from one of the IFF elements, Element No. 40.

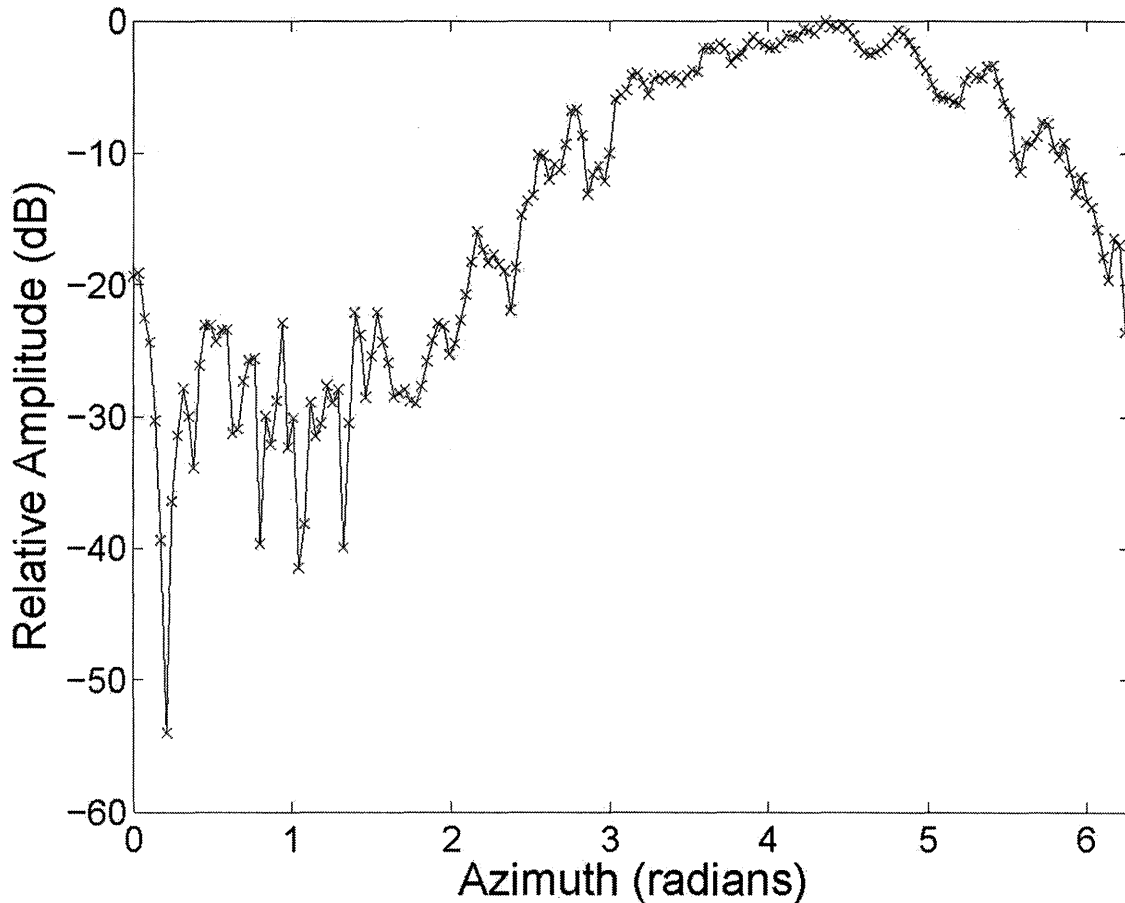


Figure 2. Element No. 40's amplitude data at 1030 MHz

### 2.1. Phase Calculation

To determine the element pattern phase variation  $\alpha_n(\theta)$  from the collected phase data, we have to remove the phase effects created by the geometry of the experimental set-up. The phase of the incident electromagnetic wave depends on the distance the wave has to travel to the element. The rotation of the array alters the elements' positions and therefore the incoming phases the elements receive. This effect must be accounted for when estimating the phase variation  $\alpha_n(\theta)$ . If we let  $R$  denote the distance of the source horn to the  $n$ -th element,  $r$  be the radius of the circular array, and  $\theta$  be the angle which the

array has been rotated, the distance from the source horn to the  $n$ -th element is given by  $\sqrt{R^2 + r^2 - 2Rr \cos(\theta - \varphi_n)}$ . Thus, the phase of an incoming electromagnetic wave that has traveled to the  $n$ -th element which has rotated through an angle of  $\theta$  is given by

$$\Omega_n(\theta) = \frac{2\pi}{\lambda} \sqrt{R^2 + r^2 - 2Rr \cos(\theta - \varphi_n)}, \quad (2)$$

with  $\lambda$  being the wavelength of the wave. We rewrite this expression for the incoming phase  $\Omega_n(\theta)$  as

$$\Omega_n(\theta) = \frac{2\pi}{\lambda} \sqrt{[R - r \cos(\theta - \varphi_n)]^2 + r^2 \sin^2(\theta - \varphi_n)}. \quad (3)$$

For  $\theta \approx \varphi_n$ , we have  $\sin^2(\theta - \varphi_n) \approx 0$ , and therefore

$$\Omega_n(\theta) \approx \frac{2\pi}{\lambda} [R - r \cos(\theta - \varphi_n)] \quad (4)$$

for  $\theta \approx \varphi_n$ . For the  $n$ -th element, we concentrate on  $\theta \approx \varphi_n$  because this corresponds to when the circular array has rotated the  $n$ -th element to the front, where the element is closest to the source array. When an element is at the back of the array, metallic structures within the circular array shield the element from the source horn. These structures scatter the incoming radiation, leading to noisy data. Therefore, when we model the effects that the rotation of the array causes on the phase data, we will emphasize the angles where the element is close to the source antenna. The model we use to describe the phase data collection as a function of azimuth angle of rotation  $\theta$  is

$$d_n(\theta) = \alpha_n(\theta - \varphi_n) + b_n + a_n \cos(\theta + c_n), \quad (5)$$

where  $d_n(\theta)$  is the phase data of the  $n$ -th as a function of  $\theta$  and  $a_n$ ,  $b_n$ , and  $c_n$  are curve-fit coefficients. The term  $\alpha_n(\theta - \varphi_n)$  is used instead of  $\alpha_n(\theta)$  to compensate for the fact that the IFF elements are not all initially aligned with the horn at  $\theta = 0$  degrees. Figure 3 shows a sample phase data collection from Element No. 40. From Figure 3 we see that

the phase data appears to have a sinusoidal relationship with the azimuth angle and that the data at the trough of the wave looks noisy. When the phase data is at its crest, the element is closest to the horn element at the front of the array, and when the phase data is at its trough, the element is located at the back of the array, far away from the horn antenna.

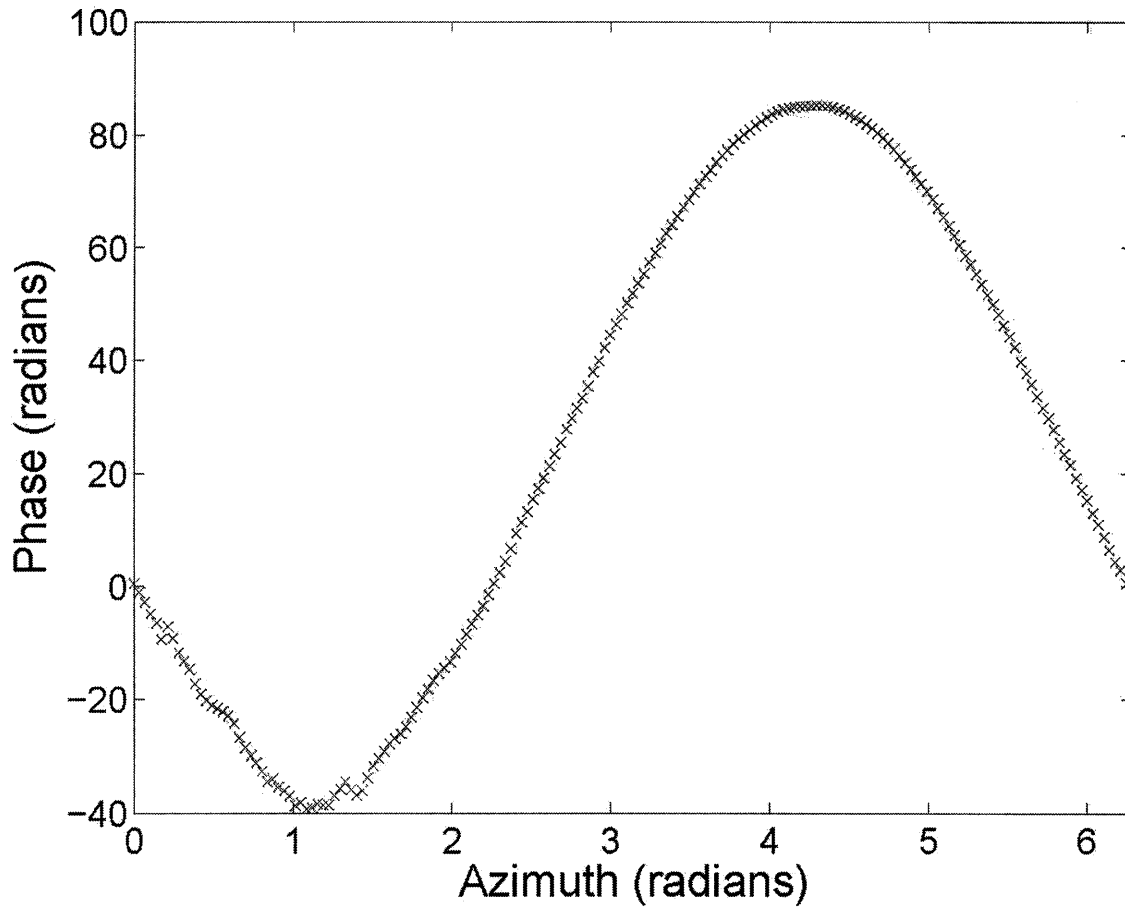


Figure 3. Element No. 40's phase data at 1030 MHz

To compute the fit coefficients  $a_n$ ,  $b_n$ , and  $c_n$  for the  $n$ -th element's phase data, we minimize the weighted nonlinear least-squares cost function

$$J(a, b, c) = \sum_{p=1}^P \mu_p [d_n(\theta_p) - a \cos(\theta_p + c) - b]^2, \quad (6)$$

over the azimuth angles where the data was collected,  $\{\theta_p\}_{p=1}^P$ , and where  $\mu_p \geq 0$  is the weight of the data collected at angle  $\theta_p$ . Figure 4 presents the data shown in Figure 3 with a curve-fit that equally weighted all the angles, and Figure 5 shows the data from Figure 3 with a curve-fit that only considered angles near the crest, where the weights were proportional to the linear amplitude. A MATLAB implementation of a Levenberg-Marquardt algorithm was used to solve the weighted nonlinear least-squares problem for the fit coefficients. As Figure 4 and Figure 5 show, using all the data is not a good idea since the noisy data at the trough corrupts the curve fitting, as we had expected.

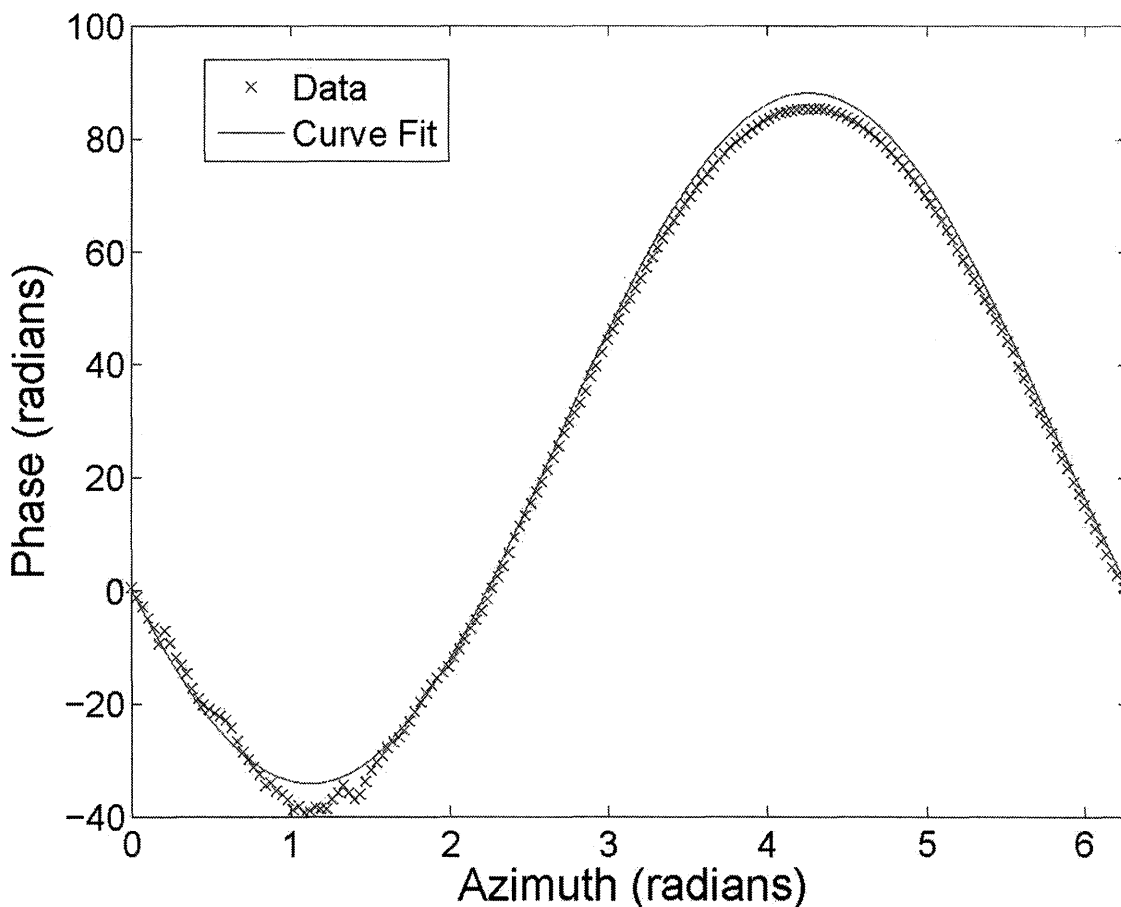


Figure 4. Curve-fitting with uniformly weighted phase data

Subtracting the curve-fit from the data gives the estimated phase variation  $\alpha_n(\theta - \varphi_n)$ . There will be large variation due to the poor signal-to-noise ratio when the element was at the back side of the array. To correct for this, we weighted the phase data by the element's corresponding amplitude data for the angles that corresponded to the element being at the back side of the array. Figure 6 compares the unweighted and weighted



estimation of the phase variation  $\alpha_n(\theta - \varphi_n)$  for Element No. 40. In the pattern synthesis algorithms, we use the weighted estimation of the phase variation. In the next section, we discuss how we utilized the phase data to estimate the azimuth location  $\varphi_n$  of each element.

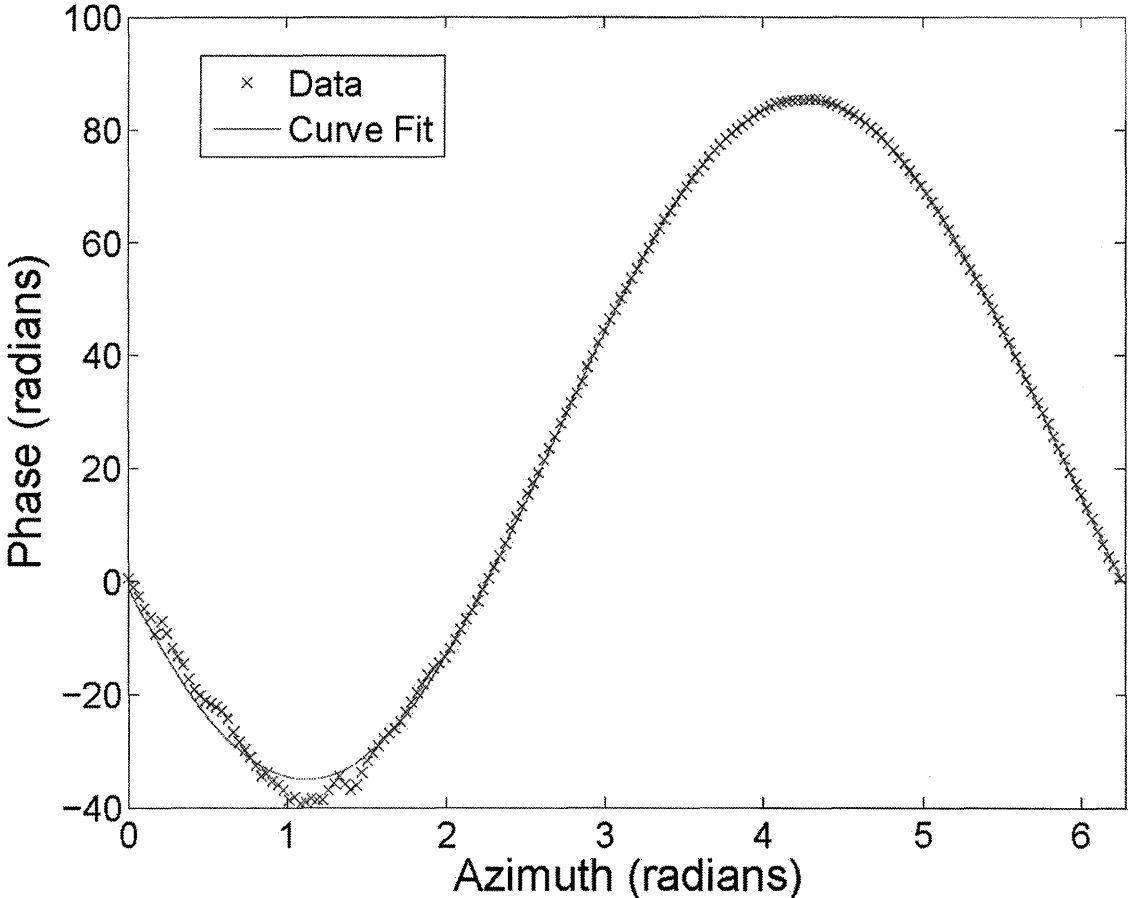


Figure 5. Curve-fitting with amplitude weighted phase data

**2.2. Azimuth Location Estimation**

As we previously stated, for each element in the array, the collected phase data appears sinusoidal with the crest occurring when the element was aligned with the source horn antenna. Therefore, we can accurately estimate the azimuth location  $\varphi_n$  of each element by determining at what azimuth rotation angle  $\theta$  the phase data was at a maximum. To compute this angle, we chose a 120 degree section about the crest of the phase data and fitted this data with a fourth degree polynomial by solving a standard least-squares problem. The estimated azimuth angle  $\varphi_n$  was the root of the derivative of this polynomial which was closest to the crest of the phase data. This method of

determining  $\varphi_n$  was easier to implement than trying to determine  $\varphi_n$  through differentiating Equation 2 and further manipulating the data. Figure 7 gives an example of the polynomial-fitting of the phase data to compute the azimuth location  $\varphi_n$ . Theoretically, since the 108 IFF elements are equally spaced along the circumference of the circle, the angular distance between two adjacent elements should be  $\frac{360}{108}$  degrees  $\approx 3.333$  degrees. Figure 8 plots the angular difference between adjacent elements from the estimated values of  $\varphi_n$ 's. As seen from Figure 8, this method closely agrees to what is theoretically predicted, producing  $\varphi_n$ 's with an average angular difference of 3.3333 degrees and standard deviation of 0.2934 degrees. A pattern of spikes in the estimated  $\varphi_n$ 's are apparent in Figure 8. The authors of [2] explain the spikes in the data by the presence of spokes in the circular array located at certain azimuth angles.

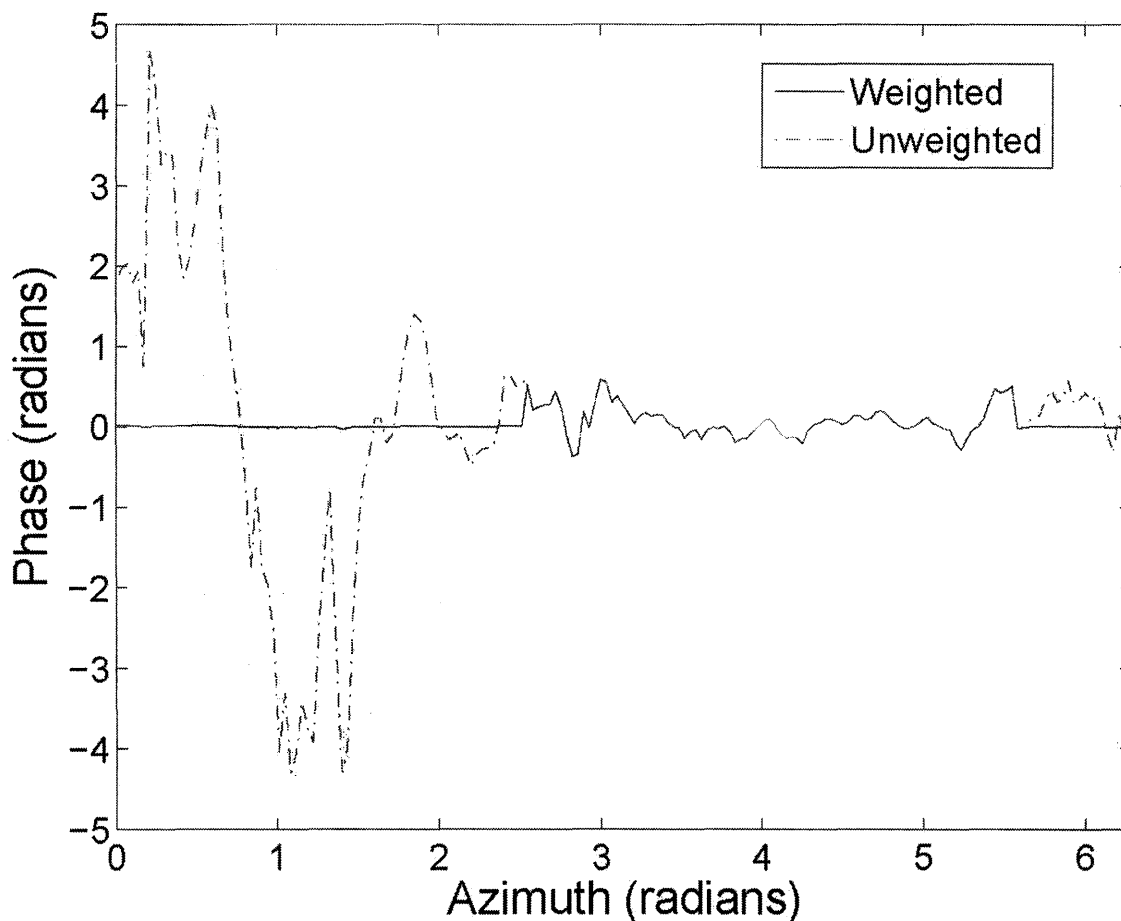


Figure 6. Weighted and unweighted estimation of  $\alpha_n(\theta - \varphi_n)$  for Element No. 40 at 1030 MHz

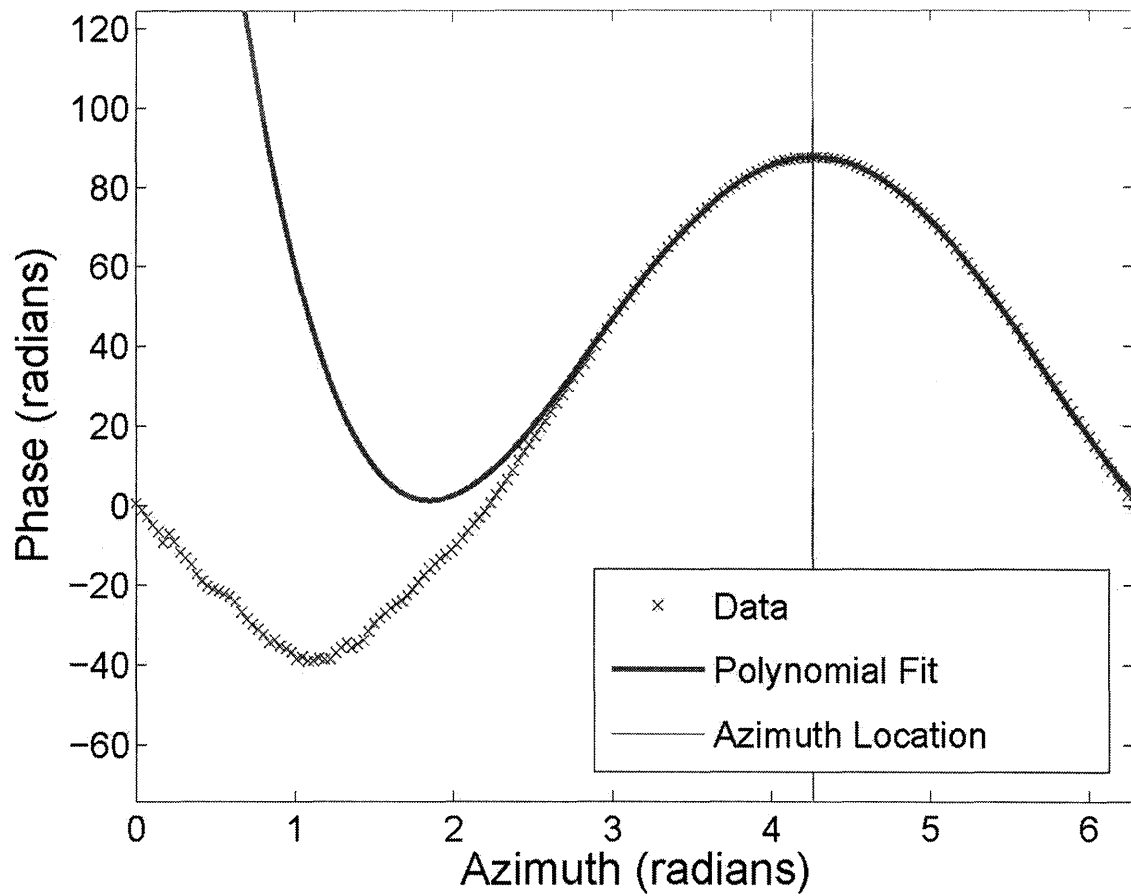


Figure 7. Example of azimuth location estimation

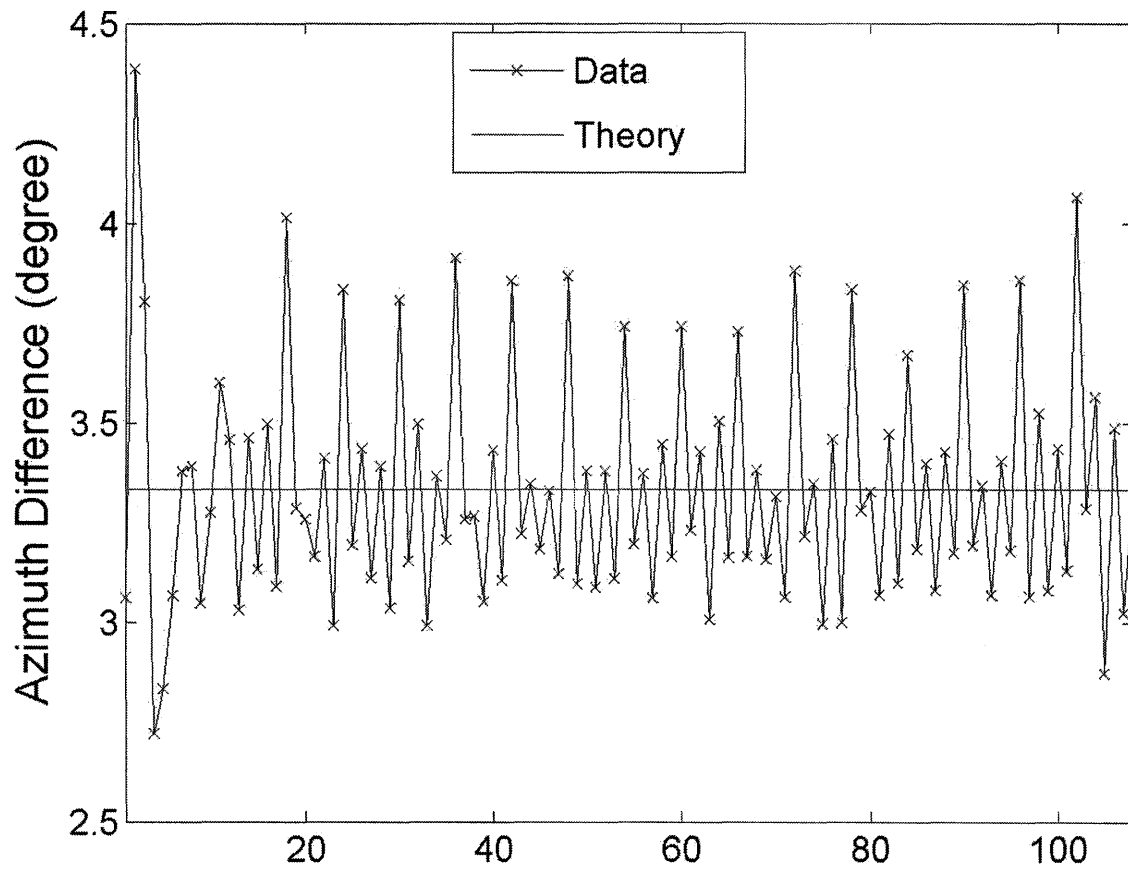


Figure 8. Azimuth differences between adjacent elements

### 3. Pattern Synthesis

After analyzing the collected data to estimate the individual element patterns of the IFF elements, we want to determine how to electrically excite these elements to generate the desired radiation patterns. Consider a circular array that has a radius  $r$  with  $N$  elements, each of which is radiating electromagnetic waves of wavelength  $\lambda$ . If  $\varphi_n$  is the angular location of the  $n$ -th element, the azimuth dependency of the far-field radiation pattern generated by the array is given by

$$F(\theta) = \sum_{n=1}^N w_n p_n(\theta - \varphi_n) e^{jkr \cos(\theta - \varphi_n)}, \quad (7)$$

where  $\theta$  is the azimuth angle,  $w_n$  is the complex excitation of the  $n$ -th element,  $p_n(\theta)$  is the element pattern of the  $n$ -th element, and  $k = \frac{2\pi}{\lambda}$ . The power in this radiation field at angle  $\theta$  is given by the formula  $P(\theta) = |F(\theta)|^2$ .

For the remainder of this paper, we will use the following notation:  $\mathbf{R}^N$  is the space of  $N$ -dimensional vectors of real numbers,  $\mathbf{C}^N$  is the space of  $N$ -dimensional vectors of complex numbers,  $\mathbf{R}^{M \times N}$  is the space of  $M \times N$  real matrices, and  $\mathbf{C}^{M \times N}$  is the space of  $M \times N$  complex matrices. Let  $\{\theta_m\}_{m=1}^M$  be the collection of  $M$  angles where the radiation pattern is sampled, and define the vectors  $\vec{w} \in \mathbf{C}^N$  and  $\vec{F} \in \mathbf{C}^M$  as

$$\vec{w} = [w_1 \quad w_2 \quad \dots \quad w_N]^T \text{ and } \vec{F} = [F(\theta_1) \quad F(\theta_2) \quad \dots \quad F(\theta_M)]^T, \quad (8)$$

where  $\vec{w}$  is the  $N$ -dimensional vector containing the element excitations and  $\vec{F}$  is the  $M$ -dimensional vector containing the radiation field samples at  $M$  angles  $\{\theta_m\}_{m=1}^M$ . Here,  $T$  denotes the transpose operation. The relationship between vectors  $\vec{w}$  and  $\vec{F}$  is defined through Equation (7) and can be specified with the matrix  $D \in \mathbf{C}^{M \times N}$

$$D = \begin{bmatrix} p_1(\theta_1 - \varphi_1) e^{jkr \cos(\theta_1 - \varphi_1)} & p_2(\theta_1 - \varphi_2) e^{jkr \cos(\theta_1 - \varphi_2)} & \dots & p_N(\theta_1 - \varphi_N) e^{jkr \cos(\theta_1 - \varphi_N)} \\ p_1(\theta_2 - \varphi_1) e^{jkr \cos(\theta_2 - \varphi_1)} & p_2(\theta_2 - \varphi_2) e^{jkr \cos(\theta_2 - \varphi_2)} & \dots & p_N(\theta_2 - \varphi_N) e^{jkr \cos(\theta_2 - \varphi_N)} \\ \vdots & \vdots & \ddots & \vdots \\ p_1(\theta_M - \varphi_1) e^{jkr \cos(\theta_M - \varphi_1)} & p_2(\theta_M - \varphi_2) e^{jkr \cos(\theta_M - \varphi_2)} & \dots & p_N(\theta_M - \varphi_N) e^{jkr \cos(\theta_M - \varphi_N)} \end{bmatrix} \quad (9)$$

by

$$\vec{F} = D\vec{w}. \quad (10)$$

We will use  $\vec{w}_S$  and  $\vec{w}_D$  to represent the excitation vectors for the sum beam and difference beam respectively. By arranging and numbering the elements accordingly, the symmetry constraints on the sum and difference weights become

$$\left(\vec{w}_S\right)_n = \left(\vec{w}_S\right)_{N+1-n} \text{ and } \left(\vec{w}_D\right)_n = -\left(\vec{w}_D\right)_{N+1-n} \text{ for } n = 1, 2, \dots, \frac{N}{2} \quad (11)$$

where the notation  $\left(\vec{w}\right)_n$  denotes the excitation of the  $n$ -th element. Note that since  $-1 = e^{j\pi}$ , the anti-symmetry expressed in the difference beam excitations by Equation 10 can be achieved by applying a phase shift of  $\pi$  radians to the appropriate half of the elements. Also, if we define the partitioned matrix  $Q \in \mathbf{R}^{N \times N}$  by

$$Q = \begin{bmatrix} -I & 0 \\ 0 & I \end{bmatrix}, \quad (12)$$

where  $I$  is the identity matrix of order  $\frac{N}{2}$ , then we can relate  $\vec{w}_S$  and  $\vec{w}_D$  by

$$\vec{w}_D = Q\vec{w}_S, \quad (13)$$

in the case where the first  $\frac{N}{2}$  elements are subtracted in the difference beam. In the case where the last  $\frac{N}{2}$  elements are subtracted in the difference beam, the same relation holds with  $Q$  replaced by  $-Q$ . We will now discuss the two synthesis algorithms to determine the excitations.

### 3.1. Generalized Eigenvalue Method

The first synthesis algorithm we considered is based on formulating a generalized eigenvalue problem. In fact, one can view this algorithm as an extension of a method for computing optimal excitations for an adaptive phased array of elements in the presence of

jammers [3]. Let  $\{\theta_m\}_{m=1}^M$  be the set of  $M$  sample angles in the sidelobe region of the interrogation beam where we will compare the sum and difference patterns. We want to determine a set of symmetric electrical excitations such that at each angle  $\theta_m$ , the power in the sum beam (interrogation beam),  $P_S(\theta_m)$ , is equal to a fraction of the power in the difference beam (control beam),  $P_D(\theta_m)$ . That is,  $P_D(\theta_m) = \beta_m P_S(\theta_m)$ , where  $\beta_m > 1$  is determined by the desired power separation between the sum and difference beams at  $\theta_m$ . Let  $\theta^*$  be the look direction of the sum beam. We will then look for the symmetric electrical excitations that minimizes

$$\frac{\sum_{m=1}^M z_m [P_D(\theta_m) - \beta_m P_S(\theta_m)]}{P_S(\theta^*)}. \quad (14)$$

This cost function will penalize excitations that create sum and difference beams with sidelobe power levels that do not meet the desired levels and where the sum beam has low gain. Here,  $z_m$  is a weighting coefficient, allowing the cost function to give more or less emphasis to each particular angle  $\theta_m$ .

To see how minimizing this cost function is equivalent to solving a generalized eigenvalue problem, we first note that the numerator in Equation 14 can be rewritten as

$$\sum_{m=1}^M z_m [P_D(\theta_m) - \beta_m P_S(\theta_m)] = \sum_{m=1}^M z_m |F_D(\theta_m)|^2 - \sum_{m=1}^M z_m \beta_m |F_S(\theta_m)|^2. \quad (15)$$

Combining Equations 10 and 12 gives

$$\sum_{m=1}^M z_m |F_D(\theta_m)|^2 = \vec{w}_S^H Q^H D^H Z D Q \vec{w}_S, \quad (16)$$

with  $H$  denoting the complex-conjugate transpose operation and  $Z \in \mathbf{R}^{M \times M}$  as the diagonal weighting matrix

$$Z = \begin{bmatrix} z_1 & 0 & 0 & 0 \\ 0 & z_2 & 0 & 0 \\ 0 & 0 & \ddots & 0 \\ 0 & 0 & 0 & z_M \end{bmatrix}. \quad (17)$$

Define  $\Psi \in \mathbf{R}^{M \times M}$  as the diagonal matrix used to specify the desired power separation at each angle  $\theta_m$

$$\Psi = \begin{bmatrix} \beta_1 & 0 & 0 & 0 \\ 0 & \beta_2 & 0 & 0 \\ 0 & 0 & \ddots & 0 \\ 0 & 0 & 0 & \beta_M \end{bmatrix}. \quad (18)$$

Then, by using Equation 10, we have

$$\sum_{m=1}^M z_m \beta_m |F_S(\theta_m)|^2 = \vec{w}_S^H D^H Z \Psi D \vec{w}_S. \quad (19)$$

Finally, defining the matrix  $A \in \mathbf{C}^{N \times N}$  as

$$A = Q^H D^H Z D Q - D^H Z \Psi Z D, \quad (20)$$

the numerator from Equation 14 can be compactly written as  $\vec{w}_S^H A \vec{w}_S$ . Setting  $\vec{R} \in \mathbf{C}^N$  as

$$\vec{R} = \left[ p_1(\theta^* - \varphi_1) e^{jkr \cos(\theta^* - \varphi_1)} \quad p_2(\theta^* - \varphi_2) e^{jkr \cos(\theta^* - \varphi_2)} \quad \dots \quad p_N(\theta^* - \varphi_N) e^{jkr \cos(\theta^* - \varphi_N)} \right], \quad (21)$$

and the matrix  $B \in \mathbf{C}^{N \times N}$  as  $B = \vec{R}^H \vec{R}$ , then by Equation 10, the denominator of Equation 13 can be written as



$$P_s(\theta^*) = |F_s(\theta^*)|^2 = \vec{w}_s^H B \vec{w}_s. \quad (22)$$

Thus, Equation 14, the cost function we are trying to minimize, is equal to

$$\frac{\vec{w}_s^H A \vec{w}_s}{\vec{w}_s^H B \vec{w}_s}. \quad (23)$$

To enforce the symmetry constraint given in Equation 11, we form the matrix  $K \in \mathbf{R}^{N/2 \times N}$

$$K = \begin{bmatrix} 1 & 0 & \dots & 0 & 0 & 0 & 0 & \dots & 0 & -1 \\ 0 & 1 & \dots & 0 & 0 & 0 & 0 & \dots & -1 & 0 \\ \vdots & \vdots & \ddots & \vdots & \vdots & \vdots & \vdots & \ddots & \vdots & \vdots \\ 0 & 0 & \dots & 1 & 0 & 0 & -1 & \dots & 0 & 0 \\ 0 & 0 & \dots & 0 & 1 & -1 & 0 & \dots & 0 & 0 \end{bmatrix}. \quad (24)$$

The minimization problem can now be stated as:

$$\min_{\vec{w}_s \in C^N} \frac{\vec{w}_s^H A \vec{w}_s}{\vec{w}_s^H B \vec{w}_s} \text{ subject to } K \vec{w}_s = \vec{0}. \quad (25)$$

The final step is to convert this constrained minimization problem into an unconstrained minimization problem. To change the problem, we need to find a basis  $V$  for the subspace of mirror symmetric excitations. The columns of  $V \in \mathbf{R}^{N \times N/2}$  given by

$$V = \begin{bmatrix} 1 & 0 & 0 & \dots & 0 \\ 0 & 1 & 0 & \dots & 0 \\ 0 & 0 & 1 & \dots & 0 \\ \vdots & \vdots & \vdots & \ddots & \vdots \\ 0 & 0 & 0 & \dots & 1 \\ 0 & 0 & 0 & \dots & 1 \\ \vdots & \vdots & \vdots & \ddots & \vdots \\ 0 & 0 & 1 & \dots & 0 \\ 0 & 1 & 0 & \dots & 0 \\ 1 & 0 & 0 & \dots & 0 \end{bmatrix} \quad (26)$$

form such a basis. Now, every mirror symmetric excitation vector can be written in the form

$$\vec{w}_S = V\vec{b}, \quad (27)$$

where  $\vec{b} \in \mathbf{C}^{N/2}$  is the coordinate vector of the excitation  $\vec{w}_S$  as expanded in the basis stored in  $V$ . For all vectors of the form  $\vec{w}_S = V\vec{b}$ , the constraint is automatically satisfied since  $K\vec{w}_S = KV\vec{b} = 0\vec{b} = \vec{0}$ . Thus, the minimization problem given in Equation 25 can be restated as

$$\min_{\vec{b} \in \mathbf{C}^{N/2}} \frac{\vec{b}^H \widehat{A} \vec{b}}{\vec{b}^H \widehat{B} \vec{b}}, \quad (28)$$

where  $\widehat{A} = V^H A V$  and  $\widehat{B} = V^H B V$ . Computing the gradient of Equation 28 and setting it to zero gives

$$\widehat{A} \vec{b} = \gamma \widehat{B} \vec{b}, \quad (29)$$

where  $\gamma = \frac{\vec{b}^H \widehat{A} \vec{b}}{\vec{b}^H \widehat{B} \vec{b}}$ . Therefore, the extremal values of Equation 28 are the generalized eigenvectors of the generalized eigenvalue problem stated in Equation 29. We want to choose the generalized eigenvector that corresponds to the smallest generalized eigenvalue  $\gamma$ . Since  $\widehat{B}$  is a rank-one, Hermitian matrix,  $\widehat{B}$  is singular with an orthonormal collection of eigenvectors such that  $\frac{N}{2} - 1$  eigenvectors of  $\widehat{B}$  correspond to a zero eigenvalue. These  $\frac{N}{2} - 1$  eigenvectors of  $\widehat{B}$  induce  $\frac{N}{2} - 1$  generalized eigenvectors for the generalized eigenvalue problem, corresponding to infinite generalized eigenvalues [4]. Thus, the generalized eigenvector of Equation 29 that pairs with the smallest generalized eigenvalue is induced by the remaining eigenvector of  $\widehat{B}$ ,  $V^H \vec{R}^H$ . This generalized eigenvector is  $\vec{b} = \widehat{A}^{-1} V^H \vec{R}^H$ . So the optimal symmetric excitation vector is

$$\vec{w}_S = V \vec{b} = V(V^H A V)^{-1} V^H \vec{R}^H. \quad (30)$$

### 3.3. Nonlinear Optimization Method

The second algorithm solves a nonlinear optimization problem to find the excitations. The cost function to be optimized is similar to the one used in the generalized eigenvalue problem. Since the separation in the power of the two beams is usually specified in decibels, this cost function uses this measurement unit to relate the power of these beams. We will again let  $\theta^*$  be the look direction and  $\{\theta_m\}_{m=1}^M$  be a collection of sidelobe directions where the sum and difference beams will be compared. Let  $\{\delta_m\}_{m=1}^M$  be the specified power separations in decibels of the sum and difference beam at the angles  $\{\theta_m\}_{m=1}^M$ . The cost function for a symmetric excitation  $\vec{w}_S$  is

$$f(\vec{w}_S) = \sum_{m=1}^M g(\theta_m)^2, \quad (31)$$

where

$$g(\theta_m) = \max\{0, 20 \log_{10}[|F_S(\theta_m)|] + \delta_m - 20 \log_{10}[|F_D(\theta_m)|]\}, \quad (32)$$

with these sum and difference field values ( $F_S(\theta_m)$  and  $F_D(\theta_m)$  respectively) calculated using Equations 10 and 13. The function  $g$  compares the separation of the sum and difference beams in decibels at angle  $\theta_m$ , and if the separation is greater than or equal to  $\delta_m$ , the function returns zero; if the separation is less than  $\delta_m$ , a penalty is incurred. The symmetry constraint is met by using the excitations on one set of  $\frac{N}{2}$  elements as optimization parameters, and then enforcing a mirror symmetry with the remaining  $\frac{N}{2}$  elements when calculating field values with Equations 10 and 13.

#### 4. Comparison of Synthesis Algorithms

Using the estimated element patterns for each of the 108 L-band elements, MATLAB simulations compared the performance of the two algorithms. The data collected from the test site at the Pacific Missile Range Facility included a contiguous numbering of the elements about the circular array. With this ordering, the look direction  $\theta^*$ , which is the azimuth angle midway between the elements number 54 and 55, was taken as  $\theta^* = 196$  degrees. In these simulations, the last half of the elements were subtracted for the difference beam. We used the following metrics to compare the results produced by the algorithms: the gain of the sum beam, the maximum sidelobe of the sum beam, and the beamwidth of the sum beam.

We considered two cases for evaluating the algorithms, one using all 108 elements and a second case using the 16 elements closest to the look direction. Table 1 lists the metrics for the results produced by the algorithms in the case of using all 108 elements as well as the run times for the two algorithms. Table 2 does the same for the case of using only 16 elements. In both cases, a desired power separation of 20 dB between the sum and difference patterns for all sample directions was specified. When using all 108 elements, the sample direction included the entire sidelobe region. When using only 16 elements though, since we did not expect to be able to control the performance of the beams far from the look direction due to the fewer number of elements used, we only sampled the sidelobes in the azimuth range of 100 degrees to 250 degrees. For the generalized eigenvalue method, all sample directions were equally weighted. For the nonlinear optimization method, we used a quasi-Newton method inherent to MATLAB for solving the optimization problem. Figures 9-16 plot the radiation patterns and excitations generated by the algorithms in both cases. The figures and tables show that the results produced by both algorithms are very similar, but their computation times were quite different. For the 108 elements case, the eigenvalue method was thousands of time faster when compared to the optimization method, while in the 16 elements case, the eigenvalue method was hundreds of time faster than the optimization method.

Table 1. Comparison of Algorithms Using 108 Elements

Method	Gain	Max Sidelobe	Beamwidth	Run Time
Eigenvalue	21.31 dBi	-30.7 dB	4.8 deg	0.025 sec
Optimization	20.82 dBi	-25.5 dB	5.2 deg	104.167 sec

Table 2. Comparison of Algorithms Using 16 Elements

Method	Gain	Max Sidelobe	Beamwidth	Run Time
Eigenvalue	19.66 dBi	-23.7 dB	7.2 deg	0.003 sec
Optimization	19.30 dBi	-24.0 dB	7.8 deg	0.890 sec

When comparing the interrogation (sum) beam to the control (difference) beam, the IFF transponder will not reply if the power in the control beam is greater than the power received from the interrogation beam. When using all 108 elements, there are sidelobe angles where this condition is not met. In both the case of using 108 elements and the case of using 16 elements, the condition is met in the sidelobe region spanning 100 degrees about the look direction. This motivates us to use only 16 elements for the IFF interrogation since the demand on the IFF system diminishes when using fewer elements. As Table 1 and 2 show, the price we pay for choosing to use fewer elements is a decrease in the sum beam's gain and an increase in the sum beam's sidelobe power. The trade-off between using all the elements and fewer elements is resolved by the demands of the operating environment in which the IFF system is working.

#### 4.1 Quantization and Proccession Effects

In this section, for the case of using 16 active elements, we study the effects that quantizing the amplitude and phase of the excitations has on the beam performance as well as the effects of processing these 16 fixed excitations about the IFF array. We use the 16 excitations calculated with the generalized eigenvalue method. For the quantization effects, we fixed the amplitude quantization to be 6 bits, which means there are only 64 possible settings for the amplitude of each element. One possible setting is for the element to be turned off. The remaining 63 states are spread out evenly in decibels from a state of  $\frac{1}{100}$  of full amplitude to a state of full amplitude. We varied the number of bits used in the phase quantization, and Table 3 lists the degradation of the beam performance as the number of phase bits varies from 1 to 4 as compared to the beams generated in Figure 13 and summarized in Table 2. As Table 3 shows, when 4 bits

are used in the phase quantization, there is only a small appreciable degradation from the original results.

Table 3. Quantization Effects on Beamforming

No. of Phase Bits	Gain Loss	Max Sidelobe Increase	Beamwidth Widening
1	3.84 dBi	12.9 dB	8.3 deg
2	0.58 dBi	7.5 dB	0.2 deg
3	0.22 dBi	5.0 dB	-0.1 deg
4	0.06 dBi	0.0 dB	0.0 deg

The second effect we considered was taking the fixed 16 excitations and processing them about the circular array through the total possible 108 arrangements. Table 4 presents the statistics collected from these 108 simulations, describing the gain of the sum beam, the maximum sidelobe of the sum beam, the sum beam's beamwidth, and the null depth of the difference beam in the look direction. While most traits of the antenna were relatively unchanged as the excitations were moved about the array, the depth of the difference beam's null changed the most. This is because the difference beam produces a perfect null in the look direction only if the array has the previously discussed mirror symmetry. We do not have this due to the heterogeneous element patterns. As the excitations are processed, the deviation from the assumed mirror symmetry changes as well, affecting the depth of the null in the difference beam.

Table 4. Effects of Processing Weights Around Array

Statistic	Gain	Max Sidelobe	Beamwidth	Null Depth
Mean	19.4 dBi	-18.2 dB	7.3 deg	-22.2 dB
Stand. Dev.	0.2 dBi	2.4 dB	0.4 deg	6.9 dB
Minimum	18.9 dBi	-24.8 dB	6.8 deg	-54.9 dB
Maximum	19.8 dBi	-13.2 dB	9.5 deg	-12.7 dB

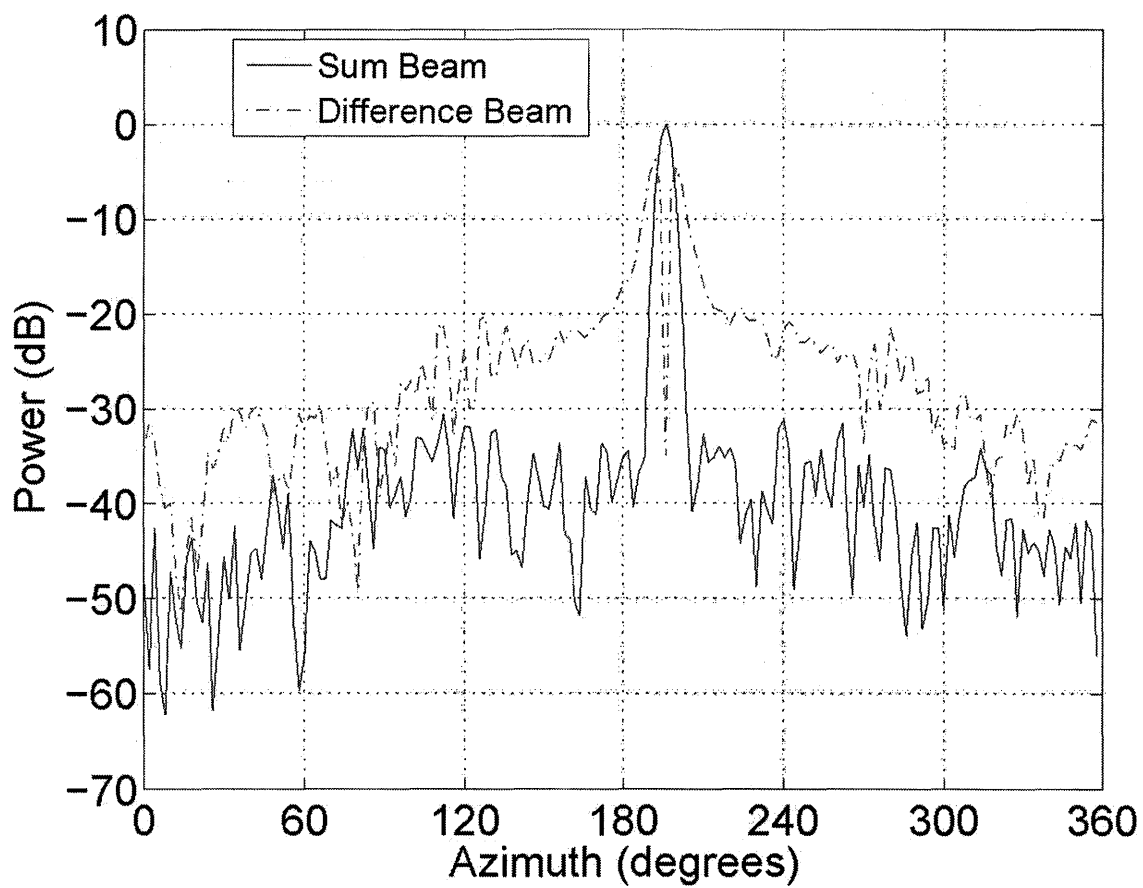


Figure 9. Sum and difference patterns from eigenvalue method with 108 elements

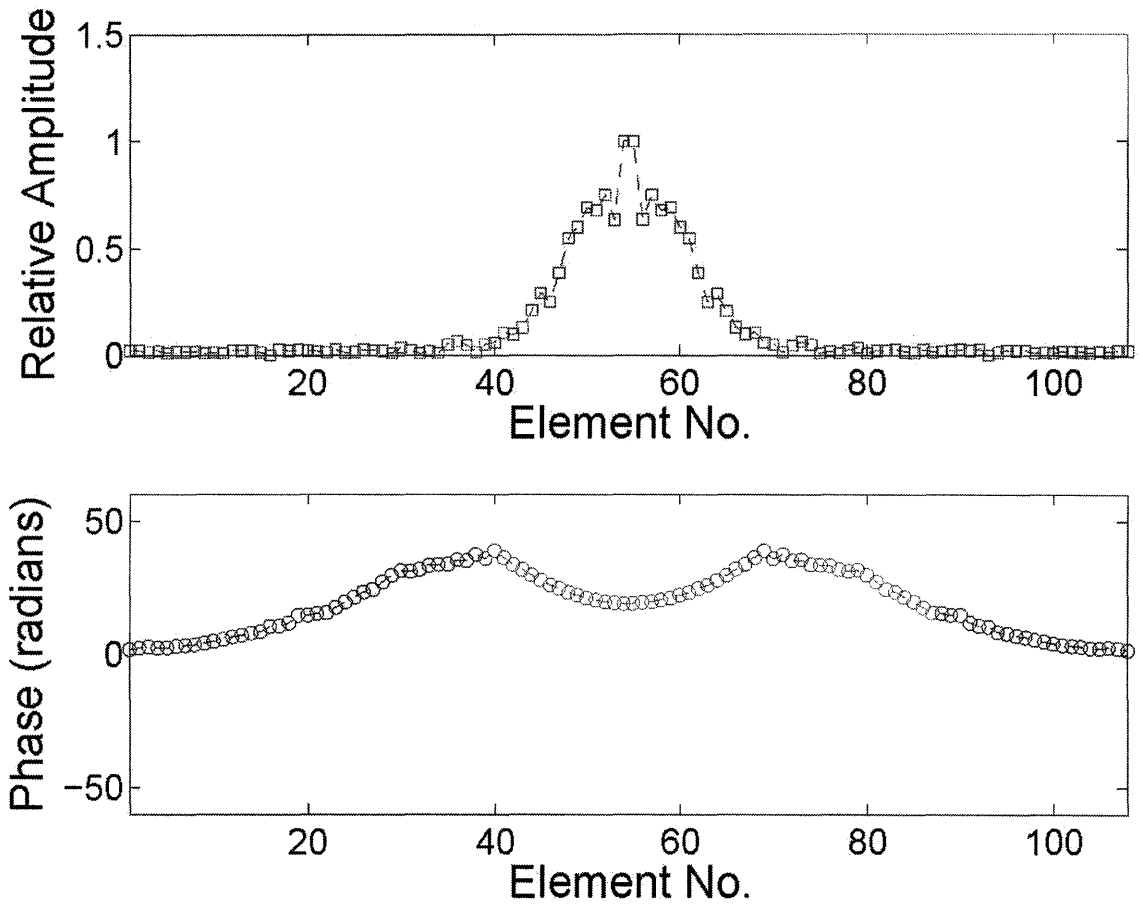


Figure 10. Sum pattern excitations (amplitudes and phases) from eigenvalue method with 108 elements



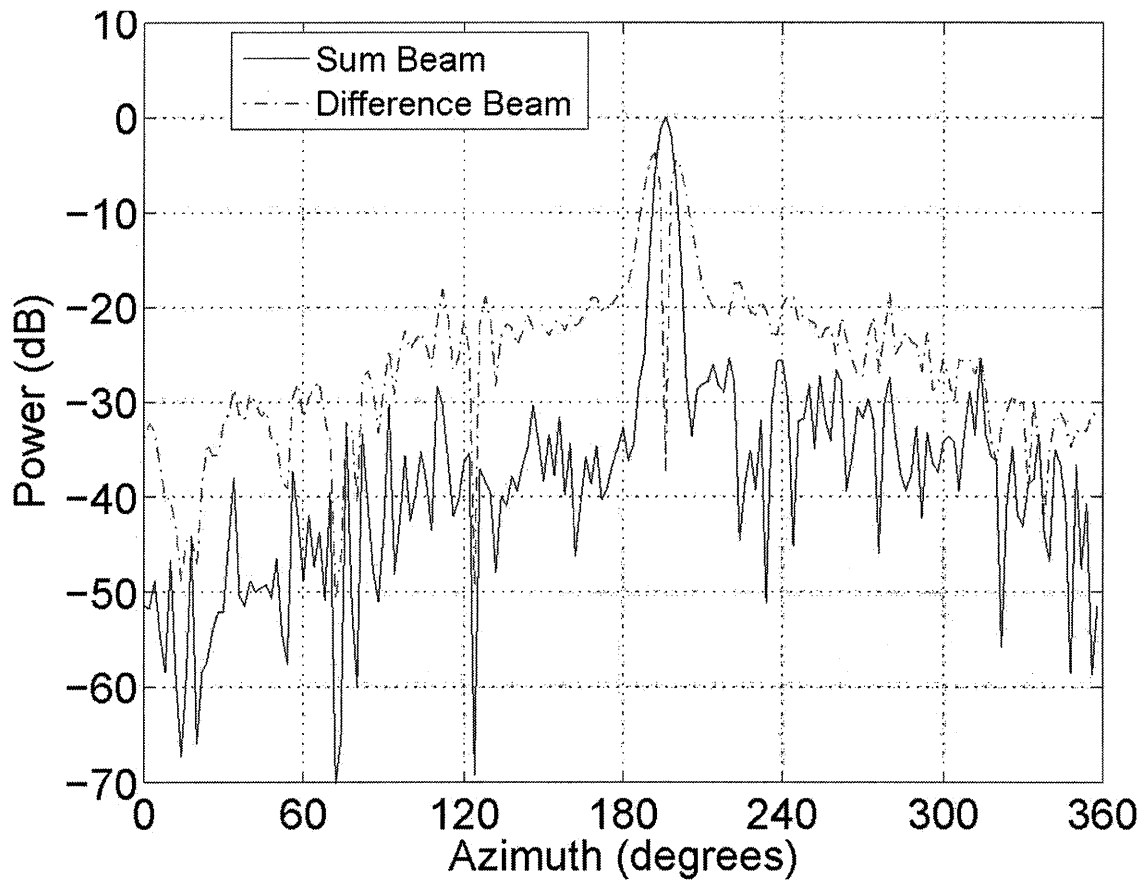


Figure 11. Sum and difference patterns from optimization method with 108 elements

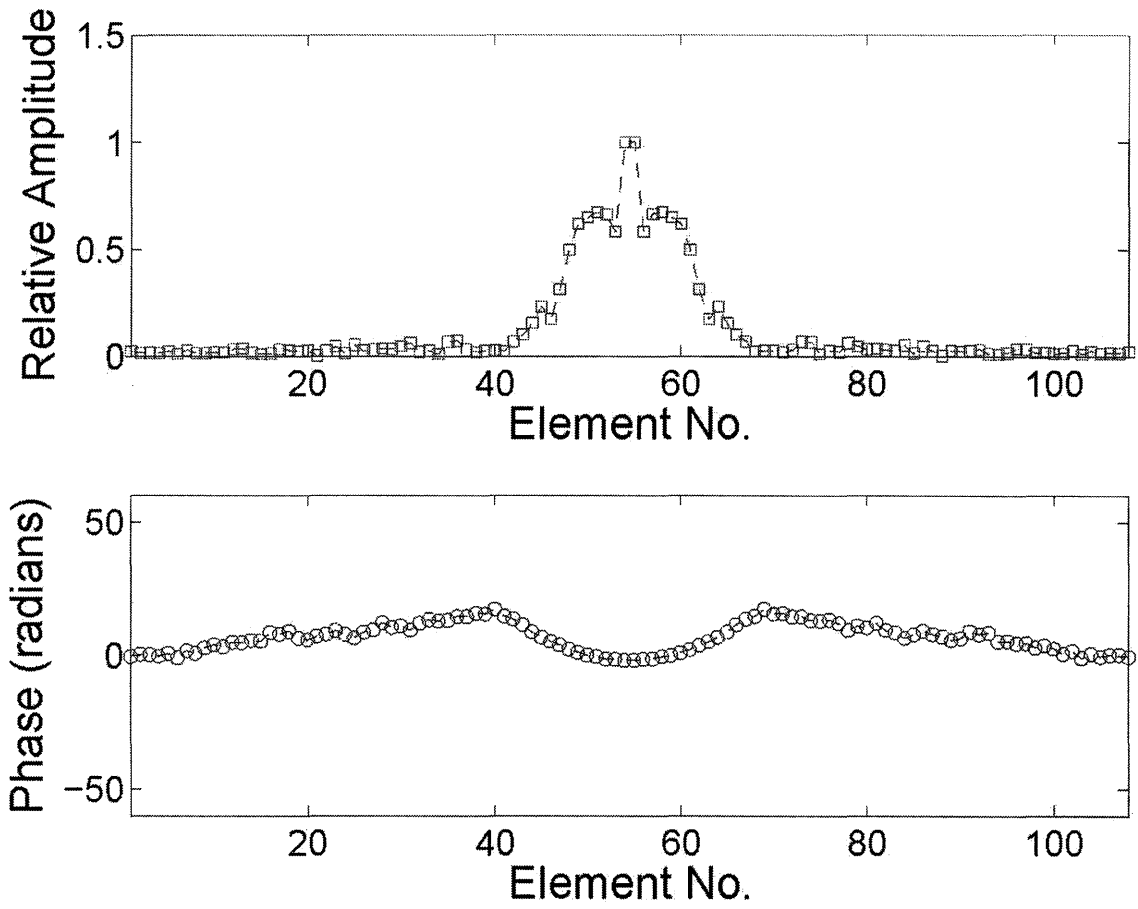


Figure 12. Sum pattern excitations (amplitudes and phases) from optimization method with 108 elements

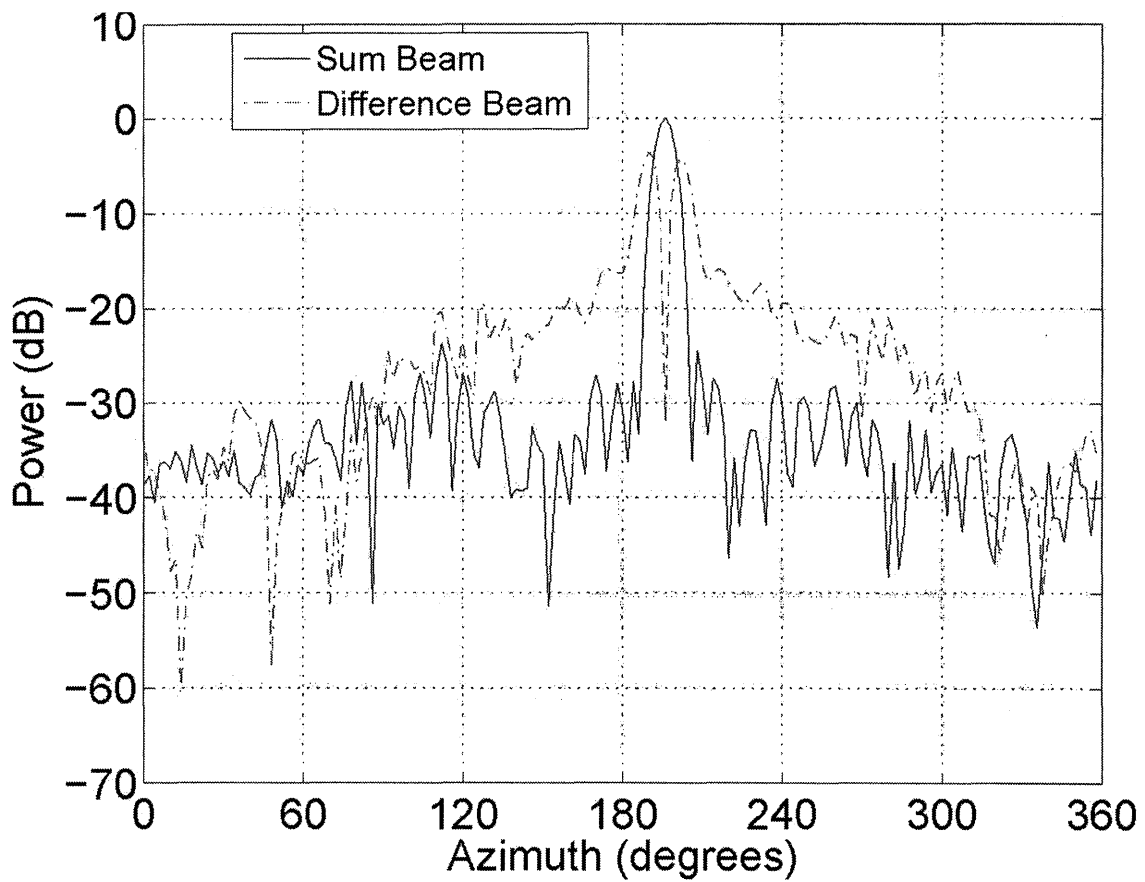


Figure 13. Sum and difference patterns from eigenvalue method with 16 elements

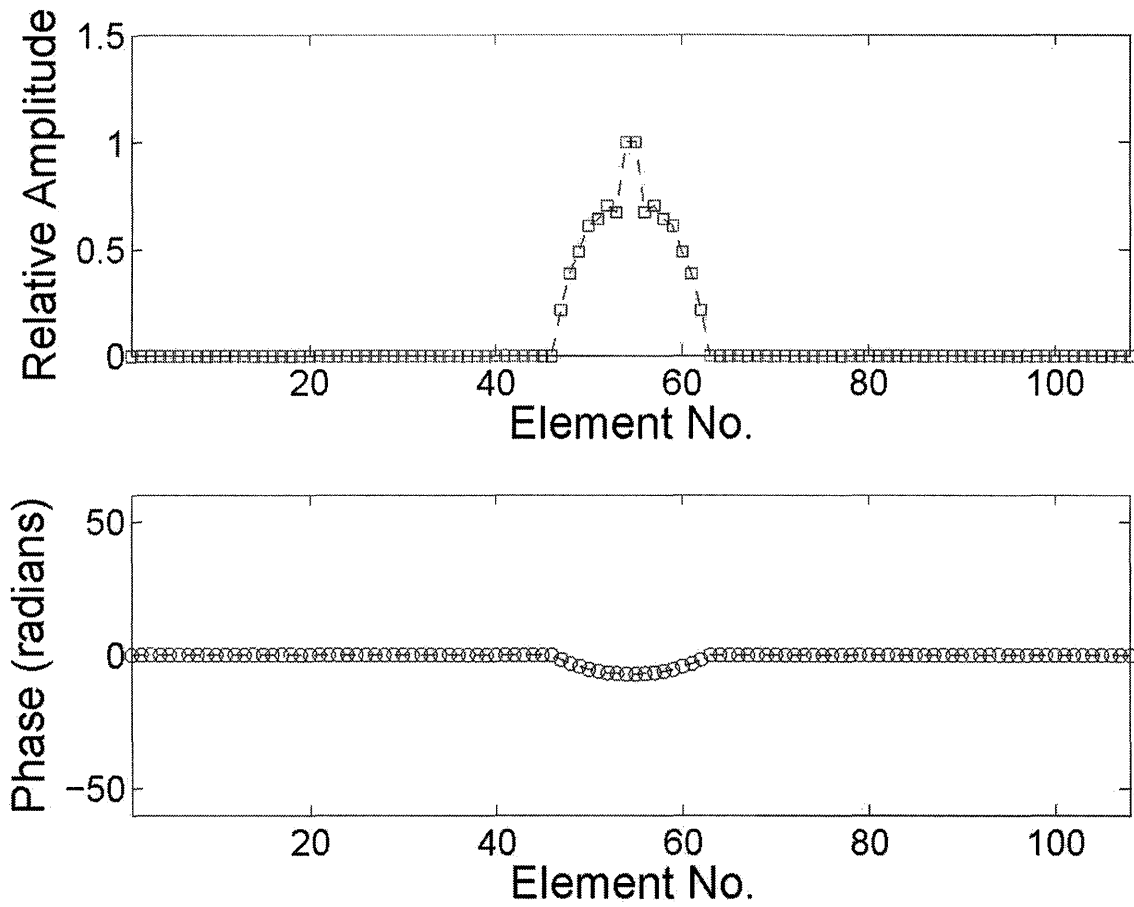


Figure 14. Sum pattern excitations (amplitudes and phases) from eigenvalue method with 16 elements

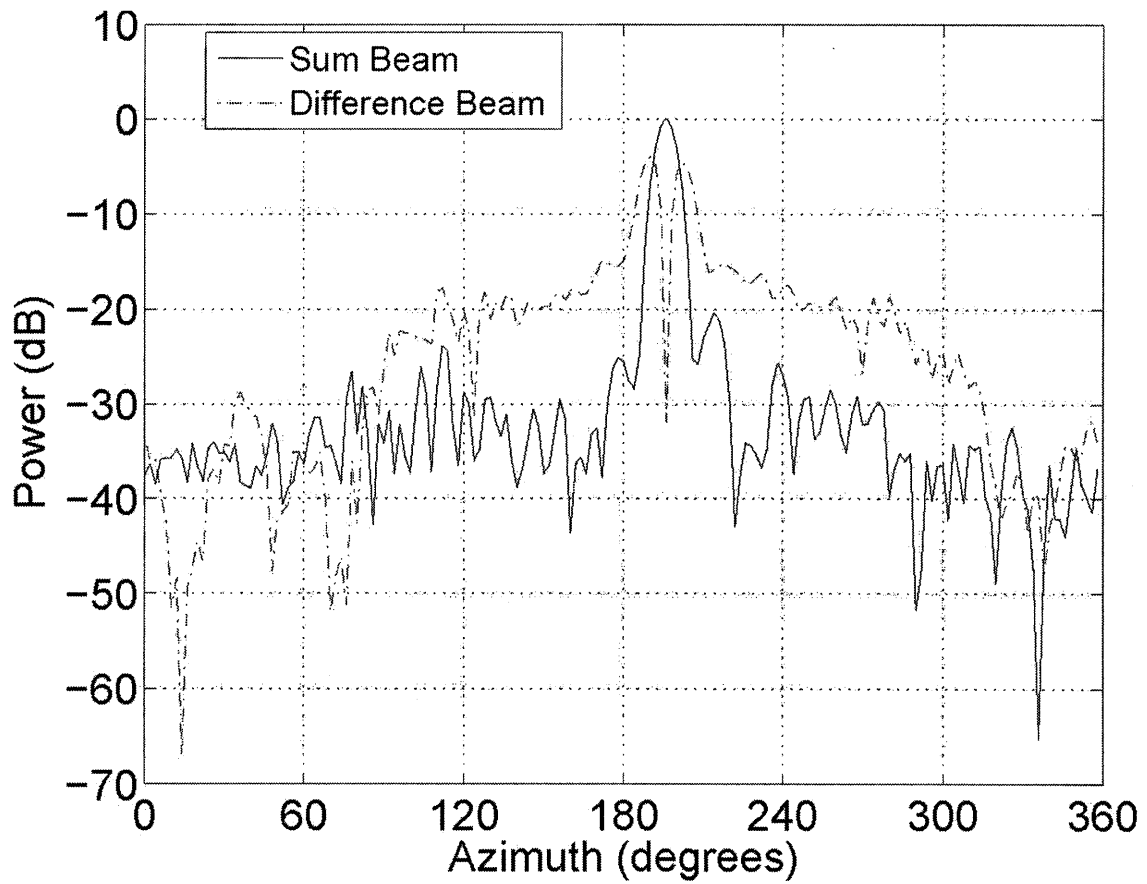


Figure 15. Sum and difference patterns from optimization method with 16 elements

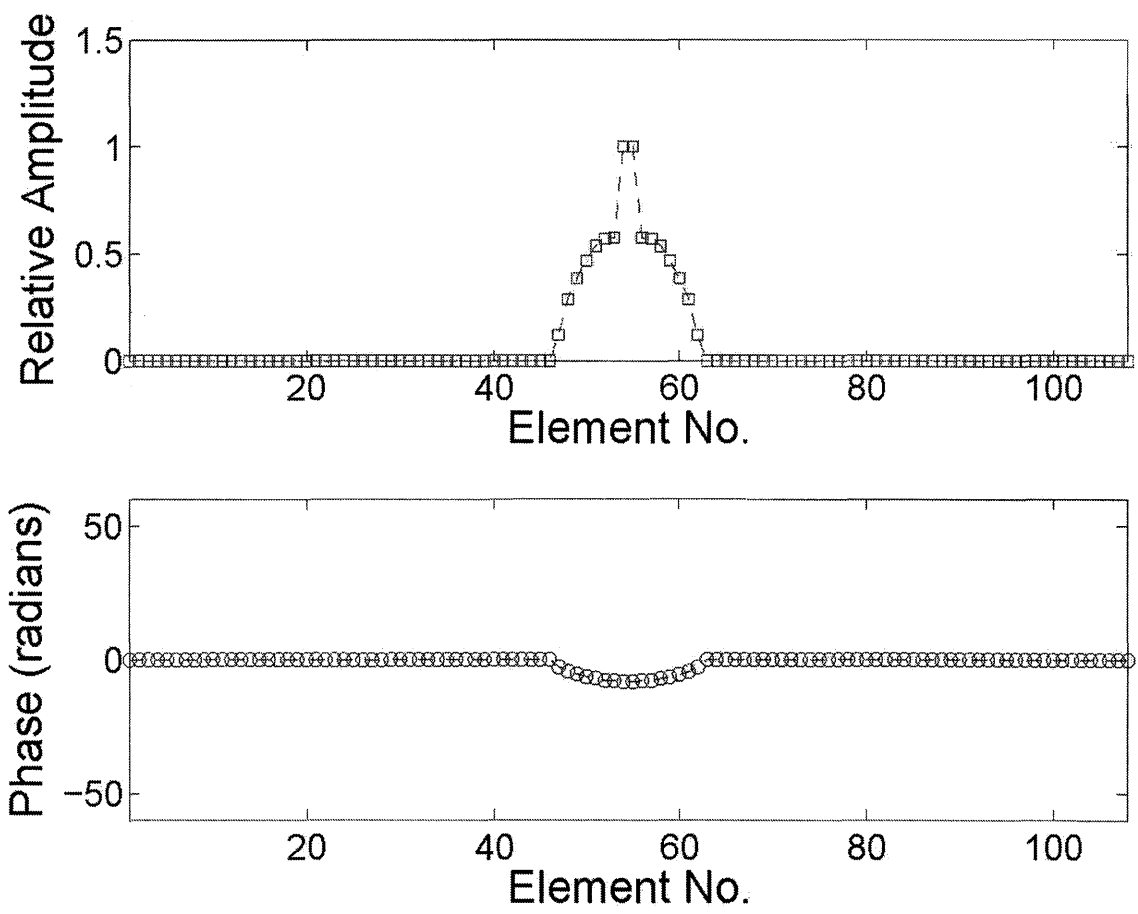


Figure 16. Sum pattern excitations (amplitudes and phases) from optimization method with 16 elements

## 5. Summary

This paper reports on the efficacy of two pattern synthesis algorithms when using data collected from an existing circular array of elements. From an analysis of experimental data, we estimated the individual element pattern for each element to compute more realistic excitations than those that would have been calculated with idealized element patterns. The method first described in the paper, the generalized eigenvalue method, can be related to a method to compute the optimal excitations for adaptive arrays and provides an analytical way of calculating the desired excitations for the sum and difference beams. The second algorithm, one that solves a nonlinear optimization problem, lacks the finesse of the eigenvalue method, requiring the use of an iterative method to perform the optimization. After comparing MATLAB simulations using the described synthesis algorithms, we found both methods yield similar results with the eigenvalue method running two or three orders of magnitude faster than the optimization method. The results of the simulations also suggest that not all 108 elements need to be in use when the IFF radar is interrogating nearby aircraft. We examined the case of using just 16 elements, including the effects of quantizing the excitations and processing a fixed set of 16 active excitations about the circular array. Since both algorithms produce comparable results, the generalized eigenvalue method is the recommended algorithm due to its greater efficiency at computing the excitations.

## 6. References

- [1] Michael C. Stevens, Secondary Surveillance Radar, Boston: Artech House, 1988.
- [2] H. M. Aumann and K. A. Tuttle, "Determination of Element Locations in a Circular Array from Measurements in the Fresnel Region". To appear in the Proceedings of the 2006 IEEE AP-S International Symposium.
- [3] S. P. Applebaum, "Adaptive Arrays", IEEE Trans. Ant. Propagat., vol. 24, no. 5, pp. 585-598, September 1976.
- [4] E. Anderson, Z. Bai, C. Bischof, S. Blackford, J. Demmel, J. Dongarra, J. Du Croz, A. Greenbaum, S. Hammarling, A. McKenney, and D. Sorensen, LAPACK User's Guide, Philadelphia: SIAM, 1999.